

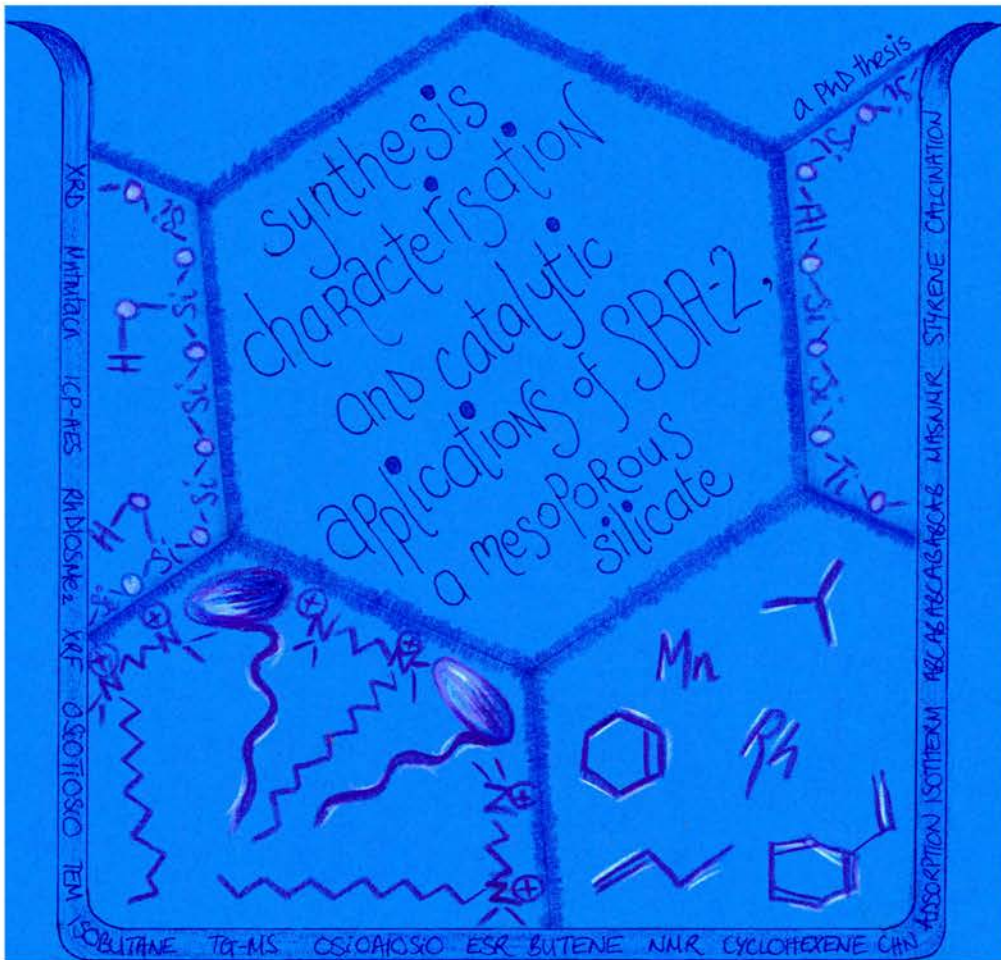
University of St Andrews



Full metadata for this thesis is available in
St Andrews Research Repository
at:

<http://research-repository.st-andrews.ac.uk/>

This thesis is protected by original copyright



St Andrews, May 2000

TH D652

Synthesis, Characterisation and Catalytic Applications of SBA-2, a Mesoporous Silicate

A thesis presented for the degree of
Doctor of Philosophy
in the Faculty of Science of the University of St. Andrews
by Hazel MA Hunter, B.Sc.



May 2000



Declarations

- (i) I, Hazel M A Hunter, hereby certify that this thesis, which is approximately 48000 words in length, has been written by me, that it is the record of work carried out by me and that it has not been submitted in any previous application for a higher degree.

- (ii) I was admitted as a research student in October, 1996 and as a candidate for the degree of PhD in October, 1997; the higher study for which this is a record was carried out in the University of St Andrews between 1996 and 2000.

- (iii) I hereby certify that the candidate has fulfilled the conditions of the Resolution and Regulations appropriate for the degree of PhD in the University of St Andrews and that the candidate is qualified to submit this thesis in application for that degree.

In submitting this thesis to the University of St Andrews I understand that I am giving permission for it to be made available for use in accordance with the regulations of the University Library for the time being in force, subject to any copyright vested in the work not being affected thereby. I also understand that the title and abstract will be published, and that a copy of the work may be made and supplied to any *bona fide* library or research worker.

for Dermot

Acknowledgements

There are lots of people I would like to thank, who have helped me during this work. Firstly, I owe a special debt to Dr Paul Wright who gave me inspiration and encouragement throughout. Secondly, Dr Wuzong Zhou was invaluable with his help imaging my samples under the HRTEM and analysing the results afterwards. Thirdly, my family and all my friends were fantastic. So in no particular order, thank you to: all the Hunters, Anne Lebas, Nick Everett, Kathryn Baker, Drs Graham Noble, Vinton Carter, Véronique Patinec, Nazira Karodia, Susan Blake, Ian Shannon, David Apperley, Enrique Sastre, Rob Gitzendanner, Richard Jennings, Prof. John Walton, Isabel Díaz, Martin Maple, Angus Calder, and the technical staff in Chemistry at St Andrews.

Abstract

The mesoporous silicate SBA-2 has been synthesised and extensively characterised. The material has subsequently been examined as a solid acid catalyst and as a transition metal catalyst support.

The SBA-2 silicate structure condenses around spherical diquatery ammonium Cn-s-1 surfactant agglomerations, in basic media. Thus the effects of reaction pH, temperature, time, surfactant/silica ratio and heteroatom incorporation upon the synthesis of well-ordered SBA-2 have been considered. A variety of characterisation techniques have been used including XRD, MAS NMR, Adsorption Isotherms and TG-MS. It appears that the unit cell dimensions and framework quality are principally influenced by the reaction pH, suggesting that subtle charge matching occurs at the surfactant-silica interface. A synthesis at pH 11-12 has the highest overall order.

The pore connectivity within the calcined solids was investigated using HRTEM. Both hcp and ccp (fcc) pore stacking sequences were imaged, and have been designated SBA-2 and STAC-1, respectively. Models of these topologies are proposed where each possesses 2D mesoporosity and can form with one of two particle morphologies: spherical or flat sheet-like. Hexagonal:cubic intergrowths have also been identified.

Direct synthesis framework aluminium incorporation is dependent upon the Al source, although in all cases the structural order and particle size are reduced compared with the pure silica forms. The resulting materials are mild solid acids, unable to catalytically crack isobutane, yet effective towards but-1-ene skeletal isomerisation. They are resistant to coking (deactivation). Analogous direct synthesis titanium incorporation does not perturb the framework order, yet evidence of oligomeric titanium species is presented. These Ti-containing solids were tested as alkene epoxidation catalysts, however, the results were inconclusive.

Attempts have been made to heterogenize Mn epoxidation and Rh hydroformylation catalytic complexes. Although surface tethering works, in general it has proved difficult to introduce the catalytic species. Most success was achieved with rhodium encapsulation, but catalyst leaching occurred during use.

Publications arising from this work

- Imaging the Pore Structure and Polytypic Intergrowths in Mesoporous Silica

W Zhou, HMA Hunter, PA Wright, Q Ge, JM Thomas,

J. Phys. Chem. B, 1998, **102**(36), 6933-6936.

- Synthesis and Characterisation of the Mesoporous Silicate SBA-2 and its Performance as an Acid Catalyst for the Isomerisation of But-1-ene

HMA Hunter, PA Wright,

in preparation

- Particle Morphology in the Mesoporous Silicate SBA-2

HMA Hunter, PA Wright, W Zhou,

in preparation

Abbreviations

1D	1-dimensional
2D	2-dimensional
3D	3-dimensional
β	Beta, a large pore zeolite of interconnecting channel structure
<i>a</i>	unit cell parameter
AAS	Atomic Absorption Spectroscopy
BET	Brunnauer-Emmett-Teller calculation of surface area (m^2g^{-1})
BJH	Barrett-Joyner-Halander calculation of pore size distribution
<i>c</i>	unit cell parameter
c.f.	compared to
<i>ca.</i>	circa
ccp	cubic close packed
CHN	elemental analysis (wt%) for carbon, hydrogen and nitrogen
cmc	critical micelle concentration
Cn-s-1	divalent quaternary ammonium surfactant of n carbons within the tail and s carbon atoms between the ammonium groups
<i>conc.</i>	concentrated
CP	Cross Polarization
CTAB	cetyltrimethylammonium bromide (16 carbons in the surfactant tail)
d_{hkl}	interplanar spacing
DIOSR ₂	(2R,3R)-2,2- <i>o</i> -isopropylidene-2,3-dihydroxy-1,4-bis(alkyl sulphanyl)butane derivatives
DP	Direct Polarization
DTA	Differential Thermal Analysis
DTG	Differential Thermal Gravimetry
EDX	Energy Dispersive X-ray spectroscopy
ESR	Electron Spin Resonance spectroscopy
EXAFS	Extended X-ray Absorption Fine Structure
FAU	faujasite (zeolite Y)
fcc	face centred cubic
FTIR	Fourier Transform Infra-red spectroscopy
FWHM	full width half maximum value
<i>g</i>	surfactant packing parameter
<i>g</i>	ESR g-factor
GC	gas chromatography
h	hour
hcp	hexagonal close packed
HRTEM	High Resolution Transmission Electron Microscopy
ICP-AES	Inductively Coupled Plasma – Atomic Emission Spectroscopy
LHS	left hand side
MAS	Magic Angle Spinning
MCM-41	Mobil Composition of Matter – 41 unidimensional channels arranged in a hexagonal close packed array
MCM-48	Mobil Composition of Matter – 48 a bicontinuous non-interconnecting channel structure
mesoporous	an open framework structure of pore dimensions 20-500 Å
min	minute

NMR	Nuclear Magnetic Resonance spectroscopy
P	pressure (bar)
Po	saturated vapour pressure (bar)
RHS	right hand side
rpm	revolutions per minute
RT	room temperature
s	second
SAED	Selected Area Electron Diffraction
SBA-2	Santa Barbara – 2
STAC-1	St Andrews Cambridge – 1
STP	standard temperature and pressure (0 °C, 1 atm)
T	temperature (°C or K)
tacn	triazacyclononane
TEM	Transmission Electron Microscopy
TEOS	tetraethylorthosilicate, Si(OEt) ₄
TGA	Thermal Gravimetric Analysis
TG-MS	Thermogravimetry-Mass Spectrometry
TMAOH	tetramethylammonium hydroxide, N(Me) ₄ OH
TMB	trimethylbenzene
TMS	tetramethylsilane, Si(Me) ₄
tmtacn	trimethyltriazacyclononane
TON	turnover number, (mol metal)(mol substrate converted) ⁻¹
TS-1	titanium silicalite – 1
ucs	unit cell size
USY	ultrastable Y, a faujasitic high silica zeolite
UV-Vis	UV-Visible spectroscopy
V	volume (m ³ or ml)
<i>vs.</i>	versus
WHSV	weight hourly space velocity, (g reactant)(g catalyst) ⁻¹ h ⁻¹
wk	week
XRD	X-ray Diffraction
XRF	X-ray Fluorescence

Contents

Declarations	i
Dedication	ii
Acknowledgements	iii
Abstract	iv
Publications arising from this work	v
Abbreviations	vi
Contents	viii
<hr/>	
Introductions & Aims	Chapter 1
<hr/>	
Introduction	1
References	6
Aims	7
<hr/>	
Synthesis	Chapter 2
<hr/>	
Synthesis Background	8
<i>Surfactants</i>	8
<i>Synthesis of Silicate Mesostructures</i>	11
Characterisation Background	16
<i>X-ray Diffraction</i>	16
<i>Adsorption Isotherms</i>	19
<i>Nuclear Magnetic Resonance</i>	24
<i>Thermal Analysis</i>	27
Experimental	29
<i>Instrumentation</i>	29
<i>Synthesis</i>	31
Analysis	34
<i>Solution NMR Spectroscopy</i>	34
<i>Elemental Analysis</i>	35
<i>MAS NMR Spectroscopy Overview</i>	35
FTIR	39
TG-MS	40
XRD Overview	44
<i>Adsorption Isotherm Overview</i>	48
<i>Effect of Surfactant Length or Swelling Agent</i>	50
<i>Effect of Mixed Surfactants</i>	54
<i>Effect of pH</i>	57
<i>Effect of Reaction Temperature and/or Reaction Time</i>	64
<i>Effect of C/Si Ratio</i>	69
<i>Effect of Continuous Stirring</i>	72
<i>Effect of Heteroatoms</i>	73
<i>Miscellaneous Effects</i>	79
<i>Mechanistic Concepts</i>	80
Summary	82
References	84

Background	86
<i>The Electron Microscope</i>	86
<i>Instrument Limitations</i>	88
<i>The Reciprocal Lattice and Electron Diffraction</i>	90
<i>Imaging</i>	95
<i>State of the Art</i>	97
<i>SBA-2 Literature</i>	100
Experimental	101
<i>Instrumentation</i>	101
<i>Synthesis</i>	102
Analysis	104
<i>Modelling mesoporous silica: SBA-2 and STAC-1</i>	104
<i>Mesoporous Domains and Particle Boundaries</i>	117
<i>Structure versus Morphology</i>	119
<i>Hexagonal : Cubic 1:1 Intergrowth</i>	128
<i>Effect of Aluminium</i>	129
Summary	134
References	136

Background	138
<i>Solid Acids</i>	138
<i>Isobutane Cracking</i>	139
<i>But-1-ene Isomerisation</i>	141
Experimental	144
<i>Instrumentation</i>	144
<i>Synthesis</i>	146
Analysis	148
<i>ICP-AES</i>	148
<i>X-ray Diffraction</i>	148
<i>MAS NMR Spectroscopy</i>	154
<i>FTIR</i>	159
<i>Isobutane Cracking</i>	159
<i>But-1-ene Isomerisation</i>	165
<i>N₂ Adsorption Isotherms</i>	176
<i>Extraction</i>	180
Summary	182
References	183

General Background	185
Ti Background	187
Ti Experimental	190
<i>Instrumentation</i>	190
<i>SBA-2-Ti Synthesis</i>	190
<i>Catalysis</i>	191
Ti Analysis	192
<i>Framework Incorporation</i>	192
<i>Catalysis</i>	193
Ti Summary	196
Mn Background	197
<i>Electron Spin Resonance Spectroscopy</i>	197
<i>Surface Modification</i>	199
<i>Manganese Oxidation Catalysts</i>	200
<i>Manganese cyclic triamine complexes</i>	202
Mn Experimental	205
<i>Instrumentation</i>	205
<i>Zeolite Ion Exchange</i>	206
<i>Mn-(tmtacn)-Zeolite Preparation</i>	206
<i>Tethering</i>	207
<i>Catalysis</i>	208
Mn Analysis	210
<i>ESR Spectroscopy</i>	210
<i>Tethering</i>	213
<i>Catalysis</i>	215
Mn Summary	218
Rh Background	219
<i>Hydroformylation</i>	219
<i>Choice of Ligands</i>	221
Rh Experimental	223
<i>Instrumentation</i>	223
<i>Ligand Synthesis</i>	223
<i>Preparation of DIOSR₂ functionalised SBA-2</i>	225
<i>Hydroformylation of Styrene</i>	226
Rh Analysis	228
Rh Summary	230
General Summary	231
References	232

Conclusions	235
<i>Synthesis</i>	235
<i>Mesoporous topology</i>	236
<i>Aluminium catalysis</i>	236
<i>Transition Metal Catalysis</i>	237
Further Work	238
Reference	239

Introduction & Aims

Introduction

Silicon, in all its forms, surrounds us in our everyday lives. In particular pure silica (sand) is manufactured into optically pure window glazing. Today's architects, meanwhile, also employ silicate glass as a construction material: glass bricks, glass laminate staircases or even to create whole buildings. Indeed these 'novel' uses can pessimistically be viewed as an emulation of what nature has been creating over millennia. Today's buildings, though, are designed on a human scale, whilst nature has perfected the art of sub-nanosopic ($<10^{-9}$ m) silicate architecture.

The natural form of a porous silicate is referred to as a zeolite. Broadly speaking a zeolite, or silicate mineral, possesses an open framework structure. This architecture, though, is perfectly suited to accommodating small molecules, in much the same way as people inhabit buildings. The synthesis, therefore, of silicate frameworks, figure 1, on a geological time scale is nothing new. A modern scientist's attempt to emulate, adapt and re-design such structures for commercial application, though, *is* worthy of investigation.

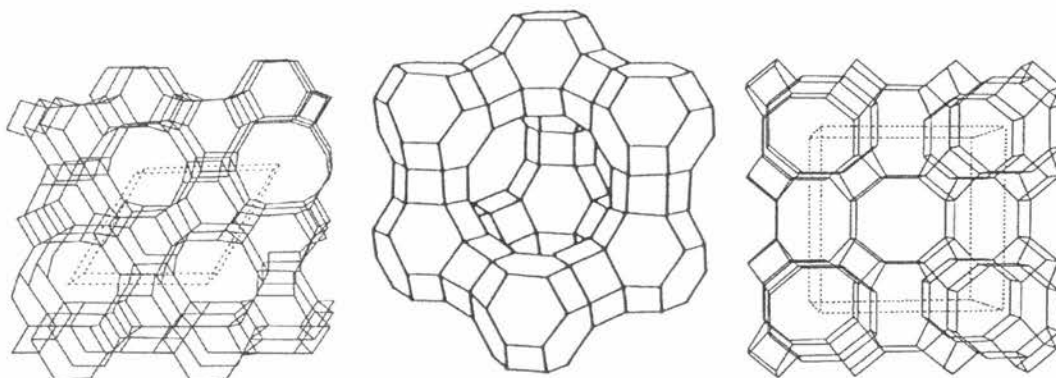


Figure 1: Some examples of naturally occurring silicate architectures. A node represents a tetrahedral atom whilst a line portrays an oxygen bridge.

Scientifically, zeolites are described as microporous materials. Such a term implies a crystalline framework, built around tetrahedra (in this case SiO_4 units) which consist of openings and cavities of less than 20 \AA . The structure obtained possesses a high internal surface area and is thermally and mechanically robust. The framework dimensions, however, restrict the use of such solids to small molecular transformations, table 1.

ion exchange	<ul style="list-style-type: none"> • water purification (heavy metal removal) • water softening (K^+/Mg^{2+} exchange in washing powders) • gadolinium incorporation for use as MRI contrast agents
adsorbents	<ul style="list-style-type: none"> • dehydrating agent: water molecular sieve • O_2 air enrichment: using the dipole interactions of N_2 v. O_2
catalysis	<ul style="list-style-type: none"> • catalytic converters: doped with Pd/Pt/Rh for gas phase conversion of $NO_x \rightarrow N_2$ and $CH_x + CO \rightarrow CO_2$ • catalytic cracking of hydrocarbons

Table 1: Some commercial applications of zeolites today.

Scientists, therefore, have been searching for equivalent materials that can cope with larger molecules. In so doing a strategic rethink of *how* microporous silicates form was necessary. Many of the new synthetic architectures (topologies) crystallise around what are known as structure directing agents, or templates. These are then removed to leave the porous material. Thus if a bigger template, or even an assembly of molecules, can be used perhaps a silicate framework with larger dimensions is within reach. This approach, to the creation of a well defined organic/inorganic material, is in effect mimicking the biomineralization process that form numerous structures in nature, e.g. silicate tests in Radiolaria and Diatom exoskeletons, figure 2.

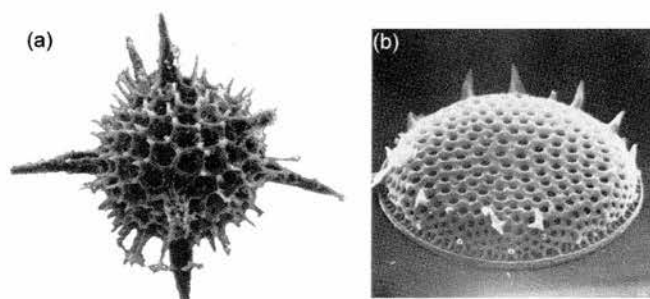


Figure 2: Examples of (a) a Radiolarian¹ and (b) a Diatom.²

A major breakthrough towards the formation of large regular porous silicates was reported³ in 1992. Researchers of the Mobil Corporation in the USA discovered that aggregates of surfactants (amphiphilic molecules e.g. possessing a charged head group and long hydrocarbon tail) can template the condensation of silica species in solution. Furthermore the resulting material, known as MCM-41 (*Mobil Composition of Matter*) figure 3a, has a well defined regular pore structure in mesoscopic space (20 – 500 Å). Thus despite having no specific ordering within the framework walls, this material consists of a hexagonal (in cross-section) arrangement of straight 1-dimensional

channels. Importantly it also possesses a very narrow pore size distribution, which marks it out from inorganic aerogels and glasses. Subsequent alteration to the MCM-41 synthesis conditions (especially the surfactant/silica ratio) has uncovered further mesoporous topologies. For example the code name MCM-48 describes⁴ a 3-dimensional network of cubic symmetry, figure 3b, consisting of two interwoven, non-intersecting channels.

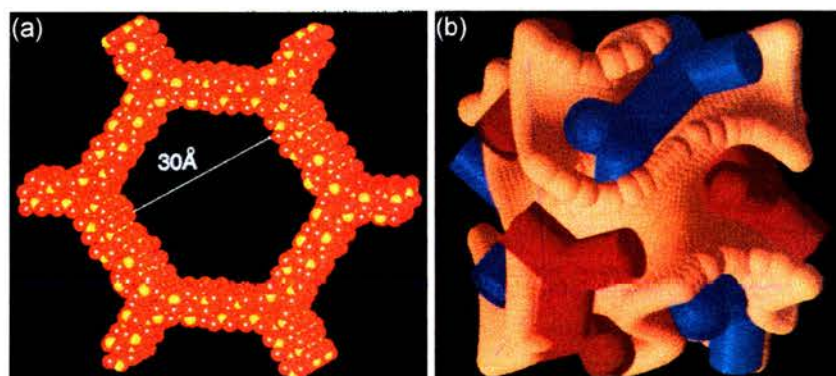


Figure 3: The mesoporous silicate structures (a) MCM-41 and (b) MCM-48.

Since 1992 much research has focussed upon this new, so-called M41S, family of materials. In particular understanding the properties and formation mechanism, developing other new mesoporous structures and finding industrial applications are specific objectives.

To this end Galen Stucky and co-workers of the University of California at Santa Barbara began to look at surfactant systems that did not use the MCM-forming cetyltrimethylammonium $\text{CH}_3(\text{CH}_2)_{15}\text{N}^+(\text{CH}_3)_3$ molecule. The outcome of their work is in several new mesoporous silicate structures, designated SBA-*n* (**S**anta **B**arbara), table 2. These investigations take their lead from the numerous surfactants known, and the notion that each will form different organic amphiphilic assemblies (micelles) that can template silica condensation. Moreover it is chemical self-organisation, particularly at the surfactant-silica interface, that induces micelle aggregation and creates the individual topologies that are observed.

designation	year reported	surfactant used*	Space Group symmetry
SBA-1	1995	CnNEt ₃	cubic Pm $\bar{3}$ n
SBA-2	1995	Cn-s-1	3D hexagonal P6 ₃ /mmc (?)
SBA-3	1995	Cn-s-n	hexagonal p6m
SBA-8	1999	bolaform	2D centred rectangular cmm
SBA-11	1998	C ₁₆ EO ₁₀	cubic Pm $\bar{3}$ n
SBA-12	1998	C ₁₈ EO ₁₀	3D hexagonal P6 ₃ /mmc
SBA-15	1998	PEO ₂₀ PPO ₇₀ PEO ₂₀	hexagonal p6mm
SBA-16	1998	PEO _n PPO _s PEO _n	cubic Im $\bar{3}$ m

*C = number of carbon atoms in the surfactant tail, n, s = alkyl chains or EO/PO repeat units.
Bolaform = rigid alkylammonium surfactants, (P)EO = (poly)ethyleneoxide, PPO = polypropyleneoxide.

Table 2: Mesoporous silicate structures designed by Stucky *et al.*^{5,6,7}

Of particular importance to this thesis, though, is the structure designated SBA-2. This silicate framework was first reported⁵ in 1995 and is unusual because it possesses a 3-dimensional architecture. Moreover it was thought to consist of ‘bottle-shaped’ cavities or a ‘network of pores’. Such 3D cage-structured mesoporous solids would have many advantages over straight channelled topologies in catalysis and separation applications. The precise connectivity, however, was particularly poorly understood in 1995. Thus an in-depth study of this material was considered worthwhile, particularly because without understanding the framework architecture it is difficult to propose any potential uses. In addition the SBA-2 structure is distinct from MCM-41 and MCM-48. Thus a direct comparison can be made with these two well-studied mesoporous topologies, as well as to those of large-pore zeolites.

Finally, to date, commercial use of all mesoporous frameworks has been disappointingly limited. Despite this numerous applications for these materials can be envisaged, table 3. Many of these will be logical extensions to the myriad of uses of microporous zeolites. For example tailoring of the mesoporous composition, pore size, structure or texture may result in a framework architecture designed towards a specific transformation involving bigger molecules or more voluminous transition states than are currently feasible. Alternatively the large accessible internal pore volume and high specific surface areas, up to *ca.* 1000 m²g⁻¹, may be modified to encapsulate or selectively absorb molecules. In addition economic pressures and public concern for the environment have forced the chemical industry to recycle and phase out its use of stoichiometric reagents. Thus, taking two examples relevant to this work, aluminosilicate zeolites are now employed in place of the traditional *conc.* H₂SO₄ as ‘solid acid’ catalysts. This allows for facile reuse and prevents toxic liquid acids from being

‘accidentally’ released into watercourses. The microporous structures currently employed, though, are prone to diffusional limitations, pore blockage and deactivation. Hopefully these problems can be overcome with the use of appropriate mesoporous frameworks. Meanwhile the heterogenization of active homogeneous catalysts has become a specific research goal. Mesoporous materials are particularly suited in such roles where the internal surfaces can be readily functionalised, yet the large and accessible pore volume mimics the solution phase reaction. In turn, these heterogenized systems can simplify recovery (filtration or centrifugation) of the expensive transition metal and complexing ligand, whilst maintaining the homogeneous catalytic activity and selectivity. As before, comparable zeolitic host-guest structures may be constrained by reactant/product diffusional limitations.

information processing	<ul style="list-style-type: none"> • semiconductor quantum wires: pores loaded with germanium • storage capacitors: aniline polymerised in the pores
adsorbents	<ul style="list-style-type: none"> • functionalised with thiol ligands to recover heavy metals (Hg, Ag, Pb) • storage of methane
membranes	<ul style="list-style-type: none"> • large molecule (e.g. protein) separations especially when the porosity runs across the mesoporous thin film (biotechnology sensors)
catalysis	<ul style="list-style-type: none"> • selective large molecule or voluminous transition state conversions (crude oil processing) • supported homogeneous reactions to allow easy recovery/recycling and with minimal diffusional limitations e.g. immobilised organometallics or enzymes • heterogeneous reactions (with, for example, well dispersed metal clusters or heteroatom incorporation) utilising the large internal surface area available

Table 3: Potential commercial applications for mesoporous materials.

It is intended, therefore, that this thesis will demonstrate the importance of mesoporous topologies to the modern-day field of porous silicate research. In particular the creation and tailoring of specific frameworks can be thought of, simply, as architectural design on a molecular scale. The use of chemical interactions to achieve these structures, therefore, is analogous to the builder’s art. Meanwhile the scale and choice of the microporous to mesoporous (5 Å to 500 Å) construction is comparable to the client’s requirements and the architect’s imagination.

References

- ¹ JH Lipps (Ed.), *Fossil Prokaryotes and Protists*, 1993, Blackwell Scientific Publications, Boston, USA.
- ² D Werner (Ed.), *The Biology of Diatoms*, 1977, **13**, Botanical Monographs, Blackwell Scientific Publications, Oxford, UK.
- ³ JS Beck, JC Vartuli, WJ Roth, ME Leonowicz, CT Kresge, KD Schmitt, CT-W Chu, DH Olson, EW Sheppard, SB McCullen, JB Higgins, JL Schlenker, *J. Am. Chem. Soc.*, 1992, **114**(27), 10834.
- ⁴ MW Anderson, *Zeolites*, 1997, **19**(4), 220.
- ⁵ Q Huo, R Leon, PM Petroff, GD Stucky, *Science*, 1995, **268**(5215), 1324.
- ⁶ D Zhao, Q Huo, J Feng, BF Chmelka, GD Stucky, *J. Am. Chem. Soc.*, 1998, **120**(24), 6024.
- ⁷ D Zhao, Q Huo, J Feng, J Kim, Y Han, GD Stucky, *Chem. Mater.*, 1999, **11**(10), 2668.

Aims

- *To synthesise and characterise the SBA-2 mesoporous silicate framework.*
- *to alter the synthesis conditions and assess their effect upon the quality of the final material*
various effects have been investigated including reaction pH, time, temperature, surfactant/silica ratio.
- *to characterise these silicates using a variety of materials chemistry techniques*
mesoporous materials are difficult to characterise mainly because each technique offers limited information. Thus by combining the results from different types of analysis a more comprehensive understanding of the solids can be obtained. The main characterisation techniques used in this work are X-ray diffraction, N₂ adsorption isotherms, solid state nuclear magnetic resonance and high resolution transmission electron microscopy.
- *To examine the SBA-2 mesoporous structure as a catalyst and as a catalyst support, and compare these results with other mesoporous and zeolitic hosts.*
- to prepare the *aluminium-containing* form by direct synthesis and investigate its ability to act as a porous *solid acid* in *isobutane cracking and but-1-ene isomerisation* reactions.
- likewise to directly synthesise the *titanosilicate* material and examine it as a catalyst for *alkene epoxidation*.
- to incorporate *manganese and rhodium organometallic complexes* to the internal surfaces and test these supported catalysts towards *epoxidation and hydroformylation*, respectively.

This thesis is divided into four chapters in order to investigate these aims. Each chapter: Synthesis, Transmission Electron Microscopy, Acid Catalysis and Transition Metal Catalysis is intended to be self-contained. Thus within each an introduction to the background literature and relevant characterisation theory is described. Subsequently the experimental procedures are reported, followed by a detailed analysis of the results. Finally the work is summarised and the references stated. The thesis ends with the Conclusions and some suggestions for areas that merit further investigation.

Synthesis

Synthesis Background

Surfactants

Mesoporous materials are built around surfactants. A surfactantⁱ can be described as an amphiphilic molecule; that is it contains both hydrophobic and hydrophilic parts. Figure 1 demonstrates this, where commonly the head group is polar or ionic and the tail is composed of a linear (or branched) hydrocarbon chain. Typically, therefore, an aqueous environment interacts weakly with this hydrophobic tail portion, whilst strong dipole-dipole or ion-dipole interactions occur between the head group and the solvating water molecules. It is this balance between the head and tail that gives rise to the special properties characteristic of surfactants.



Figure 1: Schematic of a surfactant (surface active molecule).

Surface active agents fall into four broad types classified according to the nature of the head group: anionic, cationic, non ionic or zwitterionic. Examples of each class are shown in figure 2. They all, however, undergo similar self-assembly processes. Within infinitely dilute solutions, the surfactants exist as discrete entities. As the surfactant concentration rises above a critical level, however, the surfactants agglomerate¹ into 3-dimensionally defined shapes. This critical level is known as the critical micelle concentration (cmc). The associated units are called micelles, where a micelle is an agglomeration of surfactant molecules which can then self assemble into supramolecular

ⁱ A surfactant (surface active agent) is a common term for these molecules in the USA. In Europe, meanwhile, they are also known as association colloids, paraffin chain salts, amphiphilic compounds and tensides.

arrays. Figure 3 demonstrates this with respect to temperature for the cetyltrimethylammonium bromide – water system.

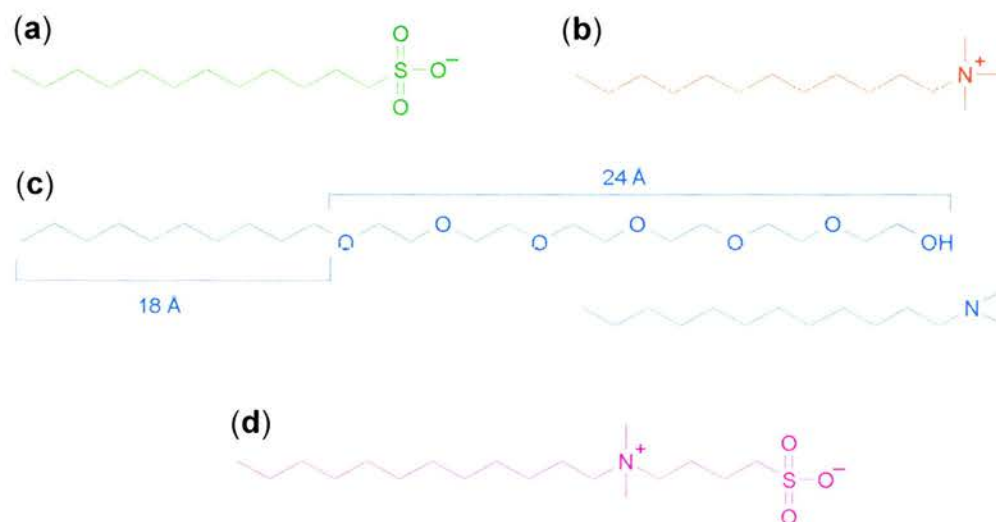


Figure 2: Examples of the four classes of surfactants: (a) anionic (b) cationic (c) non ionic and (d) zwitterionic.

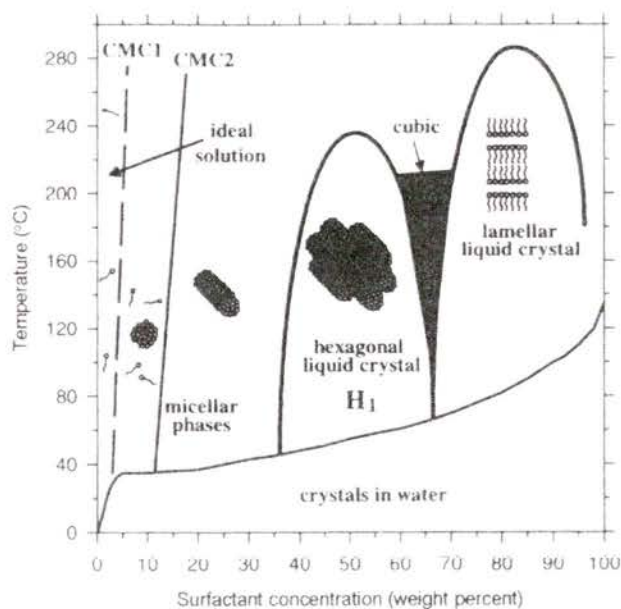


Figure 3: A cetyltrimethylammonium bromide – water phase diagram showing the different temperature ranges of each phase.²

Micelles, therefore, arise from a balance between three forces acting upon the surfactants, namely:

- a tendency for the alkyl chains to minimise their water contact and maximise their inter-organic interactions,
- a coulombic interaction between the charged head groups,
- and energies due to the solvating medium.

The balance² between these competing forces determines the overall relative stability of the micelles. Meanwhile an increase in surfactant concentration can alter the micellization geometry from a spherical (1st cmc) to a rod-like (2nd cmc) configuration. Such a transformation can be reconciled by the molecular packing parameter, g , which describes the balance between the hydrophobic and hydrophilic portions during self assembly. This concept is expressed by equation 1, where g relates the total volume of surfactant chains and co-solvent organic molecules between the chains (V) to the head group area at the micelle surface (a_0) and the kinetic surfactant tail length (l). Thus g is a dimensionless number indicative of the final micellar phase in solution, table 1. The series represents a decrease in micelle surface curvature, from cubic through vesicular to lamellar, as g increases ($a_0 \downarrow, V \uparrow, l \uparrow$).

$$g = \frac{V}{a_0 l} \quad 1$$

g	mesophase
$\frac{1}{3}$	cubic (Pm3n)
$\frac{1}{2}$	hexagonal (p6m)
$\frac{1}{2} - \frac{2}{3}$	cubic (Ia3d)
1	lamellar

Table 1: The expected mesophase sequence as a function of the packing parameter g .¹

Essentially³ when $g < \frac{1}{3}$ the surfactants characteristically form spherical micelles, whilst $g > \frac{1}{3}$ gives cylindrical surfactant agglomerations. Thus micelle mesophase transitions occur as the g value is increased through critical values. Alternatively this information can be presented within a surfactant phase diagram, e.g. figure 3.

Synthesis of Silicate Mesostructures

The breakthrough in designing large pore silicates ($> 20 \text{ \AA}$ cavity diameter) came when micelles were first employed as organic scaffolds, around which inorganic polymerisation could take place. Indeed the first surfactant used⁴ was CTAB, cetyltrimethylammonium bromide, which gave rise to MCM-41. Since then numerous other quaternary ammonium surfactants, figure 4, have been employed. Their use can be summarised as forming a S^+I^- material, in alkaline solution, where S^+ is a cationic surfactant and I^- is an anionic silicate species. In acidic conditions, meanwhile, the surfactant counterbalancing anion, X^- , is required to satisfy the interfacial charge balance. Thus the resultant $S^+X^-I^-$ material, is synthesised at $\text{pH} < 2.0$ (the isoelectric point of silica) to enable the silicate species in solution to be positively charged. The actual mesoporous phase formed, however, depends¹ upon the surfactant concentration, reaction temperature, pH and ionic strength. Indeed a silicate – CTAB surfactant – aqueous base phase diagram, figure 5, demonstrates the narrow space boundaries for a particular structure type in this tertiary system.

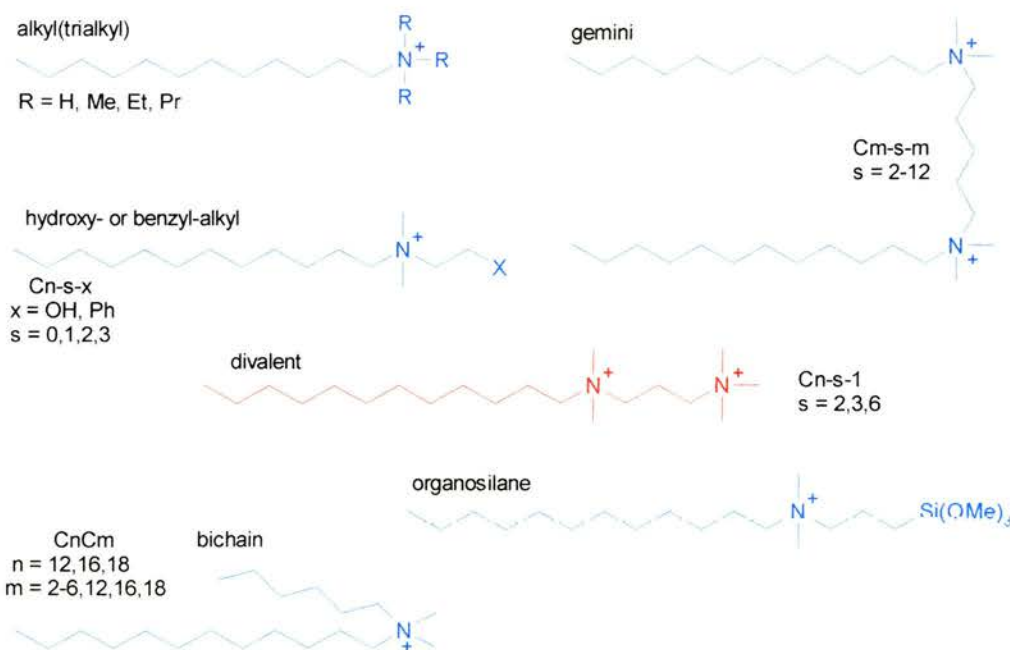


Figure 4: Quaternary ammonium surfactants investigated during mesoporous silicate syntheses.¹

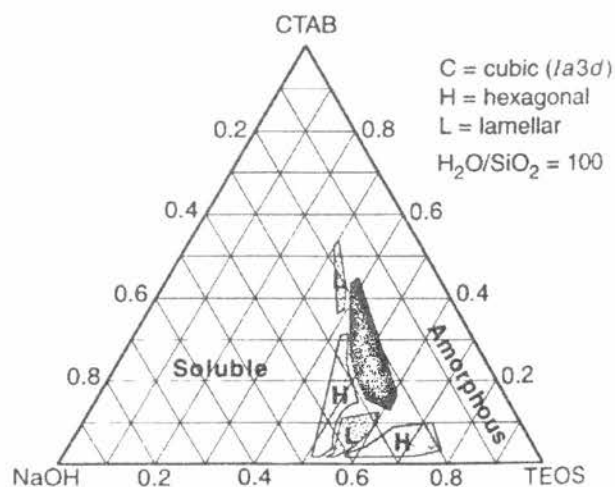


Figure 5: Synthesis – space diagram for silicate nanostructures.⁵ The materials were prepared in basic CTAB-containing aqueous solution, such that each mixture had an H_2O - SiO_2 molar ratio of 100. The solutions were stirred for 1 h at room temperature before being heated at 100 °C for 10 days.

The synthesis of SBA-2 employs a divalent quaternary ammonium surfactant. This type of surfactant, an end member of the so-called gemini series, has a general formula $[\text{H}_3\text{C}(\text{CH}_2)_n\text{N}^+(\text{CH}_3)_2(\text{CH}_2)_s\text{N}^+(\text{CH}_3)_2(\text{CH}_2)_m]\text{Br}_2^-$ and can be represented by the acronym $\text{C}_n\text{-s-m}$. In particular, the SBA-2 structure requires⁶ $m=1$, although the length of the spacer may be altered ($s = 2, 3, 6$). As a result this family of molecules possess a large head groupⁱⁱ and have a high charge density. Combined, these favour the formation of globular micellar aggregates with high surface curvatures. By altering the surfactant tail length, or addition of a polar swelling agent, such as trimethylbenzene, the micellar dimensions and thus mesoporous silicate unit cell size or type can be changed. This concept is illustrated in figure 6, where the synthesised product from $\text{C}_n\text{-s-1}$ micellization is related to the effect of co-organics within the mixture. Thus the effective micelle packing parameter, g , traditionally used to describe water-surfactant micellization can (to a first approximation) be extended for application in mesoporous silicate-surfactant systems. Polar compounds will locate in the hydrophobic - hydrophilic region thereby decreasing the surface curvature of the micelle. Furthermore the micelle possesses an appreciable surface charge density. Synthesised in a basic medium, this is charge compensated by the anionic silicate species in solution. Thus the

ⁱⁱ The head group area varies systematically as the spacer length alters.

final mesoporous topology can be thought of as a solvent-induced (lyotropic) liquid crystal system.

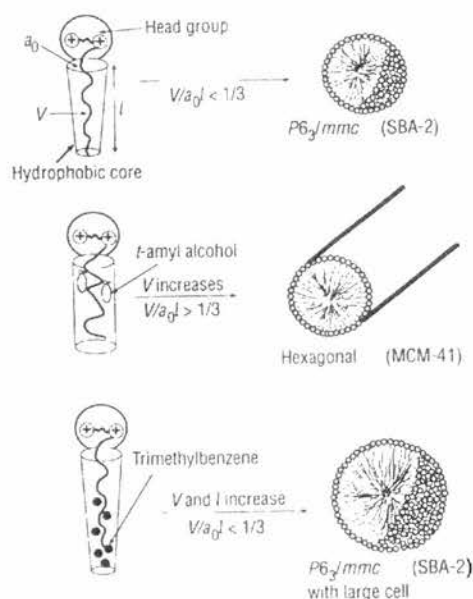


Figure 6: The effect of organic additives on the synthesis product when the Cn-s-1 surfactant is used. The silicate species around the surfactant head groups are absent, for clarity.

It is these Cn-s-1 divalent cationic moieties that will be discussed during this thesis. There is no reason, however, why all classes of surfactant cannot be used during mesoporous silicate synthesis. Indeed the non-ionic and anionic pathways have been successfully employed during the silicate synthesis of SBA-15⁷ and metallomesophases⁸ respectively. Similarly the mixing of surfactants (from within a class: cationic, anionic etc.) during silicate synthesis can be thought of as simply averaging the two respective surfactant packing parameters.

SBA-2 is reported¹ to form in both acid and base catalysed media. During this work, however, only the alkaline mediated pathway was employed. Thus initially the silicate undergoes hydrolysis, to form silanol functionalised products. Subsequently condensation polymerisation sets in, to form the silicate wall structure surrounding each micelle surface. Schematically these two processes are shown in figure 7.

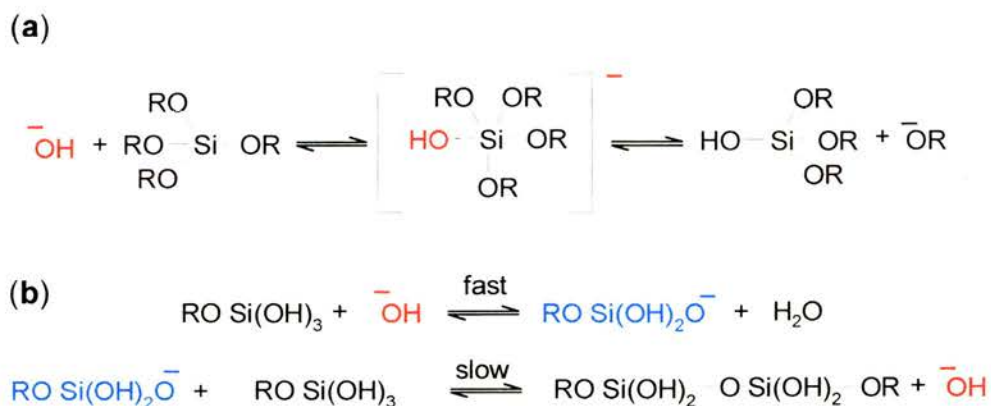


Figure 7: Base catalysed (a) hydrolysis and (b) condensation to form an inorganic silicate network.⁹

When compared with zeolitic silicates, which typically require high temperatures, autogeneous pressures and long reaction times (days) to achieve phase purity, mesoporous materials can be synthesised at ambient temperature within 2 hours. Over such a short reaction period, however, the mesoporous silicate framework is incompletely condensed and still retains many terminal silanol groupings. These undergo further condensation and Si-O-Si bond formation as the sample is (i) dried and (ii) calcined. Such processes account for the observed contraction of the unit cell. Nevertheless, it is fair to say that the final structure is composed of amorphous walls, with order occurring only through their long-range periodicity. This concept implies that, unlike in zeolites, no crystallographically controlled silicate growth around a well defined nucleus occurs. Indeed, the oligomeric silicate species that may be dissolved in solution appear to *randomly* assemble and co-condense during polymerisation.

The manner of mesostructure formation, however, continues to be the subject of some debate.

Initially Beck *et al*^{4,10} proposed a formation mechanism based on the concepts of liquid crystal templating. They suggested, figure 8, that one of two synthetic routes could explain the final observed silicate structure. The first pathway describes how the surfactant molecules self assemble to form a supramolecular array. Subsequently the silicate species condense around and between these agglomerated micelles, to charge balance the exterior micelle surfaces, and polymerise to form the inorganic network. The second suggests that the interaction of the silicate species with the surfactants

mediates the mesophase ordering. The final mesoporous array, therefore, consists of a stacked arrangement of micelles each covered by 2-3 monolayers of condensed silica. Conceptually, this second mechanism seems more appropriate (especially for SBA-2 formation with spherical micelles), and indeed Beck *et al*¹⁰ later favour this. In addition ¹⁴N MAS NMR experiments by Chen *et al*¹¹ refutes the concept of ordered hexagonal arrays without silicate condensation. Finally, Stucky and co-workers¹² developed a co-operative formation mechanism in 1994, figure 9. This suggests that to balance the charge densities within the system, the silicate-surfactant species pair up and subsequently self assemble. Such a process would minimise the overall charge effects, before silicate condensation occurs.

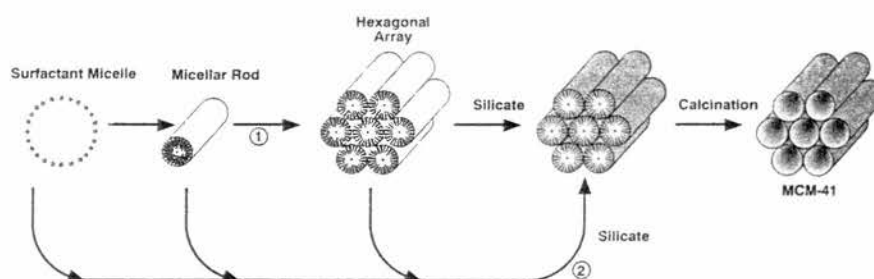


Figure 8: MCM-41 synthesis mechanism proposed¹⁰ by Beck *et al*.

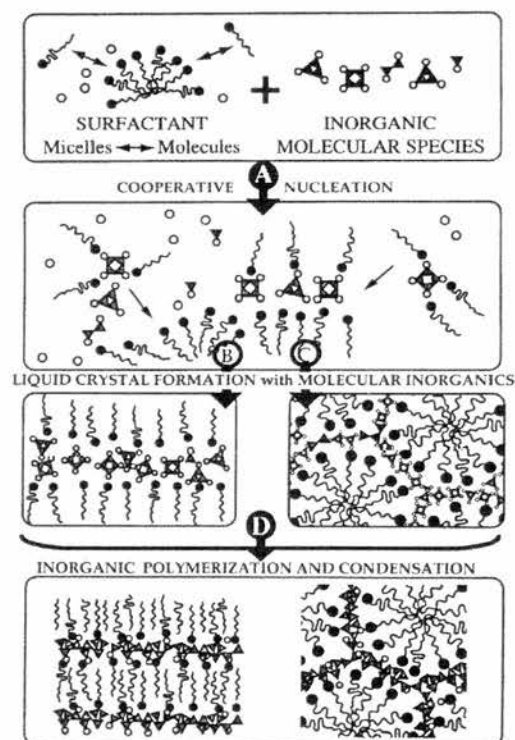


Figure 9: Co-operative templating model for biphasic materials synthesis.¹²

The type of silica available for polycondensation, however, depends¹³ on the reaction pH. The analogous pK_a valuesⁱⁱⁱ are presented in table 2. At pH > 9.5 the large silicate oligomers are ionised and can be expected to bind preferentially (electrostatic co-ordination) to the charged surfactant molecules. Subsequently this charge density matching may drive micellization. The silicate oligomers, therefore, act as multidentate ligands for the head groups, with Coulombic interaction present between the surfactant and silica species. Extensive polymerisation, however, will increase if the reaction temperature is raised and/or the synthesis time lengthened.

pK_a	species
9.8	monomeric silicate
10.7	dimeric silicate
6.5	small silicate oligomers (3-7 Si)

Table 2: pK_a of silica species in solution.¹⁴

Characterisation Background

X-ray Diffraction^{15,16,17}

X-rays are an electromagnetic radiation possessing a wavelength of about 1 Å (10^{-10} m). They were discovered in 1895 and are produced by bombarding a metal target, often Cu or Mo, with a beam of high-energy electrons. These electrons are emitted from a heated filament and used to ionise K-shell (1s) electrons within the target material. Subsequently the K-shell vacancies are filled by electrons of higher energy, and in doing so release characteristic X-rays superimposed upon a continuous 'white' spectrum.. Thus $L \rightarrow K$ and $M \rightarrow K$ transitions give rise to intense $K\alpha$ and $K\beta$ lines respectively. These lines are produced simultaneously, yet within an X-ray diffractometer only a single wavelength radiation is required. In this work a secondary monochromator is used to select the Cu $K\alpha$ wavelength; the X-ray beam is monochromated between the sample and the detector.

ⁱⁱⁱ K_a is the acid equilibrium constant: $K_a = [H^+][A^-]/[HA]$ and $pK_a = -\log K_a$.

In 1912, Max von Lauë realised that a crystal would behave like a 3D grating towards X-rays, since their wavelengths are of the same order as the interatomic distances. These concepts have become known as X-ray diffraction. Later that year WH Bragg^{iv} and his son, WL Bragg, first used X-ray diffraction to solve crystal structures. They realised that if an incident beam is diffracted by two successive lattice planes, then a path difference in the scattered X-rays results. This can be quantified in terms of the interplanar spacing, d_{hkl} figure 10 and equation 2, where θ is the angle of the incident beam. In addition they noted that for intensity maxima to occur, the diffracted beams must be in phase. To achieve this a zero phase disparity is necessary, thus the path difference of successive planes must be an integer number of wavelengths. Altogether this has become known as the Bragg equation, equation 3, which describes the condition for these diffraction maxima. λ is the radiation wavelength.

$$AB + BC = 2d_{hkl}\sin\theta \quad 2$$

$$\lambda = 2d_{hkl}\sin\theta \quad 3$$

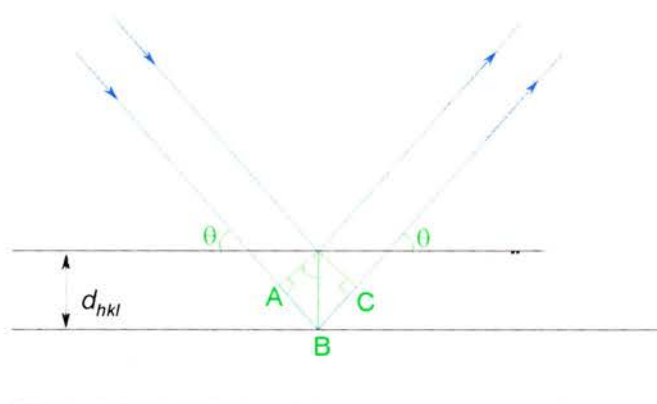


Figure 10: Bragg reflection from crystal planes of spacing d_{hkl} .

The intensity from these diffracted beams is collected on electronic counters, or on photographic film, and displayed versus the 2θ diffraction angle. For finely divided polycrystalline samples^v the result is known as a powder X-ray diffraction pattern. These patterns are collected from randomly orientated crystal particles such that all the possible hkl planes satisfy the Bragg equation simultaneously. Subsequent interpretation

^{iv} They received the Nobel Prize for Physics, for this development, in 1915.

^v The theory for single-crystal XRD is identical, however, only very fine powders were synthesised during this work.

of this XRD pattern leads to the assignment of Miller Indices to each reflection. The peak position (2θ) meanwhile designates the d spacing which is characteristic of a specific set of lattice parameters: $a, b, c, \alpha, \beta, \gamma$. In the case of a hexagonal crystal system where $a = b \neq c$ and $\alpha = \beta = 90^\circ, \gamma = 120^\circ$, this equates to equation 4. The unit cell parameters a and c can be determined from the spacings of two or more^{vi} correctly indexed reflections.

$$\frac{1}{d^2} = \frac{4}{3a^2}(h^2 + k^2 + hk) + \frac{l^2}{c^2} \quad 4$$

The Ewald sphere and reciprocal lattice concepts are implicit within X-ray diffraction theory. They will be explained in detail in the next chapter. Suffice to say here that the many different orientations of the reciprocal lattice share a common origin, figure 11. Furthermore, where each reciprocal lattice point intersects the Ewald sphere, diffraction can occur.

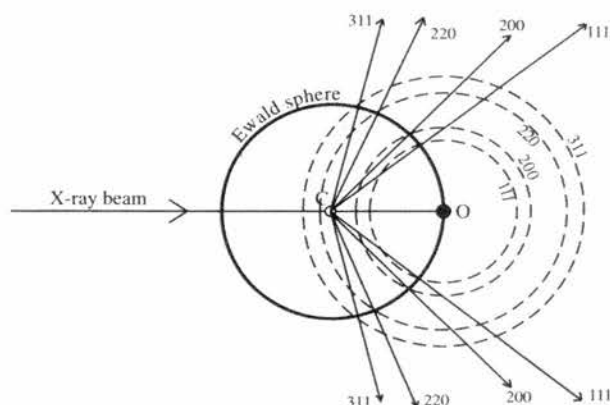


Figure 11: Powder diffraction and the Ewald sphere.¹⁶ The radius of each reciprocal lattice sphere – dashed lines – is the reciprocal of a d spacing within the crystal (indexed here for a fcc lattice).

Powder X-ray diffractograms reveal several properties about the sample under investigation. Importantly they tell us how crystalline a specimen is, where the crystallite size is reflected in the quality (breadth) of each peak: small particles possess fewer planes that satisfy the Bragg equation, thus peak definition is reduced. Mesoporous materials, however, are typified by a few low angle diffraction peaks (below $10^\circ 2\theta$), figure 12. This is a reflection of the large unit cell dimensions, compared to microporous

^{vi} Several reflections are required for unit cell constant refinements.

materials, and of the essentially amorphous frameworks. Thus although the long-range order is well defined, determination of atomic positions within the pore walls is not possible. In addition it may be difficult to determine phase purity because of the broad first (major) peak and lack of clear cut definition in the secondary peak region. This concept is illustrated by the theoretical low angle peak positions for hexagonal and cubic crystal systems, figure 13.

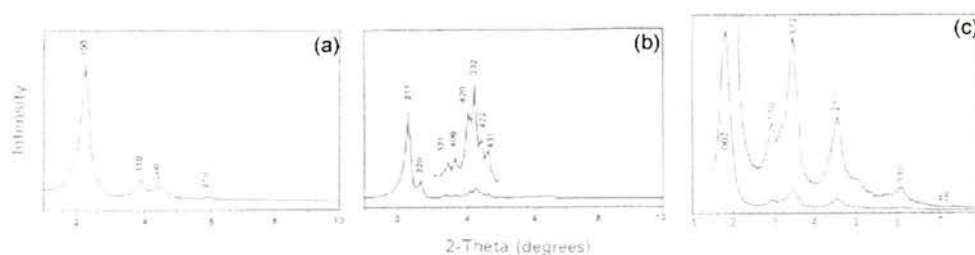


Figure 12: Examples of XRD patterns for mesoporous silicates: (a) MCM-41, (b) MCM-48 and (c) SBA-2.

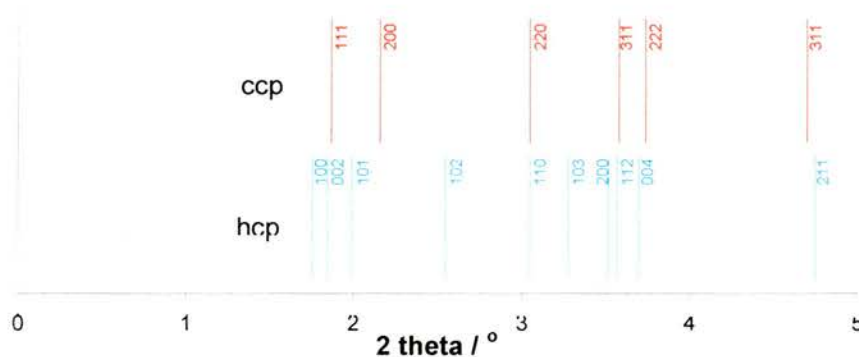


Figure 13: Theoretical XRD peak positions for hcp and ccp SBA-2 systems, indexed appropriately. The hexagonal (103) peak does not have a cubic equivalent.

Adsorption Isotherms

Working with porous solids it is important to understand the pore structure and surface area of the material/catalyst concerned. Perhaps the rate of product (or by-product) formation is dependent upon the available surface area. Alternatively potential applications or a poisoning effect may be determined by constrictions within the framework structure. In either case valuable structural information can be obtained from an adsorption isotherm measurement.

Several probe molecules are used for this purpose. Routinely these include Ar, N₂, H₂O, benzene and n-hexane. The graphs are generally plotted on the form: total number of moles (or volume at STP) per gram of adsorbate per gram of adsorbent versus partial pressure/saturated vapour pressure. Viewed empirically, for all manner of solids and adsorbates, these result in five types of adsorption isotherm: the so called Brunauer Classification¹⁸ (figure 14). Isotherm types IV and I are of special interest to this work.

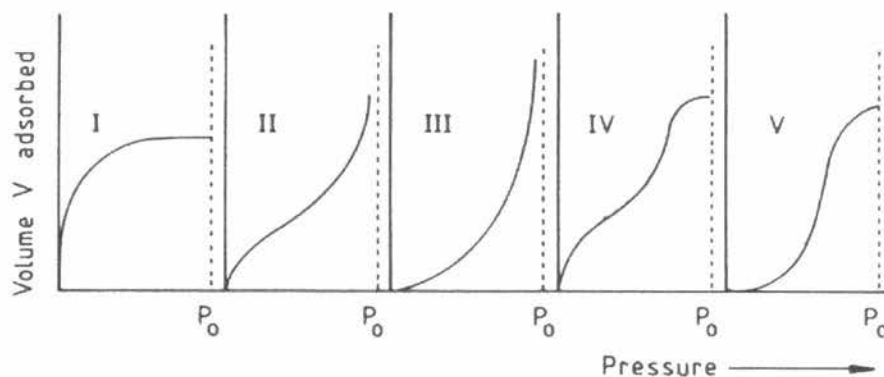


Figure 14: The five types of adsorption in the Brunauer Classification.

Mesoporous solids follow a type IV isotherm. The initial monolayer coverage is built upon by an upward deviation due to multilayer adsorption. Thus the lower reaches of a type IV curve constitute a type II isotherm, which is characteristic of adsorption on a non-porous material. As the dosing pressure increases, however, a steeper slope ensues. This is a direct result of capillary condensation within the mesopore structure and can be envisioned as follows. The internal surfaces and internal volume decrease as multilayer adsorption progresses. Above a critical partial pressure the remaining porosity will appear as hollow tubes. Thus capillary condensation occurs to preferentially fill these volumes, over and above those of larger initial diameter. Hence the significant increase in adsorbed volume over a relatively small partial pressure. The type IV isotherm reaches a plateau upon complete pore filling (P/P_0 tends to 1). The final adsorbed volume value is known as the mesopore volume.

The type I isotherm, meanwhile, is typical of microporous zeolites, with pores of <2 nm diameter. The steep initial slope corresponds to pore filling with liquid condensate. Any gradual increase in adsorption at high partial pressures, therefore, is attributable to multilayer coverage of the external surfaces. As before, the total pore volume is indicated by the plateau region of the adsorption isotherm.

There are three principal methods for collecting adsorption data: gravimetric, dynamic and volumetric. Gravimetric data is amassed by recording the weight gain of the sample (cf. reference) as precise aliquots of adsorbent gas are introduced to the system. The dynamic method relies upon the monitoring of gas concentration. Thus a continuous stream of adsorbent is passed through the sample, immersed in a liquid nitrogen bath, and the exhaust analysed by gas chromatography. This work, however, is based upon the volumetric method whereby a known volume (at STP) is adsorbed by the sample at a particular equilibrium pressure.

Subsequent interpretation of the adsorption data can lead to the determination of the surface area, and, for type IV isotherms, the pore size distribution. Each will be considered in turn.

The Brunauer-Emmett-Teller (BET) equation, equation 5, is widely used¹⁸ as a general method of obtaining the specific surface area of a sample from adsorption data. The theory is applicable^{vii} to multilayer physical adsorption. It assumes that the first layer of adsorbate will possess a fixed heat of adsorption (H_1). The second and subsequent layers, however, have heats of adsorption equal to the latent heat of evaporation (H_L). Thus equation 5 is derived¹⁹ by considering the dynamic equilibrium between each layer and the gas phase.

$$\frac{P}{V(P_0 - P)} = \frac{1}{V_m c} + \frac{c-1}{V_m c} \left(\frac{P}{P_0} \right) \quad 5$$

Taking each term in turn, V is the volume of gas adsorbed at a particular gas pressure P . P_0 is the saturated vapour pressure of the adsorbate, V_m the monolayer volume^{viii} and the BET constant, c , is explained in equation 6 where R is the gas constant ($8.314 \text{ JK}^{-1}\text{mol}^{-1}$) and T is the temperature in Kelvin.

^{vii} The BET theory extends that of the Langmuir equation (which describes the surface area covered by a monolayer of adsorbate on a solid), into the multilayer region.

^{viii} Monolayer volume: the volume occupied if a monolayer coverage of adsorbate were desorbed.

$$c = \exp\left(\frac{H_1 - H_L}{RT}\right) \quad 6$$

A subsequent BET plot of $P/V(P_0 - P)$ versus P/P_0 is linear in the range $0.05 < P/P_0 < 0.35$. Thus the y-intercept is $1/(V_m c)$ and the slope is $(c-1)/(V_m c)$. By solving these two simultaneous equations the values of V_m and c can be found (equations 7 and 8).

$$V_m = \frac{1}{\text{slope} + \text{intercept}} \quad 7$$

$$c = \frac{\text{slope}}{\text{intercept}} + 1 \quad 8$$

It is this monolayer capacity that is used to calculate the specific surface area, S_g , equation 9. Thus V_m is first converted into moles, then molecules and subsequently into a surface area (m^2g^{-1}) by multiplying by A , the area occupied by each adsorbate molecule. In the case of N_2 the molecular packing of a completed monolayer is taken²⁰ as being the same as in liquid packing, thus $A = 16.2 \text{ \AA}^2(\text{molec})^{-1}$ at 77 K.

$$S_g = \frac{V_m}{0.0224} \times 6.023 \times 10^{23} \times A \quad 9$$

Upon desorption hysteresis is sometimes²¹ seen. This observation can be reconciled by the distinctive geometric pore shapes and connectivity within the sample. On adsorption it is thought that a metastable multilayer remains on the pore wall before the onset of capillary condensation. Thus during desorption the equilibrium pressure is greater and a stepped curve results. For mesoporous solids capillary condensation hysteresis (N_2 , 77 K, $P/P_0 = ca. 0.4$) corresponds to the emptying of N_2 trapped within the cavities, since the external opening is unstable.

Pore size distribution calculations, therefore, are based upon the desorption data contained within the capillary condensation region of a type IV isotherm. Traditionally these calculations employ the Barrett-Joyner-Halendar (BJH) method. This method²² is based upon the Kelvin equation, equation 10, where P_0 , P , R and T have been defined previously, and γ , V , and r relate, respectively, to the surface tension, molar volume and

average radius of curvature (in the meniscus) of the condensed liquid. Within cylindrical pores, the spherical meniscus radius is complicated²⁰ by a multilayer adsorbed film, of thickness t , lining the pore walls. Thus in the Kelvin equation, the radius must account for the observed meniscus whose radius is larger than that of the ‘reduced’ cylindrical pore, figure 15. Simple geometry shows that the reduced pore radius (r^*) is related to the meniscus radius (r) through the angle of contact, θ , equation 11.

$$\ln \frac{P_0}{P} = \frac{2\gamma V}{rRT} \quad 10$$

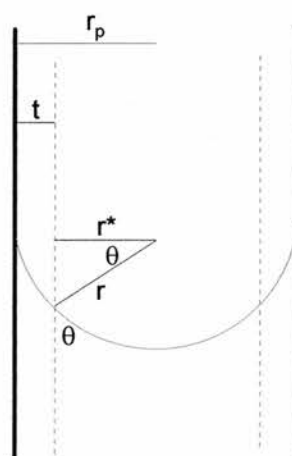


Figure 15: Vertical cross-section of a cylindrical pore showing a hemispherical meniscus. The relationship between the meniscus radius for the Kelvin equation (r) and the radius of the core (r^*) is shown. θ is the contact angle, t is the multilayer adsorbed film thickness and r_p is the pore radius ($r_p = r^* + t$).

$$r^* = r \cos\theta \quad 11$$

In practice, however, this contact angle is assumed^{ix} to equal zero, i.e. $\cos\theta = 1$. Consequently it is the Kelvin equation as expressed in equation 10 that is used to determine the pore radii, and hence pore size distribution^x curves, and pore volume from the original type IV gas adsorption isotherms.

^{ix} The contact angle is arbitrarily defined since direct accurate determination of θ is very difficult, particularly within mesoporous solids.

^x The reader is referred to ref. 18 for a detailed computational analysis of these calculations.

Nuclear Magnetic Resonance

Nuclear magnetic resonance (NMR) is a non-destructive analysis technique. It is the study of the interaction of nuclear moments with magnetic fields. A magnetic moment, μ , occurs in each nucleus possessing a spin quantum number I , i.e. $I \neq 0$. This quantum number is characteristic of a particular elemental isotope and can take positive integer or half-integer values. Thus when an external field, B_0 , is applied to the nucleus, the magnetic field may take up $2I+1$ different orientations, figure 16. Furthermore, upon irradiation with radio frequency waves the spins will invert from a lower to a higher energy state. This frequency, ν , is specific to the nuclear environment and is described in the resonance condition^x (equation 12) where γ is the magnetogyric ratio, h is Plank's constant and B_0 is the applied magnetic field.

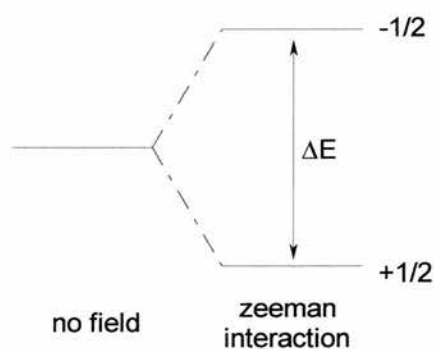


Figure 16: The nuclear spin energy levels of a spin $\frac{1}{2}$ nucleus in a magnetic field.

$$h\nu = h \frac{\gamma}{2\pi} B_0 \quad 12$$

Consequently each resonance line in the NMR spectrum corresponds to a different nuclear environment within the molecule. It is, in fact, the local electronic environment experienced by each nucleus, that determines the peak position. In a molecule the electrons which orbit each nucleus generate their own magnetic fields. Combined with B_0 these create an effective field, B_{EFF} (equation 13), where σ is the shielding constant. Consequently σB_0 is known as the *chemical shift*, since it results from the electronic state of the system, which determines (or is determined by) the chemistry of the material.

^x $h\nu = \Delta E$, the energy of absorption.

The chemical shift scale is used to plot the NMR spectrum, measured in ppm from a reference signal (arbitrarily TMS = 0 ppm).

$$B_{\text{EFF}} = (1-\sigma)B_0 \quad 13$$

In addition fine structure (splitting) of an NMR peak arises from the magnetic interactions between nuclei within the molecule. These splitting patterns, like their corresponding chemical shift positions, contain valuable information used for structural elucidation.

In liquids the molecules have random orientations and tumble rapidly with respect to the time scale of the NMR experiment. As a result the resonance lines appear as sharp well-defined peaks. In a powder sample, however, the crystallites are randomly scattered yet the atoms are held in fixed positions. Thus each orientation has a different component of μ aligned with B_0 , leading to a variation of chemical shift (differing resonance frequencies). This phenomenon is known as Chemical Shift Anisotropy (CSA) which causes peak broadening and loss of definition. The technique of magic angle spinning (MAS), though, can overcome this. Theory shows that any CSA contains a proportionality term $3\cos^2\theta - 1$, where the angle θ determines the orientation with respect to B_0 . Thus when $\theta = 54.7^\circ$ and the sample is spun sufficiently fast this term will become zero, and peak broadening due to CSA will disappear. Likewise dipolar effects^{xii} also have a $3\cos^2\theta - 1$ dependency, and can be minimised by spinning at this 'magic angle'.

Two further MAS NMR experiments can be used to enhance the observed solid state spectrum. Dipolar decoupling is a double resonance technique that eliminates homo- or heteronuclear broadening influences. In silicates these commonly arise from ^1H nuclei. Secondly, Cross Polarization (CP) overcomes the problems of low sensitivity of rare spins, and long relaxation times. This technique involves the transfer of strong polarization of abundant spins (^1H) to enhance those of weakly polarizing rare spins^{xiii} (^{13}C , ^{29}Si). In effect the signal to noise ratio increases and the total time required to

^{xii} The change in the local magnetic field as a result of magnetic dipoles on neighbouring nuclei.

^{xiii} Natural abundances: $^{13}\text{C} = 1.11\%$, $^{29}\text{Si} = 4.70\%$.

collect the experimental data decreases (the effective relaxation times are reduced). This CP technique, though, means that these spectra are no longer quantitative.

Of interest to zeolite structure determination are the use of ^{29}Si and ^{27}Al magic angle spinning experiments. In 1981 Lippmaa *et al*²³ established that the ^{29}Si chemical shifts for silicates fell into clear ranges depending upon the number of silicon atoms attached to the vertices of a given SiO_4 tetrahedron. Over time these resonances have been assigned^{15,16} a 'Qⁿ value' where n is the degree of silicate polymerization. Thus Q⁰, Q¹, Q², Q³ and Q⁴ represent, respectively, monomers, dimers, chains, sheets and frameworks of SiO_4 tetrahedra within the sample. Furthermore, as the value of n increases (0 → 4) with respect to a trimethylsilane (TMS) internal standard, the silicon resonance becomes more negative, figure 17. In mesoporous silicates, the frameworks are typically amorphous and incompletely condensed. The corresponding ^{29}Si MAS NMR spectra, therefore, often show broad resonances composed mainly of Q³ and Q⁴ (some Q²) environments. In particular the presence of Si-OH species can be detected²⁴ by a cross-polarized experiment, which discriminates in favour of their Q³ signals.

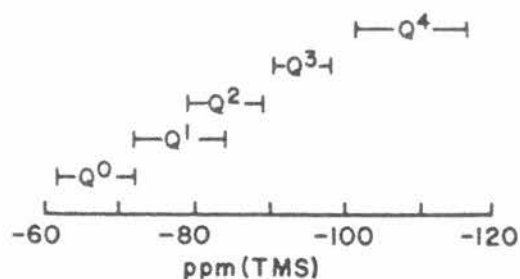


Figure 17: Variation of the ^{29}Si MAS NMR chemical shift for SiO_4 tetrahedra with respect to their degree of polymerisation, Qⁿ value.²⁵

Furthermore, in an aluminosilicate, the number of AlO_4 units adjacent to a specified SiO_4 tetrahedron also influences the observed silicon chemical shift. In the case of faujasitic zeolites, where there is one unique lattice site, the ^{29}Si MAS NMR spectra are sensitive to the aluminium loading within the structure. Thus the 5 observed Q⁴ resonances correspond to Si[4Al], Si[3Al], Si[2Al], Si[1Al] and Si[0Al] environments, figure 18. Each additional next nearest neighbour aluminium, therefore, shifts the observed Si resonance by approximately +5 ppm.

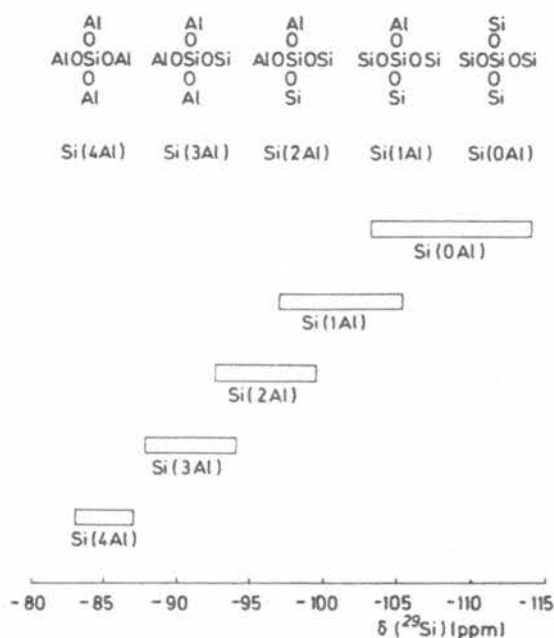


Figure 18: Variation of the ^{29}Si chemical shift for framework aluminosilicates with the number of adjacent AlO_4 tetrahedra.²³

Aluminosilicates are also amenable^{17,26} to investigation by ^{27}Al MAS NMR experiments. ^{27}Al is a quadrupolar^{xiv} nucleus ($I = 5/2$) and as such requires analysis at high fields in order to minimise the quadrupolar effects. The observed Al chemical shifts that result from the $+1/2 \rightarrow -1/2$ transition are characteristic of the aluminium environment. In particular ^{27}Al spectra can discriminate between 4-, 5- and 6-fold co-ordination. For tetrahedral (lattice) co-ordination the ^{27}Al chemical shift appears in the 50-65 ppm range, with reference to aqueous $\text{Al}[\text{H}_2\text{O}]_6^{3+}$. Octahedral (extra-framework) aluminium, meanwhile, resonates at about 0 ppm, whilst 5 co-ordinate species give a peak between these two values.

Thermal Analysis

Thermal analysis permits the measurement of the physical and chemical properties of a solid as a function of temperature. Thus thermal gravimetric analysis (TGA) records a change in weight (usually a weight loss), as the sample is heated (or cooled) at a constant

^{xiv} The quadrupolar term arises from the interaction of the nuclear spin with a non-spherically symmetric electric field gradient at the nucleus.

rate. Typically a few milligrams of solid are analysed over time during a temperature ramp (e.g. $10\text{ }^{\circ}\text{Cmin}^{-1}$). The resulting trace (weight *versus* temperature) can be used to quantitatively calculate any compositional changes occurring to the material. The specific temperature at which these events occur, though, depends upon the heating rate, particle size, experimental atmosphere used etc. In addition, when a thermogravimetry instrument is coupled to a mass spectrometer (TG-MS), any decomposition products can be identified by their fragmentation patterns. This leads to a more detailed understanding of the thermal processes occurring at a particular temperature.

Differential thermal analysis (DTA), meanwhile, measures the temperature of the sample with respect to an inert reference material (e.g. $\alpha\text{-Al}_2\text{O}_3$). These thermal events, therefore, appear as peaks in a temperature difference (ΔT) *versus* actual temperature DTA trace. The DTA peak areas obtained during this work, however, were only qualitatively related to the magnitude of the enthalpy changes taking place. Thus an endothermic event corresponds to the sample taking in heat from its surroundings, compared to the reference material, whilst an exothermic peak indicates that the sample emits heat. Finally, when DTA is obtained in conjunction with a TGA, the results can yield information pertaining to structural events where no weight loss is observed.

Experimental

Instrumentation

The purity of the synthesised surfactants was checked by ^{13}C and ^1H solution NMR. A Varian Gemini 300 MHz NMR instrument was used. Prior to analysis the samples were dissolved in a small quantity of deuterated solvent (CDCl_3 or CD_3OD). The spectra (table 3) were collected at ambient temperature in 5 mm glass tubes. Tetramethylsilane (TMS) or the solvent signal was used as a reference.

	^1H	^{13}C
spectral width (kHz)	4.5	17.7
pulse sequence	angle	45°
	delay (s)	1.0
	acquisition (s)	3.2
repetitions	16	≥ 1028
line broadening (Hz)	0.1	2.0

Table 3: Solution NMR experimental conditions.

Powder X-ray diffraction patterns were collected on a Philips PW 1830 Diffractometer equipped with a secondary monochromator and a Philips mpd control unit. The data were accumulated using PC-APD diffraction software at ambient temperature. $\text{Cu K}\alpha$ radiation, $\lambda = 1.5418 \text{ \AA}$, was employed. For a mesoporous sample a typical pattern was collected, using $\frac{1}{4}^\circ$ slits, between $1.5 - 8.0^\circ 2\theta$. A continuous scan was employed with a step size of 0.02° . At each step the diffraction data were collected for 2 s. For well-defined samples overnight runs were performed on the secondary diffraction peak region (*ca.* $3 - 8^\circ 2\theta$). A step scan of 0.01° was employed while the overnight diffraction data were collected for *ca.* 90 s per step. All reported unit cell parameters were refined on Powder Diffraction VAX/VMS V5.2 software using the 'celref' programme.

Adsorption Isotherm measurements were performed on an in-house designed vacuum line, calibrated with helium gas. The samples (0.06 – 1.50 g) were slowly degassed, so as to avoid bumping, before being gradually heated under vacuum to 280°C . This

temperature was maintained overnight under a roughing pump vacuum of *ca.* 8×10^{-3} torr. A final temperature of 300-350 °C was achieved (and maintained for 1 hour) under a diffusion pump vacuum of *ca.* 4×10^{-5} torr. Subsequently the furnace was removed and the sample cooled to room temperature under 4×10^{-5} torr, before being closed to vacuum. The sample tube was cooled in a liquid nitrogen bath (77K) and the upper liquid surface maintained at a constant height on the sample tube throughout the measurement. Nitrogen gas was used as the adsorbate. Thus aliquots of *ca.* 30 torr were adsorbed or desorbed. Complete equilibrium was achieved before the pressure values were recorded. Data plots are standardised per gram of material, and in comparison to the adsorption of He upon the empty sample tube, at 77 K.

MAS NMR spectra were obtained on a Varian UNITYplus spectrometer, operating at 300 MHz for ^1H and accompanied by a Doty Scientific MAS probe. The experimental details are shown in table 4. The ^{13}C and ^{29}Si measurements used a 7 mm rotor, whilst a 5 mm rotor was used for the ^{27}Al experiments.

	^{13}C	^{29}Si	^{27}Al
frequency (MHz)	75.430	59.582	78.158
spectral width (kHz)	30.0	30.0	400
spin rate (kHz)	4.2	≥ 4.5	10.1
polarization	CP	DP (CP)	DP
pulse sequence	contact time (ms)	3	- (5)
	angle	-	90° (-)
	delay (s)	1	>120 (1)
	acquisition (ms)	29.9	9.6 or 10
shift scale	TMS	TMS	1M AlCl_3

Notes: CP = cross polarization from ^1H . DP = direct polarization. The numbers in brackets refer to the pulse sequence used for CP experiments. TMS = tetramethylsilane.

Table 4: MAS NMR experimental conditions.

Thermal gravimetric analysis (TGA) was performed on a TA Instruments SDT 2960 simultaneous TGA-DTA. The samples were heated at $10 \text{ }^\circ\text{Cmin}^{-1}$ under flowing oxygen. Calcined alumina was used as the reference material. The TG-MS data was collected from a Perkin Elmer TGA 7A under flowing helium (100 mlmin^{-1}). During analysis the furnace was ramped from $30 \text{ }^\circ\text{C}$ to $900 \text{ }^\circ\text{C}$ at $20 \text{ }^\circ\text{Cmin}^{-1}$. The associated mass spectra were recorded on a Fisons MD-800 spectrometer, linked to the TGA by a transfer line developed by Perkin Elmer. No particular sample drying procedures were undertaken prior to analysis.

Elemental analyses were carried out on a Carlo Erba Elemental Analyser model 1106, suitable for C, H and N determination.

Infrared (FTIR) spectra were recorded on a wavelength dispersive instrument. The samples were prepared as self-supporting KBr pellets.

Energy dispersive X-ray (EDX) spectroscopy was carried out in Cambridge on an Oxford Instruments instrument.

Inductively Coupled Plasma – Atomic Emission Spectroscopy (ICP-AES) was used to determine the elemental analysis of silicon and aluminium in two aluminosilicate SBA-2 solids. Thus a weighed amount of the sample was dissolved by fusion with LiBO_4 . The fusates were dissolved in nitric acid and diluted to an appropriate volume prior to analysis. The results were obtained on a Jobin Yvon – JY70+ sequential simultaneous ICP spectrometer and were standardised using a reagent blank. Approximate detection limits, expressed in parts per million (ppm), are Si = 24 ppm and Al = 20 ppm, for ICP measurements in a 5 % HNO_3 matrix.

Synthesis

Surfactants were prepared according to the synthetic route described by Zana *et al*²⁷ and shown in figure 19. The synthesis is a typical nucleophilic substitution ($\text{S}_{\text{N}}2$) reaction, where the product is an amine salt, in this case a diquatery ammonium cationic molecule.

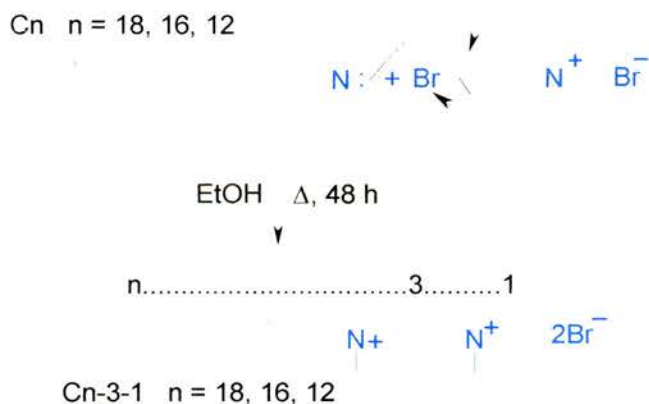


Figure 19: Cn-3-1 surfactant synthesis reaction mechanism.

Depending upon the final hydrocarbon tail length required the appropriate alkyl dimethylamine was used: N,N dimethyldodecylamine (C12), N,N dimethylhexadecylamine (C16) or N,N dimethyloctadecylamine (C18). For simplicity, the final product is designated Cn-s-1, where n and s denote, respectively, the number of carbon atoms in the tail and between the quaternary nitrogens. The number '1' indicates that this is the (asymmetric) end member of the so-called gemini surfactant family. The synthesis of C16-3-1, therefore, can be described as follows.

N,N Dimethylhexadecylamine (7.41 ml, 20 mmol) and (3-bromopropyl)trimethyl ammonium bromide (5.22 g, 20 mmol) were refluxed, with stirring, in dry ethanol for 48 hours. A 5-10 % excess of N,N dimethylhexadecylamine was used to ensure complete reaction. Subsequently the solvent was removed under reduced pressure and the colourless crude product recrystallised from an ethylacetate-ethanol mixture. A typical preparation gave an 93-96 % yield of the pure surfactant, which decomposed on heating (223 – 224 °C).

Specific synthetic strategies for SBA-2 will be described during the analysis. A general preparation route, however, is as follows. The base, as tetramethylammonium hydroxide (25 wt% TMAOH in water), was added to distilled water with stirring. Subsequently the diquaternary ammonium surfactant was dissolved in this solution. Following complete homogenisation (*ca.* 30 min) the silicate, as tetraethylorthosilicate (TEOS), was added. At this point any extra species e.g.: heteroatoms (as a metal source) or swelling agents (trimethylbenzene, TMB) was added immediately following the TEOS. Thus the final mixture possessed a molar composition of 0.05 surfactant : 0.5 base : 1 TEOS : 150 H₂O (:x additional species). The pH of the mixture was monitored

throughout. The reaction period varied from between 1 h and 1 wk. Likewise different reaction temperatures of between ambient and 160 °C were chosen. Syntheses were performed under both static and stirred conditions, after TEOS addition and initial homogenization. Finally the mesoporous silicate was recovered by filtration (Büchner apparatus) and washed repeatedly with distilled water before drying in air at ambient temperature overnight.

The surfactant molecules were removed by calcination in a tube furnace. The sample was first heated under flowing nitrogen at 10 °Cmin⁻¹ to 550 °C. The nitrogen flow was maintained at this temperature for 1 hour, before being switched to oxygen for a further 6 hours. Finally the sample was cooled to room temperature (nominally at 20 °Cmin⁻¹), under flowing oxygen, to form the porous material.

Analysis

Solution NMR Spectroscopy

The purity of the synthesised surfactants was checked by ^1H and ^{13}C solution NMR, prior to their use as SBA-2 templating (micellization) molecules. Thus for C16-3-1 the ^1H spectrum, figure 20, can be identified as follows: δ (CDCl_3): 4.00(s), 3.80(m), 6H, CH_2N^+ ; 3.50(s), 9H, $\text{N}^+(\text{CH}_3)_3$; 3.40(s), 6H, $\text{N}^+(\text{CH}_3)_2$; 2.63(dt), 2H, $\text{N}^+\text{CH}_2\text{CH}_2\text{CH}_2\text{N}^+$; 1.80(dt), 2H, $\text{CH}_3(\text{CH}_2)_{13}\text{CH}_2$; 1.38(bs), 1.25(bs), 26H, $\text{CH}_3(\text{CH}_2)_{13}$; 0.90(t), 3H, $\omega\text{-CH}_3$.

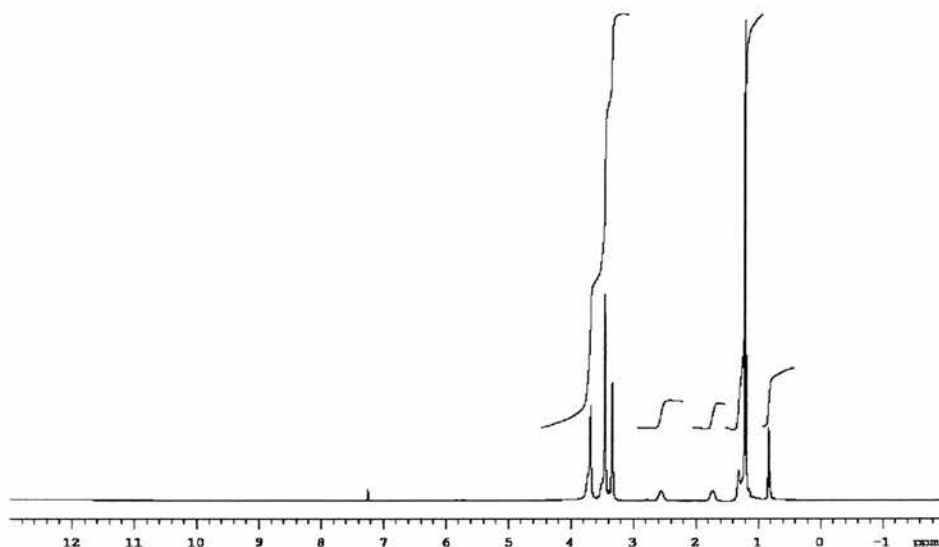


Figure 20: ^1H solution NMR spectrum of the pure C16-3-1 surfactant.

The corresponding ^{13}C spectrum, figure 21, similarly shows resonances consistent with hydrocarbon chain and quaternary ammonium carbon shifts. Thus δ (CDCl_3): 65.97 $\text{CH}_2\text{N}^+(\text{CH}_3)_3$; 62.56 $(\text{CH}_2)_{15}\text{N}^+(\text{CH}_3)_2\text{CH}_2$; 60.79 $\text{CH}_3(\text{CH}_2)_{14}\text{CH}_2$; 53.83 $\text{N}^+(\text{CH}_3)_3$; 50.90 $\text{N}^+(\text{CH}_3)_2$; 31.78 $\text{CH}_3\text{CH}_2\text{CH}_2$; 29.61, 29.54, 29.46, 29.23, 26.26 $\text{CH}_3(\text{CH}_2)_2(\text{CH}_2)_{11}$; 22.83 $\text{CH}_3(\text{CH}_2)_{13}\text{CH}_2$; 22.54 CH_2CH_3 ; 18.69 $\text{N}^+\text{CH}_2\text{CH}_2\text{CH}_2\text{N}^+$; 13.98 $\omega\text{-CH}_3$.

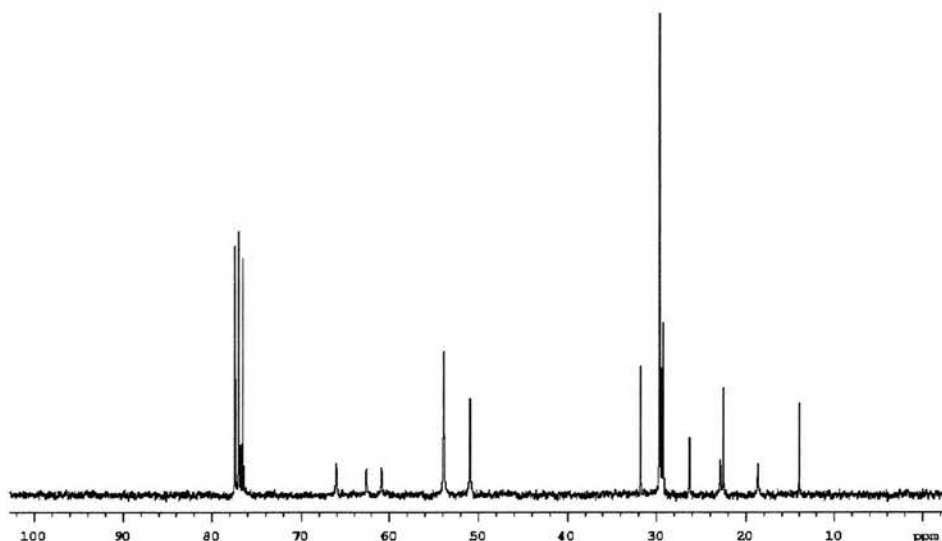


Figure 21: ^{13}C solution NMR of the pure C16-3-1 surfactant.

Elemental Analysis

The theoretical and actual elemental analyses of the C16-3-1 surfactant are presented in table 5. No special precautions were taken prior to analysis. Thus the apparent disparity between the calculated and measured values may be due to the presence of hydrating water molecules. Indeed a more critical guide is the C/N ratio, which match each other well.

	%C	%H	%N	C/N
theoretical	54.34	10.26	5.28	10.29
actual	51.78	10.48	4.97	10.42

Table 5: Elemental analysis of the pure C16-3-1 surfactant.

MAS NMR Spectroscopy Overview

The ^{13}C CP MAS NMR spectrum of an as-prepared SBA-2 material, figure 22, shows resonances consistent with the signals expected from the intact diquaternary ammonium surfactant, C16-3-1. Thus δ : 63.3 CH_2N^+ ; 54.6 $\text{N}^+(\text{CH}_3)_3$; 50.4 $\text{N}^+(\text{CH}_3)_2$; 32.5, 30.5 $\text{CH}_3\text{CH}_2(\text{CH}_2)_{12}$; 26.8 CH_3CH_2 ; 23.1 $\text{CH}_2(\text{CH}_2)_{13}\text{CH}_3$; 17.9 $\text{CH}_2\text{CH}_2\text{N}^+(\text{CH}_3)_3$; 14.2 $\omega\text{-CH}_3$.

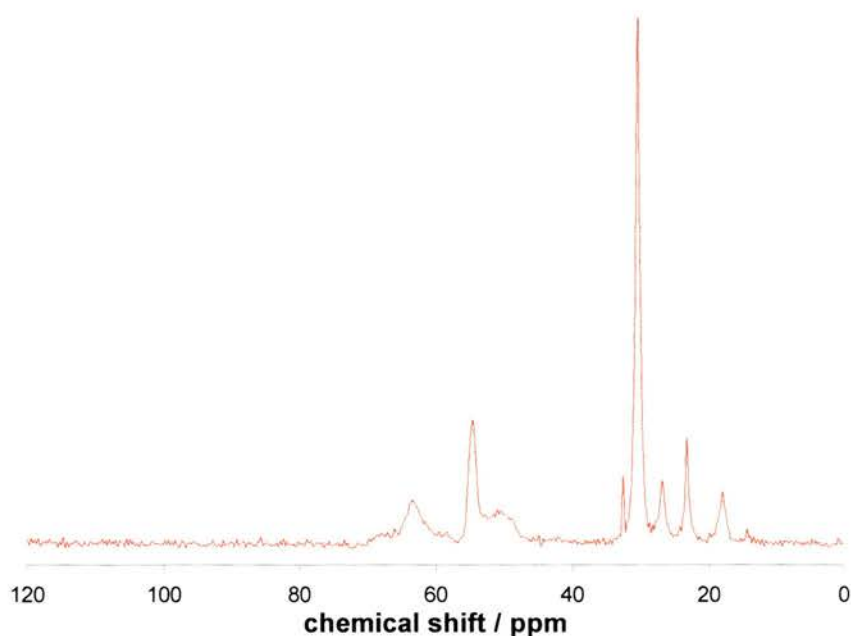


Figure 22: ^{13}C CP MAS NMR of as-prepared SBA-2 C16-3-1.

^{29}Si MAS NMR is used to determine the degree of polymerisation and concentration of silanol species present. The relatively broad resonances arise because the silicon occupies a range of environments in the structure. In other words the SBA-2 walls are amorphous and therefore do not contain crystallographically-defined silicon environments. As a result the atomic nuclei resonate over a range of frequencies, and hence generate broad lines

The chemical shift and relative intensities for ^{29}Si MAS NMR spectra collected for SBA-2 materials of differing surfactant lengths, are all similar. This reflects the fact that the final unit cell size is independent of the silicate polymerisation mechanism. Illustrated for a C12-3-1 material, the observed as-prepared spectrum, figure 23a, obtained after reaction at RT for 2 hours, clearly shows three different silicon environments. These can be deconvoluted, table 6, to reveal that the Q^3 signal predominates. In turn, this resonance indicates that silanol species^{xv} are present within the framework structure. Following calcination, however, the ^{29}Si spectrum significantly alters, figure 23b. Obviously these changes arise from framework processes initiated

^{xv} The possibility of incomplete hydrolysis, i.e. Q^3 signal due to Si-OEt species, is unlikely since no resonances corresponding to -OEt (18.22, 57.97 ppm) appear in the as-prepared ^{13}C MAS NMR spectra.

during calcination. They can be summarised as follows: an increase in Q^4 intensity with associated decrease in Q^2 and Q^3 signal strengths. For completeness the deconvoluted numerical description, corresponding to this calcined material, is also presented in table 6. Thus overall these spectra indicate that an increase in framework silicate condensation occurs during calcination. A concept that is consistent with the unit cell contraction observed by XRD.

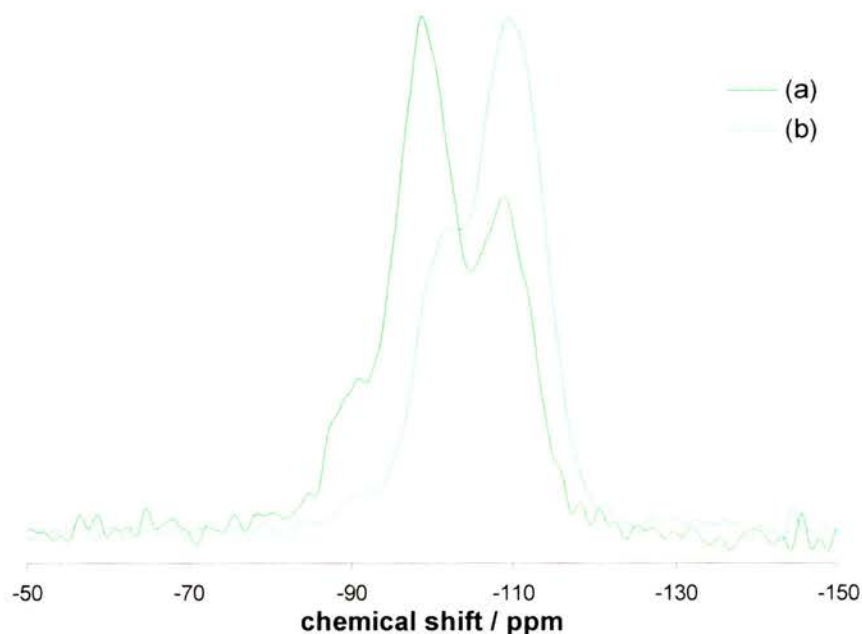


Figure 23: ^{29}Si DP MAS NMR spectra for SBA-2: (a) as-prepared and (b) calcined.

Si species	ppm	as-prepared	calcined
Q^2	-91	11.0	2.4
Q^3	-99	51.1	25.4
Q^4	-109	37.9	72.2
Q^3/Q^4		1.35	0.35

Table 6: Integrated intensities for ^{29}Si DP MAS NMR deconvoluted spectra of SBA-2 (RT, 2 h).

Comparison, meanwhile, of the direct and cross-polarised spectra for each sample (as-prepared and calcined) reveals some interesting results. The CP technique discriminates in favour of Si-OH species, due to the proximity of abundant ^1H spins. Considering the as-prepared^{xm} material, however, figure 24, the CP experiment appears not to significantly improve the Q^3 signal intensity relative to Q^4 . This is unexpected, but suggests that CP from the organic surfactant within the sample swamps any Si-OH

^{xm} The as-prepared RT (2 h) or 80 °C (1 wk) spectra are identical in this respect.

signals pertaining to the framework structure. The calcined solid, however, presents a Q^3 intensity enhancement consistent with the anticipated CP spectrum, figure 25. This can be reconciled by the many Si-OH species now covering the internal and external surfaces of the framework.

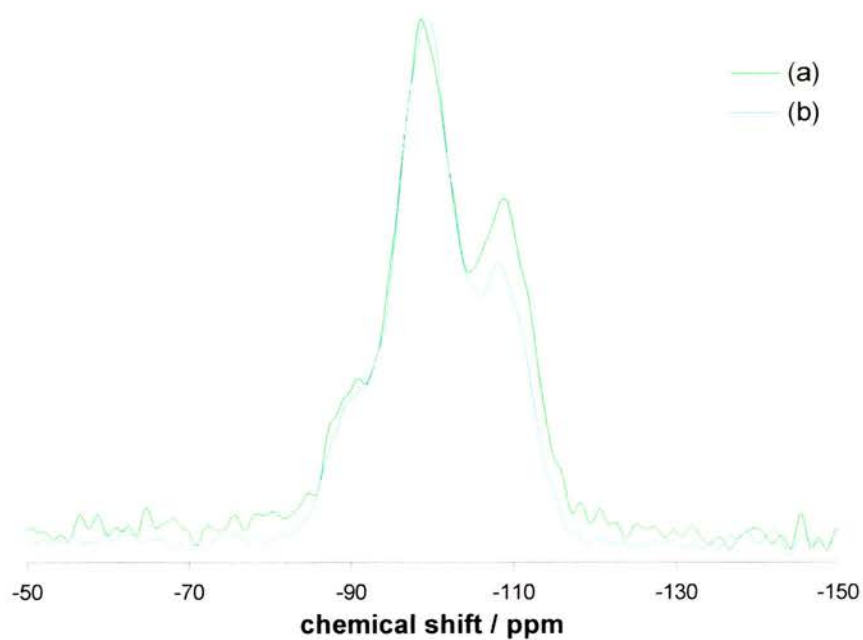


Figure 24: ^{29}Si MAS NMR spectra of as-prepared SBA-2: (a) direct polarization and (b) cross-polarised.

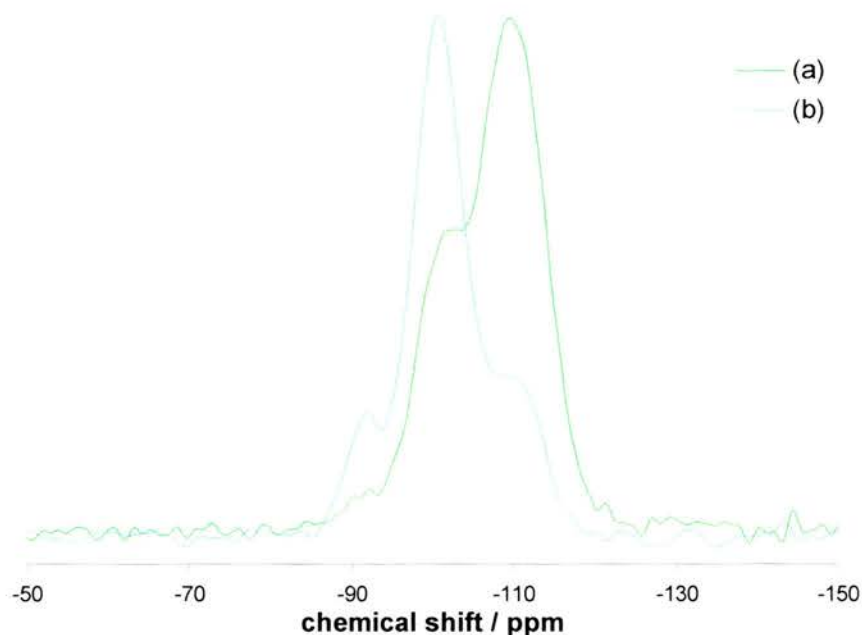


Figure 25: ^{29}Si MAS NMR spectra of calcined SBA-2: (a) direct polarization and (b) cross-polarised.

FTIR

FTIR spectra of as-prepared and calcined SBA-2 are shown in figure 26. Of primary note is the dominance of the absorption band at 1100 cm^{-1} . This strong and broad peak is attributable to the Si-O vibration within silicates. Furthermore, it is clear from the loss of C-H stretching peaks at 2925 cm^{-1} and 2825 cm^{-1} , and the disappearance of the C-H bending deformation at 1500 cm^{-1} , that calcination removes all^{xvii} of the organic surfactant molecules. All other expected IR active bonds (e.g. N-C) are weak IR absorbers, in comparison to Si-O, and are present in low concentrations. They, therefore, are not discernible in the observed as-prepared spectra. Likewise, no peaks attributable to a change in surfactant tail length or addition of co-organics to the surfactant mixture can be detected.

^{xvii} This is confirmed by elemental analysis, where an as-prepared solid contains ca. 28 wt% carbon, whilst the corresponding calcined material possesses <1 wt% carbon.

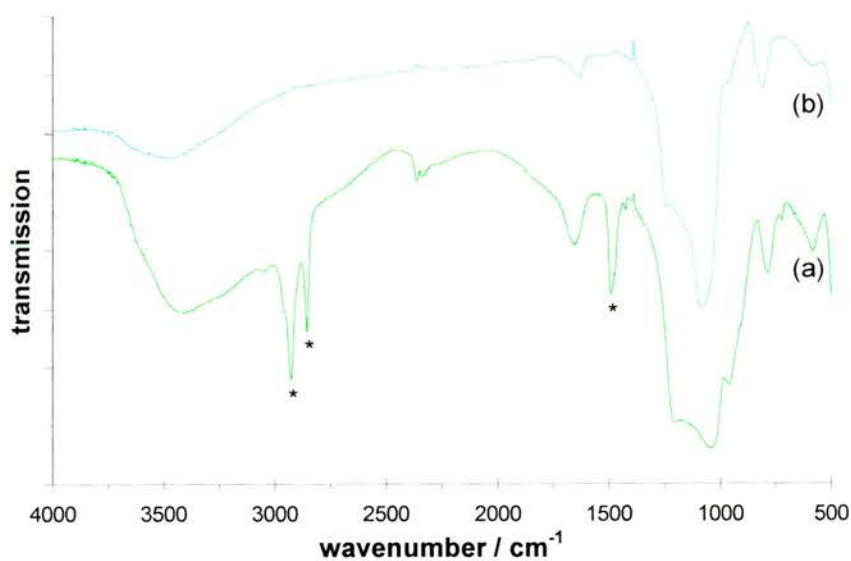


Figure 26: Characteristic FTIR spectra of (a) as-prepared and (b) calcined SBA-2.

TG-MS

A TG-MS experiment was performed on an as-prepared SBA-2 sample. The result, figure 27, shows that the C16-3-1 surfactant molecule decomposes in three steps.

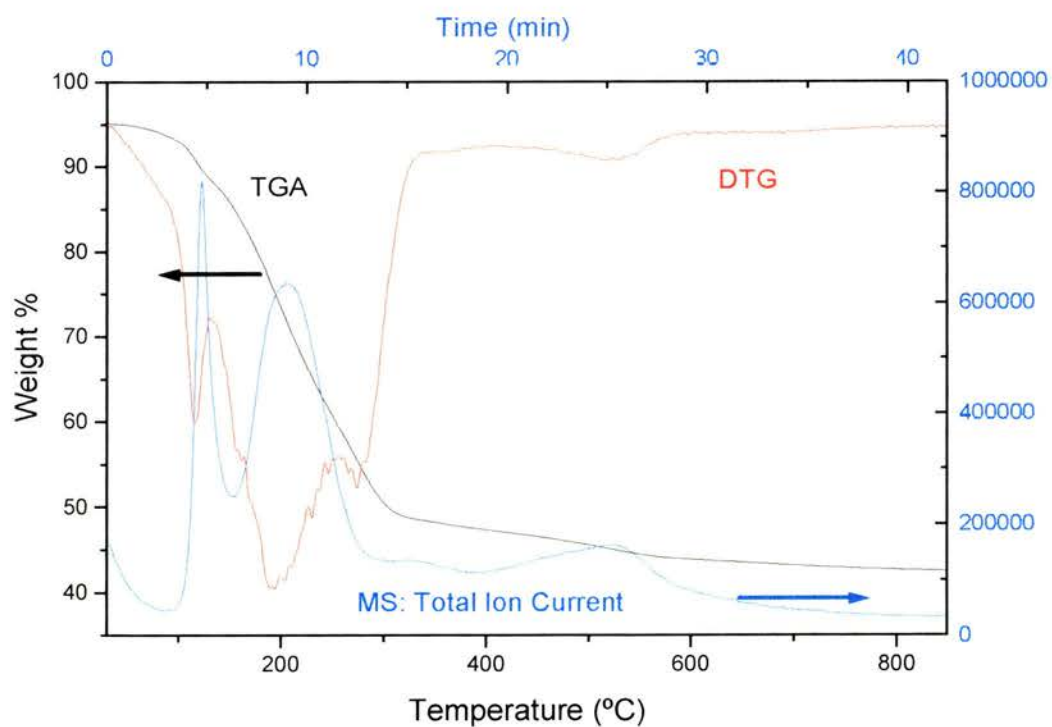


Figure 27: TG-MS result for SBA-2 C16-3-1.

The first weight loss occurs below 150 °C and corresponds to a sharp increase in total ion current.^{xviii} Identified from the mass spectrum^{xx} obtained after 4.7 min, this fragmentation pattern correlates well with the standard MS library spectrum for trimethylamine, figure 28. Such a molecular ion would originate from the terminal nitrogen grouping of the C16-3-1 surfactant head group. Furthermore TGA-DTA traces of analogous as-prepared materials identify this 7.0 % weight loss as a thermal degradation product. Such an endothermic event suggests that the surfactant breaks down via a Hofmann rearrangement reaction, figure 29a. It is interesting that this occurs at the low temperature of *ca.* 120 °C, considering that the pure surfactant has a decomposition temperature of 223-224 °C. Presumably the organic-silicate interface destabilises the head group, due to the close proximity of the cationic charges. Any weight loss occurring below 100 °C, meanwhile, can be attributable to the removal of water and/or ethanol from within (or on the external surface of) the as-prepared structure.

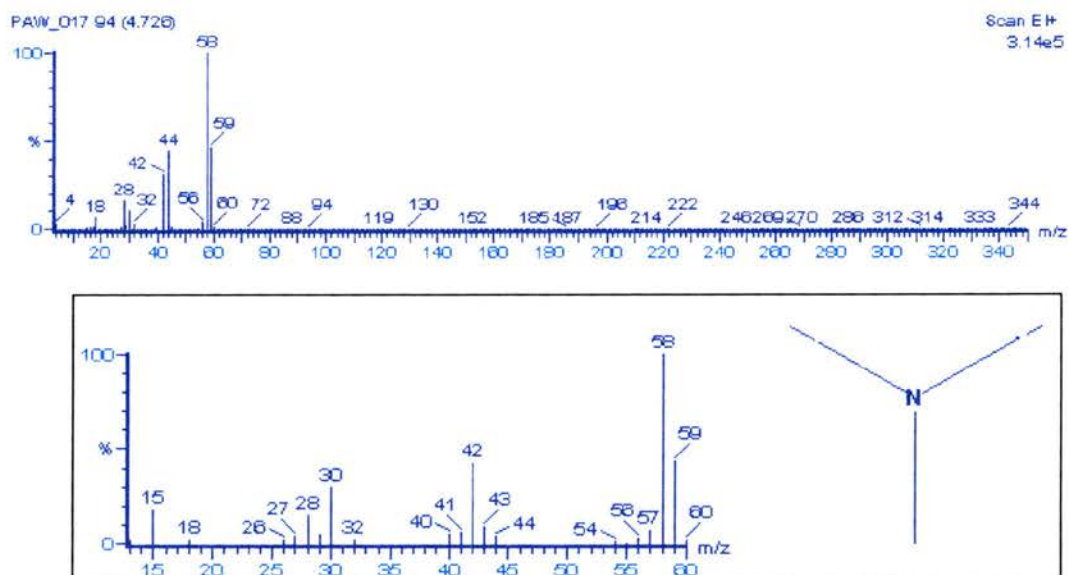


Figure 28: MS taken after 4.7 min (top) and the correlating library spectrum for trimethylamine (bottom).

^{xviii} Total Ion Current (TIC): the total number of ions present in the spectrometer at one time.

^{xx} The intense peak at $m/z = 44$ corresponds, mainly, to CO_2 and can be attributed to the oxidation of organic compounds; O_2 being present in the equipment, even although an inert atmosphere is used.

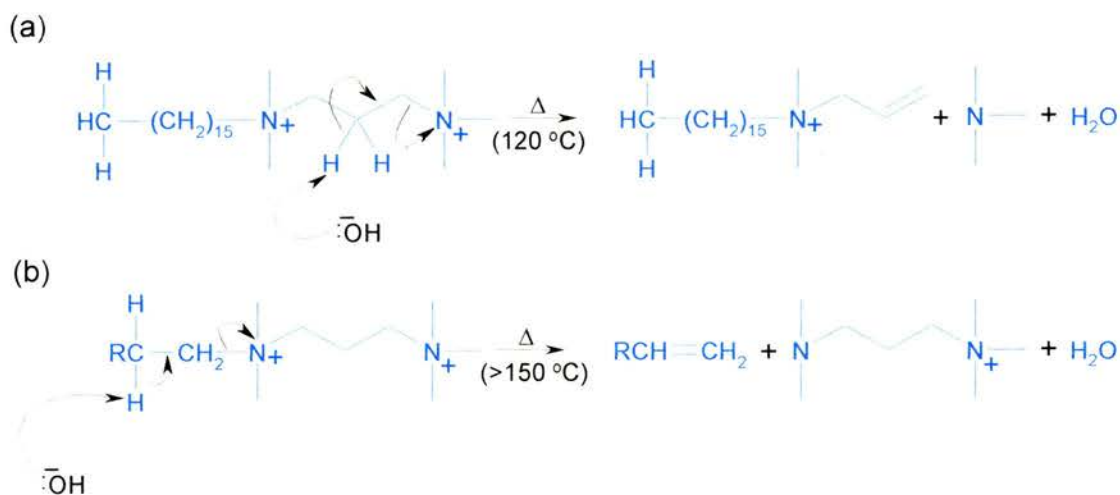


Figure 29: The Hofmann rearrangement reaction.²⁸

The second weight loss occurs between 150 – 350 °C. Similarly this can be assigned to the break up of the gemini surfactant. In particular, the mass spectrum taken after 9.1 min, figure 30, indicates that the diquaternary ammonium head group (N,N,N',N'-tetramethyl-1,3-propane diamine) fragments in this temperature region. Such a process further suggests that the remaining surfactant decomposes via the Hofmann rearrangement reaction, figure 29b. In this temperature region, therefore, the thermally induced E2 elimination creates a long C16 hydrocarbon alkene and a diamine as its products. Combined these account for the observed 37.9 % weight loss.

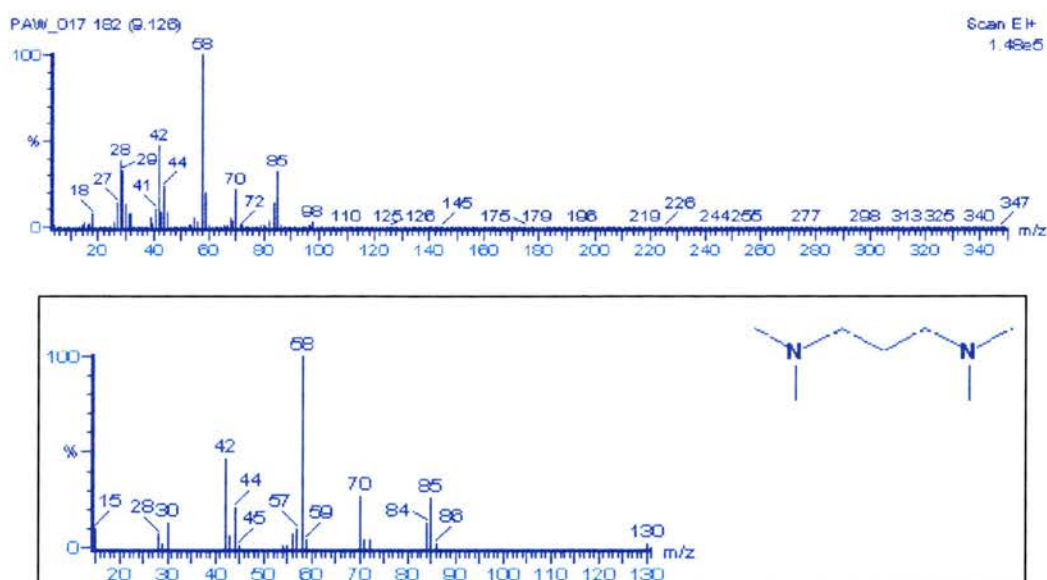


Figure 30: MS taken after 9.1 min (top) and the correlating library spectrum for N,N,N',N'-tetramethyl-1,3-propane diamine (bottom).

The third weight loss region occurs above 350 °C. The accompanying total ion current peak at 25.6 min, figure 31, presents a fragmentation pattern typical of the decomposition of a long chain hydrocarbon (the surfactant tail). Again this corresponds to a non-trivial weight loss (approx. 6.5 %). Above *ca.* 600 °C, however, no further decomposition products are detected (no identifiable peaks in the differential thermal gravimetry, DTG, trace).



Figure 31: MS taken after 25.6 min showing a fragmentation pattern typical of a long chain hydrocarbon (the surfactant tail).

Finally, it is worth noting that during each total ion current analysis there is no evidence of a peak at $m/z = 81$. Such a molecular ion would be attributable to HBr. Its absence, however, indicates that the bromide ion is not involved in the creation of the as-prepared material.

Thus overall, approximately^{xx} 51.4 %, by weight, of a C16-3-1 as-prepared SBA-2 material is organic. Such a conclusion, is in line with the elemental analysis of this sample: total 44.5 wt %, and the correspondingly observed 41.0 % weight loss after calcination. Furthermore it is also comparable to the organic content^{xxi} of other as-prepared mesoporous silicates: 34 wt % MCM-41 and 50 wt % MCM-48.

^{xx} The organic content, however, is known to vary between preparations of the same mesoporous material. In particular insufficient washing during filtration may leave the recovered solid containing extra surfactant, even although C16-3-1 is noticeably more water soluble than CTAB.

^{xxi} Determined by CHN analysis; like SBA-2 these values are dependent upon the sample preparation.

XRD Overview

The XRD pattern of pure C16-3-1 surfactant is shown, for reference, alongside that of an as-prepared C16-3-1 SBA-2 solid, figure 32. Clearly the well-ordered SBA-2 material does not show a reflection attributable to pure C16-3-1 (at $2.46^\circ 2\theta$) in its powder pattern. If such an intensity does occur, however, it indicates a considerable presence of unreacted surfactant in the sample. Moreover it suggests that silicate mesophase formation has not occurred and/or the excess surfactant has not been removed during washing.

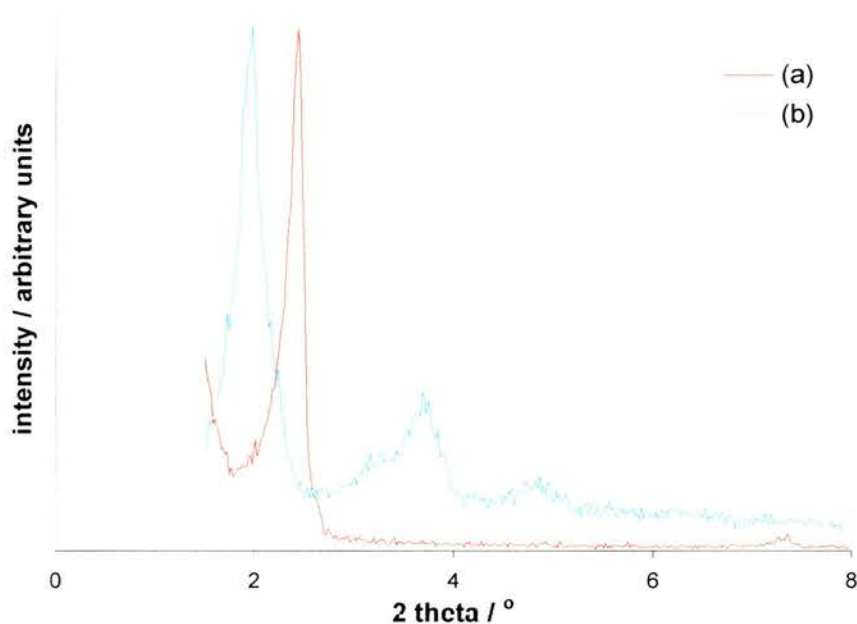


Figure 32: XRD patterns of (a) pure C16-3-1 and (b) an as-prepared C16-3-1 SBA-2 solid.

Focussing upon SBA-2, a typical X-ray pattern is presented in figure 33. Such a diffractogram is analogous to that first reported⁶ for SBA-2 by Stucky *et al* in 1995. Thus, as illustrated, the pattern can be indexed by a hexagonal unit cell. The resulting refined unit cell parameters are $a = 56.2 \text{ \AA}$, $c = 91.5 \text{ \AA}$, $\alpha = \beta = 90^\circ$ and $\gamma = 120^\circ$ for this as-prepared solid. In addition the calculated c/a ratio of 1.63 is close to that of an ideal hexagonally close packed array, $c/a = 1.63$. Upon calcination a weight loss^{xvii} is observed, and the framework structure contracts. This is characteristic of all mesoporous silicates, and can be reconciled by further condensation within the walls.

^{xvii} In SBA-2 a typical solid loses 46 wt % after the organic surfactant is removed.

In XRD such a phenomenon is illustrated by a shift to lower d spacings (higher $^{\circ}2\theta$) of all the SBA-2 reflections, figure 34. Subsequent unit cell calculations, therefore, show that the calcined material now has the dimensions $a = 49.3 \text{ \AA}$ and $c = 80.0 \text{ \AA}$. This corresponds to a 12.5 % d_{002} peak contraction, or a 32.8 % unit cell volume^{xxiii} loss. In addition the peak intensities^{xxv} simultaneously increase, since there are no longer carbon atoms (to generate destructive interference) within the mesopores. Presumably this is why the d_{110} reflection increases (proportionally) more than the d_{112} peak. Overall, however, all the diffraction peaks broaden slightly following calcination (*ca.* 0.07 $^{\circ}2\theta$ major peak FWHM value) but the structural order is largely retained. Indeed the calcined SBA-2 framework structure is stable up to 1000 $^{\circ}\text{C}$, under flowing N_2 (XRD pattern not shown).

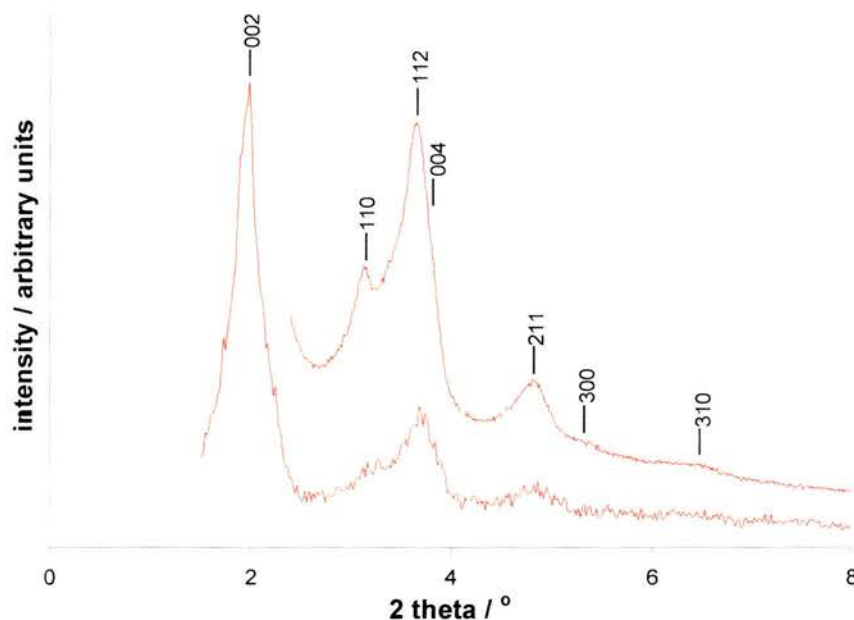


Figure 33: XRD patterns for as-prepared SBA-2.

^{xxiii} Hexagonal unit cell volume = $a^2c \sin 60$.

^{xxv} It is difficult to quantitatively assess the XRD peak intensities because they very much depend upon the preparation of the sample plate for analysis (ideally as flat as possible).

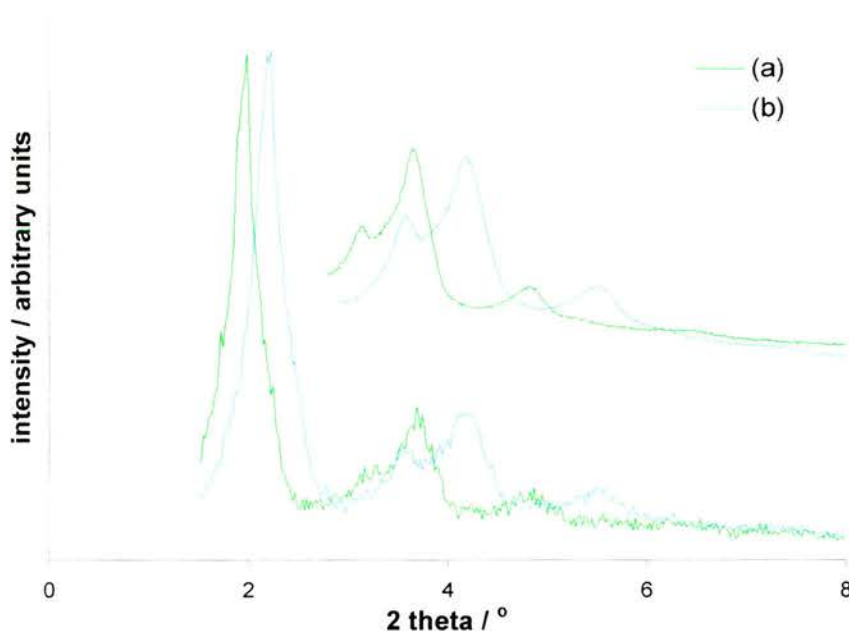


Figure 34: XRD patterns for (a) as-prepared and (b) calcined SBA-2.

An as-prepared sample heated (550 °C, 7 h) in flowing N₂ only, however, does not^{xxx} remove *all* the organic surfactant present. Likewise the exothermic reaction created by surfactant removal in oxygen alone is vigorous. Such an experiment leads to severe framework degradation and occasionally a tube furnace explosion. Thus the 550 °C 1 h N₂, 6 h O₂ calcination^{xxvi} programme was employed to ensure an organic-free calcined material for subsequent applications.

As alluded to in the XRD background theory, SBA-2 may form around spherical micelles stacked either in a hexagonal or a cubic close packed arrangement. A predominance of hcp stacking manifests^{xxvii} itself as a d_{103} peak in a XRD pattern, appearing in the secondary 3 – 5 °2θ peak region, figure 35. Theoretically^{29,30} there is a very slight entropic preference for ccp stacking of spheres. This, however, does not prevent many materials (e.g. metals) from possessing either close packed arrangement.

^{xxx} Elemental analysis shows that 1.2 wt% carbon remains, whilst the resulting solid is grey-brown coloured.

^{xxvi} Surfactant removal by ethanol : *conc.* HCl extraction is also feasible for SBA-2. As with calcination a contraction of the unit cell (of comparable order) is observed following extraction. This work was done in collaboration with Miss Isabel Díaz.

^{xxvii} The differences at lower angles (*ca.* 2.4 °2θ) are hidden by the breadth of the major mesoporous XRD peak.

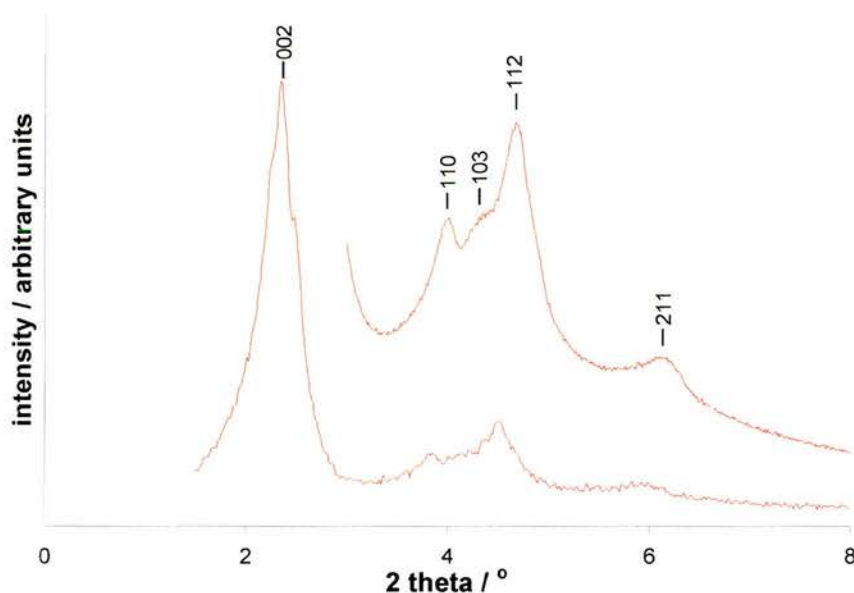


Figure 35: XRD patterns for calcined SBA-2 displaying a hcp micelle stacking preference (d_{103} presence).

Finally, for comparison, the X-ray patterns for SBA-2, MCM-41 and MCM-48 are plotted in figure 36. It is obvious that a 0.05 C16-3-1 : 0.5 TMAOH : 1 TEOS : 150 H₂O synthesis composition cannot (and does not) form either of these well studied MCM materials. This can be reconciled by the surfactant used, and, in particular the micelle forming effects due to the doubly charged head group of the C16-3-1 molecule.

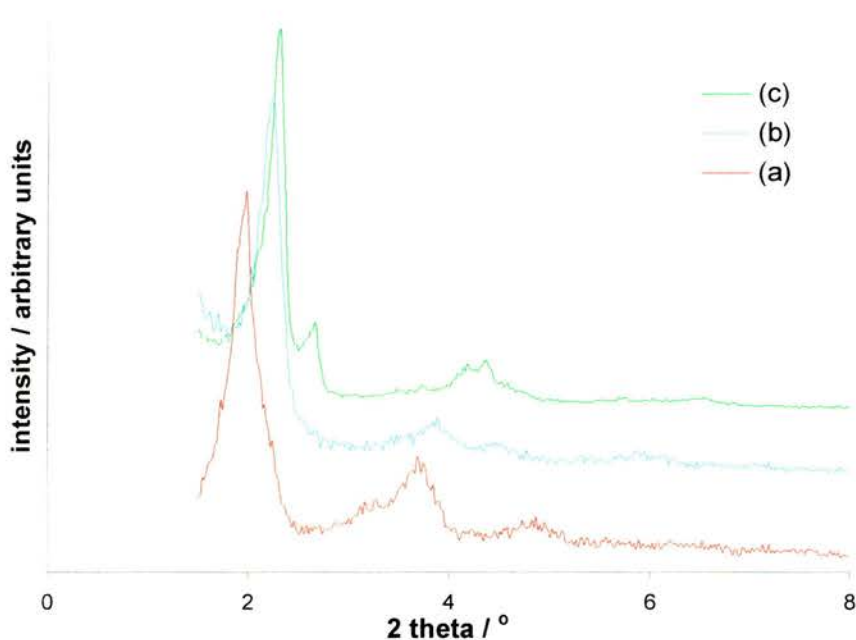


Figure 36: XRD patterns for (a) SBA-2, (b) MCM-41 and (c) MCM-48.

Adsorption Isotherm Overview

As mentioned earlier, mesoporous materials show type IV adsorption isotherm behaviour. This is what is observed for SBA-2, figure 37. The isotherm can be described as follows. Initially all gaseous nitrogen is adsorbed immediately, forming a uniform monolayer coverage across all the (predominantly internal) sample surfaces. This is represented by the steep (near vertical) section of the isotherm below $P/P_0 = 0.1$. As consecutive aliquots of nitrogen adsorbate are introduced, though, a gradual deviation from the near vertical occurs. For SBA-2 this corresponds to the $0.02 \leq P/P_0 \leq 0.2$ region and can be explained by a build-up of multiple layers of adsorbed nitrogen within the mesopores. Careful analysis of this multilayer adsorption, using the BET equation, can indicate the surface area for the solid under investigation. Above $P/P_0 = 0.2$, however, a second rapid rise in adsorption (over a small partial pressure increase) ensues. This can be reconciled by the now near cylindrical form of the remaining volume, whose preferential filling is known as capillary condensation. It is from this section of the desorption isotherm that the Kelvin equation is applied, to calculate the pore size distribution in the sample. Once all the mesopores are filled the isotherm levels off, since there is no remaining volume available for filling. Thus any subsequent adsorbate uptake is minimal, and due only to multilayer condensation on the external surface. A type IV isotherm, therefore, can be described by this maximum (mesopore) volume, whose value is independent of the gaseous partial pressure. Finally the SBA-2 isotherm does not possess a significant hysteresis loop. This can be reconciled by the silicate structure which contains few constrictions that could act as 'bottle necks' during adsorbate desorption. Hence, the adsorption and desorption branches of this isotherm are almost identical.

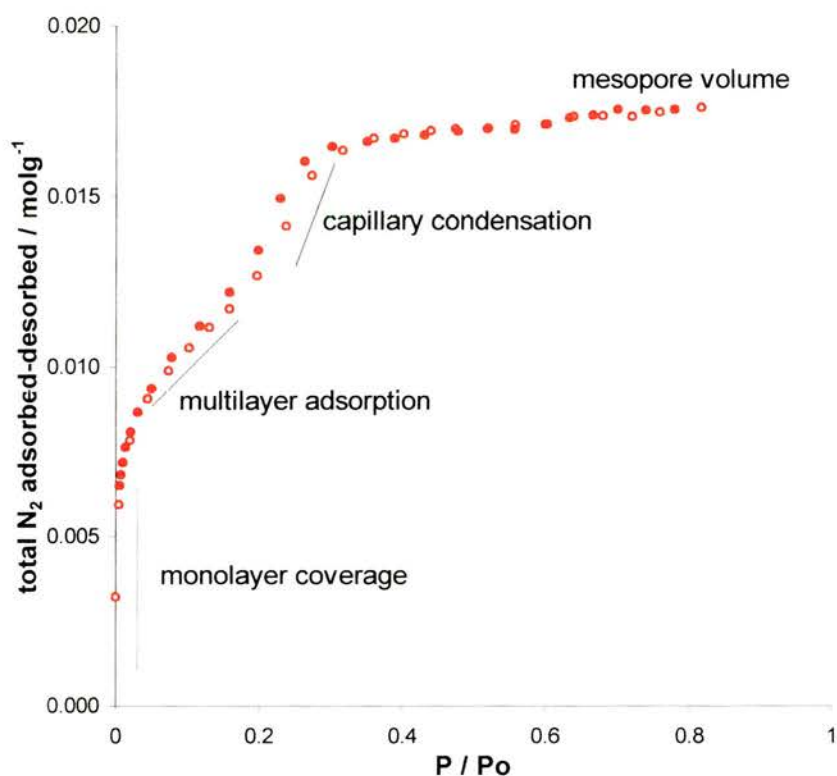


Figure 37: Adsorption Isotherm of a typical SBA-2 C16-3-1 solid. Adsorption = open symbols, desorption = filled symbols.

A second isotherm, figure 38, unequivocally illustrates the differences between porous silicates and their corresponding framework structures. Of first note is the clear distinction between a type I and a type IV isotherm, represented by Zeolite Y and SBA-2 or MCM-41 respectively. The rectilinear zeolite plot is typical of all microporous solids and shows that for cavities of <2 nm there can be no multilayer adsorption. Thus the isotherm plateaus when pore filling is complete and any subsequent (gradual) increase in adsorption is then attributable to multilayer coverage on the external surfaces. The mesoporous solids, however, are capable of containing multiple adsorbate layers. Consequently their final adsorption volumes can be many times larger^{xxviii} than that of a zeolite. In this case SBA-2 and MCM-41 adsorb a maximum of 0.017 and 0.027 mol g^{-1} respectively. Significantly though, these values are *not* identical, despite the fact that they were both made with surfactants of 16-membered carbon tails. This illustrates the structural differences between these two mesoporous frameworks. Thus,

^{xxviii} The precise mesopore volume depends upon the particular preparation, since the use of different surfactants and/or swelling agents can significantly enlarge/reduce the micelle size and hence the final unit cell size i.e. mesoporosity of the structure.

per gram, the SBA-2 structure adsorbs 37.0 % less. In other words there is more (or thicker or denser) silicate framework in SBA-2 than in MCM-41. This must be reconciled with the knowledge that MCM-41 is a hexagonal uni-dimensional channel structure, yet SBA-2 is 2-dimensionally mesoporous (FEM chapter). It is also conceivable that in the SBA-2 structure some pores may be blocked from the external surface, thereby contributing to the reduced adsorption volume c.f. MCM-41.

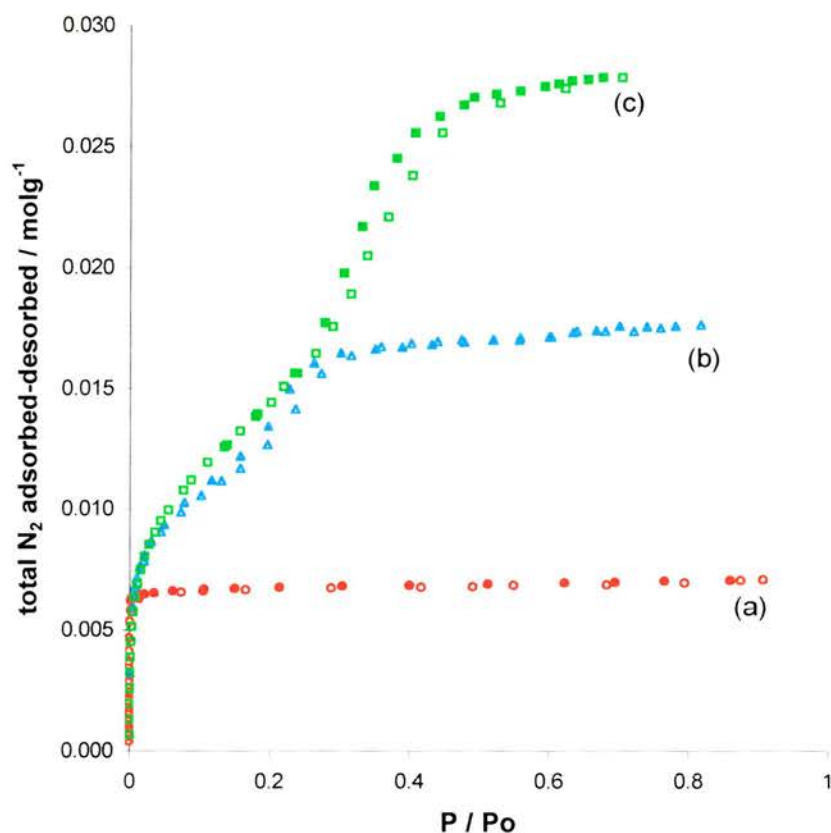


Figure 38: Multiple adsorption isotherm for (a) Zeolite Y, (b) SBA-2 and (c) MCM-41. Adsorption = open symbols, desorption = filled symbols.

Effect of Surfactant Length or Swelling Agent

Three surfactants, of differing tail lengths, were used to illustrate how the unit cell dimensions of SBA-2 vary with micelle size. Thus either C12-3-1, C16-3-1 or C18-3-1 was employed in a RT, 2 hour synthesis. The resulting XRD patterns are shown in figure 39.

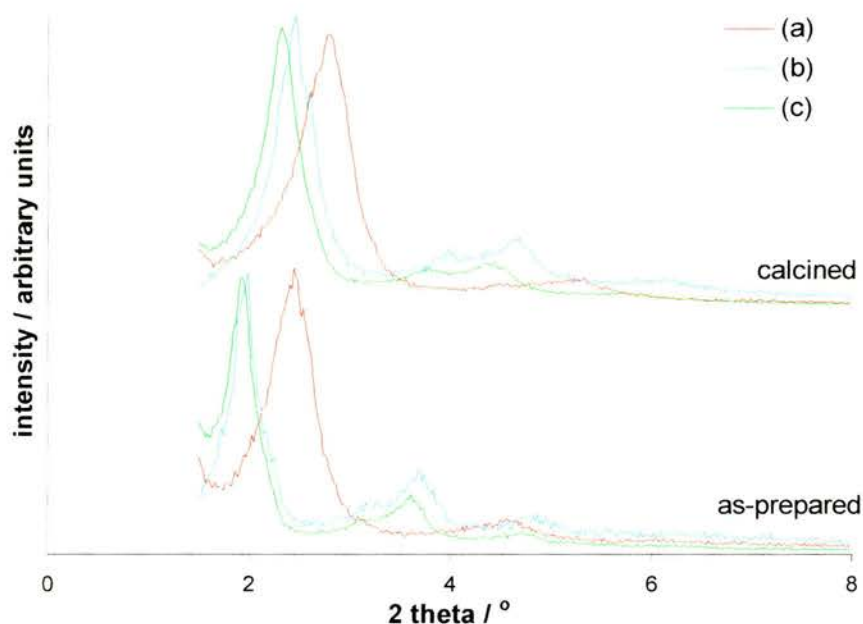


Figure 39: XRD patterns of SBA-2 synthesised using different surfactants: (a) C12-3-1, (b) C16-3-1 and (c) C18-3-1.

Of first note is that the C12-3-1 surfactant creates a diffractogram whose major peak occurs at higher $^{\circ}2\theta$ values than those of longer carbon tails. This indicates that the templating molecular assembly is smaller and therefore results in reduced unit cell size for SBA-2. Presumably the C12-3-1 micelles are smaller because they are 8 or 12 carbons less per diameter (and composed of fewer^{xxx} molecules) than the materials containing longer surfactant micelles. The effective micelle packing parameter, g , meanwhile, changes only slightly thus the SBA-2 mesophase forms in all three cases (indexable peaks).

As would be expected, the major peak positions (d spacing), and thus unit cell size, increases with increasing surfactant tail length: C12-3-1 < C16-3-1 < C18-3-1. This is intuitive and confirms that the C18-3-1 micelle is of slightly larger diameter than that of a C16-3-1 surfactant agglomeration. Furthermore this logical C $_n$ -3-1:XRD major peak relationship is maintained following calcination.

^{xxx} The highly charged head groups of these surfactants force any contraction in the micelle dimensions to be accompanied by a reduction in numbers of head groups. To do otherwise means that the charge on the exterior surface (i.e. head group repulsions) increases compared to the total micelle volume.

Adsorption Isotherms were subsequently measured for these three calcined materials, figure 40 and table 7. Each solid exhibits a type IV isotherm. The C12-3-1 templated material, however, is at the limit of this classification, verging towards a microporous type I adsorption plot. This can be reconciled by the reduced micelle dimensions, which when removed leave a framework that can barely accommodate any capillary condensation. Thus the mesopores are filled^{xxx} during multilayer adsorption and the mesopore volume can be determined at this point.

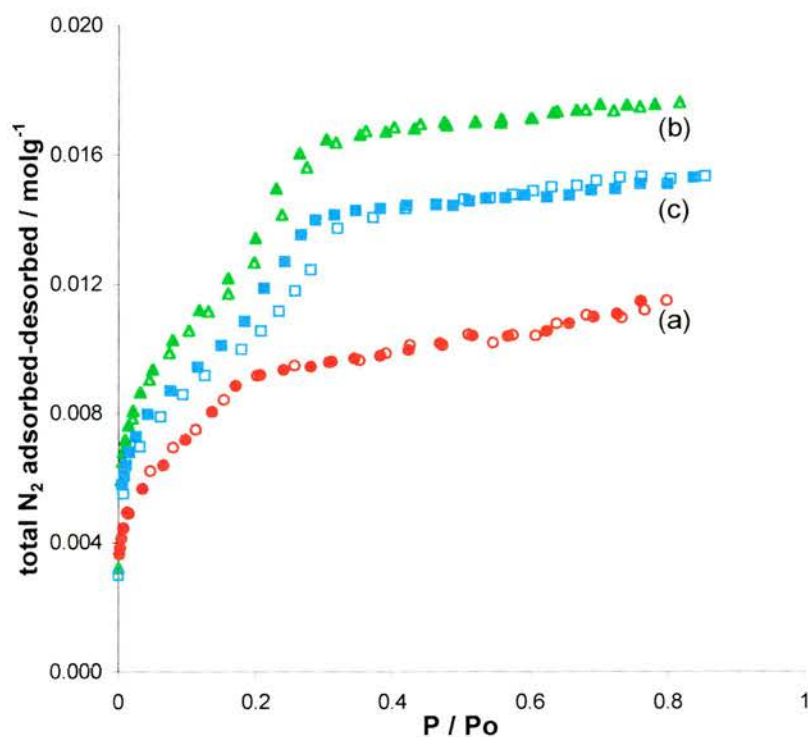


Figure 40: Adsorption Isotherms for calcined SBA-2 materials synthesised using (a) C12-3-1, (b) C16-3-1 and (c) C18-3-1. Adsorption = open symbols, desorption = filled symbols.

	C12-3-1	C16-3-1	C18-3-1
av. pore diameter (Å)	22.14	25.13	25.83
mesopore volume (cm ³ g ⁻¹)	212 [*]	395	342
BET surface area (m ² g ⁻¹)	700±6	996±8	831±5

^{*} mesopore volume at P/Po = 0.26

Table 7: Adsorption Isotherm values for calcined SBA-2 materials synthesised using different surfactants.

^{xxx} With such a poorly defined capillary condensation region the calculated 22.14 Å average pore diameter is not reliable. Moreover microporous materials (cavities <2 nm) exhibit type I isotherms and no multilayer adsorption.

The C16-3-1 and C18-3-1 materials, meanwhile, exhibit capillary condensation. Their respective average pore sizes, therefore, confirm the unit cell size differences observed by XRD. The final mesopore volume, however, is lower for the C18-3-1 templated material. This could be attributed to enhanced framework condensation, during synthesis, which results in a smaller void volume per gram following calcination. The mechanistic reasons for this, however, remain unclear. Finally the BET values broadly mirror the final mesopore volumes. Each solid possess the same structure, thus these surface areas can also be rationalised by their corresponding void/framework density ratios.

An SBA-2 synthesis including 0.58 mol trimethylbenzene (TMB) has also been performed. The XRD result is presented in figure 41 alongside an analogous C16-3-1 SBA-2 experiment (no TMB). It is clear that the effect of the TMB swelling agent is as such, demonstrated by the significant major peak shift to higher d spacings: 7.6 % (as-prepared) and 9.6% (after calcination). The secondary region, however, continues to show structural detail. This confirms that the subtleties contained within the silicate framework are not dependent upon the micelle size.

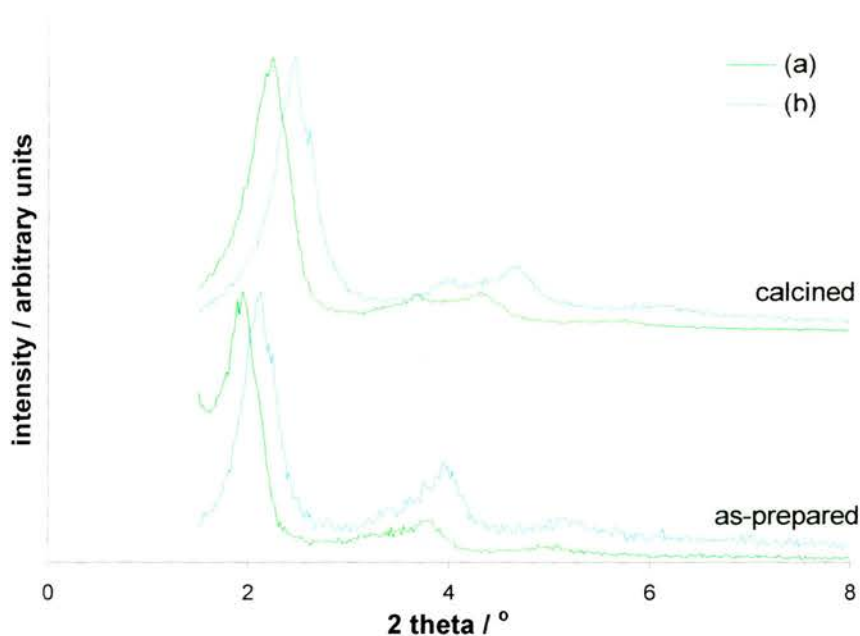


Figure 41: XRD patterns for C16-3-1 SBA-2 synthesised (a) with and (b) without TMB.

The adsorption isotherms for these two solids tell a similar story, figure 42. The larger unit cell dimensions of the TMB templated material is shown by the location of the

capillary condensation region at higher adsorbate partial pressures. This is reflected in the average pore diameters: 28.70 Å (with) *versus* 25.13 Å (without TMB). The similarity in the mesopore volumes, though, indicates that these solids have comparable framework densities.

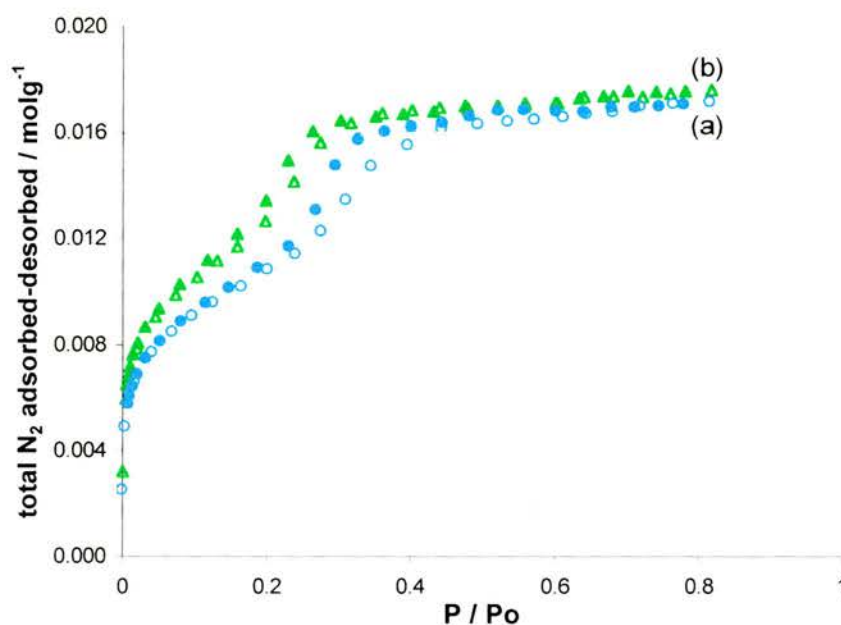


Figure 42: Adsorption Isotherms for C16-3-1 SBA-2 synthesised (a) with and (b) without TMB. Adsorption = open symbols, desorption = filled symbols.

Effect of Mixed Surfactants

A synthesis was performed to examine the effect of mixing two surfactants of different tail lengths. Thus SBA-2 was prepared containing 0.05 mol surfactant, as 0.015 mol C12-3-1 and 0.035 mol C16-3-1. The resultant as-prepared XRD pattern is shown in figure 43, alongside^{xxx} those of pure (0.05 mol) C12-3-1 and C16-3-1 materials. It is clear that a mixed surfactant synthesis acts to accommodate the differing carbon chain lengths, whilst maintaining a well-ordered SBA-2 structure. The resultant micelle, therefore, appears to be an average of the two molecular packing parameters.

^{xxx} The choice of comparable SBA-2 XRD patterns, though, is critically dependent upon the reaction pH (see Effect of pH).

Consequently, the overall effect is a reduction in the apparent micelle size (major peak position), in line with the C12-3-1:C16-3-1 ratio.

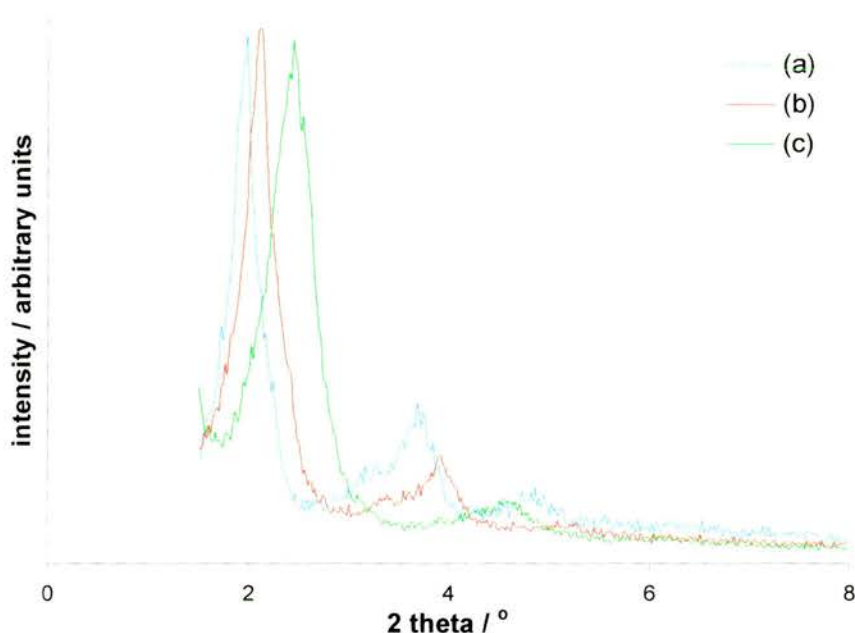


Figure 43: XRD patterns of SBA-2 prepared with (a) 100 % C16-3-1, (b) a 30 % C12-3-1, 70 % C16-3-1 mixture and (c) 100 % C12-3-1.

This trend is maintained following calcination, and is illustrated by the corresponding adsorption isotherms, figure 44. As the structural dimensions decrease, the region of capillary condensation, likewise, migrates to lower partial pressures. The average pore diameter, therefore, mirrors the XRD major peak position, table 8, and increases as the percentage of C16-3-1 surfactant increases in the synthesis mixture. Similarly the mesopore volume confirms that as the micelle diameter increases, so too does the void volume in the calcined material. The BET surface areas, however, do not follow this trend. Instead they indicate that the mixed surfactant preparation retains the largest surface area, which may be attributable to more local curvature within this structure.

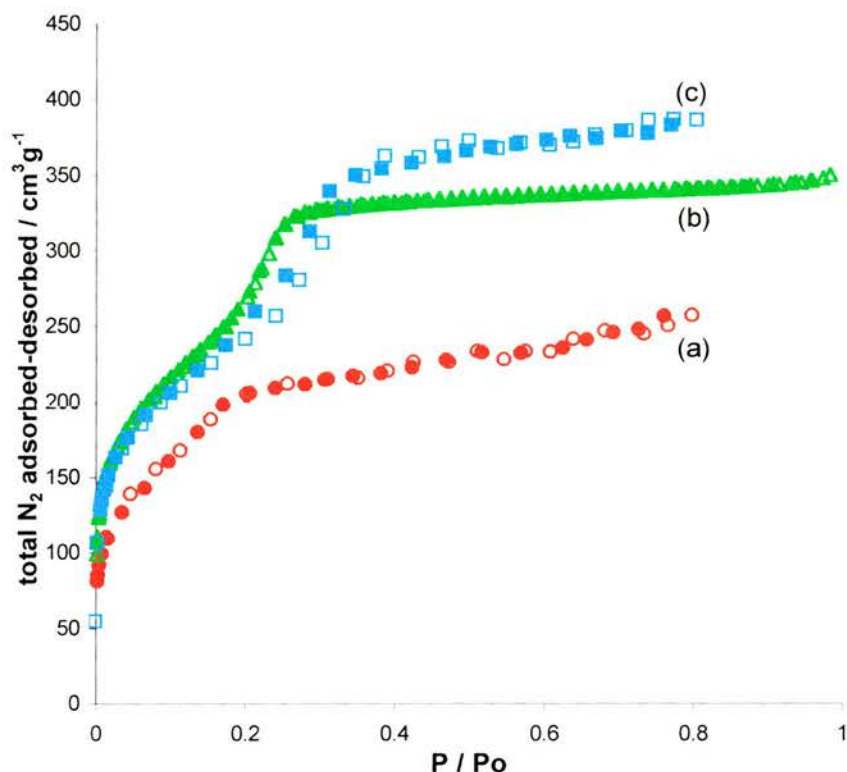


Figure 44: Adsorption Isotherms for SBA-2 prepared with (a) 100 % C12-3-1, (b) a 30 % C12-3-1, 70 % C16-3-1 mixture and (c) 100 % C16-3-1. Adsorption = open symbols, desorption = closed symbols.

	C16-3-1	C12-3-1:C16-3-1	C12-3-1
d_{002} (Å)	39.7	37.0	31.3
av. pore diameter (Å)	28.88	25.93	22.14
mesopore volume (cm^3g^{-1})	386	342	257
BET surface area (m^2g^{-1})	874 ± 3	938 ± 5	700 ± 6

Table 8: Adsorption Isotherms values for calcined SBA-2 materials prepared with different surfactant mixtures.

Meanwhile, a 0.015 mol CTAB : 0.035 mol C16-3-1 SBA-2 experiment was also undertaken. The resulting XRD patterns, figure 45, are shown in comparison to a pure C16-3-1 SBA-2 material. Since both surfactants possess the same length of tail, there is no difference in the micelle size, nor in the major XRD reflection position. It was hoped, however, that XRD could ascertain the affect of the surfactant head group size (i.e. charge) upon the final synthesised material. In reality, though, this technique is insensitive to such subtleties, since no significant disturbance to the secondary peak region is observable. The micelle surface charge, therefore, must still be above the threshold limit for SBA-2 formation, at this surfactant concentration.

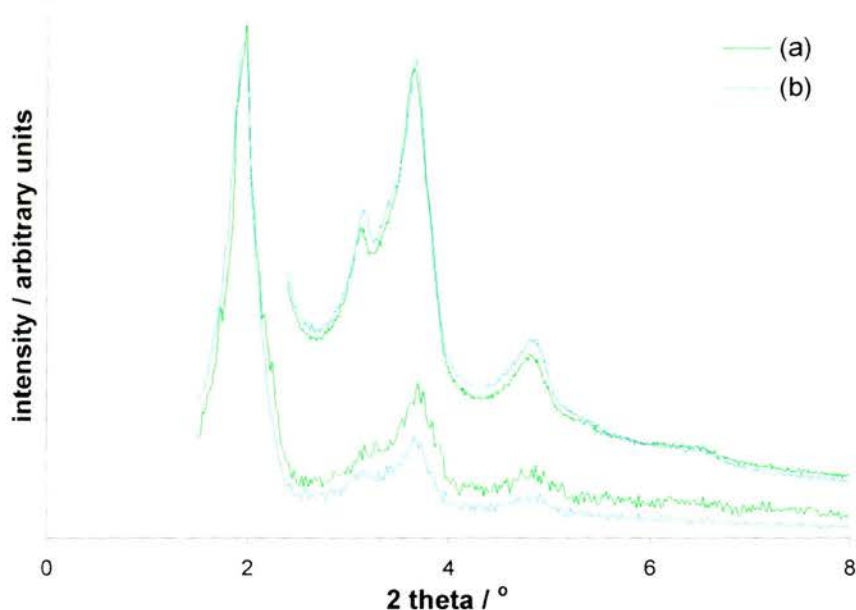


Figure 45: XRD patterns of SBA-2 prepared with (a) 100 % C16-3-1 and (b) a 30 % CTAB, 70 % C16-3-1 mixture.

Effect of pH

The effect of pH upon final unit cell size and ‘order’ of the material was specifically investigated. These preparations employed a pH meter to monitor the pH as the starting materials were added, and over the course of the reaction. In doing so it was found that the reaction pH dropped rapidly 2-3 min after TEOS addition, figure 46. This can be attributed to the involvement of hydroxyl ions in silica hydrolysis, and its corresponding formation of an ethanol by-product. Either process would lower the pH. Furthermore removal of OH^- ions from solution may also occur as a result of their possible involvement in charge matching at the organic-silicate interface. It appears, though, that the pH rebounds after this initial ‘acidification’. This is likely to be simply due to the return to equilibrium of the silicate hydrolysis and condensation (hydroxide ion involving) reactions. The gradual reduction in reaction pH over time (20-120 min) though, can again be attributed to the involvement of hydroxide ions in a charge compensation mechanism at the micelle surface.

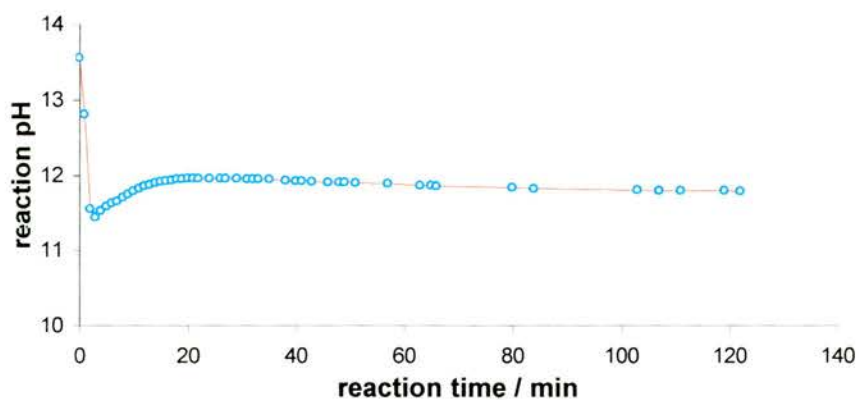


Figure 46: A typical solution pH curve during a 2 hour synthesis of SBA-2.

To obtain the desired pH synthesis window *conc.* H_2SO_4 was added to the reaction, 3-5 min after TEOS addition, to lower the pH below pH 11; alternatively further TMAOH was added dropwise (for reactions of pH >12). The XRD results for this 5-sample series are presented in figure 47. For each sample the powder pattern can be indexed by a hexagonal unit cell.

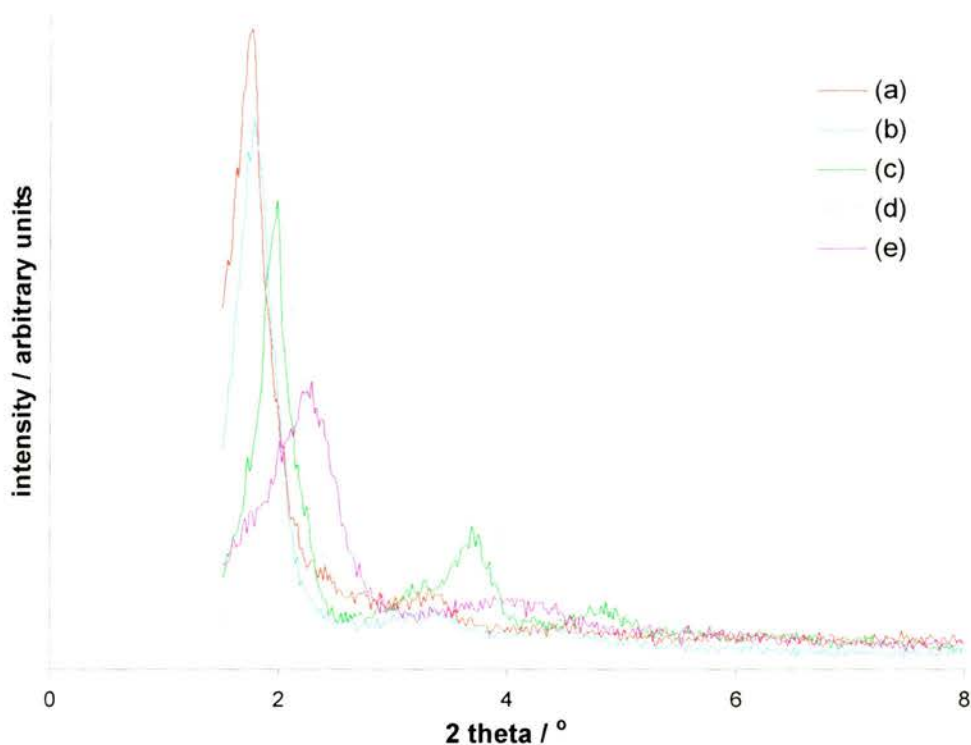


Figure 47: XRD patterns showing the effect of reaction pH on SBA-2 synthesis (RT, 2 h, stirring): (a) pH 10-10.5, (b) pH 10.5-11, (c) pH 11-11.5, (d) pH 11.5-12, (e) pH 12-12.5.

Of first note is that the major peak shifts to lower 2θ (larger unit cell) as the reaction pH decreases. This relationship is known³¹ to occur in MCM-41. Secondly, as the reaction pH deviates away from *ca.* pH 11, the major peak gets progressively broader and less intense. Such a feature is characteristic of smaller particle dimensions and poorer long range order. Meanwhile the loss of major peak definition is also reflected in the secondary 3-5 2θ peak region, figure 48. The reduction of mesoporous order is clearly visible outside the pH 11-12 range. At pH >12 the secondary region appears as a broad featureless hump. Below this pH range, however, the d_{110} and d_{112} peaks (although present) are less sharp. These observations can be described numerically by a full width half maximum (FWHM) value for the major diffraction peak, table 9. This suggests that the SBA-2 sample made between pH 11-11.5 is most ordered (lowest FWHM, strongest maximum intensity). Unlike the pH 11.5-12 sample, though, the d_{103} reflection is not observed. This is taken to indicate that the sample has less hexagonal ordering.

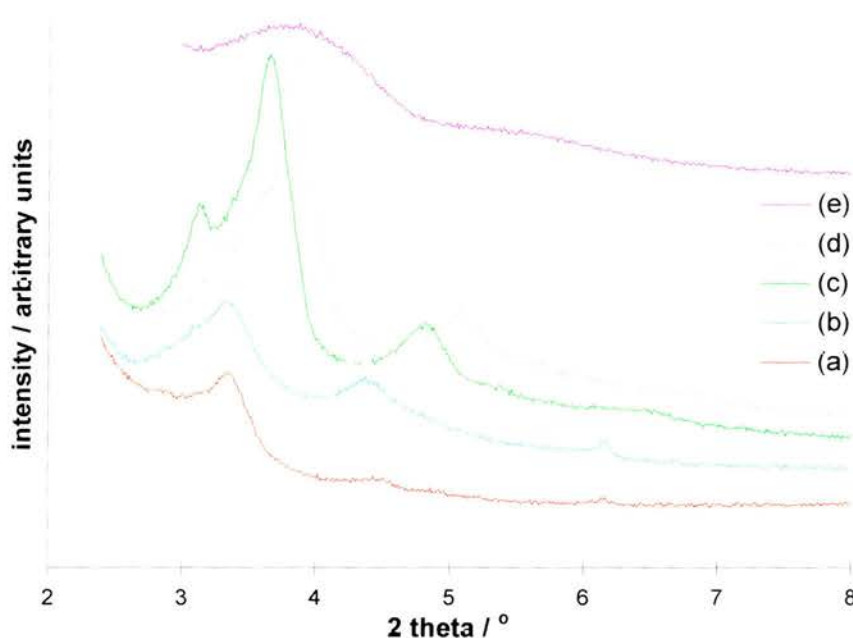


Figure 48: Overnight XRD patterns showing the effect of reaction pH on SBA-2 synthesis (RT, 2 h, stirring): (a) pH 10-10.5, (b) pH 10.5-11, (c) pH 11-11.5, (d) pH 11.5-12, (e) pH 12-12.5.

reaction pH	10-10.5	10.5-11	11-11.5	11.5-12	12-12.5
<i>a</i> (Å)	63.4 (56.3)	62.9 ^(b) (58.4)	57.9 (49.9)	54.2 (45.5)	(c)
<i>c</i> (Å)	105.8 (93.0)	98.8 ^(b) (95.9)	95.6 (81.2)	87.3 (74.0)	(c)
FWHM (°2θ)	>0.45 (0.52)	0.43 (0.49)	0.34 (0.40)	0.40 (0.47)	0.96 (1.35)
%contraction in <i>d</i> ₀₀₂	10.4	11.5	12.5	18.5	18.9
wt% C ^(d)	-	28.59 (0.105)	-	34.00 (0.87)	-
%wt loss ^(e)	53.3	52.0	47.6	43.7	33.4

0.03 < 2θ zero point error < 0.1 ± 20 %, unit cell parameter error = ca. 1 %. (a) numbers in brackets are for the calcined materials, (b) observed values, this XRD pattern would not refine, (c) the unit cell dimensions for this sample cannot be accurately determined from such an indistinct XRD pattern, (d) from elemental analysis, (e) during calcination.

Table 9: Analysis of five SBA-2 (C16-3-1 RT 2 h stirring) samples synthesised over different reaction pH windows.^(a)

As expected, the process of calcination leads to a unit cell contraction in all 5 samples. Furthermore the resultant FWHM values of the major peaks increase, which can be justified by the further framework silicate condensation (and therefore slight framework degradation) experienced during the thermal removal of surfactant. Overall, however, the sequence of peak positions with respect to reaction pH is maintained. The % contraction, though, increases in line with the increasing reaction pH.

Since each powder pattern is indexable, values for the hexagonal unit cell dimensions a and c can be obtained and are also presented in table 9. In particular this allows calculation, equation 14, of the unit cell volume for these calcined materials. The results, figure 49, further confirm the reduction in unit cell dimensions as reaction pH increases.

$$V = a^2 c \sin 60$$

14

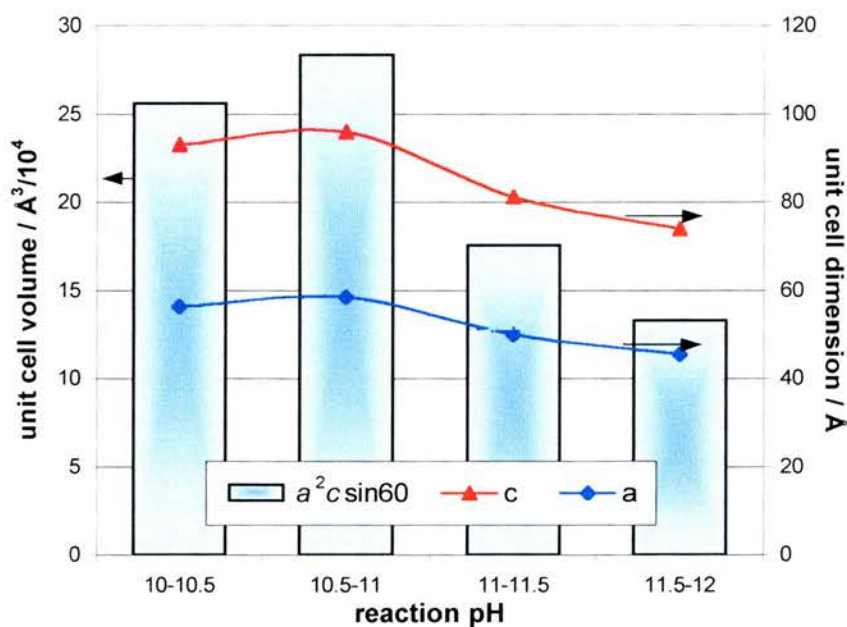


Figure 49: SBA-2 unit cell volume and dimensions compared to reaction synthesis pH.

Adsorption isotherms were subsequently performed on three of these ‘pH’ samples: namely pH 10-10.5, 11-11.5 and 11.5-12, figure 50. Clearly all three solids exhibit type IV isotherm behaviour. Furthermore, as the unit cell size increases (reduction in reaction pH), the partial pressure required to induce capillary condensation correspondingly increases. This is expected and can be explained by the progressive increase in average pore size diameter (25.14 → 29.69 → 31.32 Å as pH decreases).

Meanwhile, the adsorption capacity of each solid is not as simply justified. Perhaps the wall thickness increases as the size of the pore increases. Such a scenario would then suggest that the volume adsorbed per gram of solid remains constant, irrespective of the unit cell dimensions. As observed, therefore, the total volume adsorbed for the three samples is similar ($\approx 0.017 \text{ mol g}^{-1}$). A reaction mechanism-type justification for this, though, is less obvious.

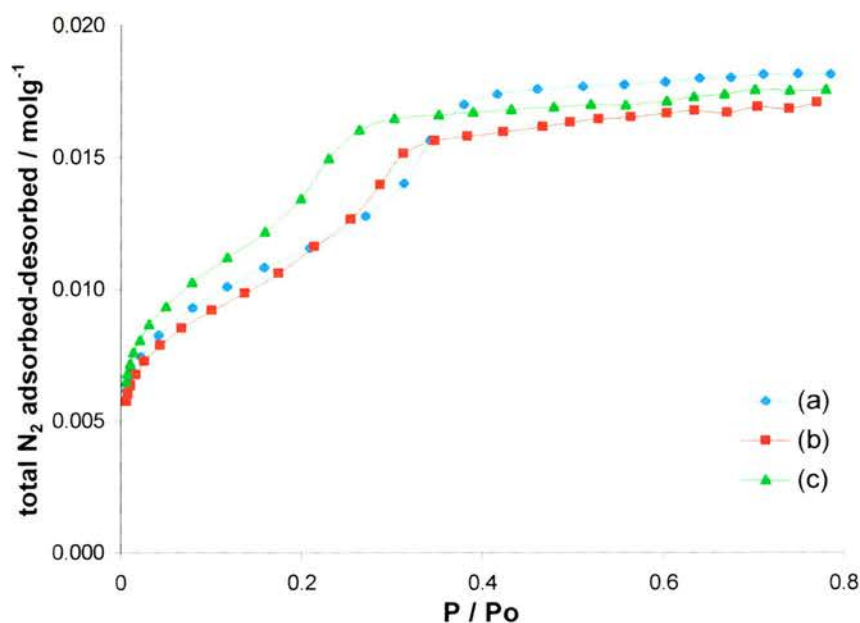


Figure 50: Adsorption Isotherms for SBA-2 materials synthesised at (a) pH10-10.5, (b) pH11-11.5 and (c) pH11.5-12. For clarity only the desorption branch is shown.

In a second series of pH experiments the OH^-/SiO_2 ratio was altered solely by an increase/decrease in the starting volume of TMAOH. These four preparations can be described by the molar composition $0.05 \text{ C16-3-1} : y \text{ TMAOH} : 1 \text{ TEOS} : 150 \text{ H}_2\text{O}$ where $y = 0.3, 0.4, 0.5, \text{ or } 0.6$. Like the previous series these materials were synthesised at room temperature over 2 hours with stirring (300 rpm). Figure 51 shows that the same pH-major peak position trend exists; namely as the concentration of hydroxide ions in solution is reduced so too is the major peak position. This relationship is also maintained following calcination. The $3\text{-}5^\circ 2\theta$ region of these calcined materials, figure 52, however, clearly describes the mesoporosity and structural finesse within each solid. It appears that as the OH^- concentration decreases, so too does the presence of the d_{103} reflection. Reasons for this behaviour are unclear, however, one can hypothesise that OH^- ions are involved in some charge compensation role at the micelle-silica

interface. As such, therefore, they could influence the final stacking arrangement of mesopores, where a predominance of hcp arrays are shown by the existence of this d_{103} peak. As before there seems to be no general correlation between the weight lost during calcination, the degree of unit cell contraction, the FWHM value and the major peak position, table 10. Each sample is essentially alike.

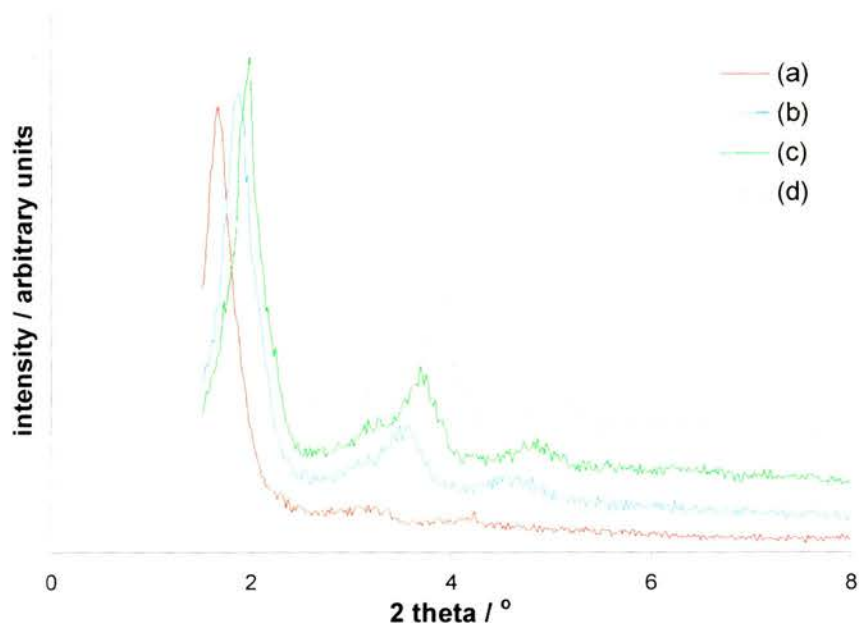


Figure 51: XRD patterns of as-prepared SBA-2 showing the effect of number of moles TMAOH in the synthesis (RT, 2 h, stirring 300 rpm): (a) 0.3, (b) 0.4, (c) 0.5 and (d) 0.6.

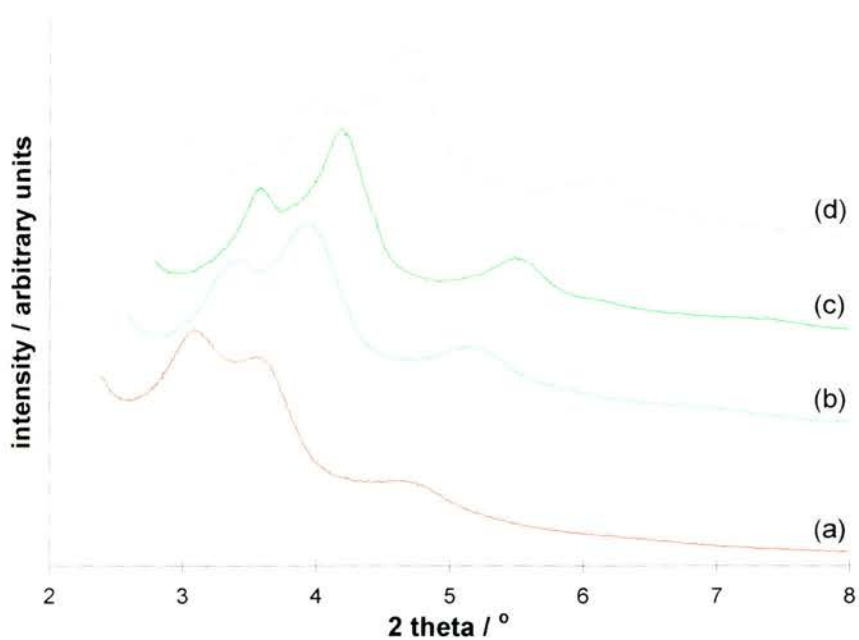


Figure 52: Overnight XRD patterns of calcined SBA-2 showing the effect of number of moles TMAOH in the synthesis (RT, 2 h, stirring 300 rpm): (a) 0.3, (b) 0.4, (c) 0.5 and (d) 0.6.

	0.3	0.4	0.5	0.6
%contraction in d_{002}	13.8	8.7	12.5	12.6
%wt loss ^(a)	49.7	47.9	47.6	45.8
final pH	11.23	11.50	11.48	11.77
d_{002} (Å) ^(b)	52.9 (45.6)	46.9 (42.8)	45.7 (40.0)	42.8 (37.4)
FWHM ($^{\circ}2\theta$) ^(b)	>0.37 (0.44)	0.44 (0.43)	0.34 (0.40)	0.44 (0.44)

(a): during calcination, (b): values in brackets refer to the calcined materials.

Table 10: Structural parameters of SBA-2 prepared with differing TMAOH molar compositions at RT over 2 h, stirring at 300 rpm.

Effect of Reaction Temperature and/or Reaction Time

To assess the effect of temperature upon SBA-2 formation, four solids were synthesised, over 1 week, at RT, 80 °C, 100 °C, and 160 °C (without stirring). The resultant XRD patterns are presented in figure 53. Clearly lower temperatures favour mesophase formation in this system. This can be reconciled by the TG-MS analysis, which indicates that the surfactant begins to degrade at 120 °C. Thus presumably at 160 °C few completely intact C16-3-1 surfactants survive in solution. Micelle formation therefore, is inhibited, and the solid recovered from the 160 °C experiment is composed of amorphous silica only (i.e. no low angle XRD peak).

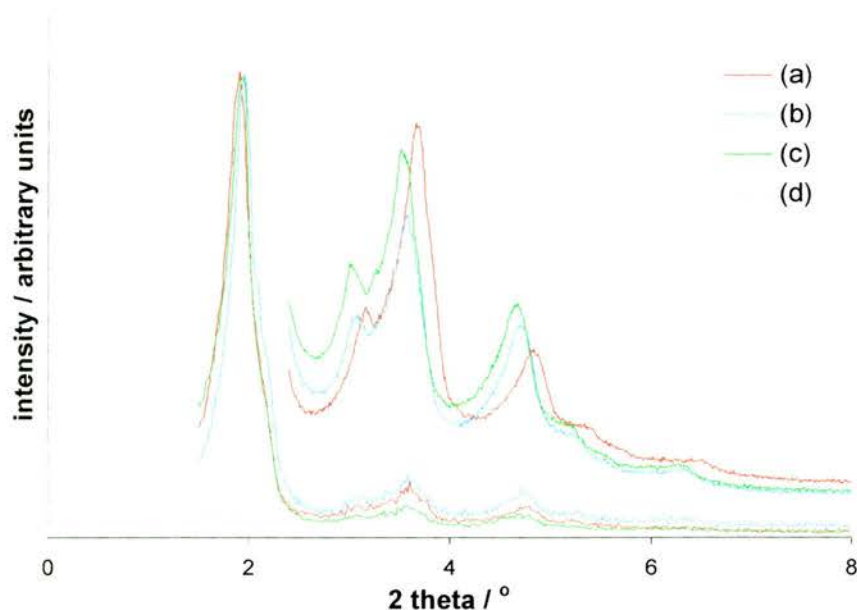


Figure 53: XRD patterns for as-prepared SBA-2 synthesised over 1 week at (a) RT, (b) 80 °C, (c) 100 °C and (d) 160 °C.

Within the remaining three samples, however, the as-prepared diffractograms show no discernible differences. Each material generates a major reflection in the narrow 1.90-1.94 $^{\circ}2\theta$ range, with overlap similarly occurring in the secondary peak region. Furthermore there is no indication of a d_{103} reflection in any of these patterns. This can be reconciled by the initial pH, table 11, being below the threshold (*ca.* pH 11.65) required for hcp micelle domination (see Effect of pH). In addition, this table illustrates that over the course of 1 week the reaction pH continues to alter. Again this demonstrates that mesophase formation is a dynamic process involving OH^- ions throughout. In this case the extended reaction period would conceivably enhance framework silicate condensation. Thus any silicate-OH anionic species present in solution, would have undergone framework condensation during the 1 week synthesis. Consequently hydroxide ions, re-released into solution would account for the final pH (of each solution) and observed pH increase.

	RT	80 $^{\circ}\text{C}$	100 $^{\circ}\text{C}$	160 $^{\circ}\text{C}$
2 hours (initial)	11.51	11.54	11.56	11.93
1 week (final)	11.61	11.72	11.34	11.68

Table 11: pH of SBA-2 syntheses over time.

Upon calcination all three well ordered materials contract, figure 54. The amount of contraction, however, appears to depend not solely upon reaction pH, but also on the synthesis temperature. Thus although the total unit cell volume decreases for each, the samples can be arranged by increasing volume loss: 19.4 % (100 $^{\circ}\text{C}$) < 20.3 % (80 $^{\circ}\text{C}$) < 28.2 % (RT). This order is intuitive and indicates that as the reaction temperature increases more silicate condensation occurs, leading to a smaller unit cell contraction during calcination. The secondary peak region further shows this contraction effect. Thus over 80 $^{\circ}\text{C}$ or 100 $^{\circ}\text{C}$ there is little alteration in the peak positions with respect to each other. The RT secondary peaks, meanwhile, shift significantly to larger $^{\circ}2\theta$ values. Again this can be reconciled by the lower reaction temperature hindering extensive silicate polymerisation and hence framework thermal resilience.

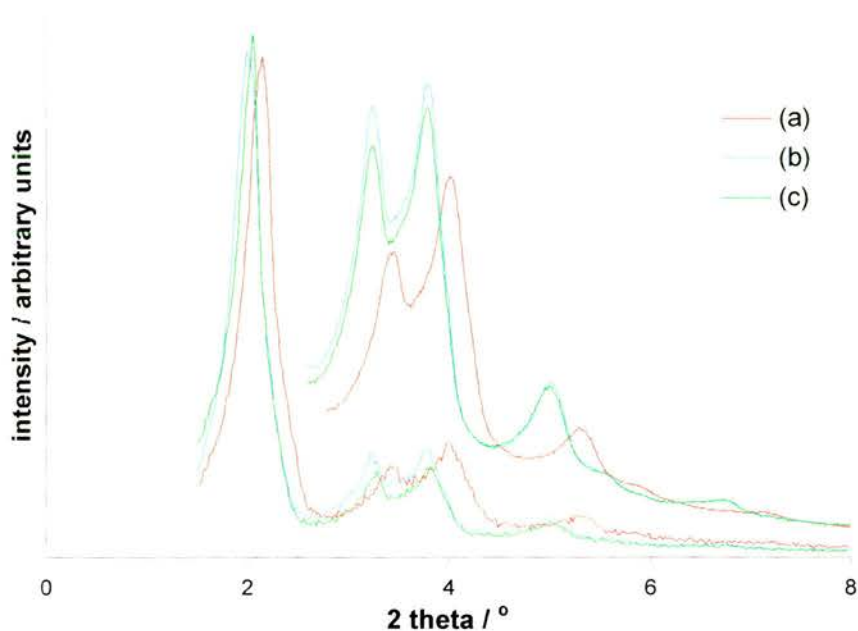


Figure 54: XRD patterns for calcined SBA-2 materials prepared after reaction for 1 week at (a) RT, (b) 80 °C and (c) 100 °C.

Considering reaction at 80 °C, the 1 week synthesis can also be compared to that over the shorter time of 2 hours. The appropriate XRD patterns are presented in figure 55. It is clear that the peak positions for the as-prepared materials are alike. On calcination, however, the shorter reaction time leads to a greater $d_{(112)}$ peak contraction (7.9 % (2 h) *vs.* 4.2 % (1 wk)). As before this can be reconciled by the extent of polymerisation within the framework, in this case being limited by reaction time. The RT (2h *vs.* 1 wk) XRD patterns similarly exhibit this behaviour.

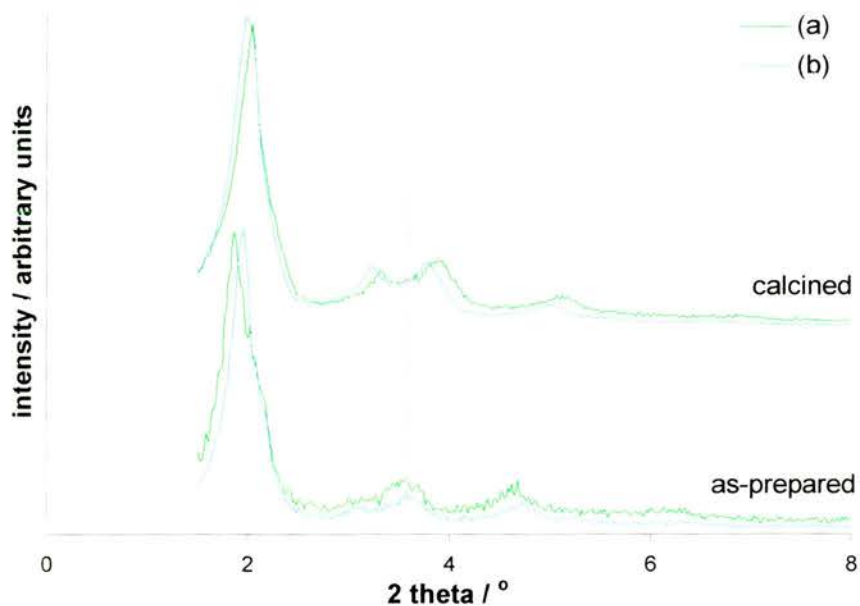


Figure 55: XRD patterns for SBA-2 synthesised at 80 °C over (a) 2 hours and (b) 1 week.

The extent of silicate condensation, can be further confirmed by analysis of the associated ^{29}Si MAS NMR spectra. Intended to illustrate the effect of the largest change in reaction conditions, the DP spectra for as-prepared SBA-2 synthesised at RT (2 h) and 80 °C (1 wk) are shown in figure 56. It is clear that an increase in both temperature and reaction time favour further framework condensation (enhanced Q^4 signal). The Q^3 signal, however, remains strong, which suggests that complete framework condensation based upon synthesis conditions alone (i.e. no calcination) is not easily achievable. The enhanced SiO_2 condensation, following an extended reaction time (at 80 °C) is confirmed by the greatly reduced Q^3/Q^4 ratio, table 12.

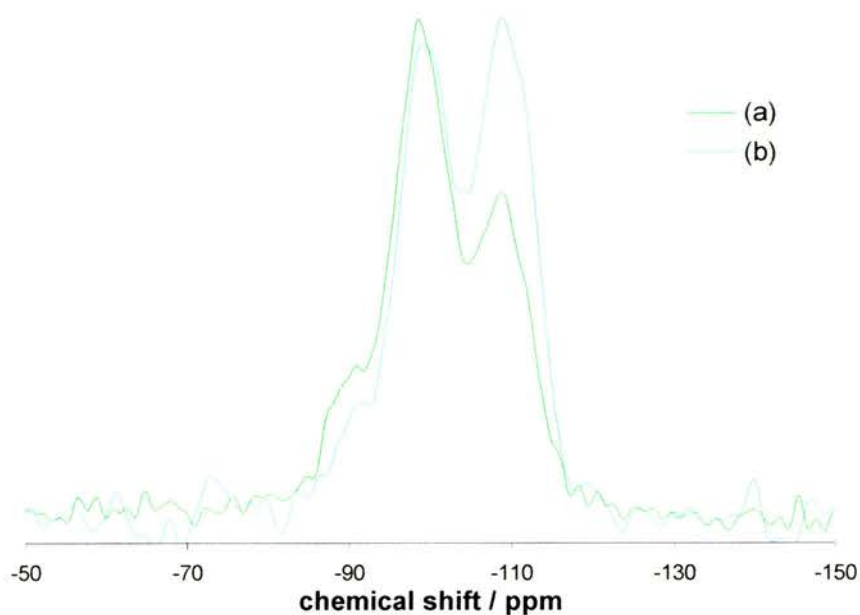


Figure 56: ^{29}Si DP MAS NMR spectra for as-prepared SBA-2 synthesised (a) at RT for 2 hours and (b) at 80 °C for 1 week.

Si species	ppm	RT 2 h	80 °C 1 wk
Q^2	-91	11.0	7.9
Q^3	-99	51.1	41.9
Q^4	-109	37.9	50.2
Q^3/Q^4 ratio		1.35	0.83

Table 12: Integrated intensities for ^{29}Si DP MAS NMR deconvoluted spectra of as-prepared SBA-2.

Furthermore the corresponding cross-polarized spectra, figure 57, also shows that an 80 °C, 1 week SBA-2 experiment increases the framework condensation.^{xxdii} In spite of the enhanced Q^4 signal (and reduced Q^2 intensity), though, it appears that Si-OH species remain within the as-prepared structure.

^{xxdii} The 80 °C 1 week reaction conditions, however, do not alter the as-prepared DP vs. CP spectra, as described in the MAS NMR overview.

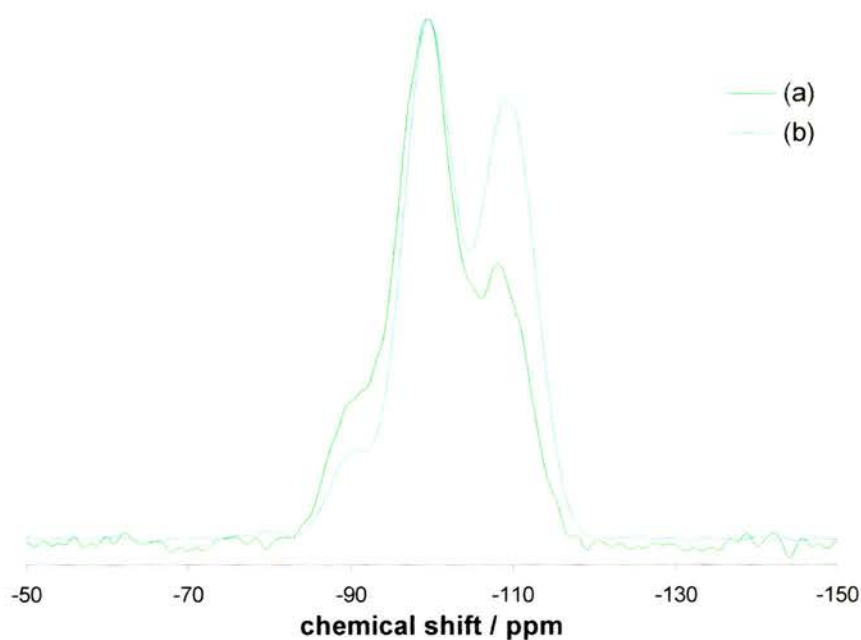


Figure 57: ^{29}Si CP MAS NMR spectra for as-prepared SBA-2 synthesised at: (a) RT (2 h) and (b) 80 °C (1wk).

Effect of C/Si Ratio

The TG-MS result, however, poses one question with regard to the final product composition, as compared to the intended synthesis composition. The initial composition used for the C16-3-1 sample under discussion in the TG-MS paragraph is presented in table 13. On the basis of a 0.4480 g recovered dry weight, and using the weight losses from TGA, the % yield can be calculated. This indicates that the recovered material contains 0.2178 g SiO_2 , which equates to a 29.02 % yield. The surfactant, however, accounts for 0.2302 g and can be described as a 69.42 % yield of the C16-3-1 initially added. Thus the use of surfactant in this preparation is far more efficient than the silica incorporated into the final solid; although over this short reaction period neither is perfect. This analysis also assumes that all the recovered material is composed of well ordered mesopores (no amorphous silica). In other words the starting materials are lost because they underwent no reaction (i.e. remained water soluble), or because they formed very fine agglomerations that could easily pass through the filter paper.

	surfactant C16-3-1	TMAOH	TEOS	H ₂ O
gfw	530.51	91.16	208.33	18
no. moles	0.05	0.5	1	150

Table 13: Initial composition of a C16-3-1 SBA-2 preparation.

In addition the final C16-3-1/SiO₂ molar ratio is 0.171, significantly more than the 0.05 value based on the starting molar composition. Two subsequent preparations, therefore, have been undertaken. These can be described by doubling the molar surfactant composition and secondly halving the amount of TEOS used initially.

The surfactant and silica yields for each solid were determined from TGA-DTA analyses. Figure 58 shows typical traces for the removal of C16-3-1 from the framework by burning (O₂ gas flow). Thus below *ca.* 275 °C the TGA trace is identical to that obtained from the TG-MS helium experiment. Around 300 °C, however, a large exothermic event occurs. This corresponds to the burning of the remaining surfactant within the mesopores. The temperature emitted (due to formation of stable CO₂ bonds) and the corresponding peak sharpness, therefore, reflect the quantity of surfactant and extent of pore connectivity within the solid. Finally above *ca.* 550 °C no further weight losses are observed. This suggests that the calcination programme employed (RT → 550 °C, 1 h N₂, 6 h O₂) is sufficient to remove *all*^{xxiii} the organic material present.

^{xxiii} In addition the elemental analysis of the colourless calcined materials typically gives a carbon content of <1 wt %.

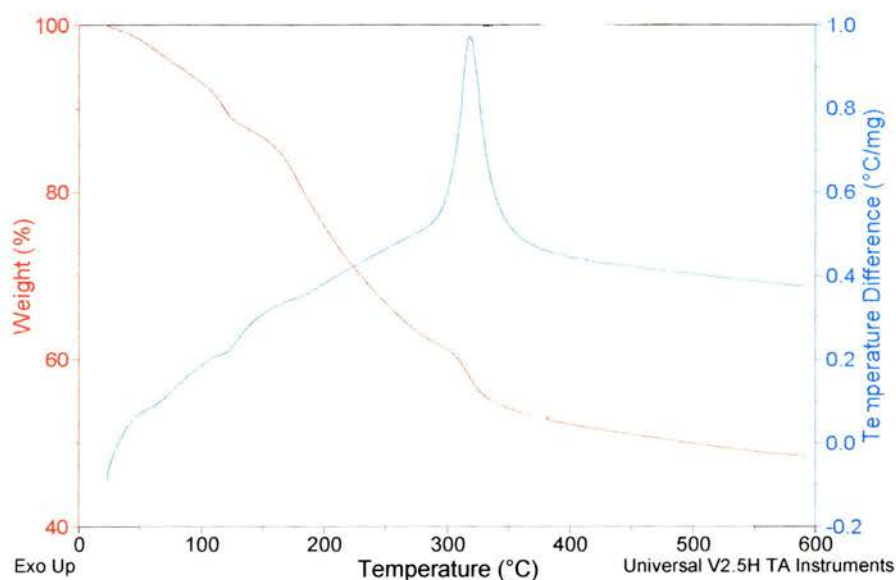


Figure 58: TGA-DTA trace for C16-3-1 surfactant removal from SBA-2.

The % yield calculations for these two subsequent experiments are presented in table 14, alongside that of a normal experiment. Clearly doubling the amount of surfactant initially present doubles the % yield in silicate. In turn the XRD pattern remains well ordered, figure 59, and the final C16-3-1/SiO₂ ratio remains constant. The reduction in initial silicate concentration, however, has an adverse effect upon the SBA-2 framework structure. Thus although the 0.5 mol TEOS experiment is now more efficient in silica, this is at a cost to the surfactant yield and quality of the final solid. It appears therefore that under these reaction conditions (temperature, time, pH etc) the optimum C16-3-1/SiO₂ ratio in the final as-prepared material is 0.171. To achieve this, though, an increase in silica yield was *not* simultaneously accompanied by an increase in surfactant yield, during the 0.1 mol C16-3-1 preparation. Furthermore a large amount of time, effort and expensive starting materials are required to first synthesise the C16-3-1 prior to use as the SBA-2 templating surfactant molecule. The 0.05 surfactant : 1 TEOS molar composition ratio, therefore, was used throughout to make SBA-2.

	% C16-3-1	% SiO ₂	C16-3-1/SiO ₂
0.05 C16-3-1 : 1 TEOS	69.42	29.02	0.171
0.1 C16-3-1 : 1 TEOS	71.12	58.98	0.172
0.05 C16-3-1 : 0.5 TEOS	27.39	56.18	0.293

Table 14: % yield and as-prepared C16-3-1/SiO₂ molar ratios for three SBA-2 experiments, based upon TGA weight loss calculations.

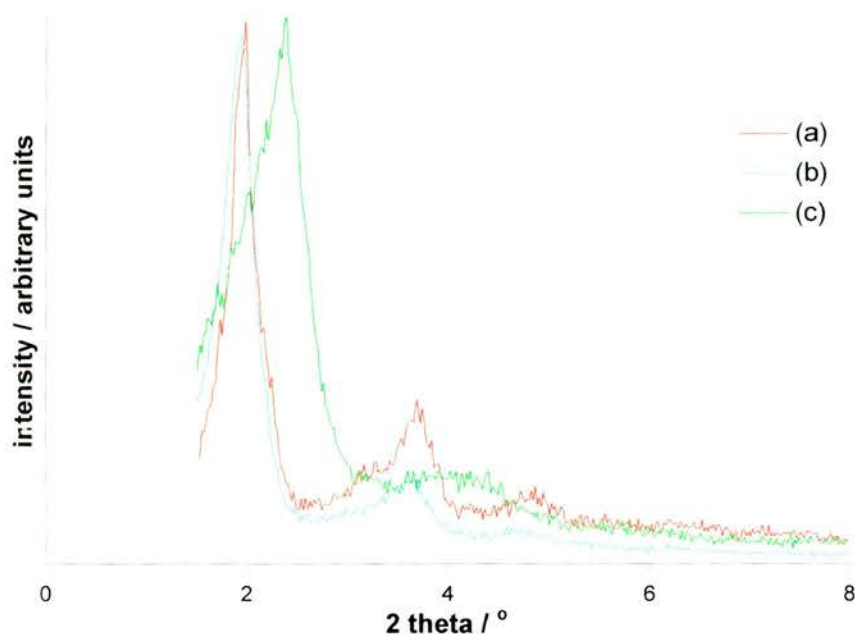


Figure 59: XRD patterns for SBA-2 synthesised with differing C:Si ratios: (a) 0.05 C16-3-1 : 1 TEOS, (b) 0.1 C16-3-1 : 1 TEOS and (c) 0.05 C16-3-1 : 0.5 TEOS.

Effect of Continuous Stirring

Three RT 2 hour SBA-2 preparations were undertaken at different stirring rates and compared amongst themselves and to a similar reaction prepared without stirring (though initially homogenised for 10 min). It was thought that the shear forces created during stirring, at a known speed, might affect the micelle stacking arrangements and thus the silicate mesophase (and quality of that phase) formed. The resultant XRD patterns presented in figure 60, however, do not reveal this information. Thus it appears that the precise reaction stirring speed does not impinge upon the type or order of the final mesoporous silicate. Furthermore, there is no obvious relationship between stirring speed and % contraction of the major XRD peak following calcination.

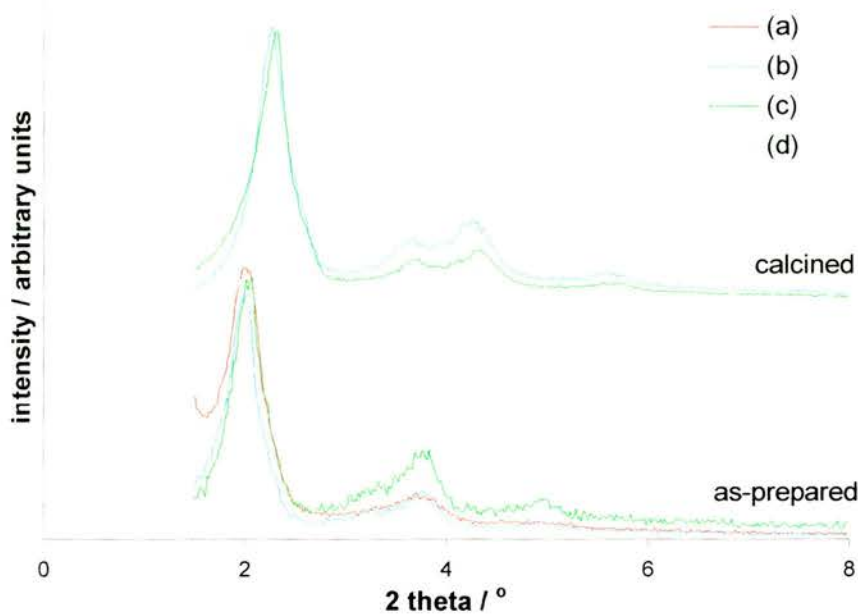


Figure 60: XRD patterns for SBA-2 synthesised over 2 hours at RT and at (a) 0 rpm, (b) 300 rpm, (c) 400 rpm and (d) 500 rpm.

Effect of Heteroatoms

The direct synthesis of titanium- and aluminium-containing SBA-2 has been attempted. Each will be discussed in turn.

Microporous titanosilicates, in particular the TS-1 material, are widely employed as oxidation (epoxidation) catalysts. Incorporation of titanium into the silicate framework of SBA-2, therefore, offers the potential for large molecular processes, where, for example, voluminous transition states are not inhibited by the framework dimensions. Thus a series of titanium containing SBA-2 materials have been synthesised. These employed titanium tetraethoxide, $\text{Ti}(\text{OEt})_4$, as the metal source, and are denoted SBA-2 Ti_x where x , the Si/Ti ratio in the initial mixture, is 60, 50 or 40. The resulting as-prepared XRD patterns are presented in figure 61. These titanosilicate frameworks are maintained following calcination. Clearly, for all three loadings, a well-ordered SBA-2 structure forms. Furthermore the change in titanium concentration does not adversely affect the peak quality [major peak FWHM values: 0.52° (Ti_{60}) *vs.* 0.41° (Ti_{50}) *vs.* 0.48° (Ti_{40})]. It appears, therefore, that the SBA-2 mesoporous silicate

structure is not perturbed by the presence of tetravalent (Ti^{4+}) heteroatoms. In addition the XRD patterns suggest that the titanasilicate framework has no bearing upon the presence or absence of the d_{103} reflection. This further confirms that the degree of 'hexagonal-ness' is influenced, and mediated, by the hydroxide species in solution (reaction pH), and not the hydrolysis/condensation mechanism. Finally no EXAFS measurements have been undertaken to identify the titanium co-ordination. Energy Dispersive X-ray (EDX) spectroscopy, however, indicates that titanium *is* present (Ti $K\alpha$ and $K\beta$ lines) following calcination, figure 62, although a quantitative measurement of the Si:Ti ratio was not possible. Instead it was observed that the titanium species are widely dispersed throughout the solid particulates.

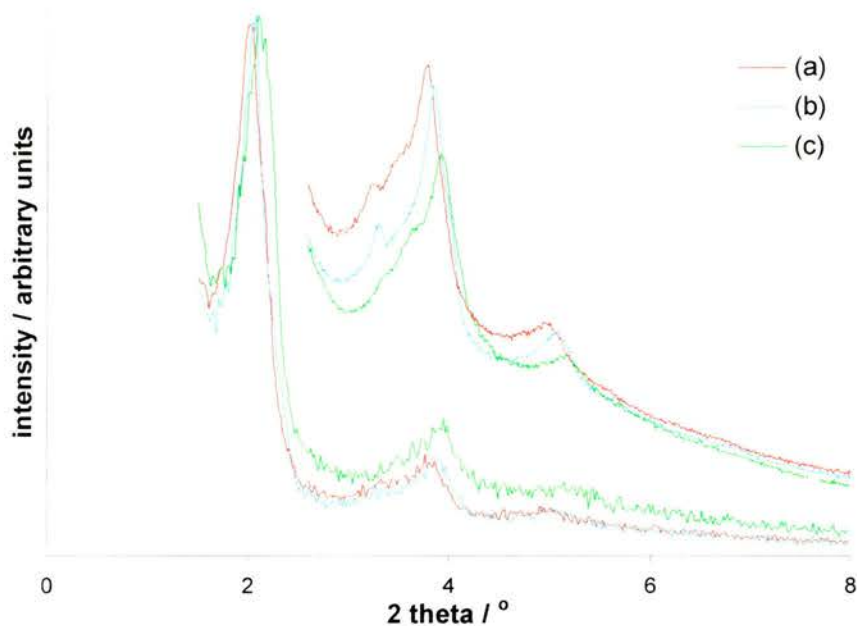


Figure 61: XRD patterns of as-prepared SBA-2 materials: (a) Ti60, (b) Ti50 and (c) Ti40.

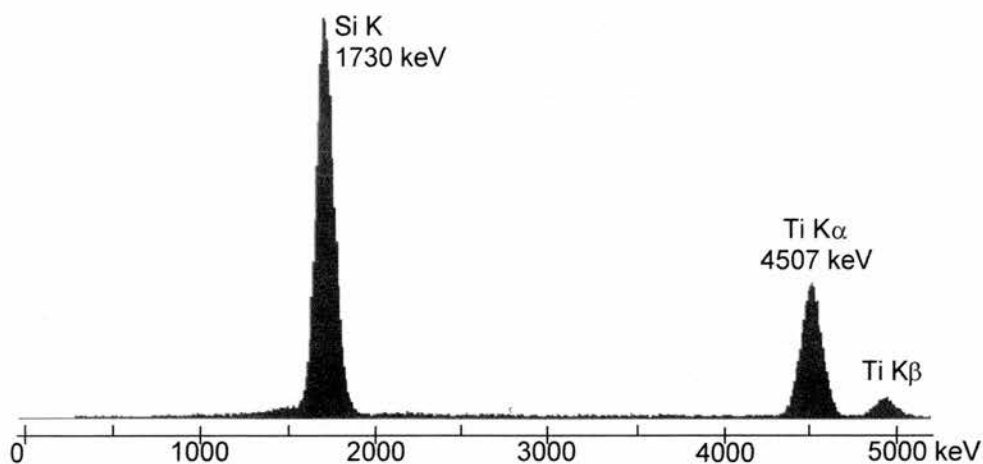


Figure 62: EDX spectrum for calcined SBA-2 Ti60.

On a parallel note, some microporous titanosilicate literature assigns the presence of a 960 cm^{-1} FTIR peak to a Si-O-Ti stretch. A peak at this wavenumber is also seen in these titanium-containing SBA-2 solids. Specific assignment to this framework silicate grouping, however, is unlikely, since a stretch at 960 cm^{-1} also occurs in the FTIR spectra of pure silicate SBA-2 materials.

Secondly, aluminium incorporation into porous silicate frameworks can impart acidity (Brønsted and Lewis), and an ion-exchange capacity, to the material. As before, the structural mesoporosity would allow for the reaction of larger reagents than can currently fit through a zeolitic opening. For these reasons the aluminosilicate synthesis of SBA-2 has been attempted. These experiments used either aluminium sulphate, $\text{Al}_2(\text{SO}_4)_3 \cdot 16\text{H}_2\text{O}$, or aluminium isopropoxide, $\text{Al}(\text{O}^i\text{Pr})_3$, as the metal source. They have been designated SBA-2 Al x where x , the Si/Al ratio in the initial mixture, is 50, 30 or 25. A typical series of XRD powder patterns, for solids prepared from the aluminium sulphate precursor, is presented in figure 63. Unlike the titanosilicates, it can be seen that as the aluminium content in the synthesis mixture increases, the long-range framework quality reduces. Thus there is a gradual loss of definition in the $3\text{-}5^\circ 2\theta$ region, and correspondingly a progressive broadening of the major peak. This can be reconciled by the trivalent nature of this heteroatom, which imparts an additional negative charge upon the final mesoporous structure. In theory such a framework might be better able to balance the micelle surface charge. Instead it appears that the aluminium presence is incompatible with the creation of well-ordered SBA-2. Nevertheless, the adsorption isotherm of an $\text{Al}_2(\text{SO}_4)_3$ -derived SBA-2 Al50 framework is

almost identical to its siliceous analogue, figure 64. These results, in turn, confirm that despite a loss in order (secondary XRD peak region) mesoporosity is retained. Indeed the surface areas and average pore diameters are comparable, table 15.

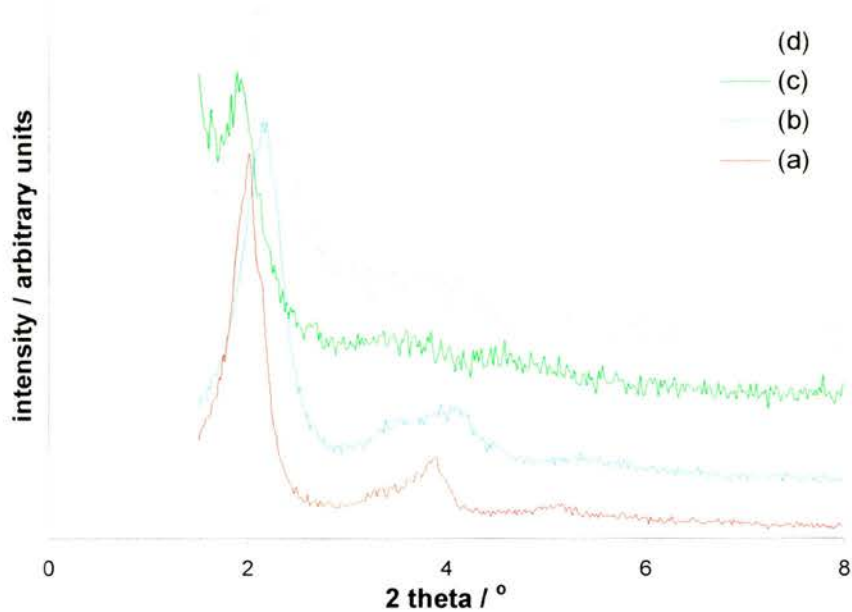


Figure 63: XRD patterns for as-prepared SBA-2 containing aluminium sulphate: (a) Al_{∞} , (b) Al50, (c) Al30 and (d) Al25.

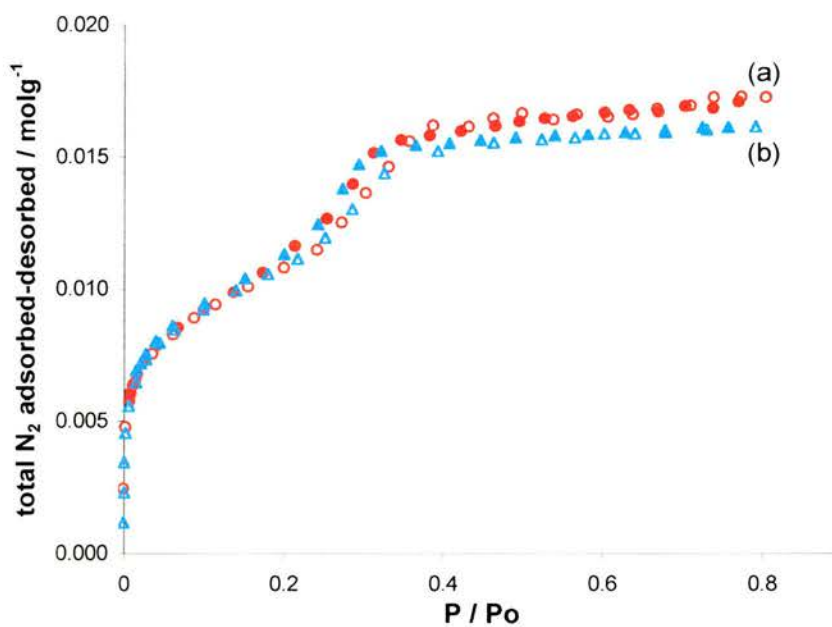


Figure 64: Adsorption Isotherms for calcined C16-3-1 SBA-2 synthesised (a) with and (b) without Al50. Adsorption = open symbols, desorption = filled symbols.

	BET surface area (m^2g^{-1})	av. pore diameter (\AA)
SBA-2 Al50	893 ± 3	28.20
siliceous SBA-2	873 ± 3	28.88

Table 15: Adsorption Isotherm values for calcined SBA-2 materials.

By contrast, there is no correlation between the aluminium loading and resultant framework order of the aluminium isopropoxide synthesised materials (although the structural quality has diminished). This is interesting and curious. A comparison of the X-ray patterns for two materials prepared as initial Al50 mixtures, yet using the different metal sources, is therefore shown in figure 65. Clearly the isopropoxide starting material perturbs the SBA-2 framework more than the sulphate.

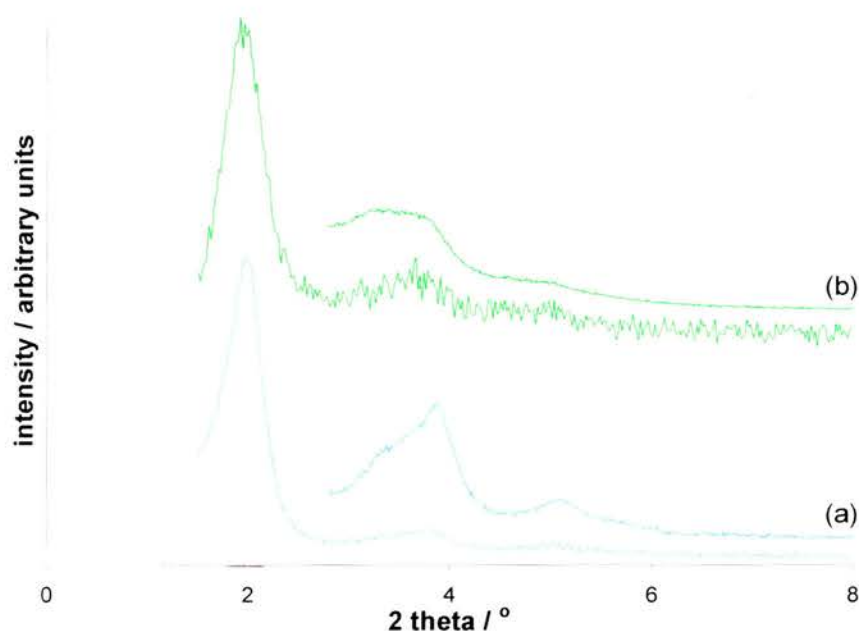


Figure 65: XRD patterns for SBA-2 Al50 prepared with (a) aluminium sulphate and (b) aluminium isopropoxide.

In view of the fact that these aluminosilicate materials were to be used in acid catalysis, a precise knowledge of the aluminium loading was required. Thus the elemental analysis of two calcined Al50 samples was undertaken by Inductively Coupled Plasma – Atomic Emission Spectroscopy (ICP-AES). Again these results, table 16, were unexpected. It can be seen that neither calcined solid possesses the intended Si/Al = 50/1 molar ratio. Moreover both solids are richer in aluminium than the initial synthesis mixture. Based on TG-MS calculations, though, a normal SBA-2 preparation only gives a 29 % SiO_2 yield. Thus an equivalent (29 %) initial molar composition of SiO_2 indicates that only

36 % of the sulphate-sourced aluminium, compared to 75 % of the isopropoxide-derived, can be found in the calcined framework structure. Again this is curious, although it is similar to reported¹⁴ Al-MCM-41 findings. Perhaps the initial monomeric nature of the aluminium isopropoxide, or indeed the alkoxy nature of this precursor (comparable to TEOS), benefits aluminium incorporation within the structure.

Al source	sulphate	isopropoxide
Si (ppm)	3.16×10^5	2.84×10^5
Al (ppm)	1.51×10^4	2.58×10^4
Si/Al ratio	20.9	11.0

Table 16: ICP-AES results for two calcined SBA-2 Al50 solids.

²⁷Al MAS NMR experiments were performed upon these two aluminosilicate SBA-2 samples, figure 66. The materials show similar spectra with comparable peak intensities. Thus the aluminium source, and hence aluminium concentration in the sample, does not appear to affect the final coordination environment. In addition these aluminium NMR experiments mirror those findings inferred from the ²⁹Si MAS NMR spectra. Thus for both concentrations calcination leads to a significant change in the aluminium co-ordination. Initially the as-prepared spectra indicate that almost entirely tetrahedral aluminium species (53.3 ppm) are present, presumably in the framework walls.



Figure 66: ²⁷Al MAS NMR spectra for aluminium-containing SBA-2: (a) as-prepared and (b) calcined.

Calcination, however, results in a mixture of aluminium environments. Although a 4-co-ordinate species (47 ppm) is still present, the spread of peaks suggest that some aluminium no longer remains in the framework. Instead these species now exist in octahedral (-1.1 ppm) and also possibly in 5-fold (≈ 30 ppm) environments. A more detailed analysis of these ^{27}Al MAS NMR results can be found in the Acid Catalysis chapter.

Miscellaneous Effects

An SBA-2 experiment was performed by adding the surfactant to a basic solution already containing TEOS. It appears that this reversed order of addition does not affect the quality of the final (recovered) material. Similarly SBA-2 can be prepared with a variety of bases: NaOH, KOH, TEAOH and TMAOH without adverse structural degradation. It is not clear, however, what role (if any) the cation plays during mesopore formation. Presumably it remains in solution as a hydrated ionic species throughout.

Various acids and acid strengths (0.1 M, *conc.* etc.) have been used to alter the solution pH during the initial stages of reaction. Analysis of the XRD major peak FWHM values, however, is inconclusive. It is therefore not possible to make a judgement about the influence of additional anionic species (Cl^- , SO_4^{2-}) on the quality of the SBA-2 silicate structure formed.

There have been no scale-up problems between 37 ml and 168 ml, provided that the solutions are well homogenised during the initial minutes of reaction (after TEOS addition).

Several as-prepared and calcined solids have been re-examined by XRD >6 months after the initial synthesis. The materials were chosen at random to express a wide range of experimental conditions (RT, 80 °C, 100 °C, 2 h and 1 wk). All the powder patterns, however, continue to indicate the existence of a well-ordered SBA-2 structure. Thus the silicate framework appears to be stable over long periods of time in both the as-prepared and calcined states.

Mechanistic Concepts

From the analysis of SBA-2, using the various characterisation techniques outlined, one can begin to get a feel for the formation mechanism of this material. It is only from the final recovered solid, though, that this characterisation can start.

Thus the roles of each starting material can be described as follows:

TEOS: silica source, and source of ethanol by-product during silicate hydrolysis/condensation. There is no evidence, however, of ethanol involvement in the final as-prepared silicate material, although it may just evaporate from the solution over the course of the reaction.

TMAOH: organic base, the OH^- ion drives silicate hydrolysis and subsequent condensation. It may also co-ordinate with the silicon species to give an overall negatively charged surface available for non-bonding interactions with the micelle, and/or mediate the charge interactions at the organic-inorganic interface. The TMA^+ cation, meanwhile appears to remain in solution and is not involved in the mesophase creation process.

C16-3-1(Br)₂: diquatery ammonium surfactant, self-assembles to template the formation of micelle sized mesopores. The highly charged head group appears to form spherical micelles, in this system, to minimise the overall surface tension. Meanwhile there is no evidence of bromide ions participating in the mesophase formation process. Presumably the Br^- ions remain in solution along with the base-derived cations.

H₂O: reaction medium, no apparent involvement in final recovered material.

Without a doubt, SBA-2 possesses large pores and an amorphous framework: judged by the type IV adsorption isotherm and by the broad ^{29}Si MAS NMR and XRD peaks. Mesoporous silicates distinguish themselves from high silica zeolites primarily by (i) their large unit cell sizes, (ii) their incompletely condensed silicate wall structures and (iii) their lack of short-range crystallographic order. In spite of this one can envisage that an interaction between the templating molecules and silica species in solution is similar in both scenarios. Thus although the 'template' for a mesoporous framework is an agglomeration of surfactant molecules, it seems to induce silicate condensation in an analogous manner to that of a single zeolitic molecule. Likewise, the silica species may

also have pre-formed into the secondary building units (SBUs), figure 67, well documented³² in zeolite syntheses. Subsequent co-condensation in a random manner between these units, and around the charged micelle surface, would then occur. Once these organic-inorganic spheres have formed, however, it appears that the mesoporous self-assembly proceeds via the well documented^{10,12} liquid crystal templating mechanism (route II, figure 8), and the wall structure develops through the condensation of these randomly-orientated micelle-located silica units.

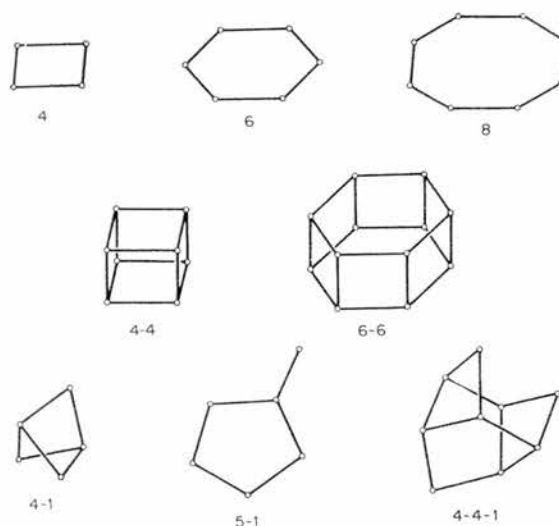


Figure 67: Secondary Building Units (SBUs) identifiable in zeolites.³²

The particular species present at the organic-inorganic interface, however, remains uncertain. What is plausible, though, is that the hydroxide ions play a pivotal role in this process. It seems that the reaction pH, i.e. the hydroxide ion concentration, can alter the apparent micelle dimensions and packing arrangements. Perhaps, therefore, OH^- ions are involved in charge matching at this interface. On a secondary note, the Si/Al ratios are surprisingly low. Perhaps, again, hydroxide ions mediate a faster path for aluminium condensation, than that for silica, due simply to the trivalent nature of this heteroatom. The reasons for this, though, remain unclear.

Summary

The mesoporous silicate SBA-2 was first reported by Stucky and co-workers⁶ in 1995. Since then there have been few publications and the synthesis and complete characterisation of this solid has remained unclear. This work, therefore, has attempted to understand the mechanistic factors involved during formation of this mesophase.

SBA-2, like other mesoporous silicates, is formed by SiO_2 condensation around a micelle, or surfactant agglomeration. In this particular case the surfactant is a diquatery ammonium molecule, C_n-3-1 (n = 12, 16 18), which is first synthesised, via a $\text{S}_\text{N}2$ reaction, and then purified. It appears that, due to the size and highly charged nature of the head group, this molecule is solely able to form spherical agglomerations in an SBA-2 synthesis of molar composition 0.05 surfactant : 0.5 TMAOH : 1 TEOS : 150 H_2O . Moreover the surfactant remains intact within the as-prepared material, accounting for *ca.* 46 wt%, and providing a surfactant:silica ratio of 0.171 (i.e. inefficient silica use). It can, however, be removed by calcination, where the molecule thermally decomposes via a Hofmann E2 reaction. Typically the structure contracts during calcination (*ca.* 12 % in d_{002}), which coincides with increased silicate condensation (²⁹Si MAS NMR) in the remaining framework. The X-ray patterns of both the as-prepared and calcined solids can be indexed on a hexagonal unit cell. The calcined structure exhibits a type IV adsorption isotherm, typical of other mesoporous silicates, although the total volume available for nitrogen condensation is much reduced. This indicates that there is less void space (more framework) per gram in SBA-2, than in either MCM-41 or MCM-48. Indeed a SBA-2 material synthesised with the (short) C12-3-1 surfactant tends towards exhibiting microporous adsorption behaviour.

It has become apparent, that the specific framework dimensions can be altered depending upon the synthesis conditions. Intuitively an expansion/contraction in the surfactant tail length (or presence of an organic swelling agent) has the desired, and corresponding, effect upon the unit cell size. Indeed this can also be controlled by the reaction pH ($10 < \text{pH} < 12$). As the pH drops, a larger framework is formed (and thus larger unit cell volume) and the d_{002} major peak shifts to lower $^\circ 2\theta$ angles.

The mesophase structure, meanwhile, seems to alter over the higher pH range $11.5 < \text{pH} < 12$, in so far as the presence of a third peak in the $3\text{-}5^\circ 2\theta$ region can solely be attributable to a hexagonal d_{103} reflection. Synthesis at higher reaction temperatures and over longer time scales (c.f. a RT, 2 hour preparation) indicate that such conditions lead to increased framework condensation. The reaction temperature, however, must remain below 120°C , since surfactant decomposition is induced at this temperature. In addition, and provided that the synthesis mixture is well homogenised during the initial stages of reaction, the order of starting material addition, the choice of base used, the effect of stirring speed or the influence of reaction scale-up (total volume) do not appear to affect the final framework quality. The SBA-2 structure is also thermally stable (1000°C) and stable over time (>6 months).

Isomorphous metal incorporation within the SBA-2 silicate framework has been investigated. Analysis of the titanium-containing materials shows that this tetravalent heteroatom does not significantly perturb the final structure, in spite of the loading. The aluminosilicate analogue, though, shows that the SBA-2 quality is dependent upon the aluminium source and Si/Al ratio. Consequently it appears that a monomeric alkoxy precursor is most easily assimilated into the silicate framework. Overall, however, inclusion of a trivalent heteroatom degrades the structural mesoporosity.

Finally these synthesis and analyses tend to suggest that the base-derived cation and surfactant-derived bromide ion are not involved in the mesoporous formation mechanism of SBA-2. Moreover the hydroxide ion concentration in solution critically determines the quality of, and micelle packing arrangement in, the final as-prepared mesophase. Presumably, therefore, the OH^- ions are involved in a charge compensation process at the organic-silicate interface. It is believed, though, that SBA-2 forms via a surfactant-silica mediated liquid crystal templating mechanism.

References

- ¹ Q Huo, DI Margolese, GD Stucky, *Chem. Mater.*, 1996, **8**(5), 1147.
- ² NK Raman, MT Anderson, CJ Brinker, *Chem. Mater.*, 1996, **8**(8), 1682.
- ³ R Zana, Y Talmon, *Nature*, 1993, **362**, 228.
- ⁴ CT Kresge, ME Leonowicz, WJ Roth, JC Vartuli, JS Beck, *Nature*, 1992, **359**, 710.
- ⁵ A Firouzi, D Kumar, LM Bull, T Besier, P Sieger, Q Huo, SA Walker, JA Zasadzinski, C Glinka, J Nicol, D Margolese, GD Stucky, BF Chmelka, *Science*, 1995, **267**(5201), 1138.
- ⁶ Q Huo, R Leon, PM Petroff, GD Stucky, *Science*, 1995, **268**(5215), 1324.
- ⁷ D Zhao, Q Huo, J Feng, BF Chmelka, GD Stucky, *J. Am. Chem. Soc.*, 1998, **120**(24), 6024.
- ⁸ MS Wong, JY Ying, *Chem. Mater.*, 1998, **10**(8), 2067.
- ⁹ AM Buckley, M Greenblatt, *J. Chem. Educ.*, 1994, **71**(7), 599.
- ¹⁰ JS Beck, JC Vartuli, WJ Roth, ME Leonowicz, CT Kresge, KD Schmitt, CT-W Chu, DH Olson, EW Sheppard, SB McCullen, JB Higgins, JL Schlenker, *J. Am. Chem. Soc.*, 1992, **114**(27), 10834.
- ¹¹ CY Chen, SL Burkett, H-X Li, ME Davis, *Microporous Mater.*, 1993, **2**, 27.
- ¹² Q Huo, DI Margolese, U Ciesla, DG Demuth, P Feng, TE Grier, P Sieger, A Firouzi, BF Chmelka, F Schüth, GD Stucky, *Chem. Mater.*, 1994, **6**(8), 1176.
- ¹³ RK Iler, *The Chemistry of Silica*, 1979, John Wiley & Sons, New York, USA.
- ¹⁴ S Biz, ML Occelli, *Catal. Rev. – Sci. Eng.*, 1998, **40**(3), 329.
- ¹⁵ AR West, *Basic Solid State Chemistry*, 1988, John Wiley and Sons, Chichester, UK.
- ¹⁶ A Putnis, *Introduction to Mineral Sciences*, 1992, Cambridge University Press, Cambridge, UK.
- ¹⁷ AK Cheetham, P Day, *Solid State Chemistry Techniques*, 1988, OUP, Oxford, UK.
- ¹⁸ JM Thomas, WJ Thomas, *Principles and Practice of Heterogeneous Catalysis*, 1997, VCH, Weinheim, Germany.
- ¹⁹ S Brunauer, PH Emmett, E Teller, *J. Am. Chem. Soc.*, 1938, **60**, 309.
- ²⁰ SJ Gregg, KSW Sing, *Adsorption, Surface Area and Porosity*, 1982, 2nd Ed., Academic Press, London, UK.
- ²¹ PL Llewellyn, KSW Sing, in *FEZA 3rd Euroworkshop: Sorption, Diffusion and Separation in Microporous and Mesoporous Materials*, 1997, Manchester, UK.

- ²² EP Barrett, LG Joyner, PH Halendar, *J. Am. Chem. Soc.*, 1951, **73**, 373.
- ²³ E Lippmaa, M Mägi, A Samoson, M Tarmak, G Engelhardt, *J. Am. Chem. Soc.*, 1981, **103**(17), 4992.
- ²⁴ CA Fyfe, JM Thomas, J Klinowski, GC Gobbi, *Angew. Chem. Int. Ed. Engl.*, 1983, **22**(4), 259.
- ²⁵ FC Hawthorne (Ed.), *Reviews in Mineralogy: Spectroscopic Methods in Mineralogy and Geology*, 1998, **18**, Mineralogical Society of America, Washington DC, USA.
- ²⁶ J Klinowski, JM Thomas, CA Fyfe, GC Gobbi, *Nature*, 1982, **296**, 533.
- ²⁷ R Zana, M Benrraou, R Rueft, *Langmuir*, 1991, **7**(6), 1072.
- ²⁸ TWG Solomons, *Organic Chemistry*, 1992, 5th Ed., J Wiley and Sons Ltd., New York, USA.
- ²⁹ LV Woodcock, *Nature*, 1997, **385**, 141.
- ³⁰ LV Woodcock, *Nature*, 1997, **388**, 236.
- ³¹ A Wang, T Kabe, *J. Chem. Soc. Chem. Commun.*, 1999, 2067.
- ³² RM Barrer, *Hydrothermal Chemistry of Zeolites*, 1982, Academic Press, London, UK.

Transmission Electron Microscopy

Background

Transmission electron microscopy (TEM) is frequently used in mineral sciences to understand the local structure of materials. Although the first electron microscope¹ was built in 1932, it is only in the last 20 years that this technique has been applied routinely to explore unit cell scale structural details, for example defects, dislocations, twin boundaries, stacking faults and intergrowths, within crystals.

Traditionally new crystallographic phases are identified solely on the basis of X-ray diffraction (XRD). Working with mesoporous solids, however, such structural elucidation is limited by the paucity of hkl reflections observed. As a result only the crystallographic unit cell dimensions can be identified; the walls being essentially amorphous and therefore unable to generate the high 2θ hkl reflections required to determine atomic positions and hence (indirectly) porosity. For this reason high resolution TEM (HRTEM), used in conjunction with powder XRD, is a particularly valuable tool for the structural elucidation of mesoporous materials. In addition the calcined solids are generally stable in the electron beam (low water content) and can be imaged at low magnifications without any loss of information (large unit cell sizes).

The Electron Microscope

Electrons are emitted from a heated source, often a lanthanum hexaboride (LaB_6) crystal or tungsten filament, at the top of the microscope. Subsequent acceleration through 100-1000 keV generates the required high energy beam. It is this accelerated voltage (V) that determines² the electron wavelength¹ (λ) according to the principle of conservation of energy, equation 1:

¹ At high voltages (i.e. large potential differences) the velocity of the electron (v) approaches the velocity of light (c). The mass of the electron, therefore, increases by relativistic effects, thus the precise wavelength of the electrons is given by: $\lambda = h\{2m_0eV_r\}^{1/2}$ where $m_0 = m\{1-v/c\}^{-2}$ and $V_r = V_0 + \{eV(2m_0c^2)\}V_0^{-2}$; m_0 , V_r and V_0 are the electron rest mass, the relativistic voltage and the microscope voltage, respectively.

$$\lambda = \frac{h}{\sqrt{2meV}} \quad 1$$

where m and e are the mass and charge on the electron respectively and h is Plank's constant. These high energy electrons have wavelengths smaller than the interatomic distances in a crystal lattice. Consequently, diffraction occurs as the electron beam interacts³ with the atomic electron clouds contained within the sample. As a result the diffraction angles are small and are concentrated into a narrow cone around the undiffracted beam. In order to focus and magnify the beam through the microscope, a series of lenses are required. An electron is a charged particle, therefore magnetic fields are able to alter the beam paths. These magnetic fields, known as electromagnetic lenses, are formed when an electric current is passed through wire coils encased within iron. As the current within each lens is altered, a smooth transformation of the focal length, and magnification, can be achieved.

A schematic⁴ diagram of the electron microscope is shown in figure 1.

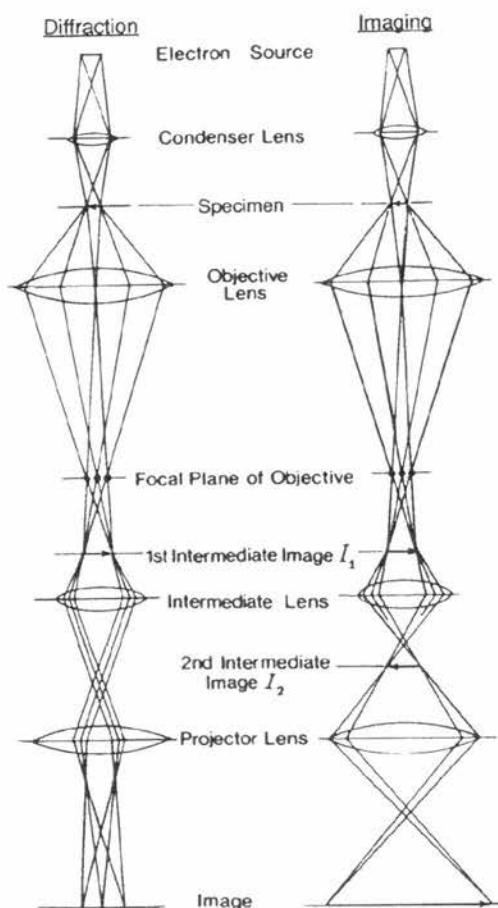


Figure 1: A diagrammatic representation of the TEM. The electron beam paths are shown in the (a) diffraction mode and (b) imaging mode.

Before reaching the sample, the electron beam passes through the condenser lens. This first lens in the microscope controls the size and angular spread of the incident beam, ultimately focussing it as a parallel beam onto the sample. The sample itself, supported on a grid, is positioned within the upper and lower halves (pole pieces) of the objective lens. This, the single most important lens, provides the initial magnification of the specimen. Apertures on the back focal plane, however, control how much diffraction passes on. In particular it is the wide angle diffracted beams, containing the fine structural information, that are most valuable. To collect this data, therefore, large apertures are necessary. Furthermore, the interference pattern formed on the back focal plane of the objective lens dictates whether the microscope operates in the diffraction or imaging mode. If the intermediate lens focuses on the back focal plane, the diffraction pattern itself is successively magnified onto the final image plane. Alternatively the current passing through the intermediate lens can be adjusted to produce an 'image', the first intermediate image, of the specimen diffraction pattern. In turn it is this image that is propagated down the microscope, being focussed by the final (projector) lens onto the fluorescent viewing screen. Finally this diffraction or image information is observable through a port at the base of the microscope column and can be recorded onto photographic film, although electronic methods (video or charge coupled devices, CCDs) are becoming more common.

Instrument Limitations

Ultimately, image resolution is constrained by the instrument. There are several contributing reasons for this, the major points of which shall be discussed in turn.

Firstly, the objective lens is not of infinite size. As a result some of the wide-angle diffracted beams cannot be refocused, and consequently never reach the intermediate lens system. The final image, therefore, is representative of the specimen in so far as it is formed from a truncated series of diffracted beams.

Secondly, the electromagnetic lenses, themselves, contain unavoidable aberrations. It is the objective lens, the most important lens in the microscope, which is most significantly affected by these distortions. The three most important, of which, are

antistigmatism and spherical and chromatic aberrations. Antistigmatism arises from a non-symmetrical magnetic field, within a lens, which ultimately distorts the observed image. Although this can be remedied by using auxiliary lenses (a stigmator), the uncorrected effect is to focus the diffracted beams in different planes coincident with the optical axis. Spherical aberrations, meanwhile, emanate from the wide angled diffracted rays that are refracted too strongly, figure 2. As a result these beams are brought into focus before the Gaussian (the critical in-focus) image plane and thereby introduce a degree of phase shift to the diffracted beams. This phase magnification is quantified by the spherical aberration constant, C_s , which indicates to what extent diffraction can occur before wave misphasing and image distortion become unacceptable. The reverse scenario is also possible, occurring when the diffracted ray paths refocus beyond the Gaussian image plane. Combined with spherical aberration, this defocus effect contributes to the overall Phase Contrast Transfer Function, $\chi(\alpha)$, which justifies image contrast, for thin film specimens, on the final image plane. Similarly chromatic (depth-of-focus) aberrations are described by the chromatic aberration constant, C_c . This limitation originates from a range of wavelengthsⁱⁱ present in the electron beams. This wavelength spread is caused by voltage instabilities (in the electron source or lens currents) or when imaging inherently thick samples. Thus as the electron beam is propagated down the microscope, a range of focal lengths are formed, which in turn lead to an inevitable blurred image on the final image plane.

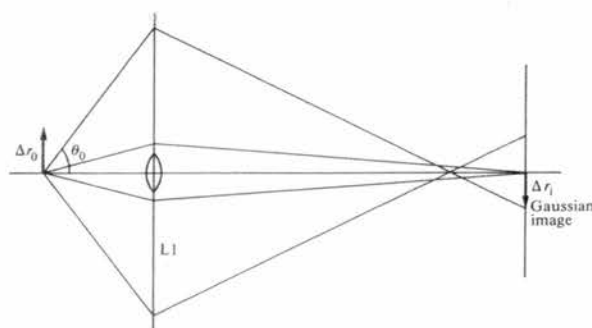


Figure 2: The effect of spherical aberration.⁴ Rays passing through the outer zones of the lens (far from the axis) are refracted more strongly than those paraxial rays passing close to the axis. These outer rays meet the axis a distance Δr_i before the Gaussian image plane.

ⁱⁱ Chromatic \equiv colour

Thirdly the incident electrons never form an infinitely small (parallel) electron beam. Thus an angular spread, or cone of illumination, exists within the incident beam itself. This is known as spatial incoherence, or beam divergence, and leads to a small circular range of illuminating beam inclination (δS) values. The diffracted amplitude and image intensities must be adjusted accordingly to take this into account.

Finally, we know that electrons are strongly scattered by matter. The existence, therefore, of heavy atoms or thick samples can lead to multiple (or dynamic) scattering events within the sample. Consequently a description of the emergent beams, requires a complicated wave function, with a complex relationship to the object potential, and direct interpretation of the observed images becomes difficult. In practice, therefore, computer-simulated multiple-scattering images are used to verify the experimental observations.

The Reciprocal Lattice and Electron Diffraction

The reciprocal lattice is a geometrical concept developed by PP Ewald. It allows us to construct an imaginary lattice from a set of real lattice points. The reciprocal lattice,ⁱⁱⁱ therefore, occupies reciprocal space. It however, is not repetitive, since each point has its own identity defined in relation to a fixed origin. To understand this geometrical construct better, let us first consider diffraction through a series of periodic gratings.

Consider a 1D grating. If an incident beam interacts with this object, figure 3, diffraction will occur. Diffraction, therefore, results from a change (of angle ϕ) in the incident wave direction. Consequently diffraction minima, formed when the transmitted wave beams are out of phase, are a product of destructive interference. If, however, coherent interference occurs, diffraction maxima result, indicating that the diffracted waves are in phase and that there is an integral number (b) of wavelengths path difference. Furthermore, if the 1D grating is placed horizontally, the observed diffraction pattern consists of a *vertical* series of spots, separated by a distance d .

ⁱⁱⁱ A lattice reciprocally related to real space.

Knowing that a path distance difference of $h\lambda$ (equation 2) is required to produce these discrete spots, simple trigonometry allows us to relate the grating split spacing, a , to that observed on the image plane, d , equation 3. L is the distance between the diffraction pattern and the object.

$$h\lambda = a \sin \phi \quad 2$$

$$d = L \tan \phi = L \frac{\sin \phi}{\cos \phi} \quad 3$$

Thus combining these relationships we obtain equation 4 which demonstrates that the observed diffraction spot spacing, d , is reciprocally related to the grating split spacing, a .

$$d = \frac{Lh\lambda}{a \cos \phi} \quad 4$$

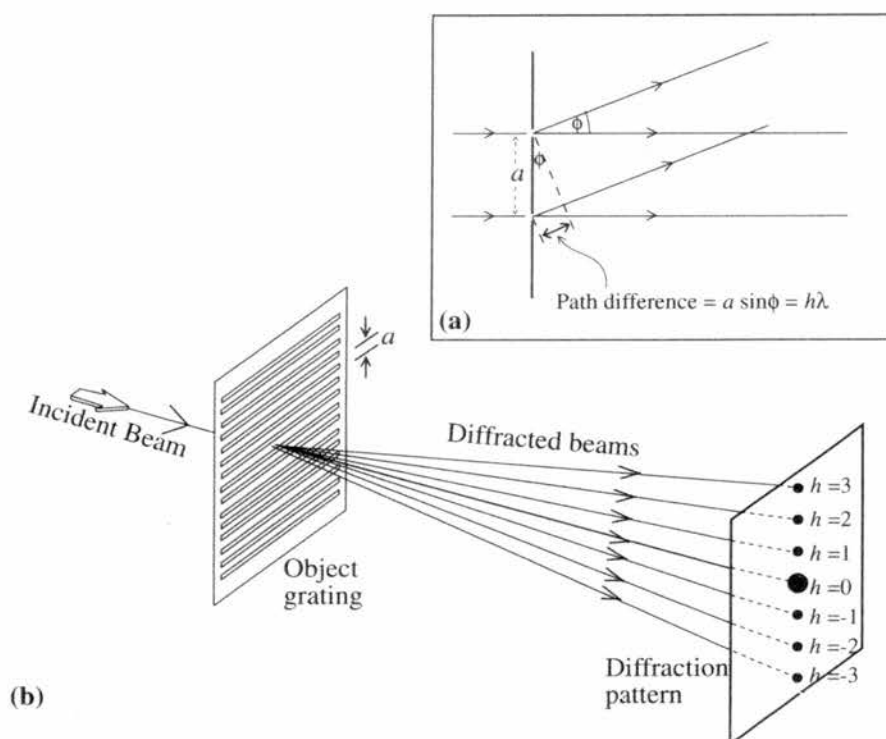


Figure 3: (a) The conditions of constructive interference required to produce a diffraction maximum and (b) the formation of a diffraction pattern from a one-dimensional grating.³

Similarly a 2D grating can be thought of as two superimposed 1D gratings, figure 4. As a result both the corresponding path difference equations (equations 5 and 6) must be satisfied before diffraction can occur. The observed diffraction pattern, therefore, consists of an array of intensity maxima where each spot corresponds to a particular

periodicity within the grating. Furthermore, from the origin, the vector direction to any spot is normal to the orientation of the h k planes which it represents, figure 5, whilst the vector length is a reciprocal distance to those planes. This brings us back to the reciprocal lattice concept, where the solutions to the diffraction equations define the reciprocal relationship between the diffraction pattern and the periodic object.

$$b\lambda = a\sin\phi_1 \quad 5$$

$$k\lambda = b\sin\phi_2 \quad 6$$

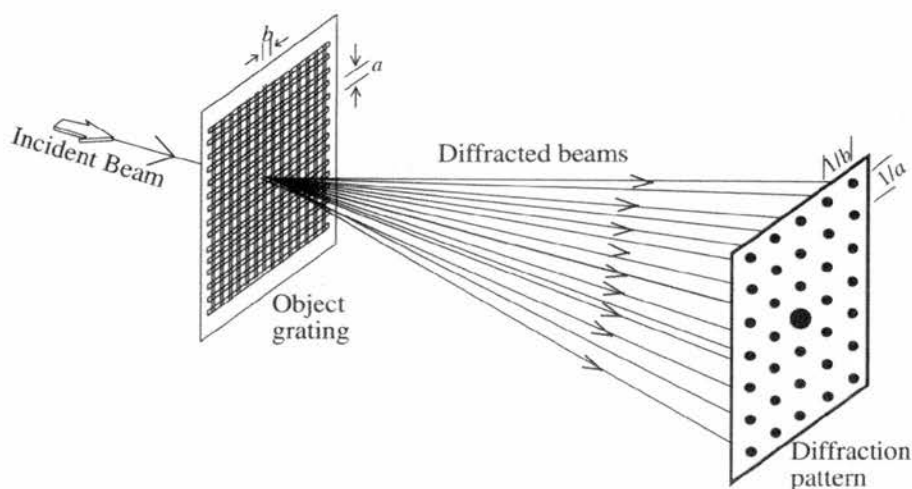


Figure 4: Diffraction from a two-dimensional grating and the formation of a rectangular array of diffraction spots, where the distance between the object and diffraction pattern, $L=1$.³

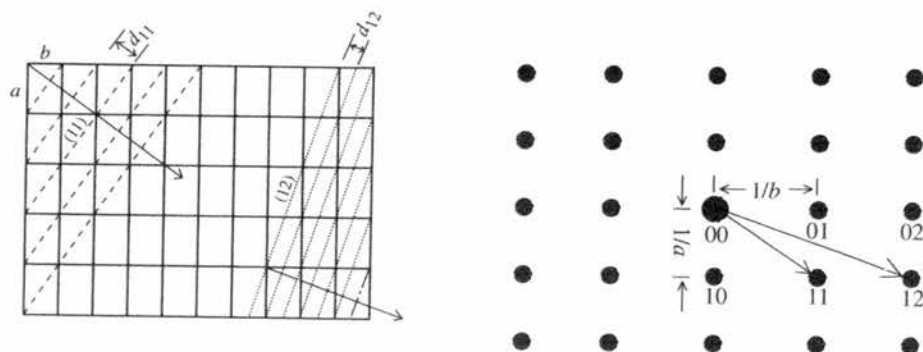


Figure 5: The relationship between (a) sets of planes on a 2D grating and (b) the position of the corresponding diffraction spots, where the distance between the object and the diffraction pattern $L=1$.³

Extending this discussion to 3D, the simultaneous solution of three equations, the Laue equations (equations 7, 8 and 9), is necessary before any diffraction can occur. The

diffracted beams, therefore, are defined by the three integers hkl , and must satisfy the specific geometrical constraints imposed by 3D periodicity. As a result, the diffraction pattern obtained is not 3-dimensional, but is bound by the zone axis down which the incident beam propagates. The reciprocal lattice, nevertheless, describes all the *possible* solutions to the diffraction equations.

$$b\lambda = a\sin\phi_1 \quad 7$$

$$c\lambda = b\sin\phi_2 \quad 8$$

$$a\lambda = c\sin\phi_3 \quad 9$$

On an electron scale, a crystal can be thought of as a 3D grating. Thus, a practical demonstration of this reciprocal lattice concept is the electron diffraction pattern. Each pattern consists of an array of sharp spots, containing information about the specimen dimensions and internal structure. More specifically, the relative positions of each spot define the (real space) interplanar spacing (d spacing) and orientation of each plane in real space. The nature of HRTEM experiments, however, require thin crystals to be used. These diffraction spots appear as spikes, whose spot lengths (perpendicular to the lattice plane) are related to the sample thickness. Furthermore, electron diffraction results in a particularly large Ewald sphere^{iv} (c.f. X-rays). Thus the TEM image plane is essentially at a tangent to the Ewald sphere, and so no precession of the detector, typical of X-ray experiments, is required to collect the diffracted data from a given zone. A selected area electron diffraction (SAED) pattern, therefore, can be viewed and recorded instantly. Its size being determined by the instrumental distance between the crystal and the photographic film, figure 6. Thus within a TEM, real and reciprocal space are related by equation 10. Rearrangement gives equation 11, where d is the interplanar distance, R is the observed distance between two diffraction spots and $L\lambda$, the camera constant, is given by the product of the distance between the crystal and photographic film (L) and the electron wavelength (λ).

$$\frac{R}{L} = \frac{1/d}{1/\lambda} \quad 10$$

^{iv} The Ewald sphere has radius, $r = 1/\lambda$. In a TEM operating at 200kV, typically the electron wavelength $\lambda = 0.0251 \text{ \AA}$, thus $r = 39.841 \text{ \AA}^{-1} = 3.9841 \times 10^{11} \text{ m}^{-1}$. By way of comparison Cu $K\alpha$ X-rays have $\lambda = 1.5418 \text{ \AA}$, thus $r = 0.648 \text{ \AA}^{-1}$.

$$d = \frac{L\lambda}{R}$$

11

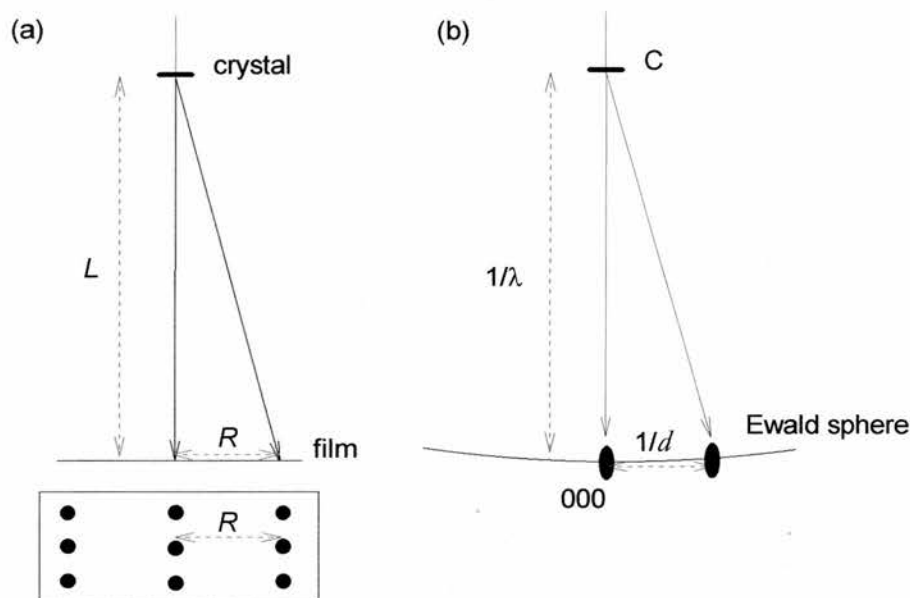


Figure 6: A comparison of (a) real and (b) reciprocal space.³

Also when two planes, in real space, lie parallel to a common direction, then this direction can be ascertained. Known as the zone axis, $[UVW]$, it is defined using the Weiss Zone Law, equation 12. Thus the zone axis for two sets of planes is the solution

$$bU + kV + lW = 0 \quad 12$$

to the corresponding simultaneous equations, and can be determined using a 3×3 matrix. As a result, the reciprocal lattice can be thought of as a cross-section, through the real space lattice, perpendicular to this direction (or zone). The axes of a reciprocal lattice are defined in relation to their real space counterparts. Thus:

- a^* lies perpendicular to the bc plane,
- b^* lies perpendicular to the ac plane,
- c^* lies perpendicular to the ab plane.

Subsequently each reciprocal lattice point can be plotted. Lying on or off the axis, the direction of the vector to each reciprocal lattice point lies at right angles to the direction of the planes that the particular point represents. The distance along that direction, meanwhile, equals the reciprocal interplanar spacing ($1/d_{hkl}$) from the origin. This is illustrated in figure 7, looking down the $[001]$ zone axis onto the ab plane of the hexagonal lattice.

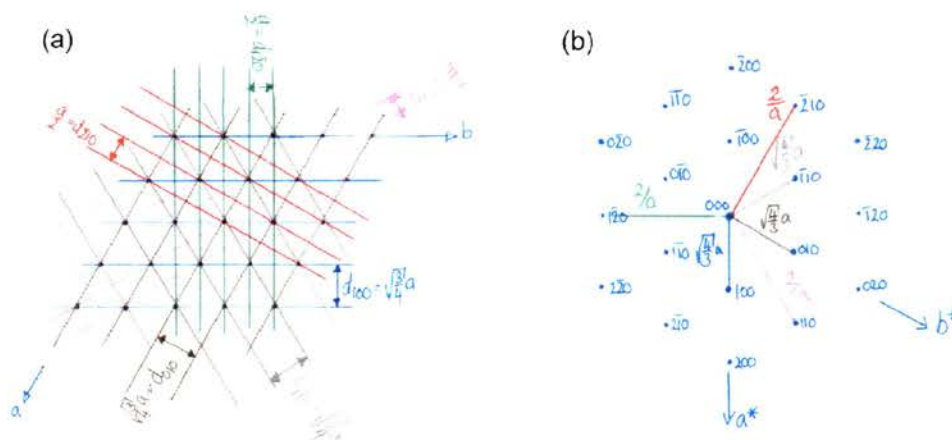


Figure 7: An example of a reciprocal lattice construction from a real lattice. (a) An ab section of a hexagonal lattice showing the d spacing of several planes, and the normals to these planes. (b) The a^*b^* reciprocal lattice section also looking down $[001]$.

Imaging

If we consider thin crystals, combination of the diffracted beams, by the intermediate lens, will produce an image which is then propagated down the microscope, figure 1. Captured as a photograph, these images can be considered as interpretable electron density representations of the sample. As the atomic potential (electron density) varies across a specimen, so too do the magnified contrast differences in the final image. As with any radiation: electrons, X-rays or visible light, these differences (or intensity variations) are proportional to the wave amplitude squared, equation 13, where $I_1(\mathbf{r})$ and $\psi_1(\mathbf{r})$ are the intensity and the amplitude of the wave at the image plane respectively.

$$I_1(\mathbf{r}) = |\psi_1(\mathbf{r})|^2 \quad 13$$

In HRTEM, however, the crystals are not thick enough to result in amplitude differences within the emergent beams, *per se*. Image contrast, therefore, results from a phase change (retardation or advance) within the transmitted beams. It is this phenomenon which accounts for the observed intensity differences in the final micrographs.

To ensure the best image resolution obtainable is captured on film, a through-focal series can be collected. This records the magnified images of a sample at a variety of

objective lens focal settings. Thus, as the focal length is systematically changed, the appearance of the final image correspondingly alters. In this way direct analysis of the sample structure and comparison to computer simulated images can be made.

This technique is of particular value when imaging mesoporous materials. As with all TEM images, the experimental observations are defined by intensity contrast differences. These greyscale colour variations delineate area of strong and weak electron density within a sample. Thus an underfocus image, obtained when the object is too close to the objective lens, consists of white spots (electron density-poor 'pores') on a black background (electron density-rich 'framework'). This is known as a structural image and is a true representation of the specimen. Continuing the focal series, an exact in-focus^v image, possesses only very faint contrast. It, therefore, acts as a baseline to calculate the deviation from exact focus imaging in the other micrographs. Finally the overfocus, reverse-contrast, image shows a series of dark spots accompanied by a white network. Although overfocus images have no direct equivalent in real space, comparison of these 'special case' observations to a computer simulated overfocus image can help to test a proposed structural model. Furthermore, if the surface is not entirely flat, the image appearance will alter with specimen thickness. This has knock-on effects during through-focal imaging and can aid in the analysis of structural details, by adding a 3rd dimension to the image information available.

Thus a through-focal series of HRTEM images greatly highlights the ultrastructural irregularities in mesoporous material. This technique is central to the understanding of pore connectivity and the nature of polytypic intergrowths and has been used extensively during the imaging of SBA-2 (see Analysis).

Lastly the fine structural detail is contained within the wide angled diffracted beams. This high spatial resolution can be quantified from both point to point (Scherzer) and line (fringe) resolution. These respectively reproduce the structure of the specimen down the direction of the incident beam and measure the sample periodicity perpendicular to the crystallographic direction.

^v In reality this is obtained at a small underfocus value, rather than at the optimum Scherzer focal length, due to instrumental limitations (spherical aberration).

State of the Art

Mesoporous silica was discovered⁵ in 1992, however, the resulting XRD patterns show only a few low angle diffraction peaks. This is a reflection of the large pore sizes within these materials and the lack of crystallinity, indicating that the framework is essentially amorphous. For this reason TEM has been used extensively during structural characterisation.

High resolution imaging of MCM-41 shows^{5,6} well defined rows of pores that lie parallel to the particle edges; the SAED pattern, therefore, presents a single line of diffraction spots, figure 8. This line-fringe image can be reconciled by the framework versus channel densities, for a thin particle. A thin section (prepared by ultramicrotomy), however, indicates that these rows align in a hexagonal arrangement, figure 9. The corresponding selected area electron diffraction pattern, viewed down the [001] direction, can therefore be indexed as the $hk0$ projection of a hexagonal unit cell. The dimension a is defined by the major (100) XRD peak ($a = 2d_{100}/\sqrt{3}$). FSM-16, a structural analogue^{7,8} of MCM-41 yet derived from the layered silicate kanemite, shows similar HRTEM contrast patterns and imaging behaviour.

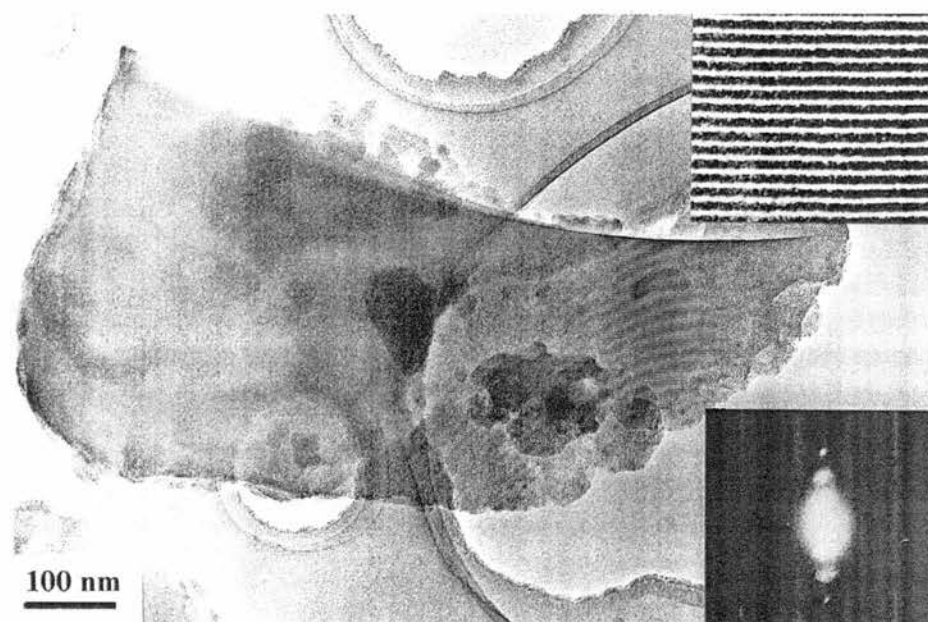


Figure 8: HRTEM image of MCM-41 showing high resolution line fringes (top inset) and the corresponding SAED pattern (bottom inset).¹⁰

and intensity of both electron and X-ray diffraction patterns. Furthermore HRTEM has shown¹³ that MCM-48 crystallises with a well-defined (cubosome) particle morphology, which reflects the underlying gyroid surface symmetry. MCM-48, therefore, can be thought of as a bi-continuous phase possessing cubic symmetry.

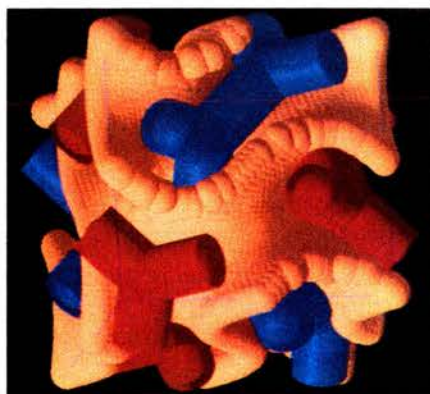


Figure 10: A gyroid representation of MCM-48 showing the two interwoven non-interconnecting channel system.¹⁴

Finally the pore structure of KIT-1,^{viii} another mesoporous molecular sieve, has been investigated¹⁵ by TEM. High resolution imaging, figure 11, revealed that the uniform cavities are arranged in a bi-continuous way, although in a disordered manner. This stable, high surface area material has subsequently been described¹⁶ as ‘worm-like’. Overall, therefore, the many short interconnecting mesoporous channels combine to form a disordered 3D solid.

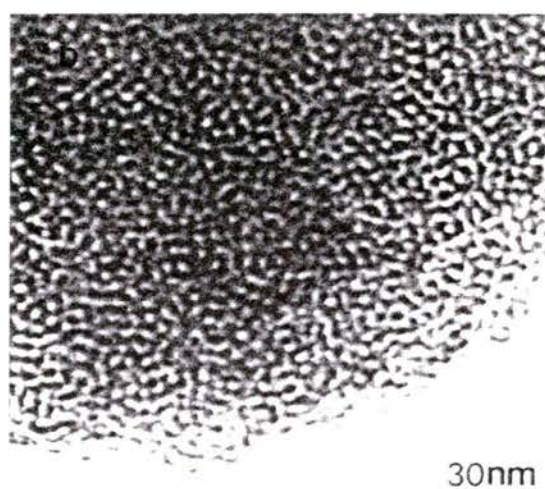


Figure 11: An HRTEM image of a fully disordered KIT-1 particle.¹⁵

^{viii} KIT-1: Korean Institute of Technology - 1

Thus high resolution imaging has helped to develop synthesis theories and structural representations of these framework silicates. Furthermore selected area electron diffraction, although limited by the paucity of the diffraction spots, can indicate the view direction (particle orientation). Meanwhile, the typical operating conditions (low magnification) of electron microscopes can provide information about the particle morphology and particle size of these fine mesoporous powders.

SBA-2 Literature

When Stucky *et al* first reported¹⁷ the synthesis of SBA-2, they attempted to understand the material's physical properties on the basis of X-ray diffraction, N₂ adsorption isotherms and HRTEM. Using these combined techniques they identified that the X-ray diffraction patterns can be indexed according to the 3-dimensional hexagonal space group P6₃/mmc. Furthermore, the HRTEM images and diffraction patterns appear to support this XRD finding, and suggest that the structure is composed of discrete large cages arranged in hexagonally close packed layers. Stucky *et al*, however, did not detail the extent and degree of connectivity within their new mesoporous material, saying only that a 'large cage-structured mesoporous silica framework' containing 'bottle-shaped pores or a network of pores' remains after calcination. Likewise, their subsequent articles^{18,19} present no new structural information.

Thus partly due to this poor understanding of pore connectivity, yet high potential as a 3-dimensional catalyst support, it was decided to investigate SBA-2 more thoroughly. In particular the HRTEM technique of through-focal imaging was employed to aid in this process. Meanwhile, previous HRTEM studies of microporous zeolites^{20,21} have uncovered intergrowth relationships between polytypic stacking sequences for structures that give quite distinct X-ray diffraction patterns. For example, the so-called FAU (ccp) polytype, characteristic of zeolite Y, may intergrow in various ways with the hcp polytype known²² as EMT. Thus a secondary aim of this study was to investigate whether HRTEM can uncover the existence of polytypic and related structural variations within mesoporous materials. This increased knowledge would, in turn, greatly elucidate the structure-property relationships in this class of uniform heterogeneous catalyst.

Experimental

Instrumentation

X-ray diffraction data were obtained on a Philips PW 1830 diffractometer accompanied by a Philips PW 3710 mpd control, and equipped with a secondary monochromator. Cu K α radiation, $\lambda = 1.5418 \text{ \AA}$, was used. The diffraction patterns were collected on PC-APD Diffraction software and acquired, for all samples, between $1.5 - 8.0^\circ 2\theta$ (slit size = $\frac{1}{4}^\circ$, step size = 0.02° , collection time = $2 \text{ s}(\text{step})^{-1}$). Subsequent overnight scans were acquired for the secondary peak region^{ix} *ca.* $3.0 - 8.0^\circ 2\theta$ counting for *ca.* 90 seconds per 0.01° step. The structural integrity of all materials was checked at ambient temperature by X-ray diffraction prior to HRTEM imaging. All reported unit cell parameters were refined on Powder Diffraction VAX/VMS V5.2 software using the 'celref' programme.

HRTEM images were recorded using a JEOL JEM-200CX electron microscope, figure 12, operating at 200 kV. SBA-2 samples were prepared by adhering them onto a holey carbon film, supported on a Cu or Au grid, before transferring them into the specimen chamber. The objective lens parameters, $C_s = 0.41 \text{ nm}$ and $C_c = 0.95 \text{ nm}$ gave an interpretable point resolution of *ca.* 1.85 \AA . Images were recorded along all the high symmetry zone axes at magnifications of $24000\times$ to $49000\times$. Selected area electron diffraction patterns were obtained using a camera length of either 820 mm or 1320 mm. It was found that the as-prepared samples decomposed in the electron beam, thus all HRTEM investigations are based on calcined samples.

^{ix} The major diffraction peak was excluded from these overnight scans to avoid potential damage to the detector, i.e. excessive count values.

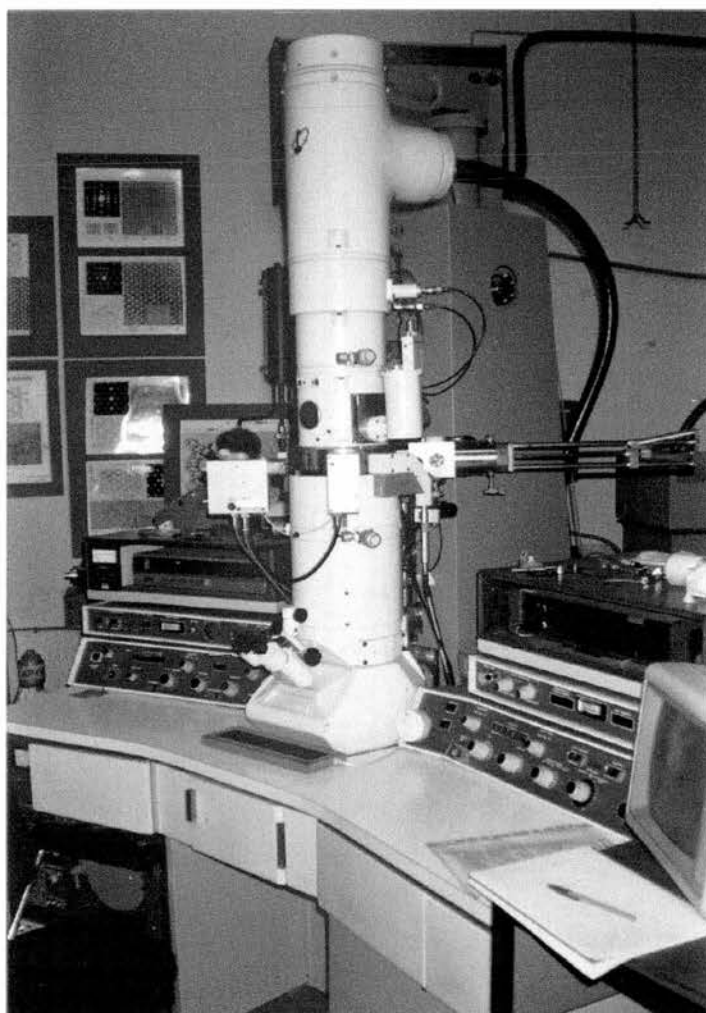


Figure 12: The JEOL JEM-200CX electron microscope used during investigation.

Computer simulation of the HRTEM images, based on the proposed models, was performed according to the multislice method. The CERIOUS HRTEM programme used was developed by Cambridge Molecular Design Ltd.

Synthesis

A general synthesis procedure for SBA-2 materials used during HRTEM imaging is as follows. Tetramethylammonium hydroxide (TMAOH) was added to distilled water, with stirring, at room temperature. Into this the diquatery ammonium surfactant, C16-3-1, $[\text{H}_3\text{C}(\text{CH}_2)_{15}\text{N}^+(\text{CH}_3)_2(\text{CH}_2)_3\text{N}^+(\text{CH}_3)_3]\text{Br}_2^-$ was dissolved. Finally tetraethylorthosilicate (TEOS) was added. The resulting synthesis mixture of molar

composition 0.05 C16-3-1 : 0.5 TMAOH : 1 TEOS : 150 H₂O was stirred at room temperature for 2 hours. The reaction pH was monitored throughout. The solid product was recovered by filtration (Büchner apparatus), washed with distilled water and dried in air at ambient temperature. The surfactant molecules were removed by calcination at 550 °C, first in N₂ (1 h) and then O₂ (6 h). Alternatively, as indicated in the text, a reaction temperature of 80 °C, a static set-up or an additional swelling agent (0.58 mol trimethylbenzene, TMB, added with the TEOS) was employed. Also titanium- and aluminium-containing SBA-2 samples were prepared using the direct synthesis approach. These are denoted SBA-2 Ti x or SBA-2 Al y where x and y represents the Si:metal ratio in the initial reaction mixture ($x = 50$ when Si/Ti = 0.02; $y = 50$ or 25 when Si/Al = 0.02 or 0.04 respectively). Thus immediately following the addition of TEOS, an appropriate amount of metal source, as Ti(OEt)₄ or Al₂(SO₄)₃·16H₂O, was added. The pH of the final mixture, of molar composition 0.05 C16-3-1 : 0.5 TMAOH : 1 TEOS : 150 H₂O : x Ti or y Al was adjusted to pH 11-11.5 with *conc.* H₂SO₄ (if necessary). The solid products were recovered and calcined as above. Each calcined aluminium-containing sample was used as a solid acid catalyst towards the butene isomerisation reaction (see Acid Catalysis chapter): SBA-2 Al50 was coked over 12 h whilst Al25 underwent a 10 h reaction period.

Analysis

Modelling mesoporous silica: SBA-2 and STAC-1

A well defined mesoporous SBA-2 sample^x was chosen on the basis of X-ray diffraction. The as-prepared and subsequently calcined patterns, figure 13, are similar to those of Huo *et al*¹⁷ and can be indexed according to a hexagonal unit cell. Although the (100), (101) and (103) peaks are indistinct, the ratio of the refined unit cell dimensions a and c , table 1, compare favourably to an ideal hcp sequence of cages.

	a (Å)	c (Å)	c/a ratio
as-prepared	56.0	92.0	1.64
calcined	48.3	79.5	1.65
ideal hcp array	-	-	1.633

zero point error = $0.2^\circ 2\theta \pm 8\%$, unit cell parameter error = ca. $0.6 \text{ \AA} \pm 1\%$

Table 1: Refined unit cell dimensions for as-prepared and calcined SBA-2. An ideal hcp array is tabulated for reference.

^x This sample actually contains titanium, Si/Ti = 0.02, however the presence of this tetrahedral heteroatom does not appear to affect the overall framework structure.

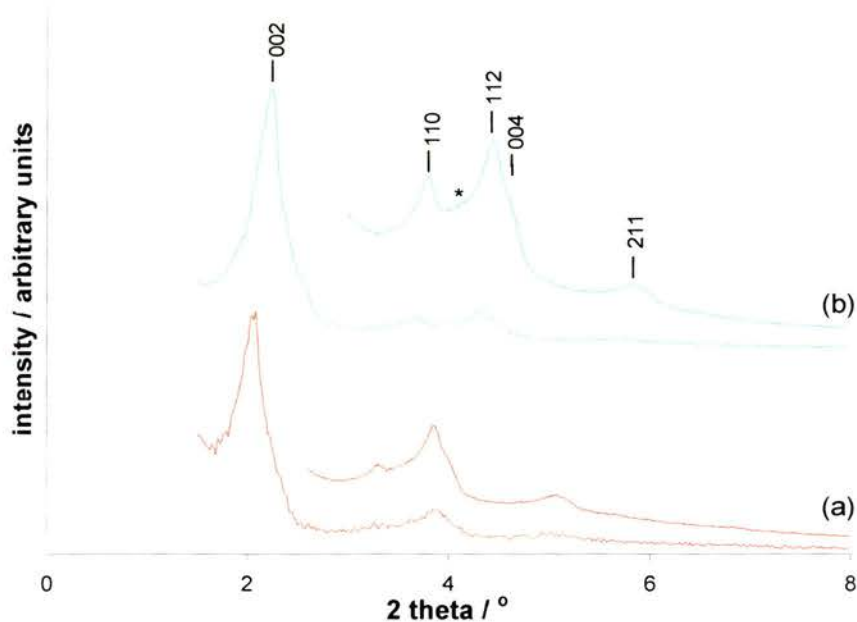


Figure 13: XRD patterns for (a) as-prepared and (b) calcined SBA-2. The calcined sample is indexed for a hexagonal unit cell. The asterisk (*) marks the expected position of a d_{103} reflection indicative of a hcp predominance within the structure.

Initial observations, figure 14, show that this sample possesses a spherical morphology. Typically these ball-like particles have dimensions in the region 1.2 – 1.8 μm and are ordered throughout. High resolution imaging, however, is limited to thin edge locations where, unlike in thicker regions, the transmitted electrons can be recombined into interpretable contrast patterns. Thus HRTEM of the spherical particle edges shows that this periodicity is due to regular mesoporous arrays, figure 14c. What follows, therefore, is a detailed inspection and a rationalised understanding of these arrays.

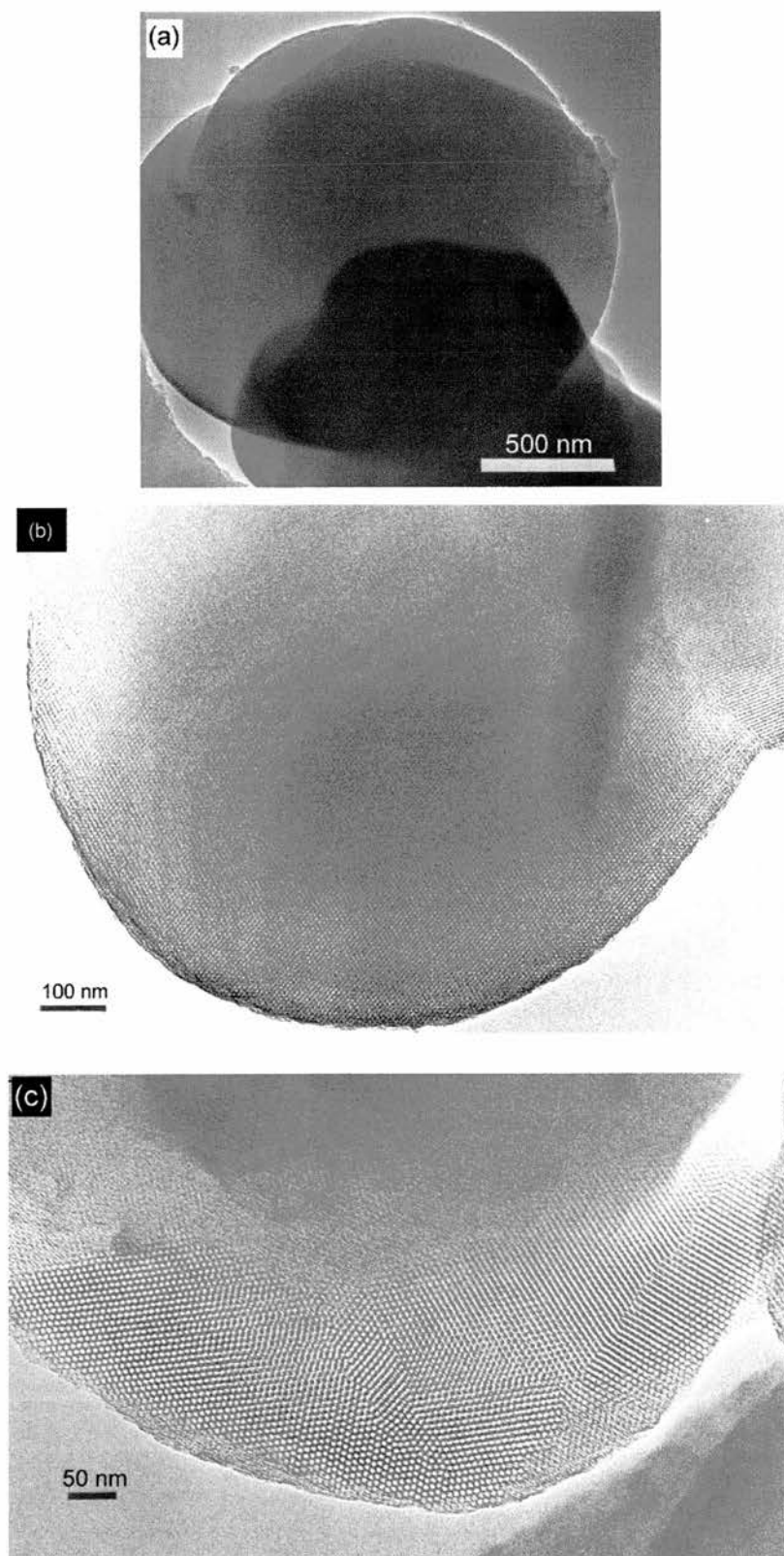


Figure 14: HRTEM images of spherical mesoporous SBA-2: (a) at low magnification, (b) showing structural order across the whole particle and (c) showing regular contrast patterns (mesoporous arrays).

A hexagonal unit cell possesses lattice points at $(0,0,0)$ and $(\frac{1}{3}, \frac{2}{3}, \frac{1}{2})$, figure 15. For SBA-2, spherical micelles are centred at these points, which leave empty cages after calcination. Thus the mesoporous lattice can be visualised schematically as arrays of spheres (cages) joined by lines^x (cage connectivity). Viewed down a , figure 16, it is clear that an ABAB... stacking sequence of layers of cages is present. This is characteristic of hexagonal close packing and has been observed during HRTEM imaging.

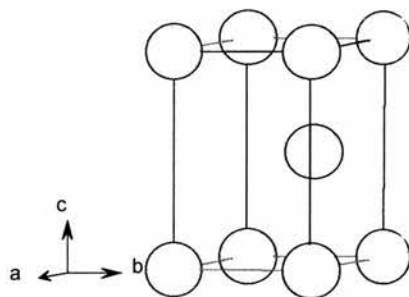


Figure 15: Schematic of a hexagonal unit cell: $a = b$, $c = \sqrt{\frac{8}{3}}a$, $\alpha = \beta = 90^\circ$, $\gamma = 120^\circ$.

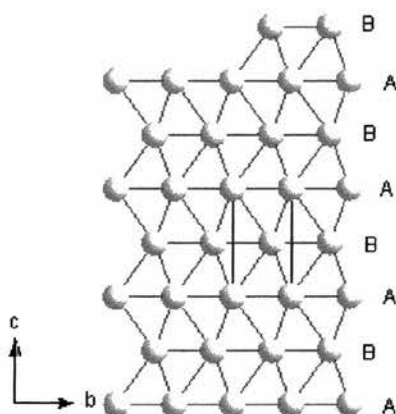


Figure 16: Schematic of an hcp array looking down a . A single hexagonal unit cell is outlined in black.

^x Every sphere, however, is unlikely to be connected to its twelve nearest neighbours. Such a scenario would give 74 % empty space when calcined. The proposed pore connectivity will be discussed later.

Thus figure 17a shows an underfocus image of SBA-2 viewed down the a axis of a hexagonal unit cell. This image appears as a series of white spots (pores), existing as well defined rows perpendicular to c yet stacked in the vertical $[001]$ direction. On closer inspection, it is apparent that the c axis is not solely composed of an 'ABAB...' stacking sequence, but also contains an 'ABCABC...' arrangement.

These, respectively, are characteristic of hexagonal and cubic close packing of micelles, and indicate that polytypic intergrowths can occur during the formation of SBA-2. Reminiscent of microporous zeolitic materials,^{20,21} these intergrowths imply that 3D mesoporous silicates, through the templating nature of their spherical surfactant micelles, are similarly prone to the concept of two end-member structural configurations.

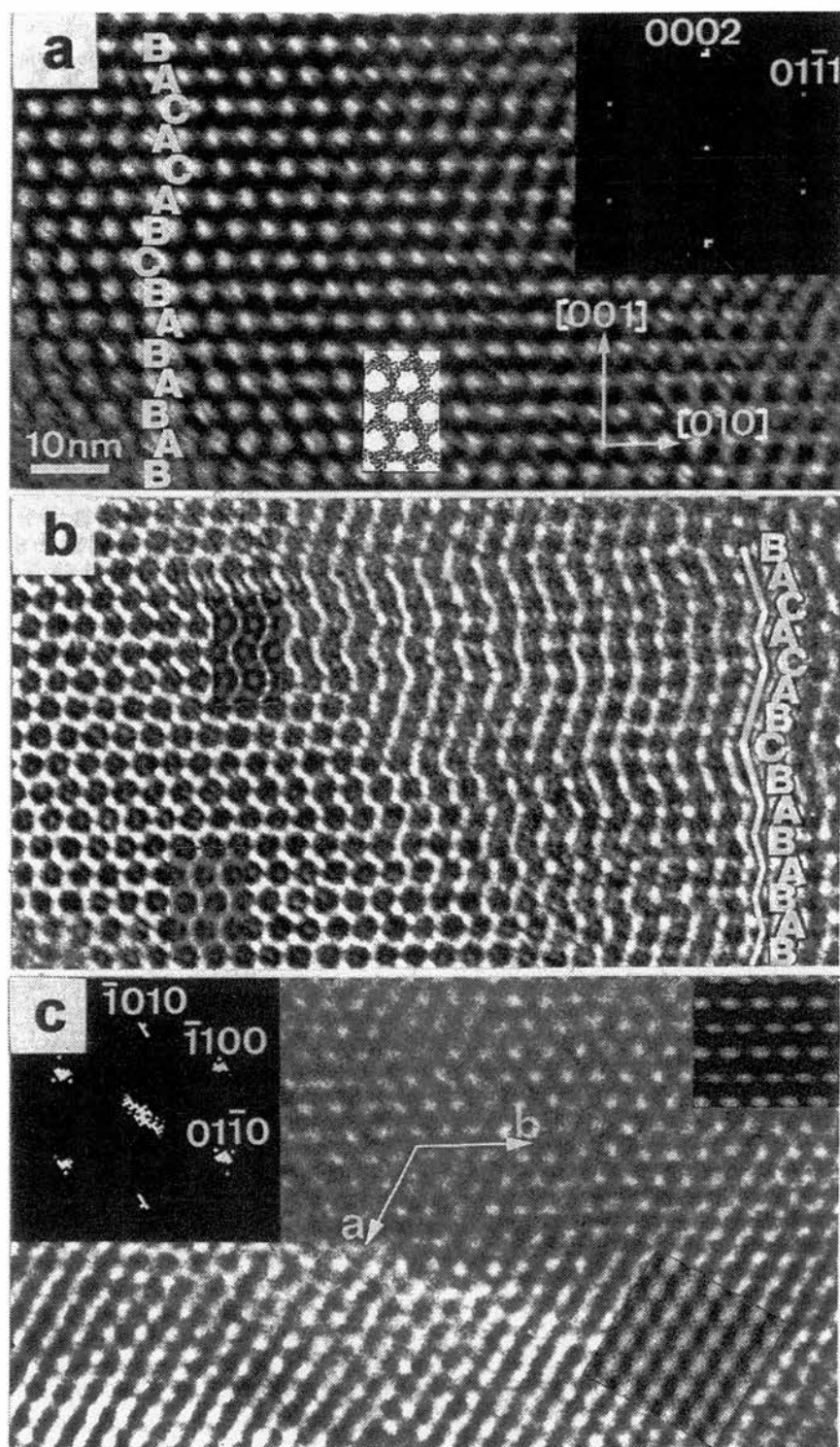


Figure 17: (a) an underfocus HRTEM image of SBA-2 looking down the a axis of the hexagonal unit cell, (b) the same crystal region as in (a) recorded as an overfocus HRTEM image and (c) an HRTEM image of SBA-2 viewed down the $[001]$ direction. See text for an explanation of the insets.

This intergrowth concept has implications for the observed electron diffraction pattern. In a pure hcp array, looking down a , the electron diffraction pattern (figure 18) possesses systematic absences along c . Indexed using the Miller-Bravais notation, these occur at (0001) and are attributable to the close packed layer which lies parallel to the ab plane at $\frac{1}{2}c$. Thus, as predicted, the (0001) diffraction spot is absent in the experimental Fourier transform optical diffraction pattern (top right inset, figure 17a). In addition the observed angles and distance ratios between the origin and designated diffraction spots strongly agree with the theoretical values, table 2. Thus we can be confident that figure 17a is being viewed down the a axis of a hexagonal unit cell. However, the optical diffraction spot at $[01\bar{1}0]$ is also absent. This can only be due to the perturbed hexagonal stacking sequence resulting from the cubic intergrowth regions. Consequently any diffraction spot at $[01\bar{1}0]$ is *very* weak, and therefore is not discernible.

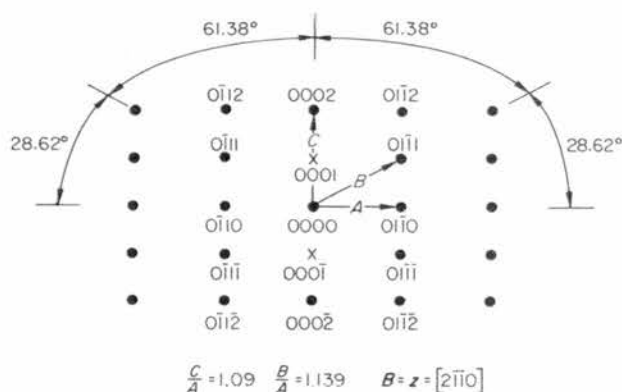


Figure 18: Single-crystal spot transmission electron diffraction pattern looking down a in the hcp crystal structure.⁹ The zone axis, z , is the beam direction, B , thus $B = z = [2\bar{1}\bar{1}0]$.

	angle		distance	
	$\angle(0002)(000)(01\bar{1}1)$	$\angle(01\bar{1}1)(000)(01\bar{1}0)$	C/A	B/A
theoretical	61.38°	28.62°	1.09	1.139
observed	61.5°	27.5°	1.03	1.14

Table 2: Comparative angles and distance ratios between the theoretical and experimentally observed hexagonal electron diffraction pattern, viewed down $[2\bar{1}\bar{1}0]$.

Employing the HRTEM technique of through focal imaging, it is possible improve our understanding of the nature of polytypic intergrowths and pore connectivity within mesoporous materials. Thus the overfocus image, taken from the same region as in

figure 17a, is shown in figure 17b. Although not strictly a structural image, this representation clearly shows a series of discrete ‘black dots’ or pores within the thin LHS region, and a pathway of channels along the c axis in the thicker RHS area. Inspection of the LHS of figures 17a and 17b shows that the spots remain as discrete entities. Knowing that these images are viewed down a , it is possible to hypothesise that these pores are also connected along the a direction: designated a type I connectivity for clarity. The contribution from the cages to image contrast is concealed by that of the low electron density within the channels. Meanwhile, the RHS of the overfocus image plainly shows a zigzag channel pathway. Clearly, therefore, no straight chain pore connections exist in the [001] direction. Moreover, it can be thought of as a hexagonal-cubic intergrowth system (highlighted). In the hexagonal region a continuous channel system exists, composed of regularly spaced *ca.* 141° turning angles. An ‘ABAB...’ stacking sequence, therefore, favours a second type of pathway (type II) in the c direction. Similarly, the straight sections running in the c direction correspond to the ‘ABCABC...’ stacking sequence. These straight pathways (a type III connectivity) can be attributed to regions of cubic close packed pores (or micelles in the as-prepared material).

Finally figure 17c supports these conjectures. Identified by the optical diffraction pattern (Miller-Bravais indexed inset), this image shows hexagonal SBA-2 viewed down the [001] direction. Thus the a and b directions are highlighted, and clear 1D fringes, along a , can be seen (lower LHS). This thin region of the specimen contrasts with the thicker (top RHS) section. Here, the hcp stacking sequence forbids a straight channel system down [001]. Instead only discrete low electron density, white spots are observed; the contribution from the pore connections along a being concealed by the particle thickness.

Combining these ideas and conjectures, it is possible to describe the complete channel system within SBA-2, figure 19. Presented as an expanded negative (pore-filled, framework-absent) model, a single hexagonal unit cell can be visualised, figure 19a. In this case, each cage, marked B as an example, is in contact with six-co-ordinated cages in neighbouring close packed layers: three below (labelled A1-A3) and three above (A4-A6). According to the previously reported¹⁷ $P6_3/mmc$ space group for SBA-2, all these

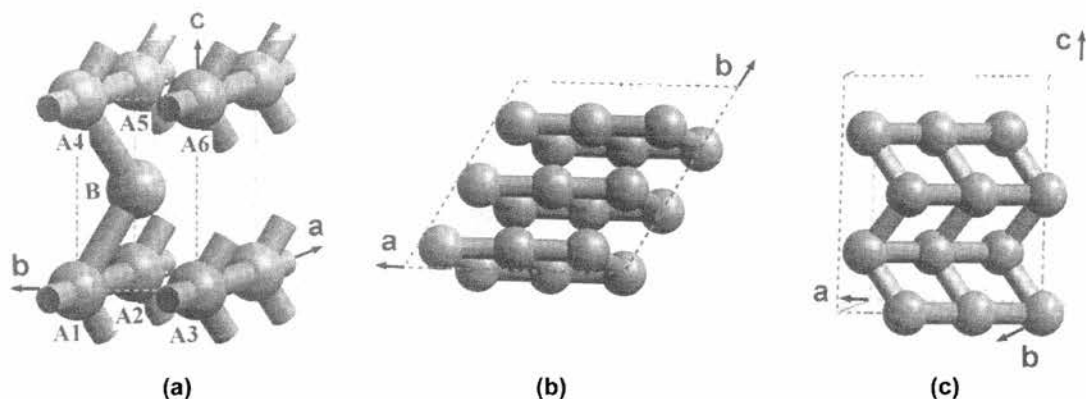


Figure 19: Proposed model of the channel systems in SBA-2 with hcp stacking, showing (a) a single unit cell, (b) a view along the [001] direction and (c) a single sheet containing the type I straight and type II (zigzag) channels

A-B connections should be identical, and all six linkages should exist simultaneously. However, through-focal imaging shows that the cages along a (e.g. A1-A2 and A4-A5) are connected to form 1D type I channels. The symmetry of the SBA-2 structure, therefore, is lower than $P6_3/mmc$, and the resulting interlayer pathways fall into two groups according to their relationships with these type I channels. In detail, a connection between B and A3 would be perpendicular to these type I channels, and should be visible as an additional zigzag line in figure 17b. This sort of linkage, though, was not observed. Instead the zigzag pathway in figure 17b corresponds to either B-A1 or B-A2 connections. It is impossible, however, to distinguish between these possibilities since both possess angles of about 60° to the type I channels. Moreover the coexistence of A1-B-A4 and A2-B-A5 linkages within the same unit cell is unlikely, since the formation of a triangular pathway connecting the three neighbouring cages would result in a very thin silica wall at the centre. Furthermore, the HRTEM images viewed down the various directions never show double zigzag channels along the c axis. Consequently, the final proposed, hexagonal unit cell model shows only two types of channel: type I and type II; the latter being single zigzag pathways lying along the c axis, figure 20. Viewed as a network, figure 19c, this 2D sheet can be thought of as MCM-41-like channels (type I) connected to each other by secondary channels (type II) possessing a micelle templated cage at each intersection, or node. These 2D sheets, therefore, exist as individual entities, since there are no cross-connections joining them.

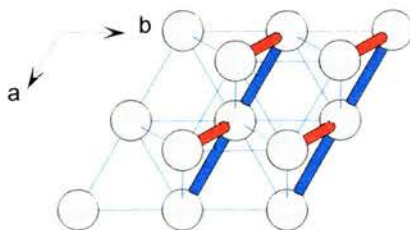


Figure 20: Schematic of a $2 \times 2 \times 2$ hcp array looking down c . The type I (blue) and type II (red) connectivities are highlighted.

In regions of ‘ABCABC...’ stacking, however, a third type of porosity has been identified: type III. Figure 21 shows two different underfocus HRTEM images of a sample dominated by such a sequence. Although disrupted by a single stacking fault, marked by a horizontal white line in (a), the close packed layers are clearly visible (highlighted). As before, the optical diffraction pattern was used to identify the view direction.

Determined as looking down the a axis of a hexagonal unit cell (similar to figure 17a) or the $[110]$ direction of a cubic unit cell;^{xii} the image directions, therefore, are denoted as $[b\bar{k}l]_h$ or $[b\bar{k}l]_c$ respectively. Similarly the Fourier transform optical diffraction pattern is indexed with both Miller-Bravais notation for the hexagonal unit cell and (in parentheses) the simple Miller notation relating to the cubic unit cell. Meanwhile the second underfocus image (figure 21b) clearly shows 1D fringes attributable to type III pore connectivity.

^{xii} Each are equivalent.

A second model, figure 22, composed solely of cubic close packed layers, must therefore be considered, in order to completely describe the experimental HRTEM observations. Obviously not of a hexagonal nature, this model is designated STAC-1 (St Andrews-Cambridge-1), a cubic structure, and thus a new mesoporous phase. The structural principle of channel formation in STAC-1, however, is similar to that in SBA-2, namely the secondary channels are never perpendicular to the type I channels. Neither are there cross-connections between the 2D sheets (figure 22b). Instead, this system is composed solely of type I and type III straight channels (figure 22c), where, in an ideal case, these two types of channels become indistinguishable.

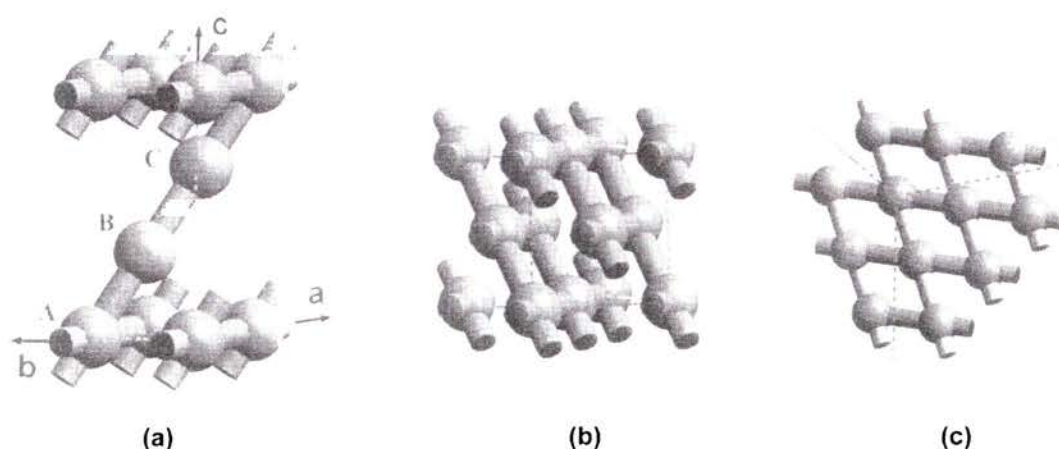


Figure 22: Proposed model of the channel system in STAC-1 with ccp stacking, showing (a) a single hexagonal unit cell for a comparison with the hcp structure of SBA-2, (b) a cubic unit cell and (c) a single sheet in a $2 \times 2 \times 2$ cubic supercell containing type I and type III channels.

To further confirm the pore connectivity conclusions, computer simulations were performed using the proposed models for SBA-2 (figure 19a) and STAC-1 (figure 22b). Created from a block of amorphous SiO_2 , the virtual structures of SBA-2 and STAC-1 were obtained by systematic removal of atoms positioned within the porous channels or cages.

Thus for SBA-2, a hexagonal unit cell of dimensions^{xiii} $a = 49.0 \text{ \AA}$, $c = 80.4 \text{ \AA}$ and $\gamma = 120^\circ$ was used. Subsequently spheres of radius 20 \AA and centred at $(0,0,0)$ and $(\frac{1}{3}, \frac{2}{3}, \frac{1}{2})$ were fashioned, to leave, at first, a hexagonal array of close packed cages. Then the atoms within cylinders of radius 15 \AA , connecting the empty cages along a were removed. This formed the type I channels proposed. To complete the undulating 2D sheet porosity, the atoms inside cylinders connecting spheres at $(0,0,0)$ to $(\frac{1}{3}, \frac{2}{3}, \frac{1}{2})$ and then to $(0,0,1)$ were deleted, to form the zigzag type II channels along the c direction. Next, this virtual hexagonal framework was used to simulate the observed HRTEM images. Thus the lower inset in figure 17a shows the simulated contrast pattern obtained when looking down a at a lens focus of -300 \AA and based on a sample thickness of 98 \AA . The complimentary overfocus pattern (focal length of 2200 \AA) is shown in figure 17b (top inset). Meanwhile the second (bottom) inset in this figure presents the computerised image of a 49 \AA thick sample at a lens focus of 2000 \AA . Thus overall these simulated contrast patterns correlate extremely well with the experimental observation. In addition the top overfocus inset faithfully reproduces the zigzag type II channels representative of the proposed undulating pore connectivity in the c direction. This particular evidence confirms that the proposed A1-B-A4 pathway (as opposed to A2-B-A5) is realistic (c.f. figure 19a). Finally figure 17c contains simulated insets looking down the hcp $[001]$ direction. These contrast patterns are based on sample thickness' of 334 \AA (top right) and 84 \AA (bottom) and are taken at lens under-focus lengths of -375 \AA and -250 \AA respectively. Again it is clear that in the thin particle region the areas of low electron density lie along the a direction (type I connectivity) whilst thicker regions of hcp stacking disguise all porosity characteristics, in both the a and c directions, and therefore only a simple hexagonal array of regularly stacked white spots is discernible.

A virtual model of STAC-1, meanwhile, was created from a cubic unit cell of amorphous SiO_2 and of dimension^{xiv} $a = 69.3 \text{ \AA}$. As before the micelle templated cages were fashioned by removal of atoms positioned within spheres (20 \AA radius) located at face-centred sites. Subsequently cylindrical connections of 15 \AA , were made between these cages, along the $[110]$ and $[10\bar{1}]$ directions, to form the straight type I and type III

^{xiii} Dimensions are derived from the indexed XRD pattern and then refined on the basis of a hexagonal unit cell.

^{xiv} $a_{\text{cub}} = \sqrt{2}a_{\text{hex}}$

connectivities proposed. The simulated contrast patterns for STAC-1 based on a specimen thickness of 300 Å are shown in figure 21. Thus the HRTEM image (figure 21a inset) obtained at -300 Å lens focus shows the distinct white spots (low electron density) indicative of channels along the viewing direction. The simulated image (figure 21b top RHS inset) obtained at a second underfocus condition (-100 Å), meanwhile, shows intermediate greytone contrast, indicative of the straight type III pore connectivities along this c direction. Thus one can be confident that the proposed model of STAC-1 is a close representation of the real structure.

Mesoporous Domains and Particle Boundaries

Traditionally HRTEM is used in the imaging of structural defects. The effect of stacking disorder has already been discussed at length, and reveals that mesoporous materials are subject to polytypic intergrowths. The study of mesoporous domains and particle boundaries, however, is also worthy of examination.

In a hexagonal 'ABAB...' or cubic 'ABCABC...' stacking sequence the underfocus white spots (cages) are each encircled by six nearest neighbour cages. Figure 23 displays such a system, attributable to a football-like particle and constructed from multiple domains. It is clear that each domain is composed of a disordered hcp/ccp intergrowth stacking arrangement, however, as indicated a hexagonal ordering of cages is present throughout. At the join of two neighbouring domains, though, this regular alignment of cages becomes perturbed. Closer inspection reveals that heptagons and pentagons (highlighted) emerge to accommodate these ruptured stacking sequences. Conceivably, therefore, the micelle packing arrangements adjust to harmonise the joining of two adjacent domains during particle formation. Thus these modifications must create additional free space, available for silicate condensation during synthesis, ultimately resulting in thicker wall frameworks^{xv} at domain interfaces. An associated perturbation

^{xv} Close packing sequences possess a minimum void space (i.e. framework volume) configuration, thus any perturbation to a close packed arrangement will increase this void space.

in pore connectivity, similarly, must occur at these boundaries; to date, however, this has not been quantified.

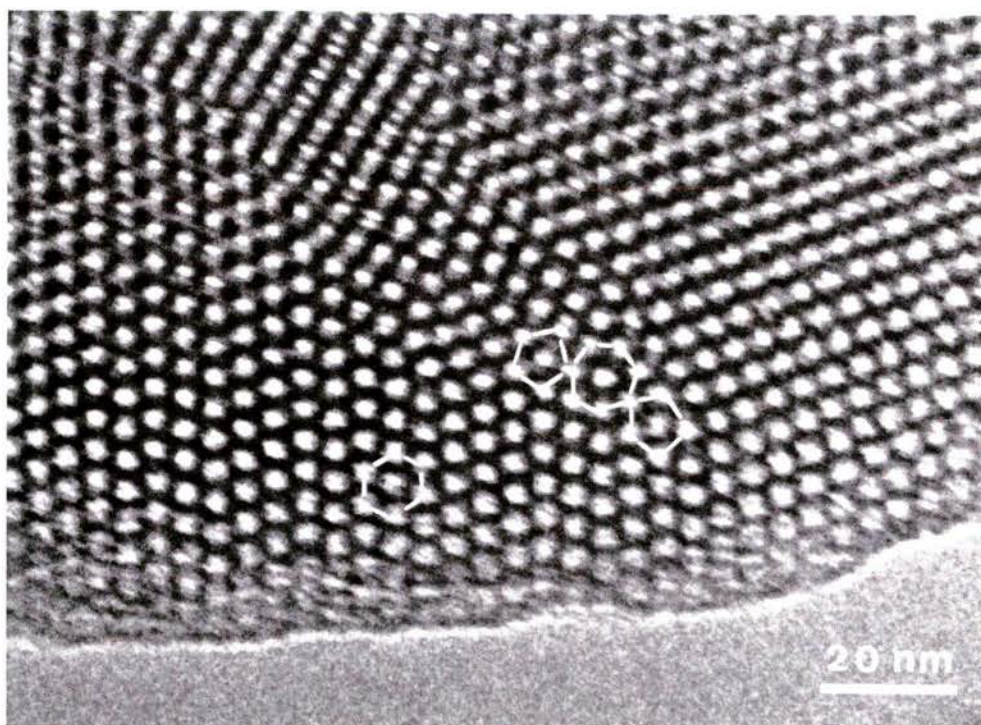


Figure 23: An underfocus HRTEM image showing domain structure within SBA-2: 5-, 6- and 7-member nearest neighbour rings are highlighted.

Particle boundaries, meanwhile, arise within agglomerations. Figure 24 presents a close up of such a scenario, clearly showing well defined domain structure within each individual particle. The inter-particle region, however, possesses no regularity. Instead a disordered, mesoporous image contrast pattern is evident, suggesting that once formed, the exterior layer of a particle exerts no control over the adjoining micelle stacking arrangements.



Figure 24: An underfocus HRTEM image of a particle boundary region in SBA-2.

Structure versus Morphology

Up until now this discussion has centred upon the local structure and in particular structural defects of a spherical particle. With the working models for SBA-2 and STAC-1, however, it would be gratifying to synthesise a whole batch of structurally pure material; or at the very least analyse the synthesis conditions required to achieve this goal. Several subsequent samples were therefore investigated using HRTEM, chosen on the basis of subtly different XRD patterns or synthesis procedures.

The selected samples and some experimental observations pertaining to them are presented in table 3. Of particular note is that a second morphology has been imaged: that of a flat sheet-like particle. What follows, therefore, is a discussion relating to these two particle types and that of their bulk structure.

sample no.	Temp	time	stirring?	pH	special composition	HRTEM morphology	XRD (103) peak?
1	RT	2 h	✓	11-11.5	Ti50	spherical	×
2	80 °C	2 h	×	11.72	SiO ₂	spherical	×
3	RT	2 h	300 rpm	10-10.5	SiO ₂	flat	×
4	RT	2 h	✓	11-12	TMB	flat	✓
5	RT	2 h	300 rpm	11-11.5	SiO ₂	flat	×
6	RT	2 h	✓	11-11.5	Ti50	spherical	×
7	RT	2 h	300 rpm	11.5-12	SiO ₂	flat + spherical	✓
8	RT	2 h	✓	11	Ti60	flat	✓
9	RT	2 h	✓	? ^a	Al50	disordered	✓
10	RT	2 h	✓	11	Al25	disordered	? ^b

a: unknown pH b: No overnight run was performed on this poorly ordered sample.

Table 3: Recorded experimental synthesis conditions and interesting observations for SBA-2. The blue highlighted row describes the sample used for the proposed models.

Comparison between the XRD patterns of the original synthesis method (sample #1: RT, stirring, Ti50) to that of a material prepared under static conditions at 80 °C (sample #2) shows them to be remarkably similar,^{xm} figure 25. This is mirrored in the HRTEM images (not shown), where each possess a spherical morphology and exhibit regions of hexagonal and cubic micelle close packing. It appears, therefore, that the presence or absence of titanium, stirring speed or high temperature do not affect the driving forces instrumental in forming a spherical particle.

^{xm} Increased silicate condensation at 80 °C produces a more stable framework. Consequently the resulting sample is more resistant to contraction during calcination, and the XRD peaks appear at lower $^{\circ}2\theta$ values.

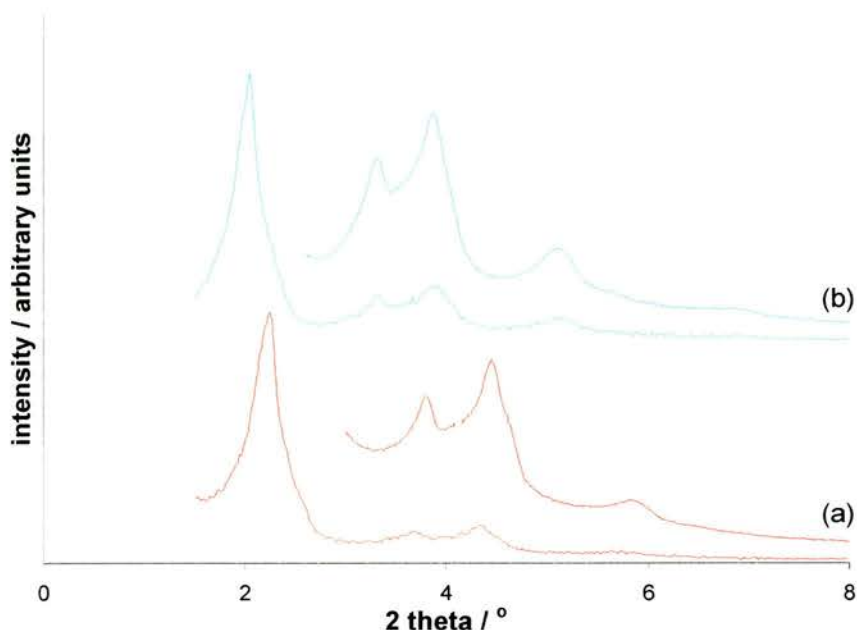


Figure 25: XRD patterns for calcined SBA-2: (a) synthesised at RT, stirring (sample #1) and (b) synthesised at 80 °C, static (sample #2). The secondary diffraction peak region was collected overnight to show detail.

In addition, occasionally, spheres possessing a ‘straight side’ are imaged, figure 26. Several theories for this behaviour can be proposed: (i) that they result from multiple collisions (with other particles or the beaker wall) during synthesis, (ii) that 3D growth was hindered by an external body (e.g. the beaker surface) or (iii) that they are caused by two spheroids that interpenetrate during growth, resulting in surface tension forces that form a flat communal wall between the initial nuclei. All of these scenarios are conceivable hypotheses.



Figure 26: An HRTEM image of a spherical mesoporous SBA-2 particle possessing a 'straight edge'.

The second morphology alluded to earlier is presented in figure 27. This specimen was synthesised at high stirring speed (300 rpm) and at (low) pH 10-10.5 (sample #3). The corresponding XRD pattern, however, shows no differences to previous samples, namely a continued absence of the hexagonal (103) peak. The first HRTEM observations of this morphology indicate that it is not a single crystal. In other words the flat particle is composed of multiple adjacent domains. Furthermore within each domain (again) both hexagonal and cubic stacking sequences exist.

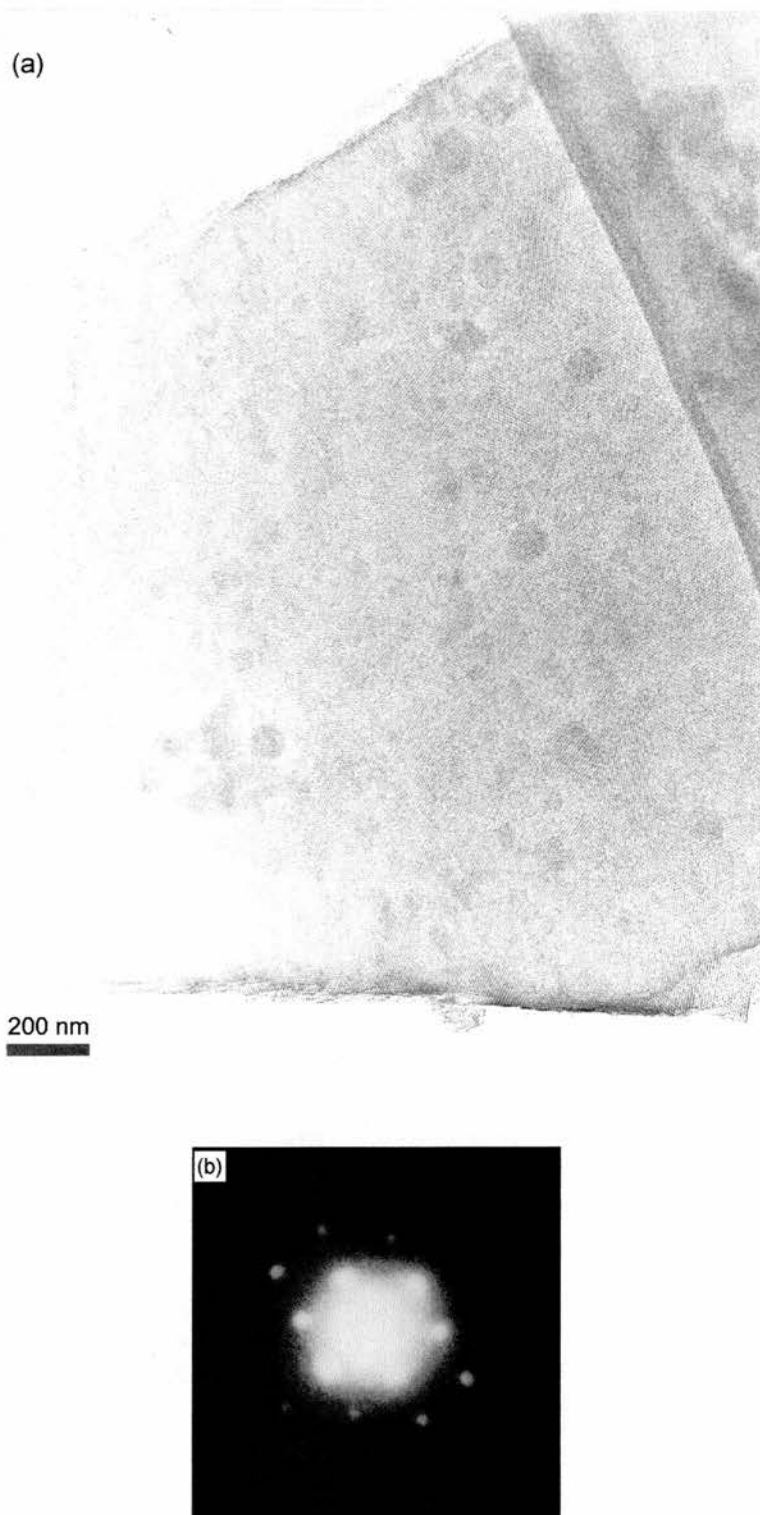


Figure 27: (a) flat sheet morphology and (b) associated SAED pattern for SBA-2. The SAED view direction is not down a simple crystallographic axis and has not been able to be determined.

This multiple domain morphology has also been observed in other flat sheet sample preparations. Interestingly some of these possess the elusive (103) XRD peak attributable^{xvii} to hexagonal crystal systems, table 3, figure 28. Observation of this bulk (XRD) structure, however, does not appear to enhance the concept of pure, hexagonally stacked, particle domains. Indeed the HRTEM images still show disordered hcp and ccp cage stacking sequences. Figure 29 displays these HRTEM images for such a '(103) containing' sample prepared with 0.58 mol TMB.

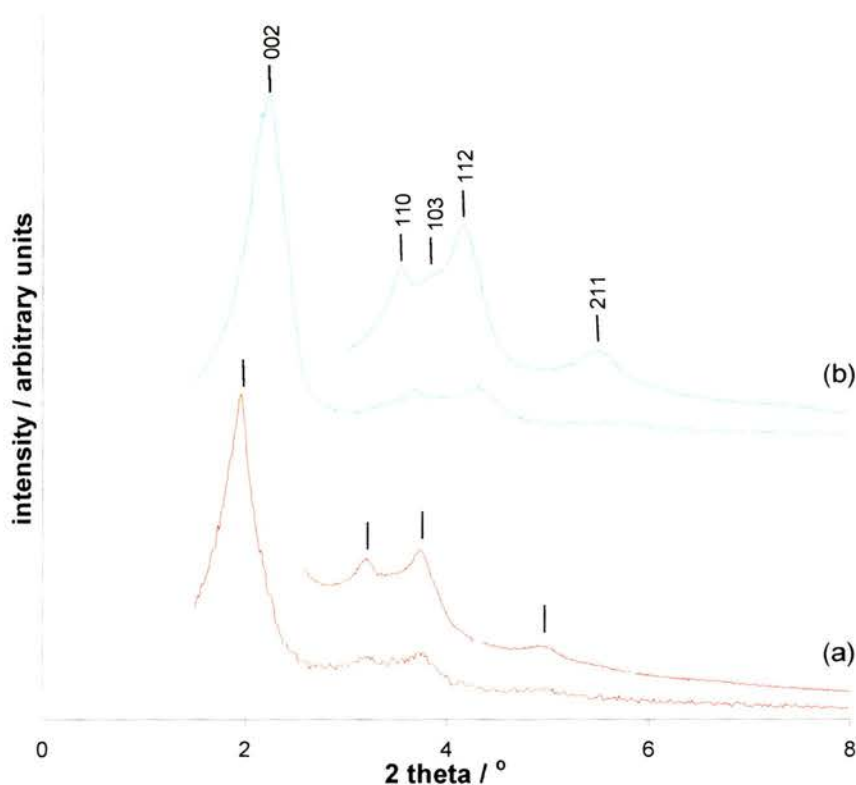


Figure 28: XRD patterns for sheet-like samples: synthesised at RT for 2 h (a) at pH 10-10.5 and stirring at 300 rpm (sample #3) and (b) whilst stirring with TMB at pH 11-12 (sample #4).

^{xvii} At this relative d spacing there are no XRD peaks corresponding to a cubic crystal system.

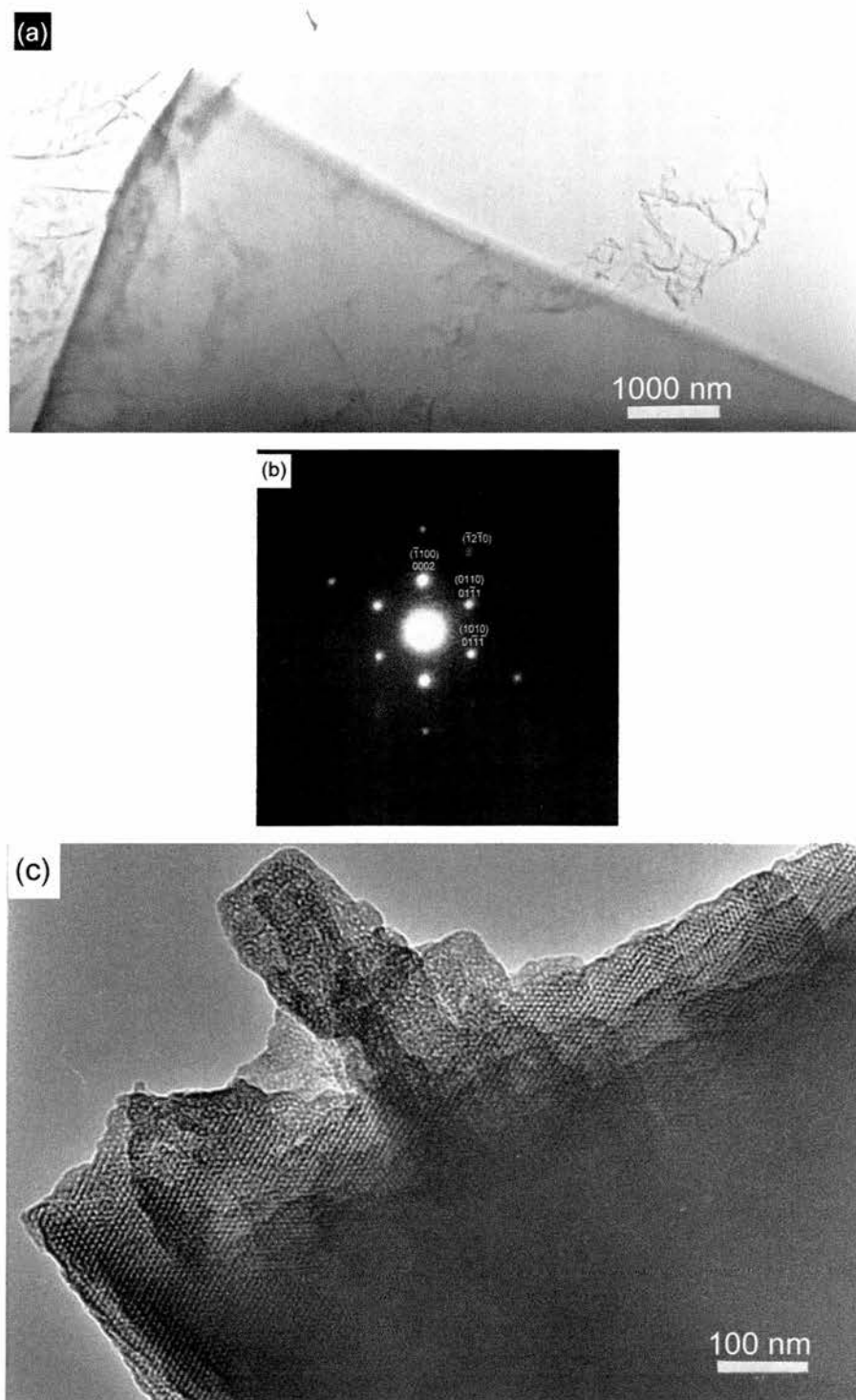


Figure 29: (a) Flat sheet morphology, (b) the associated SAED pattern indexed looking down a (and in parentheses down c) of a hexagonal crystal structure (see text) and (c) layering in a sharp edged particle of SBA-2 (sample #4: TMB).

Traditionally the view direction is determined on the basis of SAED. This hexagonal-cubic polytypic intergrowth system, however, causes a perturbation in the [001] stacking direction. Furthermore the long range order and the large unit cell dimensions of mesoporous materials compound this problem, by generating (i) few electron diffraction spots and (ii) diffraction spots very close to the origin. Consequently the SAED viewed down a becomes virtually identical to that viewed down c , figure 30. Unambiguous assignment^{xviii} of the view direction of this flat sheet is therefore difficult, as it can be interpreted as looking down either a or c within a hexagonal crystal structure. Thus the electron diffraction pattern, figure 29b is indexed as looking down a and (in parentheses) down c . Fortuitous (dis)order gives rise to outer (non first level) diffraction spots, however these cannot be indexed with any certainty. What can be ascertained, however, is that the integrity of the particle region selected for electron diffraction is mainly of a single direction.

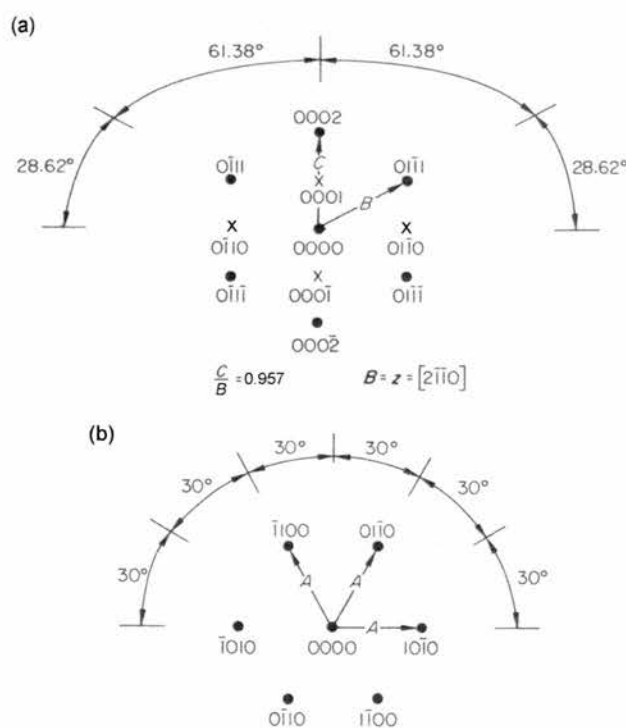


Figure 30: Comparison of hcp electron diffraction angles and distances viewed down (a) a and (b) c in a polytypic intergrowth system.

^{xviii} Since angles are within measurement errors of each other and distances are limited.

Furthermore, in each sheet the large (2.5-22 μm) particles are uniformly thin and possess sharp edges. This observation suggests that they were, at one time, part of a much larger body. These angular, sharp-edged shards may form during a shattering process. Such a process would also account for the layered edges observed in figure 29c. All the images, however, were taken of the 'natural' calcined material, i.e. these very fine powders are *not* ground prior to adhering them to a TEM grid. Thus, perhaps, the shattering process occurs as the large uniformly thin mesoporous material is bottled following drying. Shattering during calcination is unlikely since a gradual temperature ramp is employed.

When related to the proposed hexagonal model, therefore, the observed flat sheet morphology has several implications for the potential applications of SBA-2. Primarily it means that, if used as a membrane, there is either a straight (down *a*) or an undulating (down *c*) porous pathway permeating through the particle, perpendicular to the plane. Due to the 2D sheet nature of the mesoporosity, this membrane could be shape selective towards large molecule separations. Alternatively the internal surfaces could be functionalised and subsequently used as ion exchangers or as self-supporting membrane catalysts. In addition the dimensions of connectivity can be tailored to requirement, since swelling agents or short-tailed surfactant molecules can be used to modify the structure (re: Synthesis chapter).

It appears that the spinning speed used during initial synthesis may be instrumental in determining the final morphology. Consider a typical experiment: a fast speed (300 rpm) in a small total volume of reactant mixture (37 ml). In such a case the entire liquid is contained within the generated vortex. Any micelle-agglomeration silicate-condensation process, therefore, would occur under shear conditions. This in turn would prevent an extended 3D build up of micelles, conceivably limiting micelle agglomeration to two well defined directions. The third being bound by the shear factors within the solution. During filtration, therefore, the pouring process will orientate all the planar particles horizontally with respect to each other. The final particle morphology being formed as dehydration occurs during drying^{xx} (a setting

^{xx} The drying process conditions can be considered significant since reaction occurred over only 2 hours. Longer reaction times and higher drying temperatures have so far not been investigated using HRTEM.

process). Thus as imaged with HRTEM, and following calcination, the porous material is characterised by a sheet-like morphology. A second scenario can be thought of as requiring a lower stirring speed for the same reactant volume. Here, the shear effects would be much diminished, thereby increasing the possibility for 3D growth during the homogenised micelle-aggregation silicate-condensation process. The resultant porous material would have been able to develop 3-dimensionally, with subsequent layers orientating to imitate the initial well-condensed silicate-surfactant nucleus. The spherical particles presumably arise from the balanced external charge across the whole particle (hydrophobic silicate) surface. Although there is no unambiguous answer, it is fair to say that a spherical morphology offers the lowest surface area per unit volume, and presents a minimum energy configuration.

Hexagonal : Cubic 1:1 Intergrowth

A surprising, and intriguing, stacking sequence has been observed in a second location of the flat sheet particle shown in figure 29a. The HRTEM image is presented in figure 31. Based on the image angles it can be identified as looking down a of a hexagonal system, and appears to show a 3:2:3:2... regular stacking arrangement of cages. Envisioned as ABC:AB:ABC:AB... close packed layers, it is neither pure SBA-2 nor pure STAC-1. Moreover it might be described as a pure 1:1 intergrowth phase. Such a description is not inconceivable, since the stacking arrangement of close-packed spheres (hcp or ccp) is a kinetically controlled²³ process. Within metals, for example, physical forces orientate the next nearest neighbour atomic layers with respect to one another. Here, instead, physical bonding occurs within the hetero-structure: a structure composed of spherical organic micelles and an inorganic condensed-silicate framework. It appears, therefore, that these composite arrays stack with a vertical 5-tiered 'ABCAB' repeat. In turn this implies that a complicated 5-tiered model would be required to describe the pore connectivity. Constructing such a model is beyond the scope of this work.

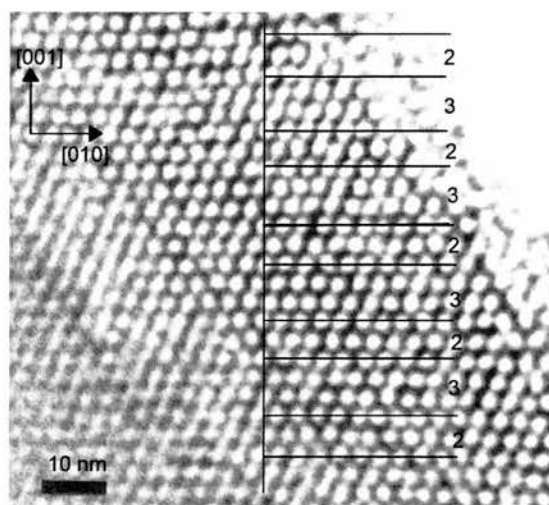


Figure 31: An HRTEM image of SBA-2 showing a domain with a suggested hexagonal : cubic 1:1 intergrowth cage stacking sequence (highlighted).

Effect of Aluminium

As detailed in the experimental section, and summarised in table 3, aluminium-containing SBA-2 Al50 and Al25 solids were prepared. These materials were to be tested as solid acids towards the isobutane cracking and butene isomerisation reactions, see Acid Catalysis chapter. From XRD it is immediately noticeable, figures 32 and 33, that addition of aluminium, a trivalent heteroatom, to a SBA-2 silicate synthesis mixture dramatically affects the overall crystallinity. Despite this, aluminium *is* incorporated within an SBA-2 structure, and thereby imparts a degree of acidity to the framework. As the aluminium loading increases, however, there is a decrease in long range order. This is shown by a broadening of the major diffraction peak and a loss of secondary peak (3-5 $^{\circ}2\theta$) definition within the calcined materials. Thus characterisation by HRTEM, to investigate their mesoporosity, and rationalise the observed XRD patterns, was considered worthwhile. In addition these solids were examined by XRD and HRTEM following acid catalysis, to assess whether the coke build-up sustained during catalysis affects the aluminosilicate framework. These resultant XRD patterns, figure 34, show no perceptible alteration in peak position or intensity compared to the (pre-catalysis) calcined parent material.

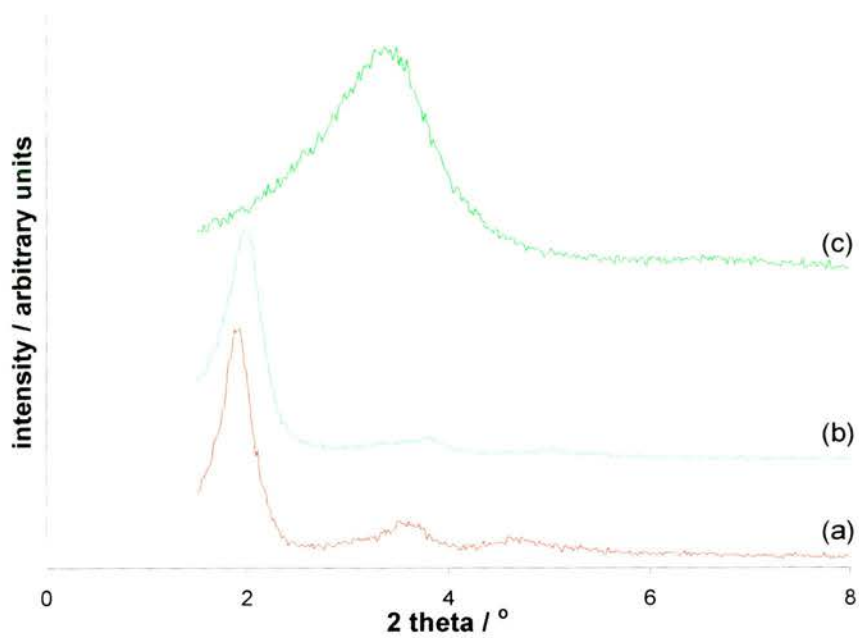


Figure 32: XRD patterns of as-prepared SBA-2 materials: (a) Al^∞ , (b) $\text{Al}50$ and (c) $\text{Al}25$.

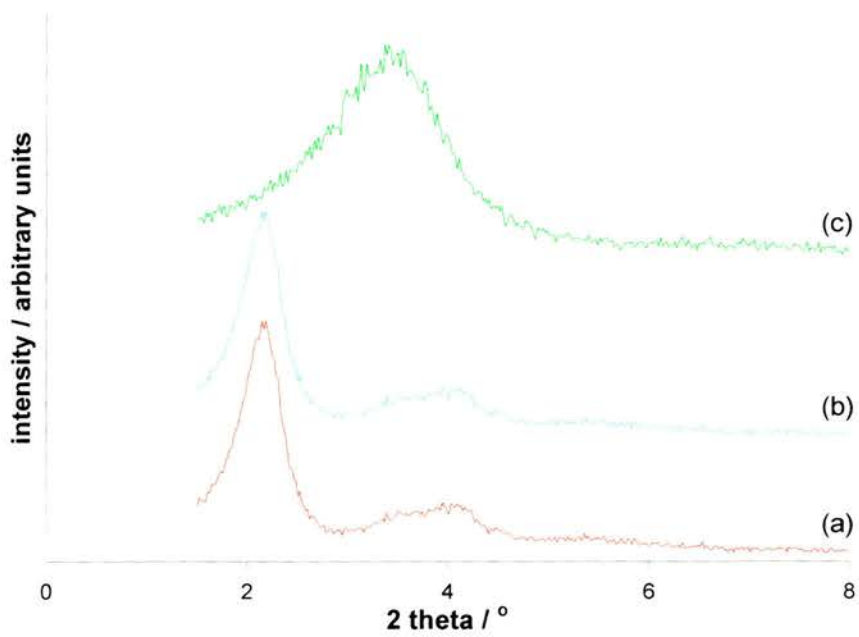


Figure 33: XRD patterns of calcined SBA-2 materials: (a) Al^∞ , (b) $\text{Al}50$ and (c) $\text{Al}25$.

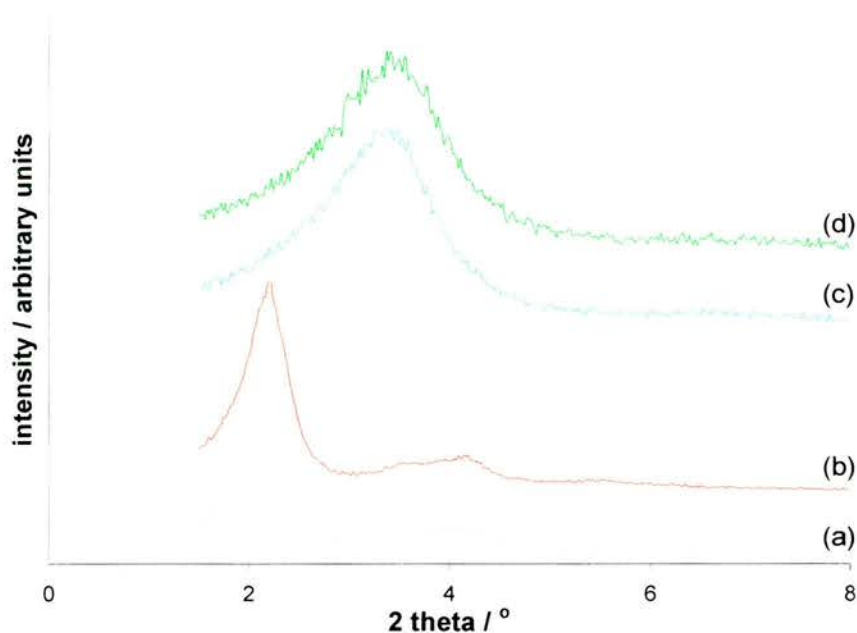


Figure 34: XRD patterns of SBA-2 materials: (a) calcined Al50, (b) coked Al50, (c) calcined Al25 and (d) coked Al25.

The HRTEM images recorded for three of these aluminium-containing SBA-2 samples: coked Al50, calcined Al25 and coked Al25 are shown in figure 35. Superficial examination of these lattice images reveals that no aluminosilicate SBA-2 crystallises with a flat sheet morphology, nor do large well-ordered mesoporous spheroids form. Instead, the particle size is much reduced, tending towards an agglomeration of small disordered domains (Al50) or crystallites with lattice fringes surrounded by extensive areas (not shown) of disordered mesoporous material (Al25). It is this bulk disordered mesoporosity that can be attributed to the observed loss of order in the XRD patterns. HRTEM imaging, however, demonstrates that mesoporosity remains, becoming extremely disordered rather than the structure collapsing.

Furthermore, the carbon deposits within the coked solids should, theoretically, show up as an additional greytone lining the internal pores. Although this is not detectable, both samples show lattice images possessing appreciable line resolution. Within SBA-2 Al50 these fringes are generally of a short and disordered nature, which is in agreement with the agglomerated disordered domain structure of the specimen. The Al25 crystallite, meanwhile, presents a ‘thumb print’ image composed of extensive curving fringes.

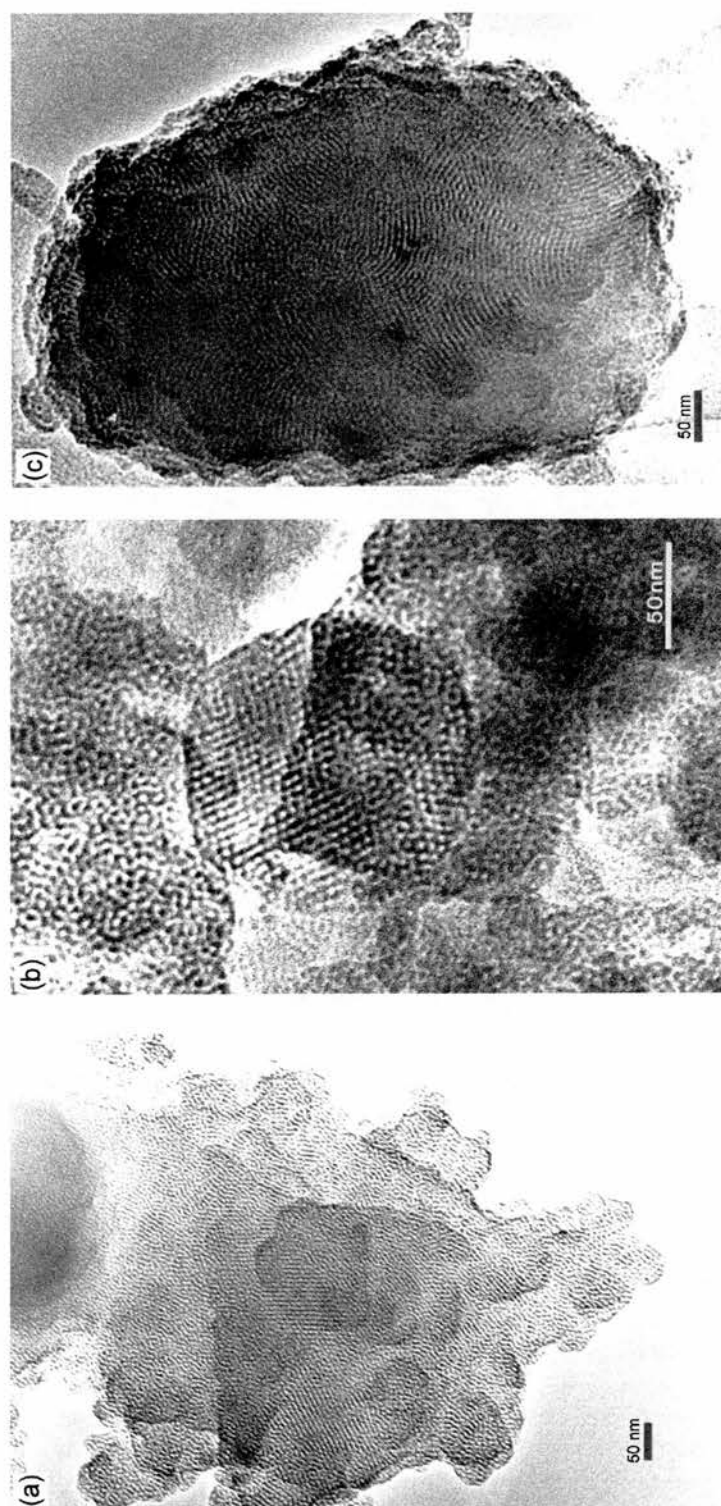


Figure 35: HRTEM images of aluminium-containing SBA-2 materials: (a) coked Al50, (b) calcined Al25 and (c) coked Al25.

Thus the complimentary techniques of HRTEM and XRD show that structural order is lost both upon aluminosilicate SBA-2 formation and as the aluminium content is increased. In spite of this it appears that the catalytic conditions employed do not destroy the initial calcined structure.

Summary

To summarise, the HRTEM technique of through-focal imaging has helped to uncover the complete pore system of SBA-2. Described within a hexagonal unit cell, this porous framework consists of type I channels running straight along the a axis, whilst the type II pathway zigzags along the $[001]$ direction. As a result the undulating 2D sheets imply that the symmetry of this hexagonal structure is lower than that predicted by the $P6_3/mmc$ space group, determined¹⁷ previously on the basis of XRD studies alone. In addition a new mesoporous phase has been discovered. Designated STAC-1, St Andrews-Cambridge-1, it can be expressed in terms of a cubic unit cell. Thus the ccp layers of cages are connected by 2D straight channels (type I and type III) to form parallel arrays of 2D porous sheets. This discovery of a hitherto unknown phase shows how powerful a tool the use of HRTEM and its associated techniques, of through-focal imaging and computer image simulations, are to the structural elucidation of mesoporous materials.

The SBA-2/STAC-1 family of mesoporous silicas, meanwhile, form with two distinct types of morphology. Described as spherical or flat sheet-like, the experimental synthesis conditions have been analysed. Perhaps significantly the ball-like particles have dimensions in the region 1.2-1.8 μm , whilst the flat sheets range up to 22 μm . There, however, does not appear to be a distinct correlation between the XRD pattern of the bulk silicate structure and the particle morphology, as observed by HRTEM. Namely the presence (or absence) of the hexagonal (103) peak is not diagnostic of the morphological type since both spheres and sheets possess hcp and ccp stacking sequences. In addition neither particle type is a 'single crystal', but appear to be composed of disordered hcp/ccp domains. Intriguingly, however, a 1:1 hexagonal : cubic intergrowth system has been observed whilst imaging a flat sheet. This suggests that the stacking sequences are subtly controlled by physical bonding forces, for reasons as yet unknown. Moreover, in flat sheets the view directions appear to show channel structure – either straight down a or undulating down c according to the proposed models – perpendicular to the particle surface. Potentially such particles could be used as large molecule membrane filters or in the field of devices.

Finally, formation of the aluminosilicate SBA-2 structure results in a loss of mesoporous order, characterised by broader (and fewer) XRD peaks and disordered HRTEM image contrast patterns.

References

- ¹ PR Buseck (Ed.), *Reviews in Mineralogy: Minerals and Reactions at the Atomic Scale: Transmission Electron Microscopy*, 1992, **27**, Mineralogical Society of America, Washington DC, USA.
- ² AR West, *Basic Solid State Chemistry*, 1988, John Wiley and Sons, Chichester, UK.
- ³ A Putnis, *Introduction to Mineral Sciences*, 1992, Cambridge University Press, Cambridge, UK.
- ⁴ JCH Spence, *Experimental High-resolution Electron Microscopy*, 1981, Oxford University Press, Oxford, UK.
- ⁵ CT Kresge, ME Leonowicz, WJ Roth, JC Vartuli, JS Beck, *Nature*, 1992, **359**, 710.
- ⁶ JS Beck, JC Vartuli, WJ Roth, ME Leonowicz, CT Kresge, KD Schmitt, CT-W Chu, DH Olson, EW Sheppard, SB McCullen, JB Higgins, JL Schlenker, *J. Am. Chem. Soc.*, 1992, **114**(27), 10834.
- ⁷ T Yanagisawa, T Shimizu, K Kuroda, C Kato, *Bull. Chem. Soc. Jpn.*, 1990, **63**(4), 988.
- ⁸ S Inagaki, A Koiwai, N Suzuki, Y Fukushima, K Kuroda, *Bull. Chem. Soc. Jpn.*, 1996, **69**(5), 1449.
- ⁹ JW Edington, *Electron Diffraction in the Electron Microscope*, Monographs in Practical Electron Microscopy in Materials Science, 1975, Philips, Eindhoven, The Netherlands.
- ¹⁰ R Mokaya, W Zhou, W Jones, *J. Chem. Soc. Chem. Commun.*, 1999, 51.
- ¹¹ H Yang, GA Ozin, CT Kresge, *Adv. Mater.* 1998, **10**(11), 883.
- ¹² A Monnier, F Schüth, Q Huo, D Kumar, D Margolese, RS Maxwell, GD Stucky, M Krishnamurty, P Petroff, A Firouzi, M Janicke, BF Chmelka, *Science*, 1993, **261**, 1299.
- ¹³ V Alfredsson, MW Anderson, T Oshuna, O Terasaki, M Jacob, M Bojrup, *Chem. Mater.*, 1997, **9**(10), 2066.
- ¹⁴ MW Anderson, *Zeolites*, 1997, **19**(4), 220.
- ¹⁵ R Ryoo, JM Kim, CH Shin, JY Lee, *Stud. Surf. Sci. Catal.*, 1997, **105**(A-C), 45.
- ¹⁶ Y Yue, Y Sun, Z Gao, *Cat. Lett.*, 1997, **47**(2), 167.
- ¹⁷ Q Huo, R Leon, PM Petroff, GD Stucky, *Science*, 1995, **268**(5215), 1324.
- ¹⁸ Q Huo, DI Margolese, GD Stucky, *Chem. Mater.*, 1996, **8**(5), 1147.
- ¹⁹ SH Tolbert, TE Schaffer, J Feng, PK Hansma, GD Stucky, *Chem. Mater.*, 1997, **9**(9), 1962.
- ²⁰ O Terasaki, T Ohsuna, V Alfredsson, J-O Bovin, D Watanabe, SW Carr, MW Anderson, *Chem. Mater.*, 1993, **5**(4), 452.

- ²¹ MW Anderson, KS Pachis, F Prébin, SW Carr, O Terasaki, T Ohsuna, V Alfreddson, *J. Chem. Soc. Chem. Commun.*, 1991, 1660.
- ²² MMJ Treacy, JB Higgins, R von Ballmoos, *Collection of Simulated XRD Powder Patterns for Zeolites*, 1996, 3rd Ed., Elsevier, New York, USA; *Zeolites*, 1996, **16**, 323.
- ²³ LV Woodcock, *Nature*, 1997, **385**, 141; LV Woodcock, *Nature*, 1997, **388**, 236.

Acid Catalysis

Background

Solid Acids

A catalyst is a substance that speeds up a chemical reaction, yet is regenerated at the end. Many industrial processes require catalysts to make them economical, and therefore profitable. In inorganic solids¹ these range from zeolites and clays, to metals, metal oxides and combinations of these. One particular example is the use of zeolites as solid acids in place of reactions traditionally involving acids in solutions or polymer matrices. It is because of their thermal stability coupled to their inbuilt shape selectivity and high active site density that the use of aluminosilicates is particularly advantageous.

This work has focused upon particular aluminosilicate solid acids and their potential role as catalysts towards hydrocarbon cracking and isomerisation reactions. More explicitly a comparison of the mesoporous structure, SBA-2, has been made with zeolites USY and Beta, two large pore 3D microporous materials, towards the probe reactions of isobutane cracking and but-1-ene isomerisation.

In the petrochemical industry the formation of 'cracked' or low-molecular-weight molecules from crude oil fractions is vital for the synthesis of subsequent products and the sale of petrol. Initially this was provided² for by using amorphous silica-alumina $\text{SiO}_2\text{-Al}_2\text{O}_3$ cracking catalyst. More recently, however, catalyst development has led to the use of rare-earth exchanged zeolite Y or partially dealuminated (ultrastable) USY suspended within a matrix of amorphous solid acid.

Pure silicate materials have an electrically neutral framework. By substituting trivalent cations into the silicate structure the material should become catalytically active. Thus, acid sites in zeolites, associated with the presence of aluminium, generate the accepted active species (carbenium ions) in catalytic mechanisms. They arise from a framework charge imbalance caused by the substitution of Al^{3+} for Si^{4+} tetrahedra. As a result a charge balancing cation is required to maintain overall framework neutrality. This can be a (poly)valent metal ion, or in the case of solid acids, a proton. Two types of acid site

exist, figure 1. Brønsted acid sites are defined² by their ability to donate protons. Lewis acid sites result¹ from co-ordinatively unsaturated Al^{3+} ions, and can be formed by the dehydroxylation of two Brønsted sites. Both types of site and their relative strengths can be assessed by temperature-programmed desorption of adsorbed bases (e.g. NH_3 , pyridine).

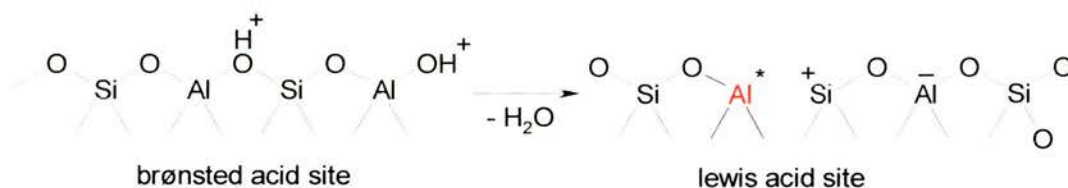


Figure 1: Brønsted and Lewis acid sites in silicates.³

Coke is a by-product of catalytic cracking. It is typically formed as cycloalkanes and (cracked) alkene fragments combine through hydrogen transfer reactions (H^- or H^+) to form high molecular weight aromatics. Often these deposits block pores and cover active sites leading to catalyst deactivation. This is an obvious disadvantage when using solid acids. Although the energy requirement for catalytic cracking (an endothermic process) is supplied¹ by the exothermic coke combustion reaction, pore blockage limits the usable lifetime of the solid acid. By using larger pores and working in the mesoporous regime it is hoped that the effect of coke formation will be reduced before regeneration is required. Furthermore, a mesoporous material which when fully coked retains its mesoporosity has a number of potential uses. One possibility is as a carbon molecular sieve⁴ (CMS) where the resultant stability, both thermal and towards acidic media, far outweighs that of its parent inorganic framework. For example, CMS could be used as a storage device for molecular weight hydrocarbons larger than methane. Another conceivable application is as an anode material in battery technology, where the graphitic carbon could channel intercalation cations (Li^+) through the well defined porous network.

Isobutane Cracking

Isobutane cracking can be described^{5,6} as a useful probe reaction for the characterisation of solid acids. A wide number of easily identifiable cracked products form, depending

on the reaction temperature, acid site strength, reactant contact time and extent of conversion. It is this product distribution that lends itself to analysis, and indicates the type of cracking mechanism employed. For many authorsⁱ the primary reaction mechanism, figure 2, involves protolytic transfer to form a 2-electron 3-centre moiety bonded to the Brønsted acid site. This penta-co-ordinate carbonium ion subsequently decomposes to form hydrogen or methane and the corresponding carbenium ions, C⁺.

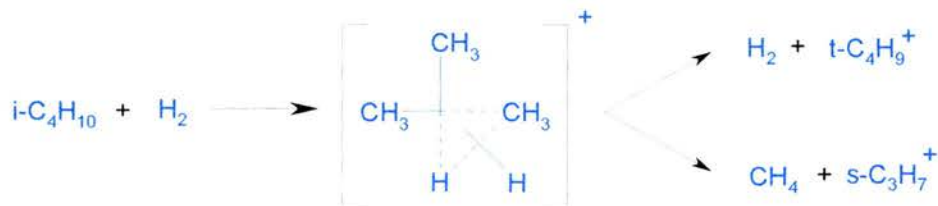


Figure 2: Proposed primary reaction mechanism for isobutane cracking.

These carbenium ions have short lifetimes and quickly desorb from the surface to yield low molecular weight alkenes and (regenerate) the active acid site. This product distribution is typical of mild acids. In spite of this, it can also be achieved⁷ on H-ZSM-5ⁱⁱ at high temperatures and low conversions,ⁱⁱⁱ where the effect of overcoming the activation barrier is counterbalanced by the decrease in carbenium ion lifetime. Ultimately, however, the product distribution will be affected⁸ by the interplay between the basicity of the intervening alkenes and the strength of the solid acid. With stronger acids, the resident lifetime of adsorbed carbenium ions increases, as does the potential for secondary reactions to occur. These include the classical carbenium ion processes⁹ (figure 3) of hydrogen and hydride transfer, oligomerisation, rearrangement and β -scission which predominantly result in C₃-C₆⁺ alkane products. Again these conditionsⁱⁱⁱ can be simulated by increasing the conversion (contact time) at lower temperatures. Further evidence of the product mechanism can be gleaned from the alkane/alkene

ⁱ M^cVicker *et al*⁵ propose that radical initiation is also possible. Similarities with gas phase reactions led them to postulate that electron acceptor sites on the solid acid will form a radical ion as a result of electron transfer from isobutene. This ion is then able to decompose into H₂, CH₄ and the corresponding carbenium ion or undergo gas phase reactions.

ⁱⁱ A medium pore microporous zeolite based upon the MFI structure type.

ⁱⁱⁱ (a) As T ↑, % conversion ↓ and primary reaction products predominate.

(b) As T ↓, % conversion ↑ and secondary reaction products predominate.

ratio e.g. C_3/C_3^- , or C_4/C_4^- . The presence of bimolecular hydride transfer processes increases the propensity for alkane products and effectively indicates the acid site strength. This ratio, therefore, measures the secondary:primary reaction mechanism pathways.

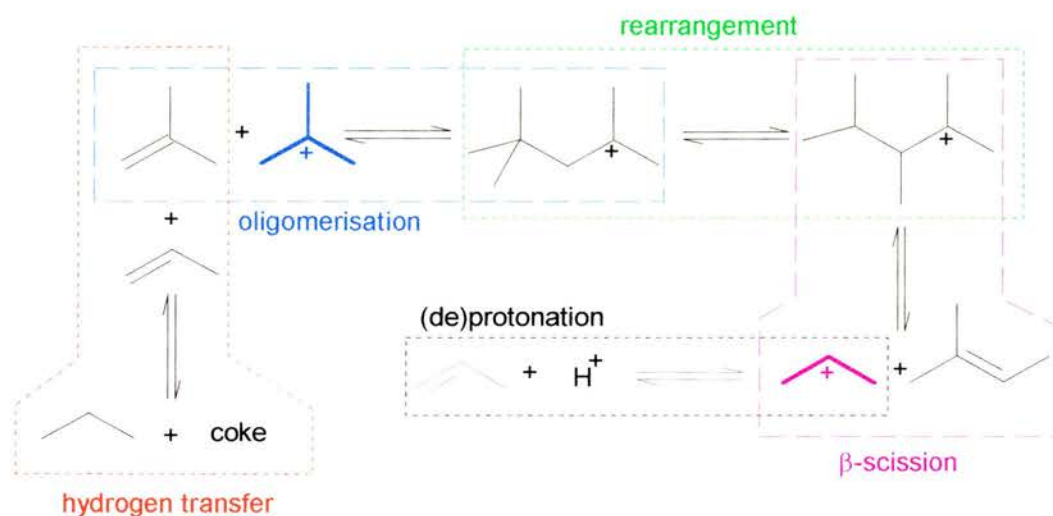


Figure 3: Examples of secondary reaction mechanism products.

But-1-ene Isomerisation

Concern for the environment has also led to the use of acidic zeolites in classical homogeneous acid catalysed organic reactions, e.g. hydrocarbon alkylations and isomerisations. A particular example is the two step production of methyl tert-butyl ether (MTBE, 2-methyl-2-methoxypropane) from the C_4 alkene byproducts of crude oil cracking. MTBE is currently used² as a replacement for lead additives in petrol, acting as a high octane blending agent, and can be synthesised¹⁰ from the catalytic addition of methanol to isobutene. In comparison to methanol, however, isobutene is a scarce commodity, even though C_4 alkenes are abundant. The butene isomerisation reaction, figure 4, catalysed by a solid acid can redress this balance. Typically¹⁰ a medium pore mild-moderate strength aluminosilicate is used e.g.: H-Theta-1 or H-ferrierite, which can selectively sustain the production of isobutene over time (or be easily, quickly and cheaply regenerated).

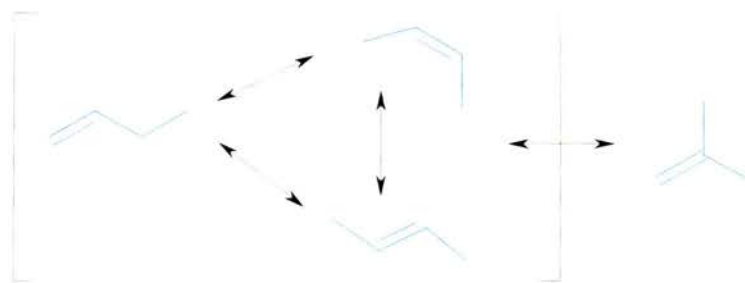


Figure 4: Butene Isomerisation reactions.

The exact mechanism of but-1-ene isomerisation has been the subject of intense study.^{11,12} Similar to cracking reactions, the solid acid acts as a 'protic solvent', where the first step (figure 5a) is the formation of a secondary^{iv} carbenium ion. The subsequent processes then depend upon the lifetime of this adsorbed species. If the lifetime is short, deprotonation can only lead to double bond migration, leaving the *cis* or *trans* isomers to desorb naturally. Alternatively skeletal isomerisation, resulting from methyl migration during adsorption, can occur with longer carbenium lifetimes. This, however, is in competition with the potential for dimerisation, a bimolecular process, and cracking (figure 5b) which occur particularly at high conversions. Furthermore, the isomerisation is thermodynamically limited, reaching equilibrium at elevated temperatures. Thus, as with catalytic cracking, the rate of reaction is dependent upon temperature, acid strength and density, contact time, degree of deactivation, % conversion and pore size. There is a consensus in the literature that a successful but-1-ene isomerisation catalyst possesses a 10-member ring pore network and has moderate acid strength. Such framework dimensions are thought to hinder the dimerisation processes that lead to coking and pore blockage. Meanwhile the solid's acidity should not be strong enough to promote rapid deactivation or the secondary reaction products associated with oligomerisation, rearrangement and cracking at the reaction temperature.

^{iv} The primary carbocation $^+\text{CH}_2\text{CH}_2\text{CH}_2\text{CH}_3$ is much less stable and consequently present in negligible concentrations.

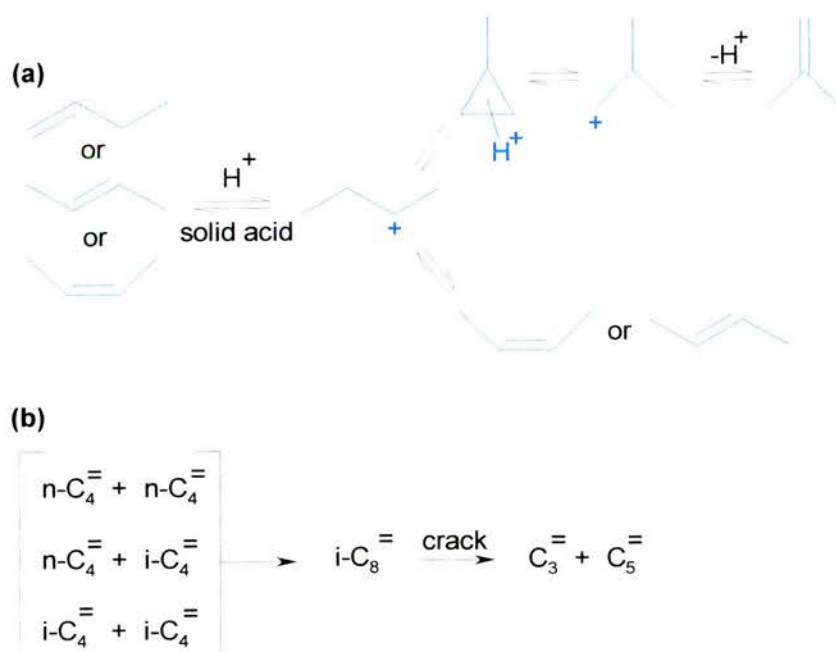


Figure 5: (a) mono and (b) bimolecular butene isomerisation mechanisms.

Experimental

Instrumentation

Powder X-ray diffraction data were obtained on a Philips PW 1830 diffractometer accompanied by a Philips PW 3710 mpd control and equipped with a secondary monochromator. Cu K α radiation, $\lambda = 1.5418 \text{ \AA}$, was used. The diffraction patterns were collected on PC-APD diffraction software at ambient temperature. The mesoporous patterns were acquired between $1.5 - 8^\circ 2\theta$ (slit size = $\frac{1}{4}^\circ$, continuous scan, step size = 0.02° , collection time $2 \text{ s}(\text{step})^{-1}$). Mesoporous overnight runs were collected as step scans for the secondary (*ca.* $3.0 - 8.0^\circ 2\theta$) peak region counting for *ca.* 90 seconds per 0.01° step. All reported unit cell parameters were refined on Powder Diffraction VAX/VMS V5.2 software using the 'celref' programme. The Philips XRD patterns for microporous zeolites, meanwhile, were collected over the range $5 - 50^\circ 2\theta$. These continuous scans used $\frac{1}{2}^\circ$ slits with a data collection time of 0.8 s per 0.02° step.

MAS NMR spectra were obtained on a Varian UNITYplus spectrometer operating at 300 MHz for ^1H and accompanied by a Doty Scientific MAS probe. The experimental details are shown in table 1. The ^{13}C and ^{29}Si measurements used a 7 mm rotor, whilst a 5 mm rotor was used for the ^{27}Al experiments.

	^{13}C	^{27}Al	^{29}Si
frequency (MHz)	75.430	78.158	59.583
spectral width (kHz)	30.0	400	30.0
spin rate (kHz)	<i>ca.</i> 4.4	10.1	<i>ca.</i> 4.4
polarisation	CP	DP	DP
pulse sequence	contact time (ms)	1	-
	angle	-	22.5°
	delay (s)	1	0.2
	acquisition (ms)	9.6	5.1
shift scale	TMS	1M AlCl ₃	TMS

CP = cross polarization from ^1H , DP = direct polarization, TMS = tetramethylsilane standard.

Table 1: MAS NMR experimental conditions.

Microanalyses were carried out on a Carlo Erba Elemental Analyser model 1106, suitable for weight % C, H and N determination.

Catalysis was performed in a continuous flow fixed bed reactor, heated by a Carbolite tube furnace, figure 6. The reactant and (nitrogen) carrier gases were metered separately, through Brooks Instruments 5850E series mass flow controllers, and well blended prior to admission to the reactor. For each experiment the gas mixture passed through the catalyst sample and the downstream hydrocarbon product distribution was monitored by on-line gas chromatography (GC). The CE Instruments 8000 TOP Series GC was fitted with a Chrompack 25 m, 0.53 mm i.d. PLOT^v fused silica Al₂O₃/KCl capillary column (film thickness 10 μm), and equipped with a heated gas-sampling valve (GSV), of volume 0.25 ml, and a flame ionisation detector (FID). The GC traces were recorded on a Fisons Instruments DP700 Data Processor (integrator). Prior to reaction the calcined samples were activated in flowing nitrogen at 350 °C for 5 hours before cooling in nitrogen to 150 °C. For each experiment the temperature was raised in 25 °C steps with two measurements taken at every second temperature to check on repeatability; the average of these results was plotted. The GC temperature programme used during all reactions started with an isothermal at 40 °C for 2 min, before the temperature was raised at 10 °Cmin⁻¹ to 60 °C and kept there for 4 min. This was followed by a second temperature ramp of 20 °Cmin⁻¹ to 110 °C and an isothermal at 110 °C for 5 min.

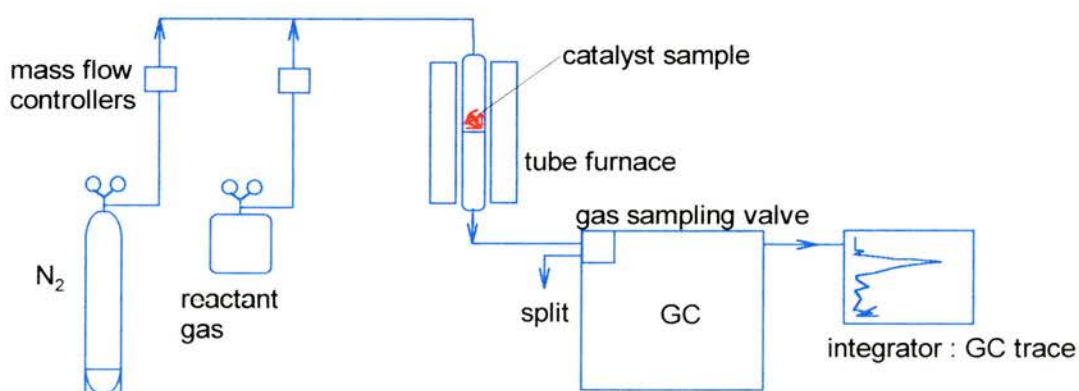


Figure 6: A diagrammatic representation of the catalytic reaction setup.

^v PLOT: porous lined open tubular.

During the isobutane cracking experiments a 0.200 g catalyst sample was subjected to a 30 mlmin⁻¹ gas flow composed of 10 % isobutane (99.98 mol% pure) in dry nitrogen. This gave a resulting weight hourly space velocity (WHSV), g reactant(g catalyst)⁻¹h⁻¹, of 2.20 h⁻¹. The catalyst activity was sampled at temperatures between 350 – 600 °C.

Throughout the but-1-ene isomerisation experiments 0.250 g catalyst was used per run. The but-1-ene gas (98.94 % pure) was diluted in dried nitrogen to give a flow of 2.1 mlmin⁻¹ but-1-ene in 33.5 mlmin⁻¹ nitrogen, and an overall WHSV = 1.2 h⁻¹. Reaction temperatures varied between 150 – 500 °C.

Adsorption isotherm measurements were performed on an in-house designed vacuum line, at 77 K, calibrated using helium. The samples (0.06 – 1.50 g) were slowly degassed, so as to avoid bumping, before being gradually heated under vacuum to 280 °C. This temperature was maintained overnight under a roughing pump vacuum of *ca.* 8 × 10⁻³ torr. A final temperature of 300 – 350 °C was achieved (and maintained for 1 hour) under a diffusion pump vacuum of *ca.* 4 × 10⁻⁵ torr, before being closed to vacuum. The sample tube was cooled in a liquid nitrogen bath (77 K) and the upper liquid surface maintained at a constant height on the sample tube throughout the measurement. Nitrogen gas was used as the adsorbate. Thus aliquots of *ca.* 30 torr were adsorbed or desorbed. Complete equilibrium was achieved before the pressure valves were recorded. Data plots are standardised per gram of material, and in comparison to the adsorption of He upon the empty sample tube, at 77 K.

Synthesis

Frequently the direct synthesis approach is used to introduce acidity into silicates. Within mesoporous aluminosilicates this has led to syntheses of aluminium-containing MCM-41^{13,14,15,16} and MCM-48^{17,18} structures using various aluminium sources. In this work the aluminium-containing SBA-2 materials were prepared as follows.

Tetramethylammonium hydroxide (TMAOH) was added to distilled water, with stirring, at room temperature. Into this a diquatery ammonium surfactant, C16-3-1,

$[\text{H}_3\text{C}(\text{CH}_2)_{15}\text{N}^+(\text{CH}_3)_2(\text{CH}_2)_3\text{N}^+(\text{CH}_3)_3]\text{Br}_2^-$ was dissolved. Finally the appropriate amount of aluminium, as $\text{Al}_2(\text{SO}_4)_3 \cdot 16\text{H}_2\text{O}$ or $\text{Al}(\text{O}^i\text{Pr})_3$, was added, immediately followed by tetraethylorthosilicate (TEOS). The pH of the resulting synthesis gel, of molar composition 0.05 C16-3-1 : 0.5 TMAOH : 1 TEOS : 150 H_2O : x Al where $x = 0$ or 0.02, was adjusted to pH 11–11.5 with *conc.* H_2SO_4 . After stirring at room temperature for 2 hours the solid product was recovered by filtration, washed with distilled water and dried in air at ambient temperature. The surfactant molecules were removed by calcination at 500 °C, first in N_2 (1 h) and then O_2 (6 h) prior to use as solid acid catalysts. The SBA-2 solid synthesised without aluminium ($x = 0$) is denoted SBA-2 Al ∞ . The $x = 0.02$ aluminium sulphate and aluminium isopropoxide analogues are denoted SBA-2 Al21 and SBA-2 Al11, respectively, where the suffix designates the Si/Al ratio in the final calcined material. This nomenclature relates to the Synthesis chapter ICP-AES results [see also Acid Catalysis Analysis].

Ammonium exchanged ultrastable Y, supplied by Crosfield (CF-810), was determined to possess a Si/Al ratio of 3/1, by X-ray fluorescence. This was then calcined in oxygen at 500 °C for 5 hours to give the protonated H^+ -USY form. The zeolite Beta solid was synthesised in-house^{vi} with a Si/Al ratio of 14/1. Prior to catalytic reaction this as-prepared form was calcined in oxygen (550 °C, 5 h) to remove the tetramethylammonium template. Subsequently it was ion exchanged twice with 1M NH_4Cl , at room temperature for 24 h, before a second calcination in oxygen formed the protonated material. The fumed silica (Aldrich) had a particle size of 0.011 micron.

^{vi} Synthesised by Dr M Sasidharan.

Analysis

ICP-AES

As discussed in the Synthesis chapter, the silicon and aluminium concentrations of the calcined SBA-2 aluminosilicate materials used here in acid catalysis were determined by Inductively Coupled Plasma – Atomic Emission Spectroscopy (ICP-AES). Surprisingly a synthesis mixture employing the aluminium sulphate precursor and possessing a Si/Al ratio of 50/1 results in the recovered SBA-2 solid containing a ratio of 20.9/1. Meanwhile, an equivalent initial loading, yet prepared with aluminium isopropoxide, yields a material with a Si/Al ratio of 11.0/1. These results might be rationalised in two ways. Firstly the monomeric alkoxy aluminium source is more easily assimilated into the SBA-2 framework because it is of a similar nature to the silicate (TEOS) precursor and hence has comparable rates of hydrolysis and condensation. Secondly that the synthesis of SBA-2 is not efficient in silica, thus the final aluminium loadings are greater than initially intended. The aluminium-containing materials discussed in this Analysis have, therefore, been designated SBA-2 Al21 or Al11 to differentiate these solids and identify their actual loadings:

- SBA-2 Al21 is synthesised with aluminium sulphate and has a Si/Al ratio of 20.9/1
- SBA-2 Al11 is prepared with aluminium isopropoxide and possesses a Si/Al ratio of 11.0/1

X-ray Diffraction

X-ray diffraction reveals, figure 7, that the order within the resulting SBA-2-Al material is inherently linked to the synthesis mixture composition. This trend is true also after calcination, figure 8. In other words, as the aluminium loading increases the structural order decreases. This is known^{15,18,19} in MCM materials, and is shown by the loss of definition in the secondary peak (3-5 °2θ) region, coupled with a slight broadening of

the major diffraction peak. It signals, therefore, that the SBA-2 structure is very composition intolerant, being susceptible to high loadings of trivalent heteroatoms. Although active-site-poor frameworks are ideal for reaction mechanism studies on a laboratory scale, industrial feasibility might be called into question. In addition, the loss of framework finesse at high aluminium loadings decreases the shape selective potential, towards larger hydrocarbons, of this mesoporous solid acid catalyst.

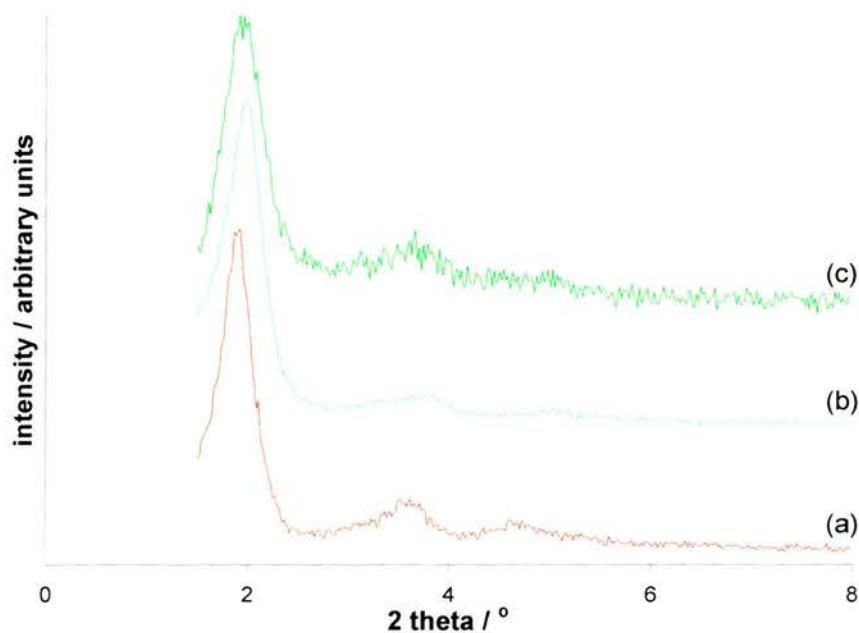


Figure 7: XRD patterns of as-prepared SBA-2 materials: (a) Al_{∞} , (b) Al_{21} and (c) Al_{11} .

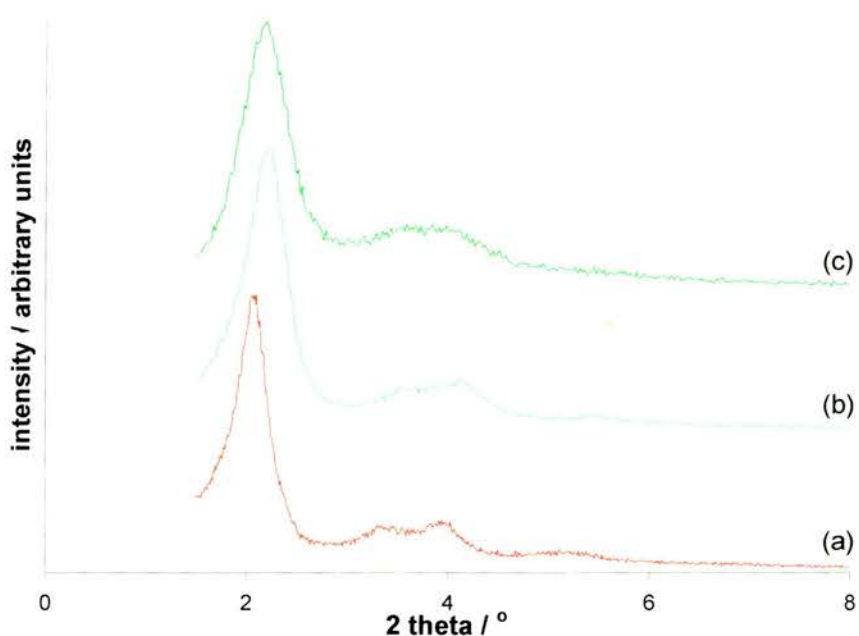


Figure 8: XRD patterns of calcined SBA-2 materials: (a) Al_{∞} , (b) Al_{21} , (c) Al_{11} .

The pure silicate SBA-2 diffractograms show no loss of order following catalysis: either during isobutane cracking or but-1-ene isomerisation. This indicates that the mesoporous structure is able to withstand periods at high temperature without framework ‘failure’. Similarly XRD of the SBA-2 Al₂₁ materials show no structural disintegration during processing, figure 9. As usual a contraction (*ca.* 5 %) of the d_{002} reflection is apparent following calcination of the as-prepared material. Subsequent (i) coking (be it through cracking or isomerisation catalysis), (ii) recycling (catalysis-calcination-catalysis) and (iii) solvent extraction (upon coked solids), however, have little affect^{vii} upon peak positions. Indeed, within experimental error the reduced unit cell size following calcination is maintained during all catalysis, table 2. This is true, also, with the SBA-2 Al₁₁ materials, figure 10. No ensuing process: calcination or catalysis, appears to change the framework order first created in the as-prepared materials. Again these results demonstrate that the SBA-2-Al mesoporous framework is stable: both thermally (during catalytic experiments up to 600 °C) and through time (during 88 hours deactivation at 400 °C).

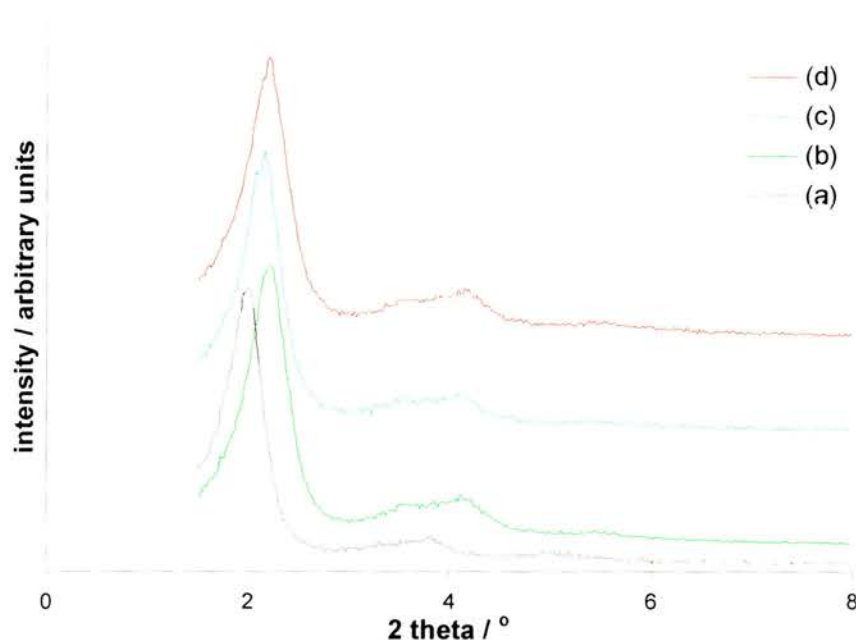


Figure 9: Selected XRD patterns for SBA-2 Al₂₁: (a) as-prepared, (b) calcined, (c) recycled following but-1-ene catalysis (12 h) and (d) extracted with ethanol (7 h) following coking.

^{vii} In mesoporous solids, absolute XRD intensity comparisons cannot be made easily, because the overall counts are highly dependent upon preparation of the sample plate.

	d_{002}	a (Å)	c (Å)	c/a	V (10^3 \AA^3)
as-prepared	42.9	55.7	91.9	1.65	247
calcined	41.0	51.4	83.4	1.62	190
coked: 500 °C, 5 h	40.4	54.2	85.9	1.58	219
extracted: ethanol, 7 h	40.2	54.5	87.6	1.61	226
coked: recycled	39.4	51.4	85.5	1.67	195

0.05 ≤ zero point error ≤ 0.25 °2θ ± 20 %, unit cell parameter error ± 3 %

Table 2: Selected hexagonal unit cell dimensions for SBA-2 Al21.

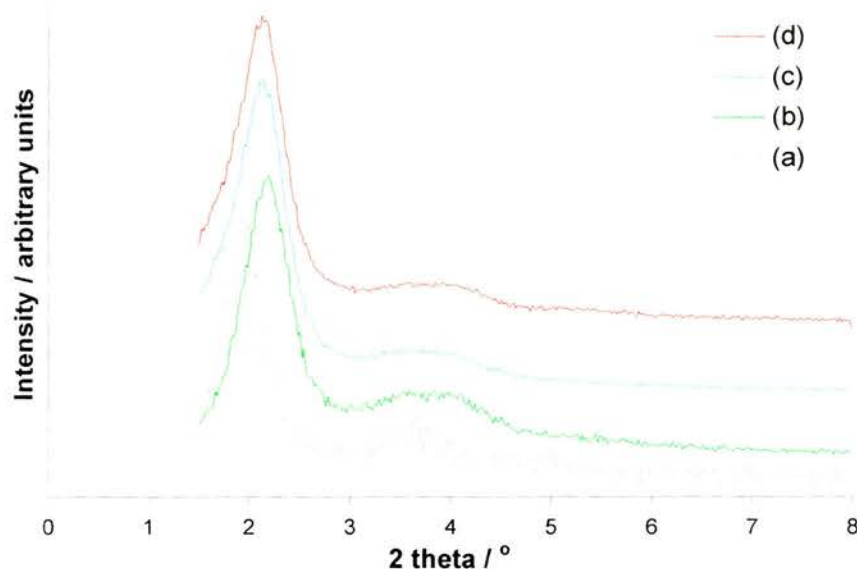


Figure 10: Selected XRD patterns for SBA-2 Al11: (a) as-prepared, (b) calcined, (c) coked with isobutane following catalytic cracking (19.5 h) and (d) deactivated with but-1-ene at 400 °C for 88 h.

Conversely the microporous materials studied: zeolites Beta and USY, show no adverse affect to heteroatom framework substitution. Zeolite Beta is a material that exhibits various polymorphs, due to stacking faults, thus a crystalline sample rarely presents the sharp well defined peaks at high $^{\circ}2\theta$ values expected of microporous solids. The collected X-ray patterns (figure 11) for Beta show, however, that crystallinity is retained throughout sample preparation and catalysis. Thus calcination of the as-prepared material results in a sharpening of the first peak at 7.7 $^{\circ}2\theta$, figure 12, and a 16.08 % weight^{viii} loss. The increase in intensity of the low angle peak, indicative of long range order within a material, can be explained by the removal of the templating tetraethylammonium moiety from within the framework channels. As a result the

^{viii} wt% carbon from elemental analysis.

diffracted X-rays are no longer scattered by channel-filling species. Following ion exchange this peak loses intensity, but as ammonia is removed during re-calcination, to yield the protonated form, the first peak again increases in intensity. It is this H-Beta material that was employed as the solid acid catalyst. Following catalysis the pores are filled with carbonaceous deposits; X-ray scattering from the channel network increases thus the $7.7^\circ 2\theta$ peak intensity is reduced. The powder patterns collected for USY, similarly, demonstrate the effect of channel filling nuclei upon the low angle peaks, figures 13 and 14. Furthermore, throughout the calcination-catalysis process the structural integrity of this solid remains intact, with no loss of peak definition at high $^\circ 2\theta$ angles. We can conclude, therefore, that both Beta and (as its name suggests) ultrastable Y possess durable framework structures towards the reaction conditions employed.

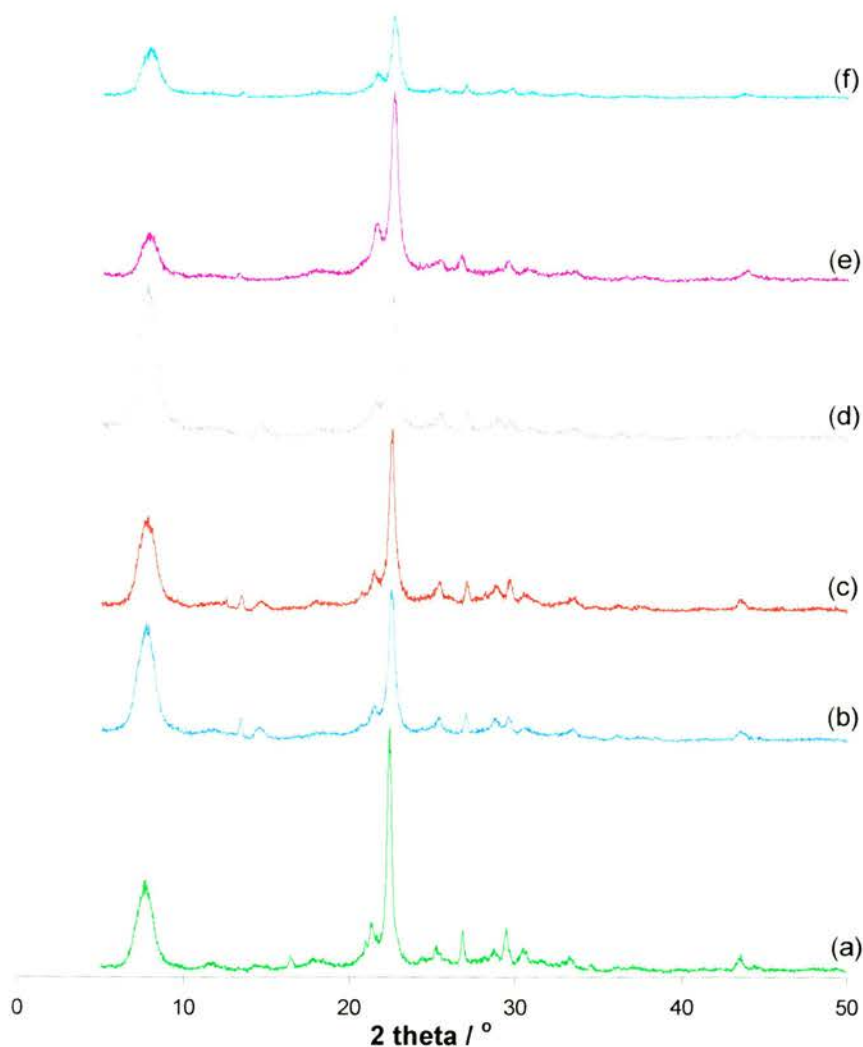


Figure 11: XRD patterns for zeolite Beta: (a) as-prepared, (b) calcined, (c) ion exchanged, (d) re-calcined, (e) coked with isobutane (12 h) and (f) coked with but-1-ene (15 h).

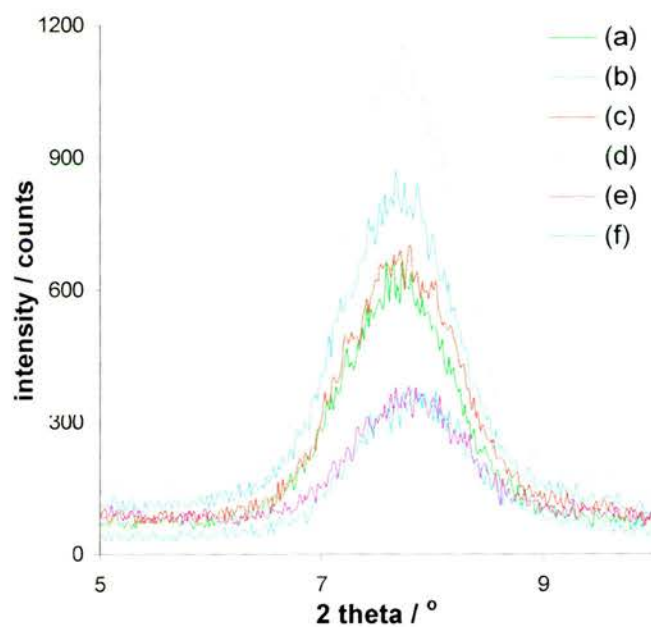


Figure 12: XRD pattern expansions for zeolite Beta: (a) as-prepared, (b) calcined, (c) ion exchanged, (d) re-calcined, (e) coked with isobutane (12 h) and (f) coked with but-1-ene (15 h).

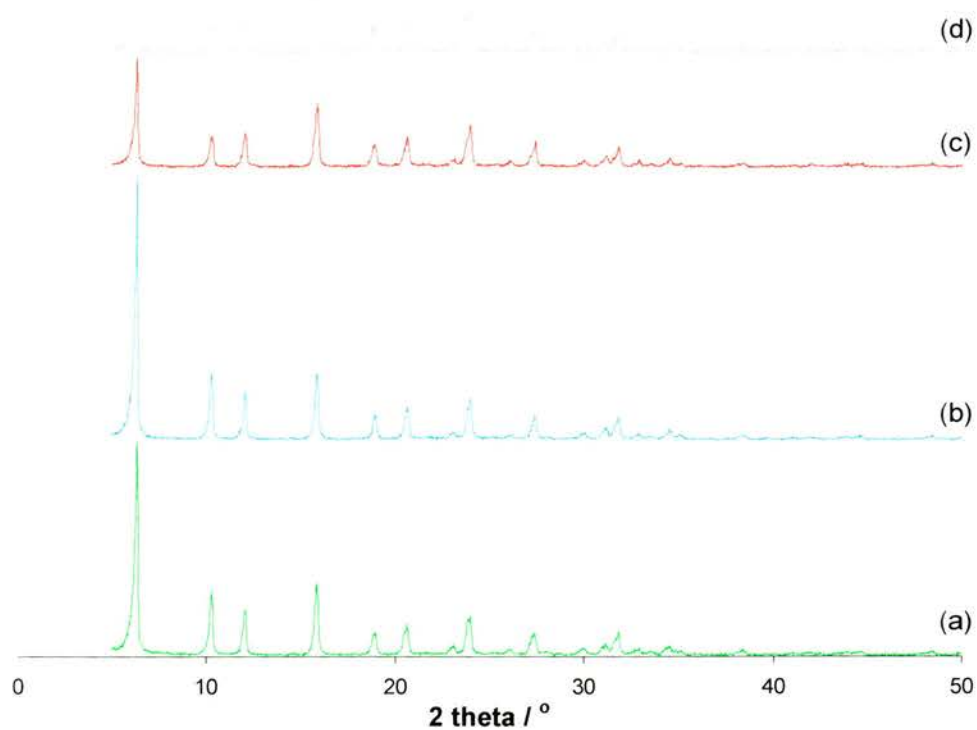


Figure 13: XRD patterns for USY: (a) ammonium exchanged, (b) calcined, (c) coked with isobutane (12 h) and (d) coked with but-1-ene (28.5 h).

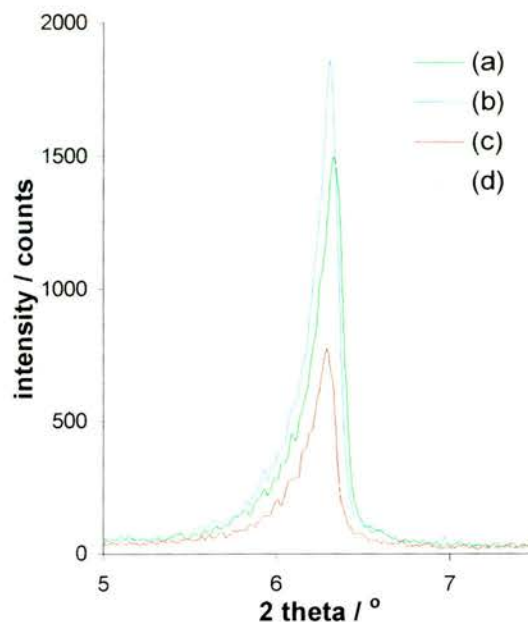


Figure 14: X-ray pattern expansions for USY: (a) ammonium exchanged, (b) calcined, (c) coked with isobutane (12 h) and (d) coked with but-1-ene (28.5 h).

MAS NMR Spectroscopy

The ^{27}Al MAS NMR of the aluminium-containing SBA-2 materials are shown in figures 15 and 16, where SBA-2 Al21 was synthesised using $\text{Al}_2(\text{SO}_4)_3 \cdot 16\text{H}_2\text{O}$ and SBA-2 Al11 used $\text{Al}(\text{O}^i\text{Pr})_3$. Casual examination of the resulting spectra shows them to be remarkably similar; thus the aluminium source can be judged to have no effect upon the final co-ordination environments. The as-prepared materials display a single resonance at 53 ppm. This is attributable to 4-co-ordinate aluminium²⁰ (AlO_4 structural unit), and indicates that, following synthesis, all aluminium exists in a tetrahedral framework environment. Upon calcination, however, the spectrum^{ix} becomes weaker and more complicated as signals at *ca.* 30 and 0 ppm are formed. These can be assigned^{21,22} to 5- and 6-co-ordinate aluminium respectively; indicating that either the co-ordination environment alters within the framework or, by analogy with dealuminated zeolites, the aluminium is no longer framework contained and in the process has become 5- or

^{ix} During calcination the Al species adopt sites of lower symmetry, thus for the calcined and coked samples the ^{27}Al MAS NMR signals were weak.

6-fold co-ordinated (extra-framework). This broadened signal is maintained following catalysis, suggesting that the 4-, 5- and 6-fold co-ordination environments are now temperature stable. From this data, however, it is not possible to say whether the 5- and 6-co-ordinate aluminium creates active surface-bound acid sites.

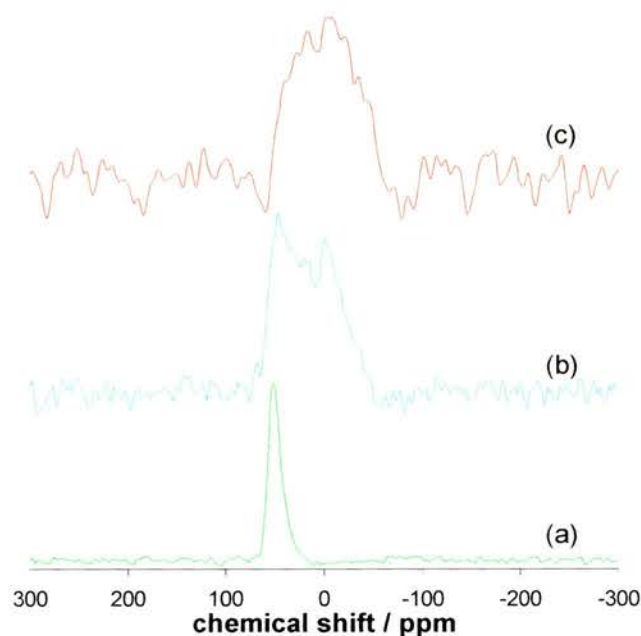


Figure 15: ^{27}Al MAS NMR of SBA-2 Al₂₁: (a) as-prepared, (b) calcined and (c) coked with but-1-ene (12 h).

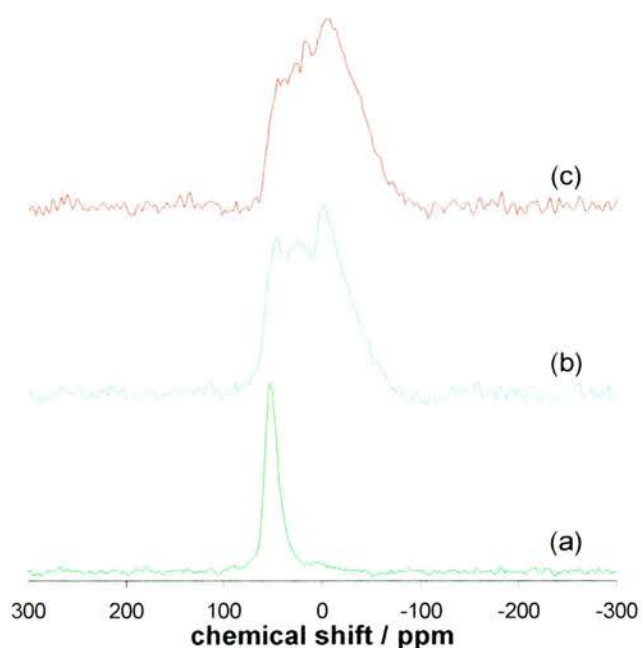


Figure 16: ^{27}Al MAS NMR of SBA-2 Al₁₁: (a) as-prepared, (b) calcined and (c) coked with but-1-ene (88 h).

The ^{29}Si MAS NMR spectra present equivalent behaviour for the Al21 and Al11 materials, figures 17 and 18 respectively. Both as-prepared solids show distinct resonances at -108, -99 and -91 ppm. These can be described²³ as Q^4 , Q^3 , and Q^2 signals, where $n = 4, 3$ or 2 indicates the degree of silicate polymerisation. This description, however, is complicated by the presence of next nearest neighbour aluminium atoms which cause a ^{29}Si nucleus to resonate at higher chemical shifts (*ca.* +5 ppm per adjacent Al).

In both spectra the Q^2 signal appears as the minor partner. In all probability this resonance can be assigned to two hydroxyl groups^x attached to silicon. The presence of framework aluminium as $\text{Si}(\text{OSi})_2(\text{OAl})(\text{OH})$ or $\text{Si}(\text{OSi})_2(\text{OAl})_2$ may also contribute to this peak intensity. Likewise the Q^3 signal is most likely to result from a single incompletely condensed silanol group, in conjunction with a (partial) $\text{Si}(\text{OSi})_3(\text{OAl})_1$ contribution. Upon calcination the ^{29}Si spectra simplify to a broad single resonance. Although the line shapes are indistinct, deconvolution^x of these spectra, table 3, suggests that the major components comprise Q^3 and Q^4 silicon resonances, in approximately equal proportions. Further framework silanol condensation (and a degree of dealumination) occurs during the calcination process; indicated by the loss of the Q^2 signal and a slight reduction in the Q^3/Q^4 ratio. This is corroborated by the reduction in the unit cell size (XRD) and the formation of extra-framework (5- and 6-co-ordinate) aluminium (^{27}Al MAS NMR). Finally, the extended heat treatment experienced per sample during catalysis appears to continue this trend. Although there is no change in either peak chemical shift, the -101 ppm shoulder is dramatically reduced following but-1-ene isomerisation. Additional framework condensation and increased dealumination can account for this. Consequently the Q^3/Q^4 ratio decreases significantly.

^x Incomplete hydrolysis is unlikely since no corresponding -OEt resonances appear in the as-prepared ^{13}C MAS NMR spectra.

^x With broad line shapes like these, the deconvoluted band shape cannot be guaranteed unique.

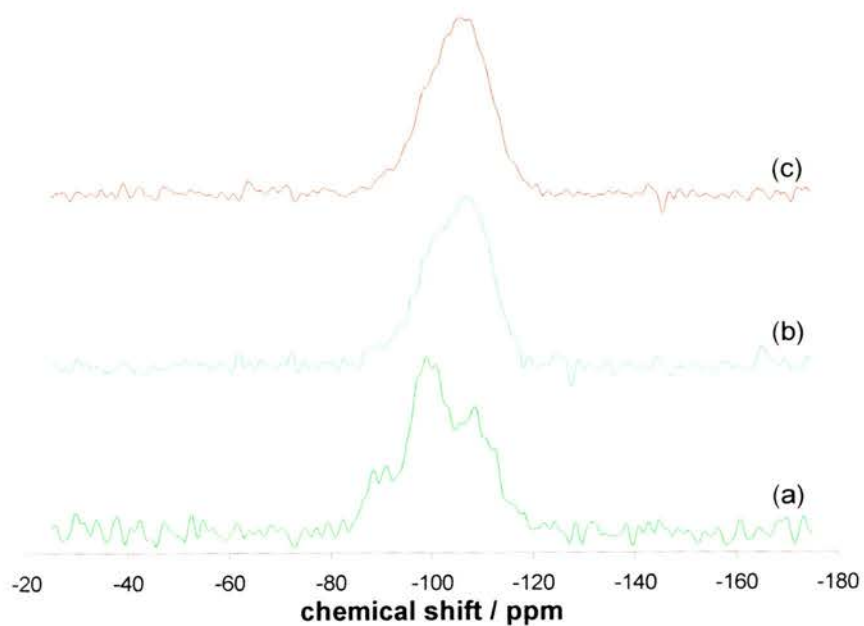


Figure 17: ^{29}Si DP MAS NMR of SBA-2 Al₂₁: (a) as-prepared, (b) calcined and (c) coked with but-1-ene (12 h).

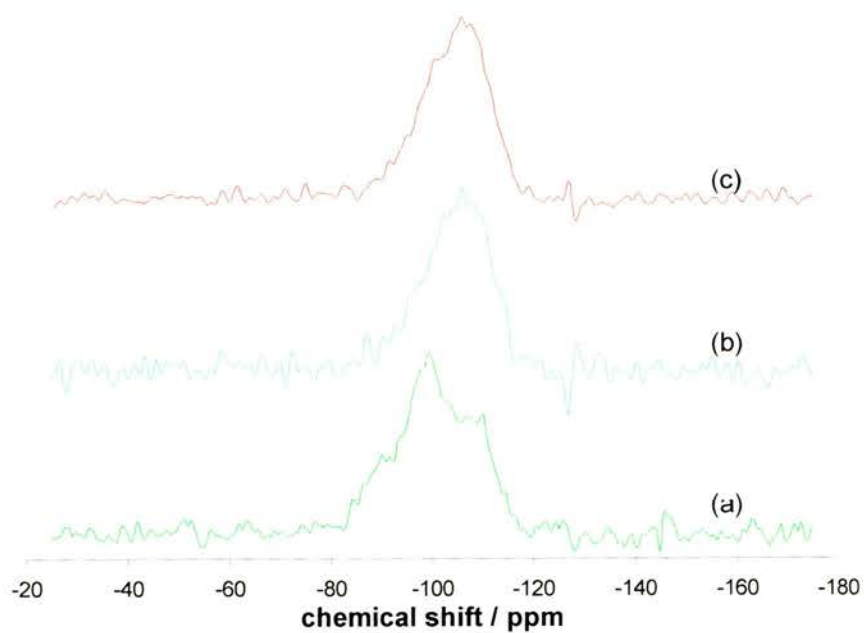


Figure 18: ^{29}Si DP MAS NMR of SBA-2 Al₁₁: (a) as-prepared, (b) calcined and (c) coked with but-1-ene (88 h).

	AI21				AI11			
	Q ²	Q ³	Q ⁴	Q ³ /Q ⁴	Q ²	Q ³	Q ⁴	Q ³ /Q ⁴
as-prepared	14.6	43.2	42.2	1.02	16.2	42.4	41.3	1.03
calcined	-	46.0	54.0	0.85	-	49.9	50.1	1.00
but-1-ene coked	-	23.1	76.9	0.30	-	29.5	70.5	0.42

Table 3: % peak shapes of the deconvoluted ²⁹Si DP MAS NMR spectra.

Following but-1-ene catalysis the coked solids gave ¹³C CP MAS NMR spectra displaying two distinct resonances, figure 19. The upfield peaks in the 20-40 ppm region indicate some aliphatic carbon is present, however they are dominated by the signal at $\delta(^{13}\text{C}) = 127$ ppm. This resonance, along with its intense sidebands,^{xii} suggest that the coke deposit is in a very condensed aromatic, or even graphitic, form.

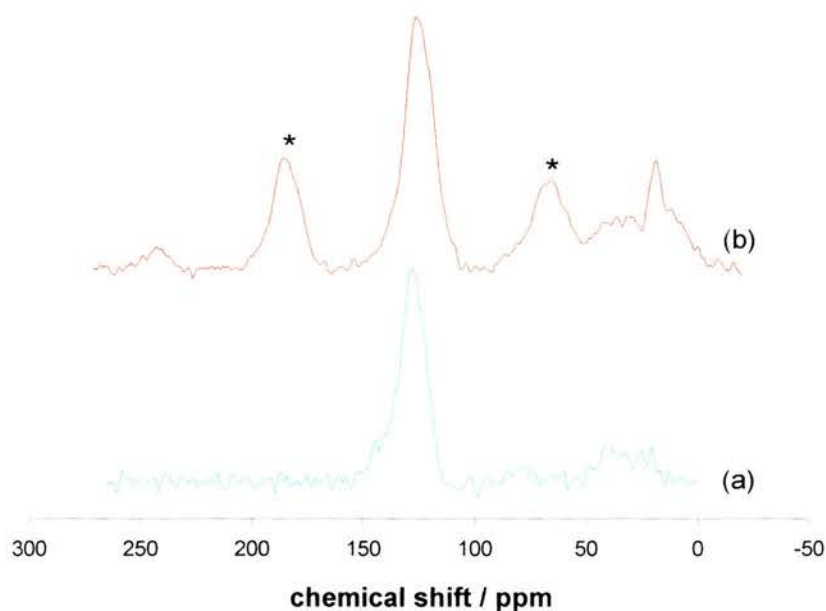


Figure 19: ¹³C CP MAS NMR of coked SBA-2 (a) AI21 and (b) AI11 (aromatic sidebands indicated *).

^{xii} The AI21 sample was able to be run as a TOSS (total suppression of sidebands) experiment, thereby eliminating the bands observed at 185 and 65 ppm. Also the coked samples contain only 12.47 wt% carbon (from CHN), thus to overcome the low intensities long acquisition times were required.

FTIR

The FTIR spectra of all the coked samples show no distinctive C-C or C-H stretching frequencies. That is not to say that there is no carbonaceous deposit present, since all the active catalytic solids turn black. It is due, however, to the inherently strong Si-O stretch at 1050 cm^{-1} , from the silicate framework, overshadowing all other vibrational frequencies.

Isobutane Cracking

The results of overall conversion for each solid^{xiii} are plotted in the Arrhenius format, figure 20. The linear relationships resulting from the $\ln(\text{rate})$ versus $1000/T$ plot indicate the apparent activation energy, E_a , associated with isobutane cracking. With the exception of H-Beta (20 kJmol^{-1}), the line gradients are all approximately the same (*ca.* 133 kJmol^{-1}), and suggest the rates for this cracking mechanism are similar in all materials. The total activity, however, varies considerably. The microporous materials: USY, H-Beta, H-ZSM-5 and MgAPO-36 are all known to possess high activity. This is evident in the elevated rate values, $\ln(\text{rate}) \approx 41.5$ at $450\text{ }^\circ\text{C}$; whereas the SBA-2 (Al ∞ -21-11) and MgAPO-5 experiments only achieve $\ln(\text{rate}) \approx 37.5$ at an equivalent temperature, thereby indicating their mild acid properties. Table 4 and figures 21 to 25 illustrate this, where the temperatures required to achieve similar conversions decrease dramatically from mild ($575\text{ }^\circ\text{C}$) to strong (*ca.* $420\text{ }^\circ\text{C}$) solid acids.

Also, as coking induces surface deactivation, the rate of conversion is affected. This can be observed during the isobutane cracking experiment on USY, where the subsequent Arrhenius plot kinks sharply at $450\text{ }^\circ\text{C}$ ($1000/K = 1.38$) resulting in a change of slope from -14.75×10^{-3} (active) to -2.290×10^{-3} (deactivating). Zeolite H-Beta, meanwhile, possesses levels of conversion well above 10%, at all sampling temperatures. This % conversion essentially distorts the observed cracking pattern and accounts for the shallow rate gradient. A comparison of this E_a with the rest is therefore meaningless since H-Beta possesses a far superior cracking activity.

^{xiii} H-ZSM-5, MgAPO-36 and MgAPO-5 data taken from ref. 6.

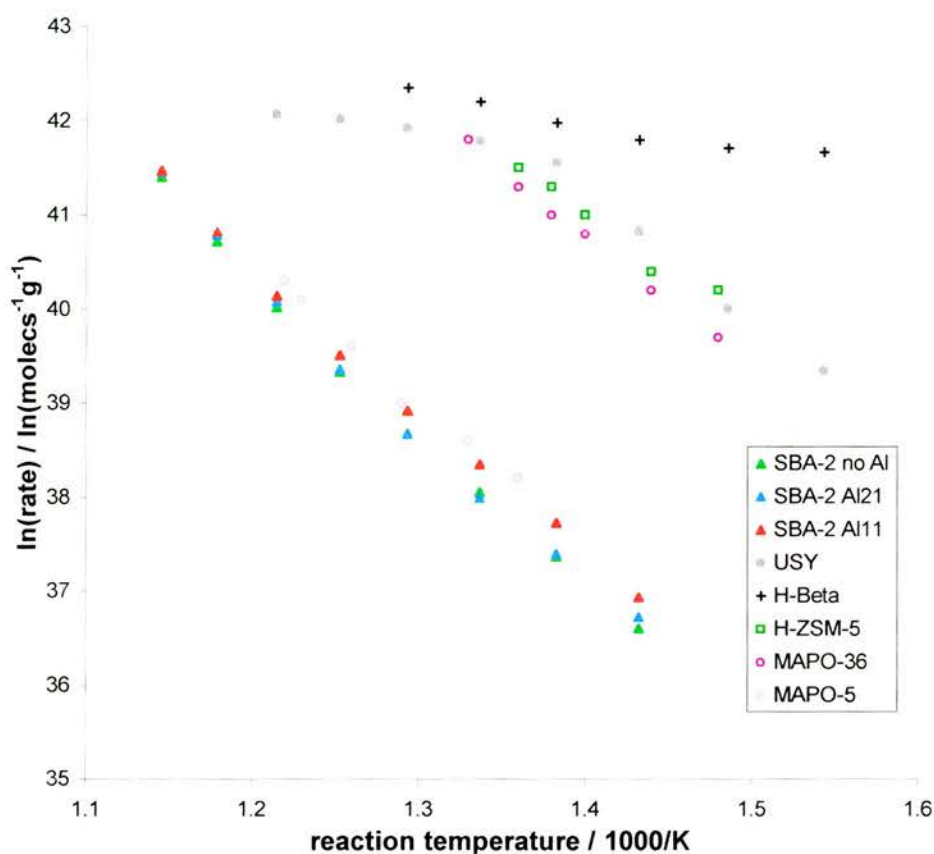


Figure 20: Arrhenius plots of rates of total isobutane conversion. Rates are given as molecules of isobutane converted per second per gram of catalyst with a WHSV of ca. 2.2 h^{-1} .

Conversion (wt %)	SBA-2			USY	H-Beta	MgAPO-5	H-ZSM-5	MgAPO-36
	Al ∞	Al21	Al11					
10	575	575	575	425	300	>550	440	450
5	550	550	550	400	<300	420	430	545

Data for MgAPO-5, H-ZSM-5 and MgAPO-36 taken from ref. 6.

Table 4: Comparative conversion temperatures ($^{\circ}\text{C}$) in the different materials studied.

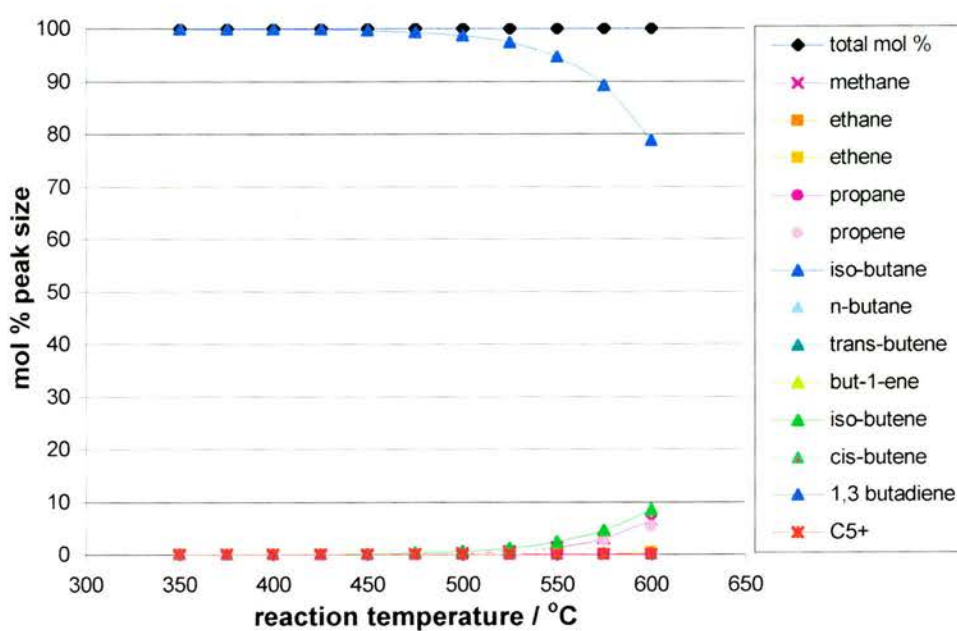


Figure 21: Isobutane conversion on SBA-2 Al ∞ .

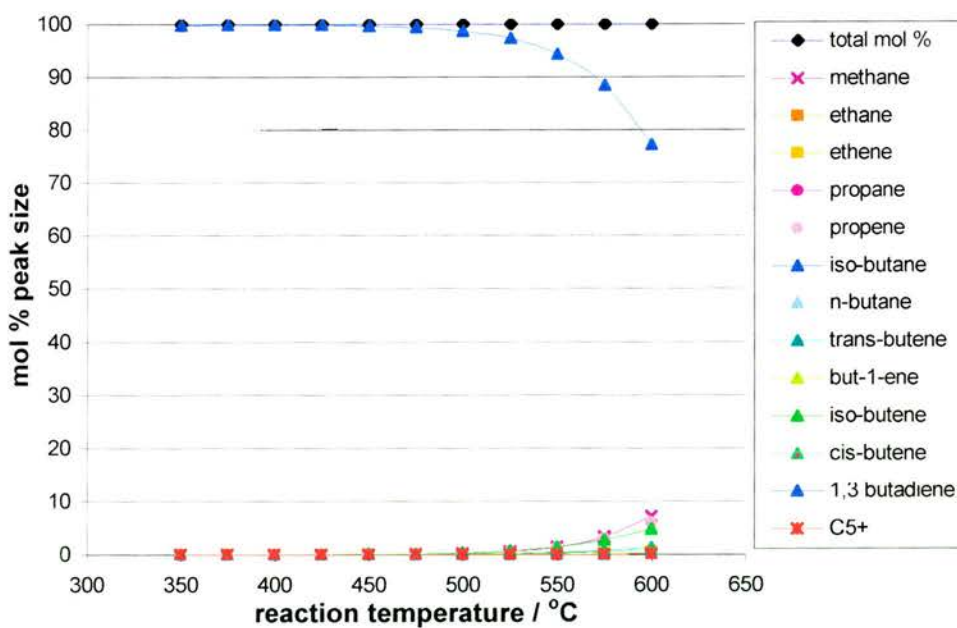


Figure 22: Isobutane conversion on SBA-2 Al $_{21}$.

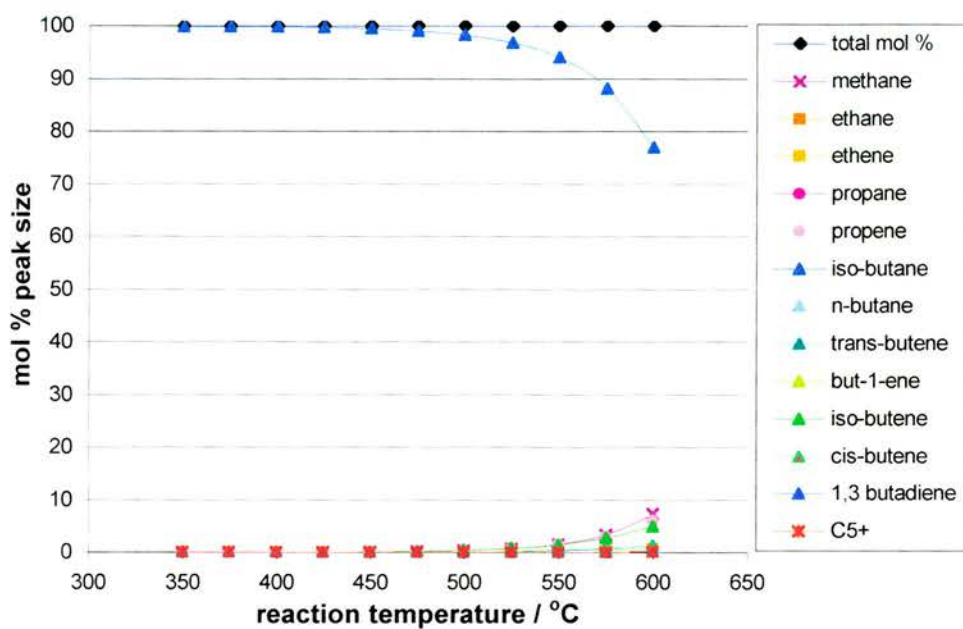


Figure 23: Isobutane conversion on SBA-2 Al11.

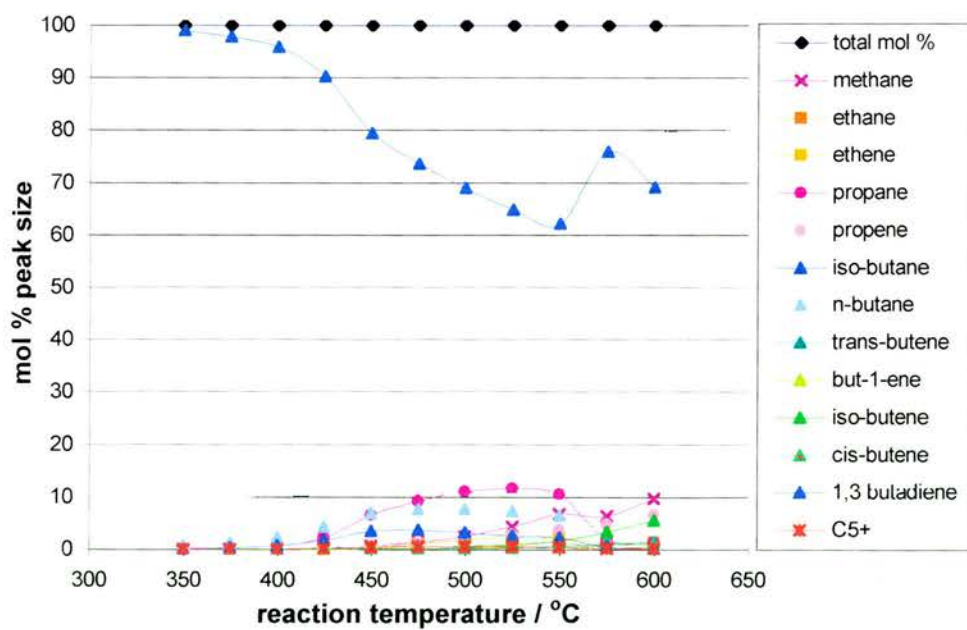


Figure 24: Isobutane conversion on USY.

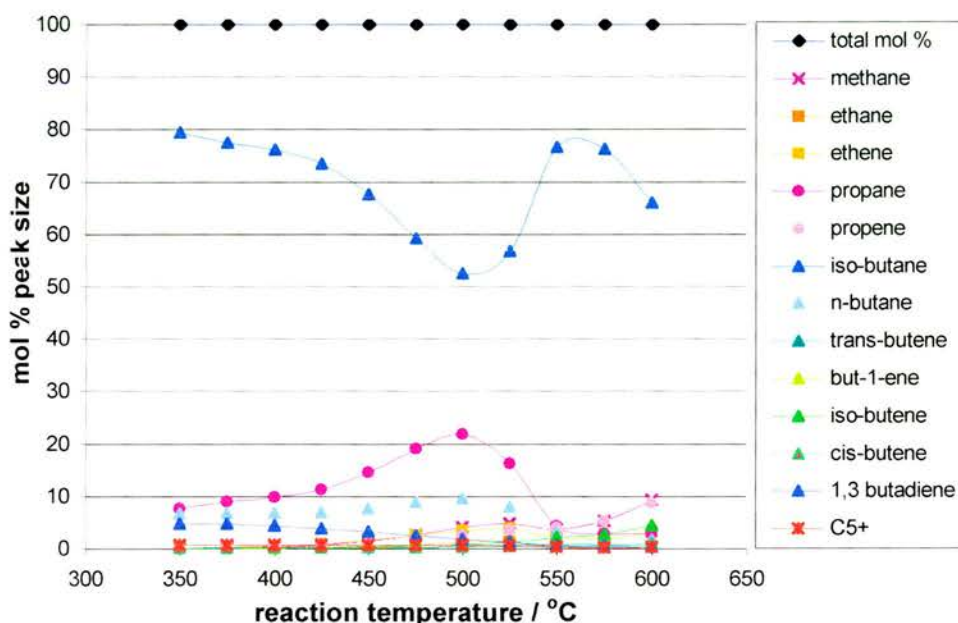


Figure 25: Isobutane conversion on H-Beta.

Isobutane selectivities can be assessed by a change in the alkane/alkene ($C_3/C_3^=$) ratio over temperature,^{xv} table 5. Thus the product selectivities of USY and H-Beta decrease rapidly with rising temperature. This can be rationalised by the decreasing importance of secondary mechanisms as the lifetime of adsorbed carbenium ions is reduced, thereby limiting the probability of subsequent reactions. This behaviour is typical of strong Brønsted acidity, however it can also be achieved by decreasing the contact time or % conversion to enable a shift of equation 1 to the right. The mesoporous materials, in contrast, demonstrate behaviour akin to that of mild acid sites, where the alkane/alkene ratio changes little with temperature. Primary mechanism products predominate at all temperatures, demonstrated by $C_3/C_3^= < 1$, and can be accounted for by the overall low % conversion of isobutane.

^{xv} As $T \uparrow$, % conversion \downarrow then $C_n/C_n^= \downarrow$ ($C_n \downarrow$, $C_n^= \uparrow$).

As $T \downarrow$, % conversion \uparrow then $C_n/C_n^= \uparrow$ ($C_n \uparrow$, $C_n^= \downarrow$).



Reaction T (°C)	SBA-2			USY	H-Beta
	Al _∞	Al21	Al11		
300	∞	∞	∞	4.21	123.92
325	∞	∞	∞	∞	100.62
350	∞	22.8	∞	16.13	53.37
375	∞	∞	∞	13.41	29.23
400	∞	∞	15.11	12.41	17.80
425	∞	5.88	3.73	11.42	12.41
450	1.07	1.08	0.68	9.74	10.22
475	0.36	0.40	0.27	7.48	9.53
500	0.17	0.18	0.15	5.64	8.43
525	0.09	0.10	0.09	4.06	4.46
550	0.05	0.06	0.06	2.72	1.10
575	0.03	0.05	0.05	0.42	0.54
600	0.03	0.04	0.04	0.21	0.35

Table 5: Propane/Propene product selectivities for the different materials studied.

Thus aluminium incorporation within SBA-2 results in a series of catalysts whose active sites are of insufficient strength for hydrocarbon (isobutane) cracking. Consequently direct comparison of these materials to microporous and other commercial solids is difficult. In spite of this some slight reaction occurred, indicating that weak acid sites exist (comparable to MAPO-5). To overcome the poor catalytic activity and effect of thermal cracking at higher temperatures there are several avenues of investigation possible. An increase in the amount of sample present in the reactor tube, or an increase in the isobutane reactant flow rate would raise the % conversion observed. In addition a direct comparison of the influence of framework porosity upon reactivity requires that the Si/Al ratio in all solids to be equal. Short of resynthesising appropriate solids comparable activities can only be 'guess-timated'. Meanwhile, accurate determination of acid site strength would require FTIR-TPD (temperature programmed desorption of bases): a technique unavailable in St Andrews. The ideal solid acid catalyst, therefore, has a sufficiently high number of acid sites for fast, efficient cracking, yet does not deactivate quickly.

But-1-ene Isomerisation

In view of the fact that the aluminium-containing SBA-2 materials are weak solid acid catalysts, it was decided to test their activity towards the isomerisation of but-1-ene. This reaction is commercially important yet is known to be less demanding of acid strength. The level of acidity must be sufficient to induce skeletal isomerisation, as opposed to simply double bond isomerisation.

The control reactions of but-1-ene (only), fumed silica and pure silicate SBA-2^{xv} (figures 26, 27 and 28) show that almost no isomerisation takes place below 300 °C. Above this temperature, however, double bond migration occurs: increasing in step with the rising temperature. At all temperatures studied these materials effected less than 0.7 % conversion to isobutene. Thus aluminium-induced acidity is required before significant but-1-ene reaction may occur. Finally, a further analysis was carried out at 600 °C during the but-1-ene (only) control experiment. The resultant product distribution again shows no isomerisation, yet significant 'other' reactions have taken place. Closer inspection of these non-isomerisation products (figure 29) shows them to be predominantly small cracked hydrocarbons: 17.8 mol % methane, 14.0 mol % propene, 8.1 mol% ethene and 2.6 mol % ethane. Presumably these result from either (i) direct unimolecular cracking or (ii) bimolecular dimerisation-cracking pathways, analogous to isobutane cracking. The C₄ alkane products can be attributed to the hydrogenation of butene.

^{xv} The significant double bond isomerisation observed for SBA-2 Al_∞ can only be attributed to impurities within the reaction tube.

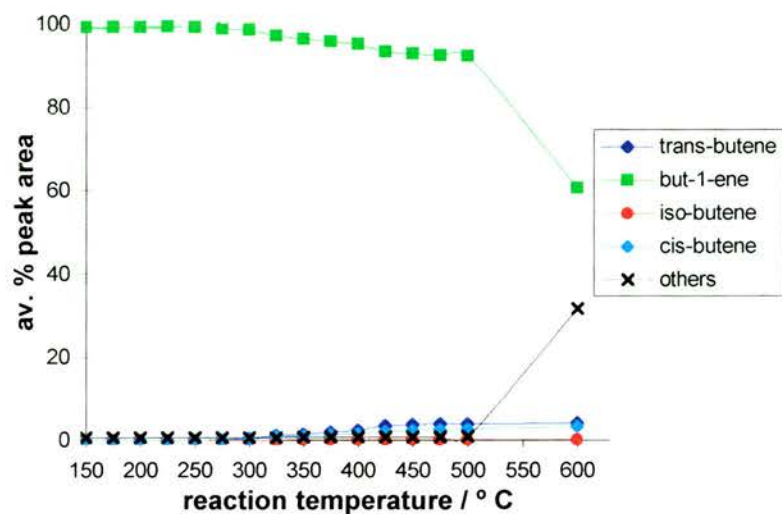


Figure 26: But-1-ene isomerisation products in the absence of any catalyst.

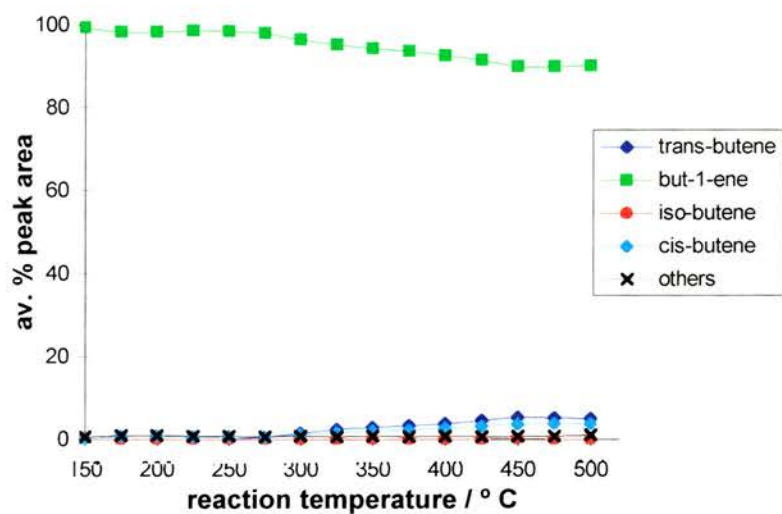


Figure 27: But-1-ene isomerisation products over fumed silica.

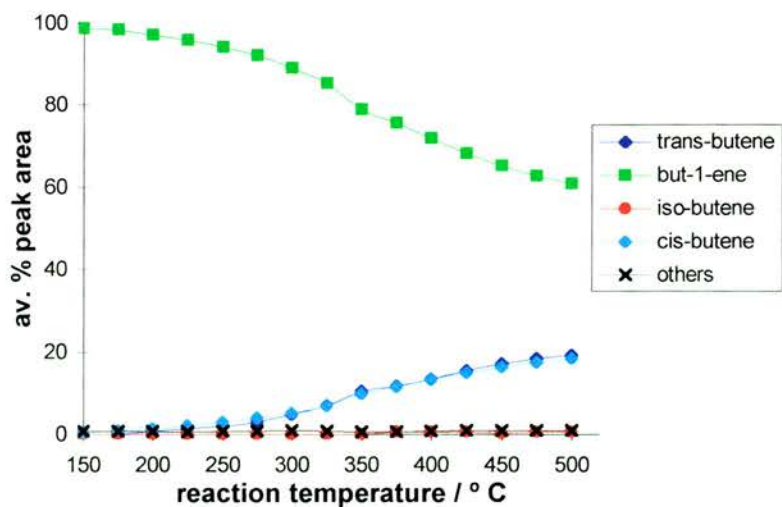


Figure 28: But-1-ene isomerisation products over pure silicate SBA-2.

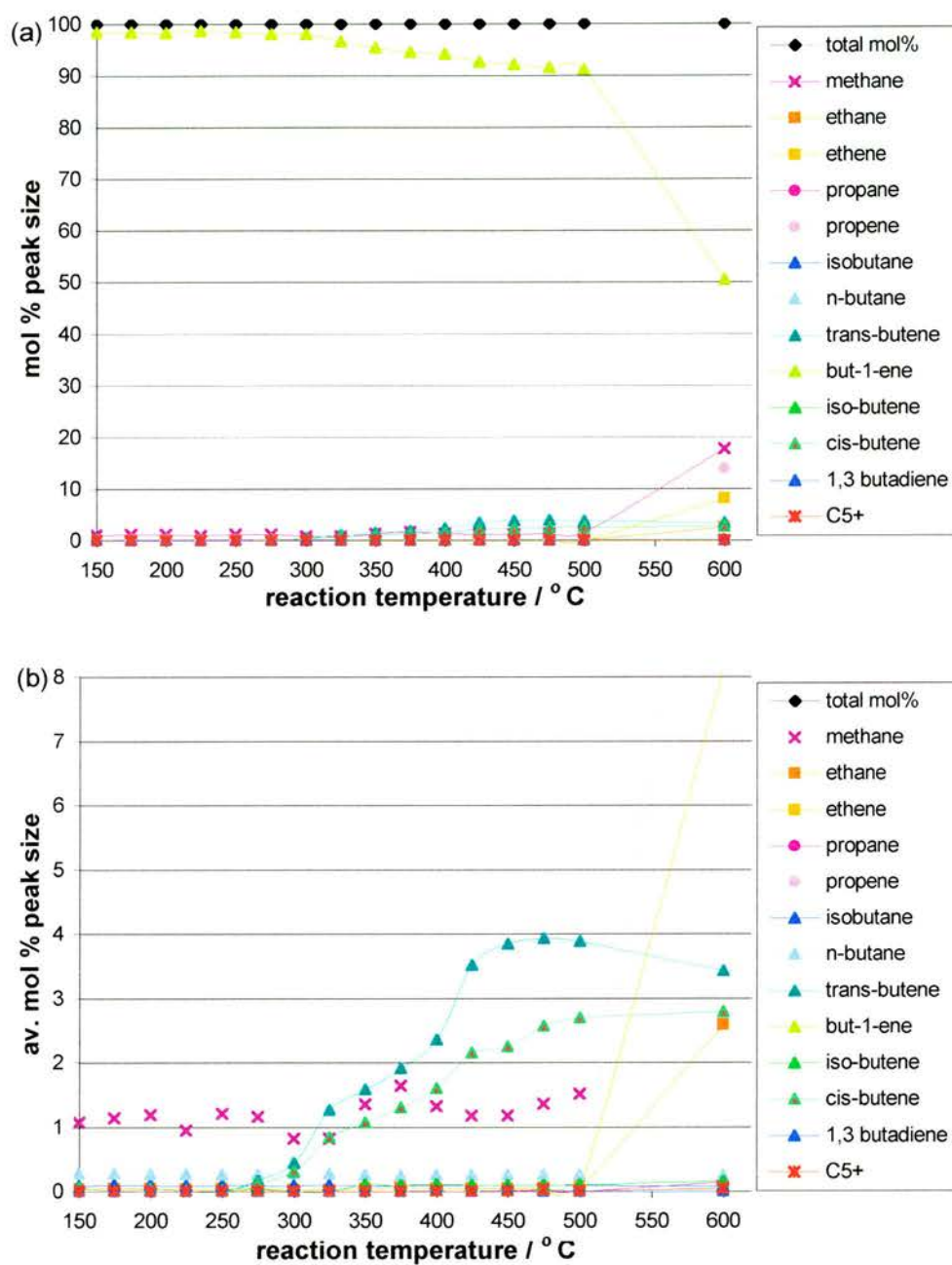


Figure 29: Thermally activated but-1-ene isomerisation products (but-1-ene only control experiment) showing: (a) total conversion and (b) expanded at low mol % yields.

The effect of Si/Al ratio within the SBA-2 framework is depicted graphically in figures 28, 30 and 32. Simple inspection shows that the presence of aluminium results in double bond isomerisation across all the temperatures studied. Taking SBA-2 Al21, we see that below *ca.* 350 °C the only significant products formed are *cis* and *trans* isomers. Above this temperature, however, significant skeletal isomerisation occurs, increasing as the temperature rises. This isobutene production accounts for the loss in double bond migration products, since the total but-1-ene conversion remains approximately constant. Even so, at all temperatures the % isobutene production is below the thermodynamically limiting equilibrium values²⁴ of 51.5 % at 350 °C, 47.7 % at 400 °C and 45.0 % at 440 °C. Meanwhile it is apparent from the mol% product graphs, figure 31, that the reaction within this SBA-2 Al21 solid follows a monomolecular pathway. The noticeable lack of dimerisation-cracking products (1.54 mol% propene and 0.96 mol% C₅+ at 500 °C) indicate this. Finally, the coked material recovered from the SBA-2 Al21 catalysis run was calcined *ex-situ* in oxygen. But-1-ene isomerisation was then repeated on this sample. The resulting product graphs are superimposable, thereby indicating that these solids are easily regenerated and fully recyclable.

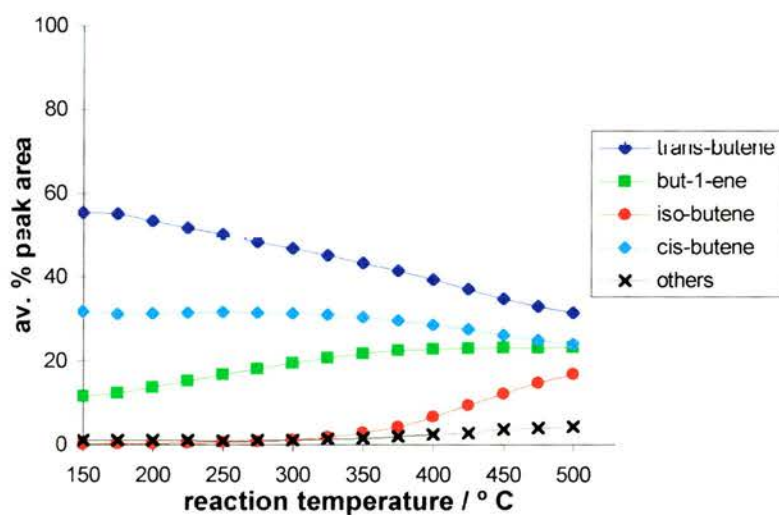


Figure 30: But-1-ene isomerisation products over SBA-2 Al21.

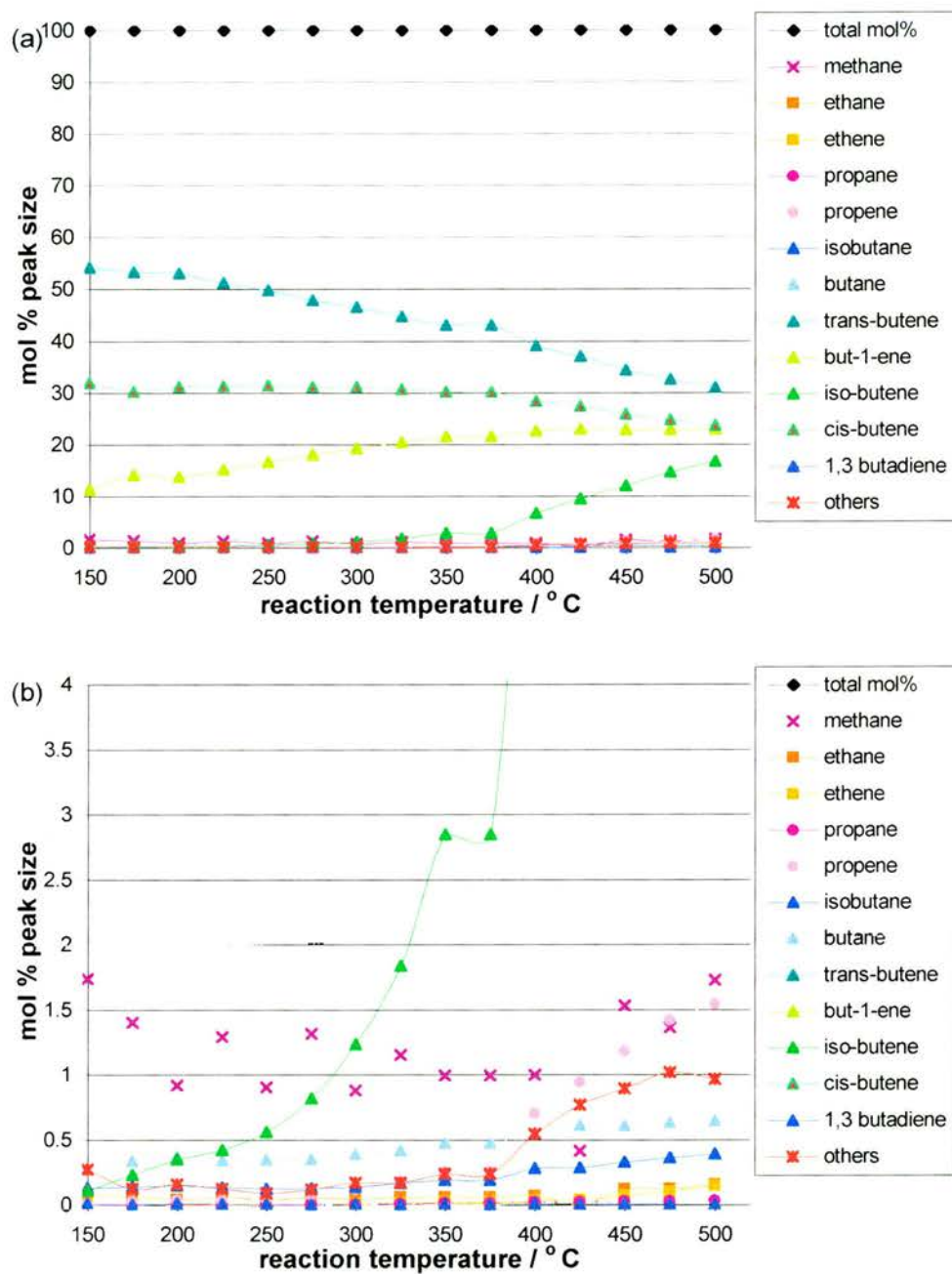


Figure 31: But-1-ene isomerisation products over Al₂O₃ showing (a) total conversion and (b) an expansion at low mol% yields.

These findings are similar to those obtained with SBA-2 Al11.^{xm} The increased aluminium concentration, however, results in equivalent conversions being achieved at lower temperatures. Furthermore the non-isomerisation species, identified in figure 33, appear to result from a combination of hydrogenation (2.80 mol% isobutane, 1.54 mol% n-butane), and cracking processes (7.17 mol% propene, 4.66 mol% C₅+, and 3.29 mol% methane). They indicate, therefore, that SBA-2 aluminosilicates are able to catalyse the competing (i) monomolecular cracking or (ii) bimolecular oligomerisation-cracking reactions at elevated temperatures. In other words the increased aluminium loading appears to correspond to more active sites within the solid (hence more cracking products) as opposed to stronger acidity per site, since there is a *ca.* 5 fold increase in both the propene and C₅+ mol% values.

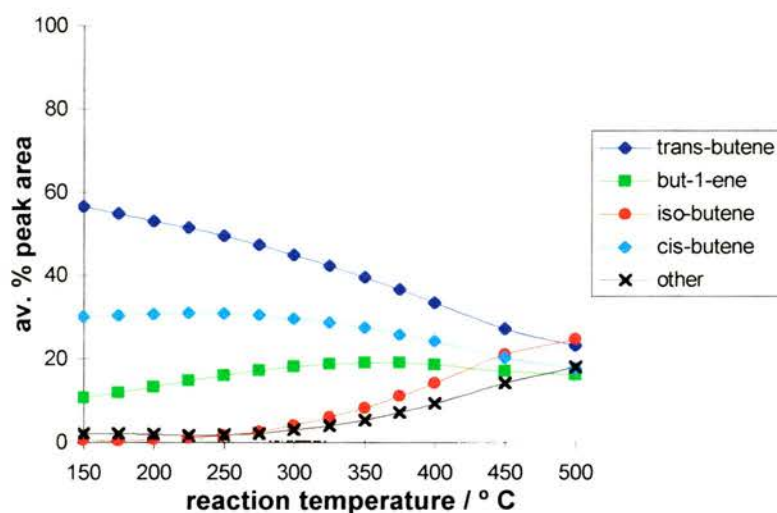


Figure 32: But-1-ene isomerisation products over SBA-2 Al11.

^{xm} This particular solid was actually made with Al₂(SO₄)₃.16H₂O and with an experimental Si/Al ratio of 25/1. Based on the ICP-AES results it is conceivable that the final material possesses a ratio of *ca.* 11/1 hence its use here.

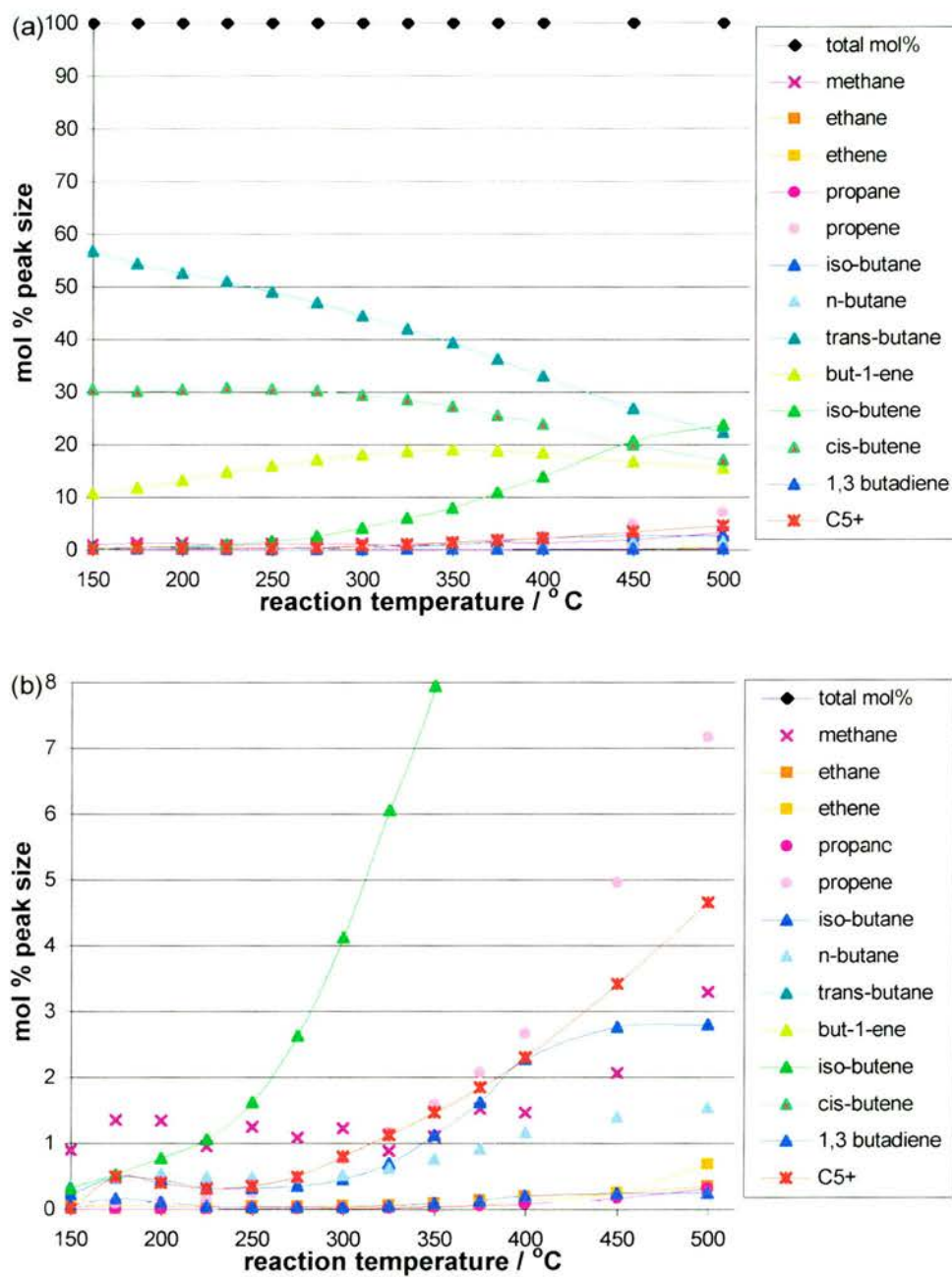


Figure 33: But-1-ene isomerisation products over SBA-2 Al11 showing (a) total conversion and (b) expanded at low mol % yields.

For comparison, the product distribution graphs for H-Beta and USY, two strong acid microporous catalysts, are shown in figures 34 and 35. In both these solids double bond isomerisation is similar to the acidic SBA-2 materials, particularly at low temperatures (figures 30 and 32). As the temperature increases, however, the % conversion to each of the *cis* and *trans* isomers diminishes. This can be attributed to the effect of coking, whereby the active sites are gradually covered and the microporous frameworks become blocked. Thus, as observed, a steady decrease in the amount of butene converted is apparent. H-Beta effects significant (8%) ‘other’ production at 275 °C, which is predominantly of a hydrogenated nature (C₄ alkanes). Meanwhile its isobutene production never reaches 3%. USY, however, creates a different picture. Here, as the reaction temperature rises, both isobutane and ‘other’ products increase in parallel. By 450 °C they account for 6.87 and 8.36 mol% but-1-ene conversion products respectively. For isobutene production this is approximately half that of SBA-2 Al21 (12.07 mol%) while the ‘others’ is about double the 4.78 mol% Al21 value. Thus overall, the strong acid sites in both H-Beta and USY contribute to more than just skeletal isomerisation, namely the secondary reactions of hydrocarbon hydrogenation, cracking and associated deactivation.

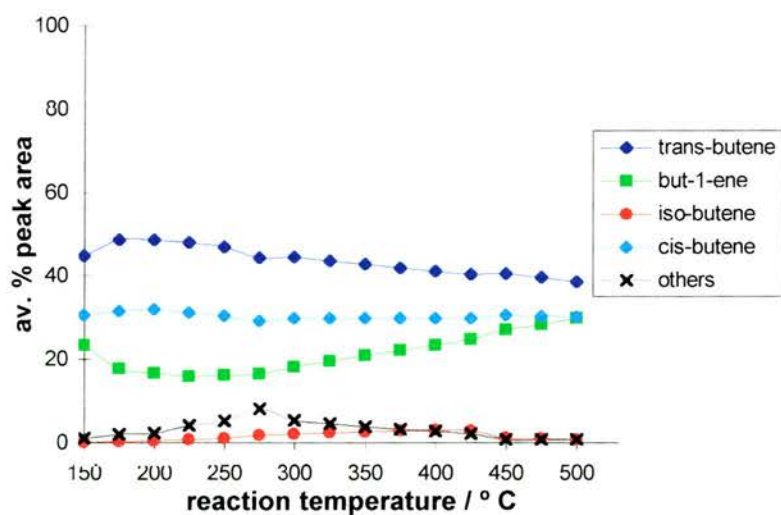


Figure 34: But-1-ene isomerisation products over H-Beta.

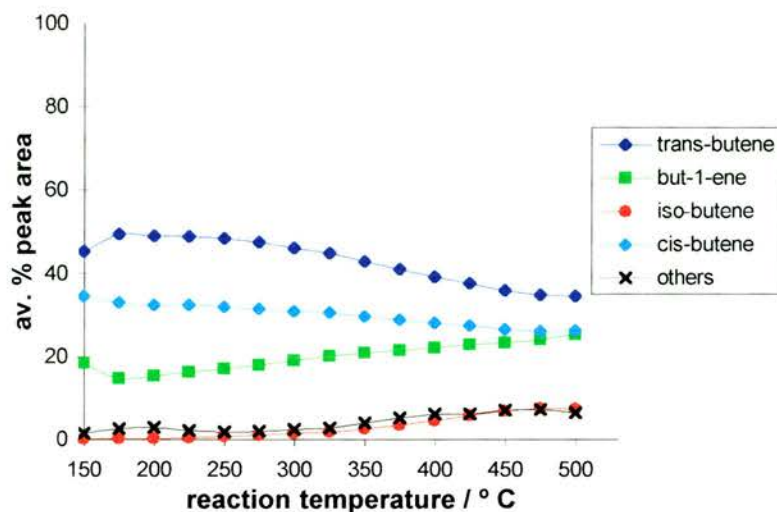


Figure 35: But-1-ene isomerisation products over USY.

The specifics of deactivation, over time, have been evaluated using SBA-2 Al11. By comparing the results obtained with USY, an assessment of framework size: mesoporous *versus* microporous can be made. The but-1-ene isomerisation product distribution at 400 °C was collected for each solid, since they facilitate approximately similar but-1-ene conversions at this temperature. Figures 36 and 37 present these results for SBA-2 Al11 over 88 h and USY over 28.5 h. Being particularly concerned with the isobutene production, the starting material for MTBE synthesis, two comparative plots are shown in figure 38. Analysis of the % conversion graph indicates that SBA-2 Al11 is slow to deactivate. This is confirmed by the normalised plot, where the isobutene production by USY declines more rapidly; achieving half its conversion after 13.5 h, while the ‘half-life’ of SBA-2 Al11 is >88 h. Overall, therefore, it appears that the larger void volume in a mesoporous framework has a positive effect upon the catalyst lifetime, extending it by *ca.* 6 times. It is worth noting, however, that USY possesses a Si/Al ratio of $\approx 3/1$. Thus the enhanced speed of deactivation can be attributed to (i) its microporosity, (ii) the stronger acid sites and (iii) the higher concentration of acid sites (compared to SBA-2 Al11). Elemental analysis, though, shows that the carbon deposits at the end of each deactivation experiment are similar: 14.21 wt%C in USY and 12.47 wt%C in SBA-2 Al11.

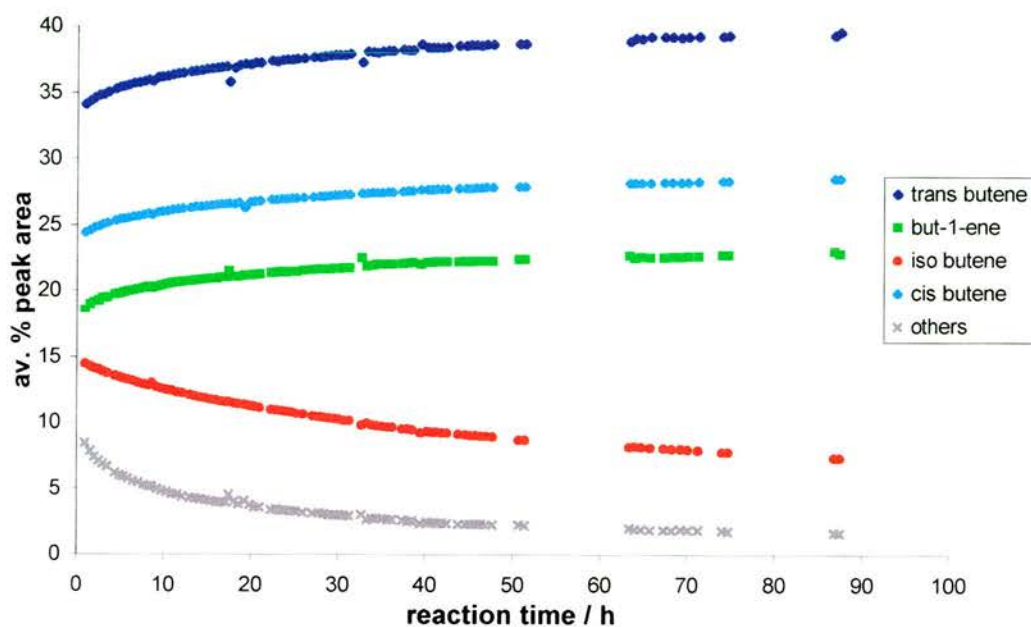


Figure 36: But-1-ene isomerisation products over SBA-2 Al11 at 400 °C, related to time on stream.

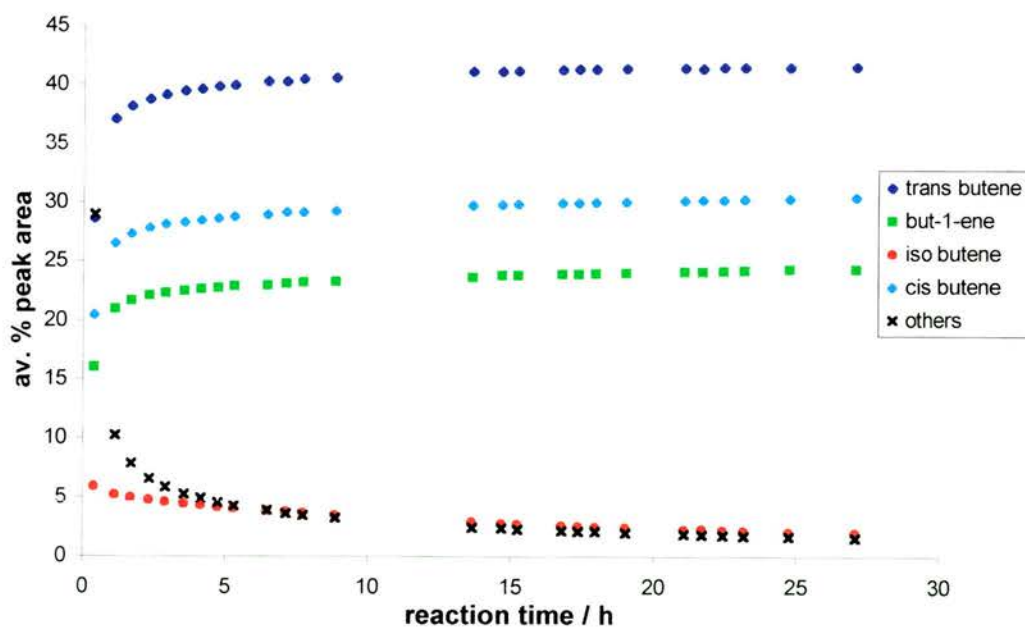


Figure 37: But-1-ene isomerisation products over USY at 400 °C, related to time on stream.

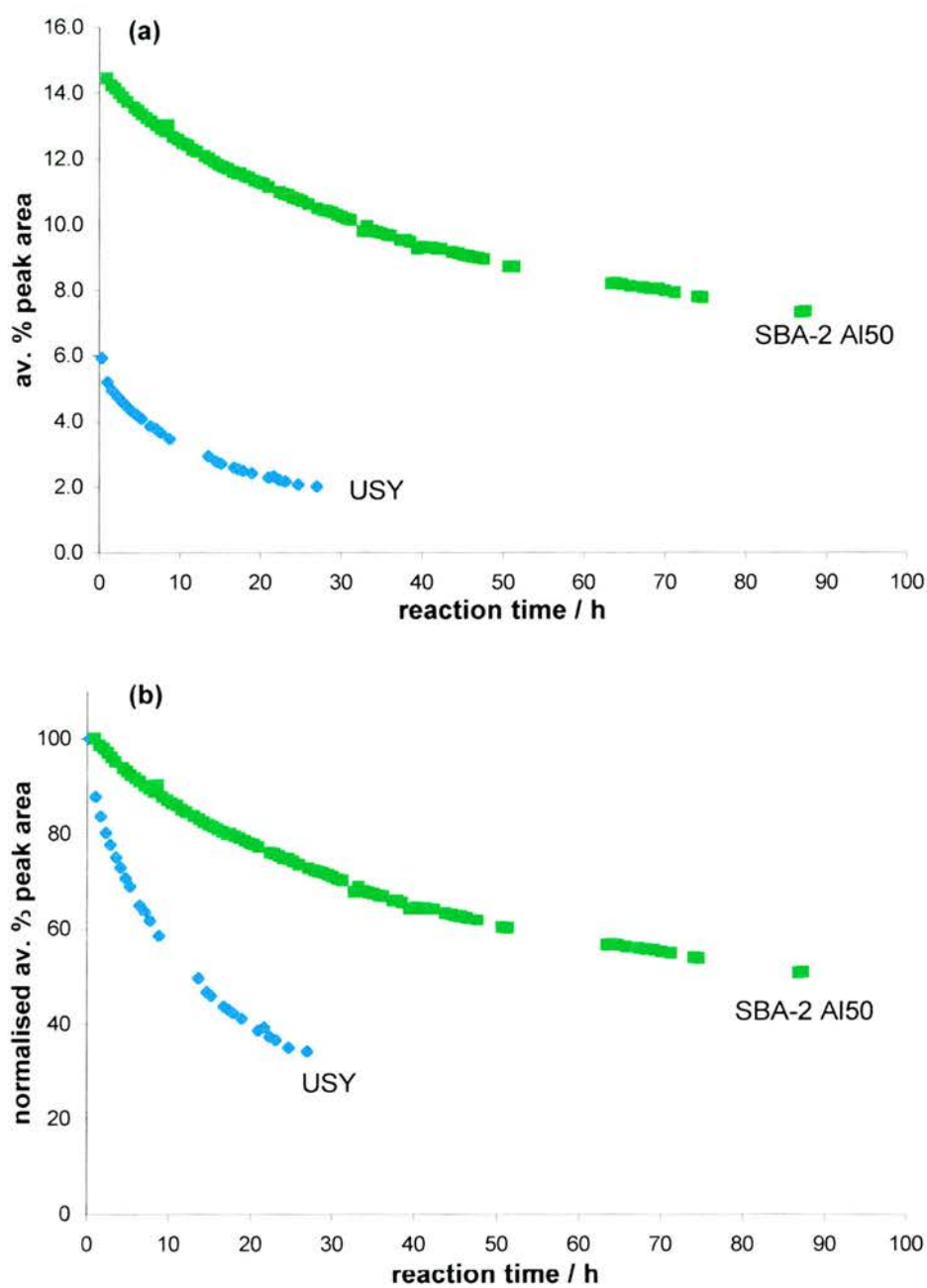


Figure 38: A comparative plot of isobutene production over SBA-2 Al11 and USY: (a) % conversion and (b) normalised % conversion (to SBA-2 Al11 initial value).

N₂ Adsorption Isotherms

Two SBA-2 Al₂₁ samples were exposed to but-1-ene for 5 hours at 400 °C and 500 °C respectively. The resultant isotherms are plotted, figure 39, in comparison to their parent SBA-2 material. Following coking both samples continue to exhibit type IV isotherms, which indicate that mesoporosity remains. Simple inspection shows, however, that the total volume available for nitrogen adsorption has decreased by *ca.* 25 %. Furthermore there is a corresponding reduction of the specific surface area calculated^{25,26} using the BET equation, table 6. Combined these suggest that coking is influenced less by the reaction temperature and more by the time on stream.

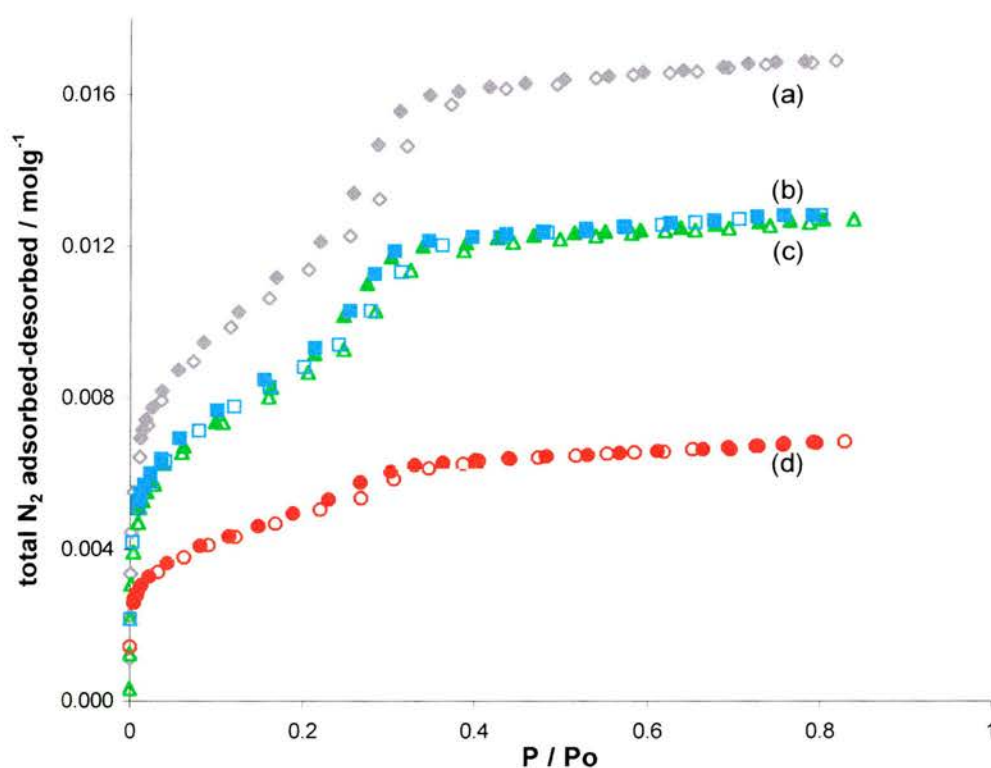


Figure 39. Nitrogen adsorption isotherm multiplot for SBA-2-Al materials: (a) Al₂₁ calcined, (b) Al₂₁ coked 400 °C 5 h, (c) Al₂₁ coked 500 °C 5 h and (d) Al₁₁ coked 400 °C 88 h. Adsorption = open symbols, desorption = filled symbols.

	volume at P/Po = 0.75 (cm ³ g ⁻¹)	BET surface area (m ² g ⁻¹)	av. pore diameter (Å)	Elemental analysis		
				%C	%H	%N
Al21 calcined	368	893 ± 3	28.20	-	-	-
Al21 coked 400 °C 5 h	281	697 ± 5	26.77	5.09	-	-
Al21 coked 500 °C 5 h	286	713 ± 2	28.02	5.45	0.36	-
Al11 coked 400 °C 88 h	152	392 ± 2	26.90 ^a	12.47	0.47	-

a: the average pore diameter obtained for this isotherm is unrealistic because the capillary condensation phase, upon which the Kelvin equation relies, is so poorly defined.

Table 6: Nitrogen adsorption values for SBA-2-Al materials.

The deactivated SBA-2 Al11 isotherm (but-1-ene, 400 °C, 88h) is also presented in figure 39. Again there is a dramatic loss of total available volume (table 6): approximately half that of Al21 coked at 400 °C over 5 hours. This can be reconciled both by the higher aluminium concentration (i.e. twice as many catalytically active sites) and the extended reaction time, thereby doubling the wt% carbon deposit. Likewise this additional coking proportionally reduces the BET surface area.

To complete this study of carbonaceous SBA-2-Al materials the normalised^{xvii} adsorption isotherms for these solids are shown in figure 40. All the SBA-2 Al21 based samples follow similar shaped curves. Compared to the parent material, however, the coked samples are (again) subtly different. Throughout there is a shift to lower P/Po values, for the same number of moles of nitrogen adsorbed. This suggests that at both 400 °C and 500 °C coke deposits build up to reduce the pore volume and perhaps subtly alter the character of that pore volume. As the internal surface is gradually covered, therefore, the partial pressure required for equivalent adsorption volumes, in the multilayer region, is lowered. In comparison, the SBA-2 Al11 material, deactivated at 400 °C for 88 hours, presents a much shallower normalised isotherm. It can be considered as part way towards exhibiting a microporous type I isotherm. Thus the number of moles adsorbed in the capillary condensation process is greatly reduced. As before, these observations can be explained by the (a) extended time period used during catalysis and (b) the increased aluminium loading within the framework.

^{xvii} The original isotherm data has been scaled towards total adsorption (100 %) in each case. A multiplot then relates variable adsorption as a function of pressure for each solid.

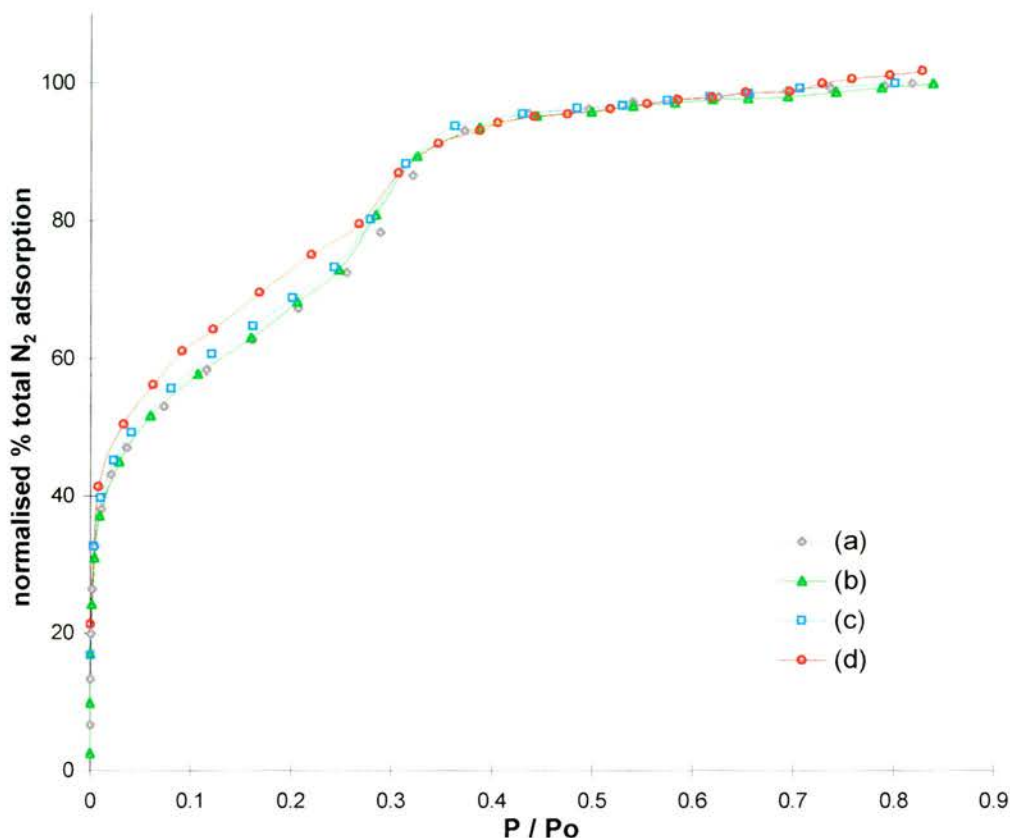


Figure 40: Normalised N_2 adsorption multiplot for SBA-2-Al materials: (a) Al21 calcined, (b) Al21 coked 400 °C 5 h, (c) Al21 coked 500 °C 5 h, (d) Al11 coked 400 °C 88 h. Normalised on calcined SBA-2 Al21. Adsorption data only.

Nitrogen adsorption isotherms were also collected for the microporous zeolite USY, figure 41. Both samples demonstrate behaviour similar to a type I isotherm, however they deviate from a rectilinear plot as the pressure increases. This can be explained by the partial breakdown in framework structure that occurs during the dealumination process, resulting in slight variation of the total cavity volume available for nitrogen condensation. In comparison, the isotherm collected following but-1-ene deactivation (400 °C for 28.5 h) shows that the pores have become largely filled with coke. The 14.21 wt% carbonaceous deposit^{xviii} has reduced the total volume available for nitrogen adsorption by approximately two thirds: from 196.4 cm^3g^{-1} to 68.4 cm^3g^{-1} at $P/P_0 = 0.75$. It is this pore blockage effect, and hence loss of activity, inherent to active microporous solids, that it is hoped can be overcome using a mesoporous regime.

^{xviii} From elemental analysis.

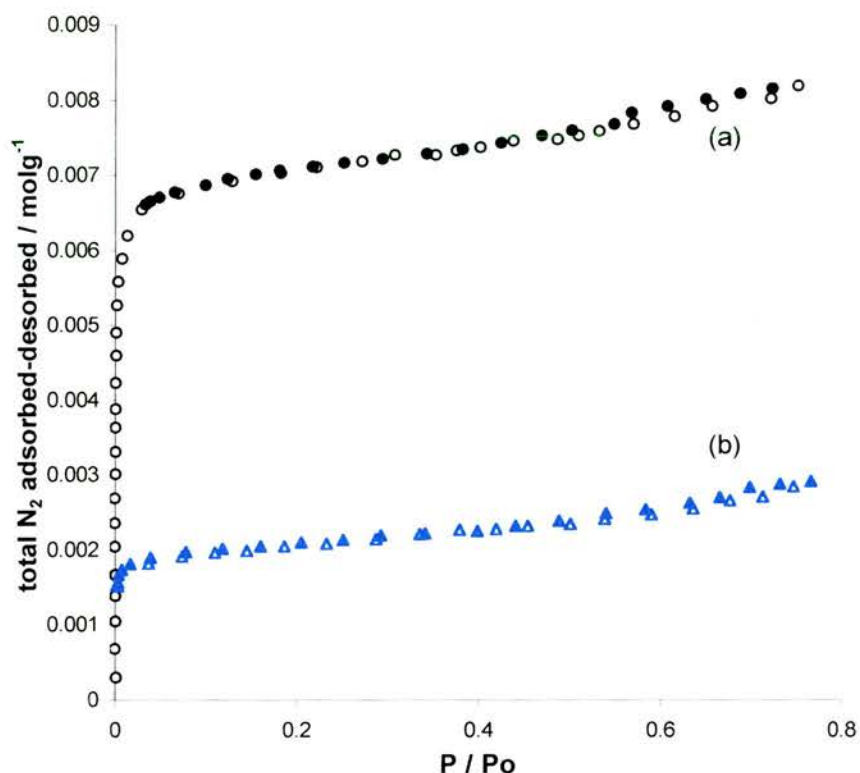


Figure 41: Nitrogen adsorption isotherms for USY: (a) calcined and (b) coked with but-1-ene at 400 °C for 28.5 hours. Adsorption = open symbols, desorption = filled symbols.

Zeolite H-Beta, similarly, exhibits this coking phenomenon, figure 42. Following 12 hours of use as an isobutane cracking catalyst a type II isotherm^{xx} results, indicating that almost all the available internal volume has been lost. This virtually non-porous material now adsorbs only $23.7 \text{ cm}^3 \text{ g}^{-1}$ at $P/P_0 = 0.75$ as compared to $198.5 \text{ cm}^3 \text{ g}^{-1}$ initially. In addition coking accounts^{xx} for 13.09 wt% of the solid acid and suggests that the carbonaceous deposits form by filling the interconnecting channel structure, thereby rendering internal surfaces redundant for (i) catalysis and (ii) nitrogen adsorption.

^{xx} The significant scatter observed in this isotherm is a result of the overall very low volumes adsorbed.

^{xx} From elemental analysis; an as-prepared sample contains 16.08 wt % carbon.

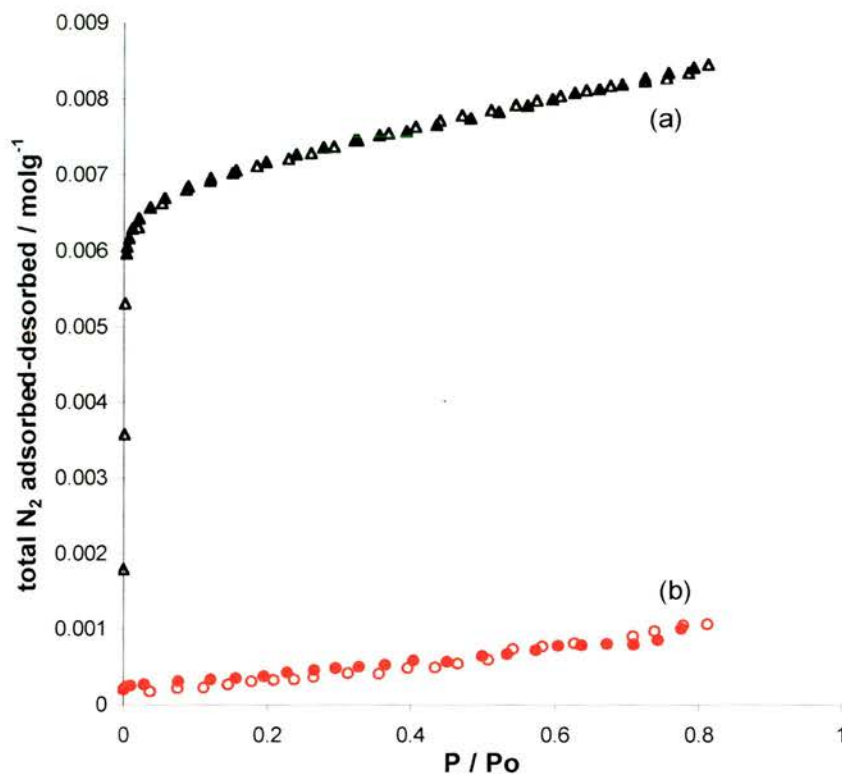


Figure 42: Nitrogen adsorption isotherms for H-Beta: (a) calcined and (b) coked with isobutane over 12 hours. Adsorption = open symbols, desorption = filled symbols.

Extraction

To test the resilience of the coked deposit to chemical attack one sample was subjected to Soxhlet extraction. Thus the SBA-2 Al21 material coked at 500 °C for 5 hours in but-1-ene was extracted with (i) toluene for 7 hours and (ii) ethanol for 6 hours. As alluded to earlier, no change in the resulting XRD pattern was observed, nor did the FTIR spectral appearances alter. Elemental analysis reiterates this, table 7, with none of the expected *loss* of wt% carbon following extraction. Moreover there appears to be a weight *gain*, suggesting that either the extraction medium becomes bound to the surface (polar solvents being most susceptible) or (unlikely) the solid was not completely free of solvent before CHN analysis. The idea of chemical bonding to the coked deposits bodes well for potential applications as carbon molecular sieves. Alternatively, such acidic silicate materials could be thought of as possessing a carbonaceous protective layer. This appears to hinder the loss of structural order due to solvation, which is

known to occur with some MCM silicate materials. The coked solids could, therefore, also be employed to catalyse acidic reactions in the liquid phase.

extraction used	wt% C	wt% H	wt% N
none	5.45	0.36	-
toluene 7 h	5.57	0.44	-
ethanol 6 h	7.10	0.56	-

Table 7: Elemental analysis on SBA-2 Al₂₁ coked with but-1-ene at 500 °C for 5 hours.

Summary

Synthesising SBA-2 aluminosilicates is possible; increasing the aluminium loading, however, decreases the observed structural order. Once made though, these materials, like their 3D large pore microporous counterparts USY and H-Beta, are thermally stable throughout catalysis and the recycling process. Furthermore, within the as-prepared SBA-2-Al samples the aluminium, irrespective of source, appears solely in a tetrahedral environment. Upon calcination, however, ^{27}Al MAS NMR shows this to alter, yielding a variety of 4-, 5- and 6-fold coordination environments. ^{29}Si MAS NMR, meanwhile, indicates that further framework condensation occurs, during calcination, confirming the observed X-ray diffraction peak shifts.

The isobutane % conversion and cracking products from these SBA-2-Al materials indicate that overall they exhibit only mild acidity (similar to MAPO-5). The SBA-2 solids, though, are effective but-1-ene isomerisation catalysts and catalyse this reaction at comparable rates to USY. Indeed the mesopore structure appears to diminish the effect of coke build up, extending the catalyst lifetime for this reaction by *ca.* 6 times, before regeneration is required. This is further demonstrated by the retention of a Type IV nitrogen adsorption isotherm following deactivation, albeit at a total adsorption volume within the calcined USY regime. By way of comparison, the coked microporous solids for USY and H-Beta adhere to Type I (although 65 % total volume has been lost) and Type II (non-porous) isotherms respectively.

Finally extraction of this heavily saturated, almost graphitic, carbon residue (^{13}C MAS NMR), with toluene or ethanol, is ineffective. Moreover, the coked solid is stable (XRD) to such a treatment. Indeed a carbon molecular sieve style polar solvent-coke binding interaction is indicated by elemental analysis.

References

- ¹ BC Gates, *Catalytic Chemistry*, 1992, J Wiley and Sons Inc., New York, USA.
- ² JM Thomas, WJ Thomas, *Principles and Practice of Heterogeneous Catalysis*, 1997, VCH, Weinheim, Germany.
- ³ RB King (Ed.), *Encyclopedia of Inorganic Chemistry*, 1994, **8**(T-Z), John Wiley and Sons, Chichester, UK.
- ⁴ J Rodriguez-Mirasol, T Cordero, LR Radovic, JJ Rodriguez, *Chem. Mater.*, 1998, **10**(2), 550.
- ⁵ GB M^cVicker, GM Kramer, JJ Ziemiak, *J. Catal.*, 1983, **83**(2), 286.
- ⁶ PA Wright, C Sayag, F Rey, DW Lewis, JD Gale, S Natarajan, JM Thomas, *J. Chem. Soc. Faraday Trans.*, 1995, **91**(19), 3537.
- ⁷ R Shigeishi, A Garforth, I Harris, J Dwyer, *J. Catal.*, 1991, **130**(2), 423.
- ⁸ EA Lombardo, WK Hall, *J. Catal.*, 1988, **112**(2), 565.
- ⁹ A Corma, PJ Miguel, AV Orchillés, *J. Catal.*, 1994, **145**(1), 171.
- ¹⁰ S Natarajan, PA Wright, JM Thomas, *J. Chem. Soc. Chem. Commun.*, 1993, 1861.
- ¹¹ MA Asensi, A Corma, A Martínez, *J. Catal.*, 1996, **158**(2), 561.
- ¹² J Čejka, B Wichterlová, P Sarv, *App. Catal. A: General*, 1999, **179**(1-2), 217.
- ¹³ MT Janicke, CC Landry, SC Christiansen, D Kumar, GD Stucky, *J. Am. Chem. Soc.*, 1998, **120**(28), 6940.
- ¹⁴ C-Y Chen, H-X Li, ME Davis, *Microporous Materials*, 1993, **2**, 17.
- ¹⁵ R Ryoo, CH Ko, RF Howe, *Chem. Mater.*, 1997, **9**(7), 1607.
- ¹⁶ C-F Cheng, J Klinowski, *J. Chem. Soc. Faraday Trans.*, 1996, **92**(2), 289.
- ¹⁷ R Schmidt, H Junggreen, M Stöcker, *J. Chem. Soc. Chem. Commun.*, 1996, 875.
- ¹⁸ AA Romero, MD Alba, J Klinowski, *J. Phys. Chem. B*, 1998, **102**(1), 123.
- ¹⁹ A Corma, V Fornés, MT Navarro, J Pérez-Pariente, *J. Catal.*, 1994, **148**(2), 569.
- ²⁰ AK Cheetham, P Day, *Solid State Chemistry Techniques*, 1988, OUP, Oxford, UK.
- ²¹ BM De Witte, PJ Grobet, JB Uytterhoeven, *J. Phys. Chem.*, 1995, **99**(18), 6961.
- ²² E Lippmaa, A Samoson, M Mägi, *J. Am. Chem. Soc.*, 1986, **108**(8), 1730.
- ²³ E Lippmaa, M Mägi, A Samoson, M Tarmak, G Engelhardt, *J. Am. Chem. Soc.*, 1981, **103**(17), 4992.
- ²⁴ J Houžvička, O Diefenbach, V Ponec, *J. Catal.*, 1996, **164**(2), 288.
- ²⁵ AW Adamson, *Physical Chemistry of Surfaces*, 1982, 4th Ed., John Wiley and Sons, New York, USA.

²⁶ JA Moulijn, PWNM van Leeuwen, RA van Santen (Eds.), *Catalysis: An Integrated Approach to Homogeneous, Heterogeneous and Industrial Catalysis*, 1993, Elsevier, Amsterdam, The Netherlands.

Transition Metal Catalysis

General Background

Catalysts¹ can be broadly divided into three areas: heterogeneous, homogeneous and enzymes. Each has its benefits and drawbacks, table 1. Due to a combination of environmental and economic pressures, though, current research aims to combine the advantages of each. The principle intention of this chapter, therefore, is to report attempts at the ‘heterogenization’ of homogeneous catalysts. In turn these hybrid systems would facilitate the easy recovery of the active catalyst. Several approaches have been taken to achieve this:

- *biphasic systems*: e.g. where the catalyst is in an aqueous or fluorous phase and the substrate/products in the organic phase. Supercritical fluids are also of interest.^{1,2,3}
- *dendrimers*: attachment of organometallic functionalities to the dendritic surface yields a nanoscale catalyst that can be recovered by ultrafiltration.⁴
- *molten salts*: e.g. $R_4P^+X^-$ are liquid at the reaction temperature but solidify at room temperature, which allows easy recovery of the solid.⁵
- *supported systems*: where the homogeneous complex is attached to a substrate e.g. inorganic silicate or polymer matrix.^{6,7,8}

heterogeneous	+ good thermal & mechanical stability • easy separation • long service life • variable activity
	– high T, P required • diffusion problems • active site determination difficult • (may deactivate)
homogeneous	+ mild conditions required • efficient • reproducible • high activity & selectivity • easy to study active site
	– separation & recycling difficult • expensive metals (& ligands) needed
enzymes	+ benign conditions required • highly specific • natural • chiral
	– slow rate of reaction

Table 1: Catalyst advantages and disadvantages.

It is the fourth route that this work has followed. Indeed the term ‘ship-in-a-bottle’ was coined⁹ by Herron *et al* to describe the physical trapping of a metal complex within a zeolitic framework. It is hoped that this hybrid system can maintain the high activity and selectivity of the homogeneous catalyst, whilst offering facile separation and recycling (by centrifugation or filtration). Furthermore encapsulation of chiral ligands (or use of a chiral framework) would open up the field of asymmetric synthesis. Such zeolitic host-guest structures, however, are constrained by diffusional limitations and may be subject to metal leaching during reaction. For these reasons the covalent

¹ Berzelius coined the associated term ‘catalysis’ in 1835.

attachment of homogeneous complexes within mesoporous materials is worthy of study.

This chapter is broadly divided into three areas: those pertaining to the catalytic affects of titanium, manganese and rhodium within the mesoporous silicate SBA-2. Furthermore the results are compared to analogous zeolitic reactions (both undertaken and literature based). Framework incorporated titanium and encapsulated manganese complexes were used towards epoxidation reactions on C₆ alkenes: hex-1-ene, cyclohexene and cyclohexeneone. Meanwhile a rhodium complex was analysed in its use as a silicate-supported hydroformylation catalyst.

These areas of work and findings for each will be discussed in turn. In general, though, the catalytic activities were disappointing.

Ti Background

A notable application of homogenous catalysis is in the synthesis of epoxides by oxygen transfer from a hydroperoxide to an alkene. This generalised process, figure 1, creates an important and versatile intermediate for both the bulk and fine chemical industries.



Figure 1: The generalised epoxidation reaction.

A number of transition metal based complexes are known^{10,11,12} to catalyse the homogenous reaction. These variously employ Mo^{VI}, W^{VI}, V^V or Ti^{IV} where, for each, a cyclic peroxo complex is thought to be the active species. In particular titanium, as Ti(OⁱPr)₄ in the presence of L(+)-diethyl tartrate, has become known as the ‘Sharpless epoxidation’ catalyst. This selectively converts allyl alcohols into chiral products, suitable for subsequent use in natural product syntheses.

It is an amorphous heterogeneous TiO₂/SiO₂ catalyst, however, that Shell employ to convert propene into 1,2 epoxypropane. Meanwhile Notari *et al* working for Enichem, the Italian chemical manufacturer, reported¹³ the first titanium containing molecular sieve in 1981. Their solid catalyst has become known as TS-1 (titanium-silicalite-1), where isomorphous substitution of titanium for silicon produces a material with the MFIⁱⁱ (ZSM-5) topology. This can then catalyse the epoxidation of many small alkenes; Enichem employ TS-1 to produce catechol and hydroquinone from phenol. It is thought that the random distribution of site isolated Ti^{IV} (d⁰) centres prevents the formation of μ-oxo bridged oligomers, and thus deactivation, characteristic of the homogeneous reaction. Moreover the solid catalyst is not prone to metal leaching and can be easily recovered (filtered) and reactivated (calcined) when necessary. The framework dimensions of TS-1, though, prevent the epoxidation of alkenes which possess kinetic dimensions larger than 5.5 Å, the pore diameter of this structure. To this end, titanium incorporation within larger pore materials is an active research area.

ⁱⁱ The International Zeolite Commission gives three letter codes to all framework structures based on tetrahedra. This aids identification of similar architectures when the chemical compositions differ: here TS-1 *versus* ZSM-5.

In particular titanium-containing zeolite β ,¹⁴ MCM-41¹⁵ and MCM-48¹⁶ have been successfully synthesised and tested towards the epoxidation of bulky alkenes. These frameworks exhibit 3-dimensional microporosity (7.5 Å pore diameter), 1- and 3-dimensional mesoporosity (20 – 100 Å pore diameter) respectively. Furthermore research has shown^{17,18} that the surface hydrophobicity/hydrophilicity can be tailored by the presence of aluminium, silanol species or surface methylation. This in turn, influences the liquid phase solvation of the solid catalyst, and may even generate further (acid catalysed) side reactions. It is hoped, therefore, that the systems can be optimised for a particular alkene, taking into account diffusion limitations of the substrate/products within the framework.

The above direct synthesis approach to heterogenization of the active Ti epoxidation catalyst is complimented by a post-synthesis grafting approach. This technique, developed by Maschmeyer *et al*¹⁹ in 1995, takes titanocene as the metal source and obtains a tripodally attached Ti centre on the internal surfaces of MCM-41, figure 2. Like other titanium-containing catalysts, the material turns yellow when a hydroperoxide complex forms. Uncertainty, though, exists as to the precise nature of the active species. Various spectroscopic, EXAFS and computational evidence^{20,21,22,23} points to a partially bound pentacyclic complex, figure 3. Indeed Maschmeyer *et al* suggest¹⁹ that their enhanced activity is due to the Ti centre sitting proud of the silicate surface, making it more accessible than the framework-imbedded analogue.

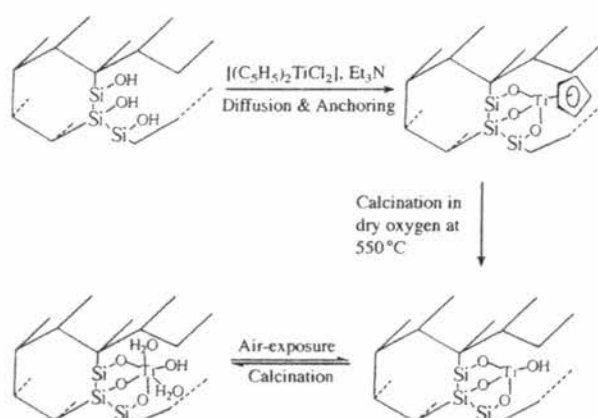


Figure 2: Titanocene anchoring in MCM-41.¹⁹

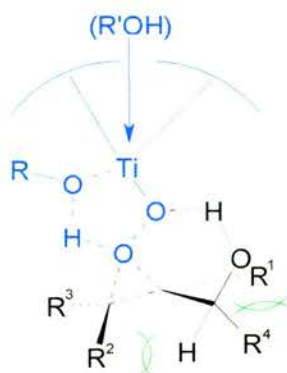


Figure 3: The proposed titanium active species in silicate molecular sieves.²⁰

Finally, hydrogen peroxide can be considered as the oxidant of choice for these heterogenized systems. With its high (47 %) active oxygen²⁴ content, the relative expense of this strong oxidant can be offset by its environmentally friendly decomposition products (H_2O , O_2). Furthermore the epoxidation mechanism appears²⁵ to operate as a radical-free reaction under the mild conditions (reflux) required by this Ti redox centre.

Ti Experimental

Instrumentation

Gas Chromatography was performed on a CE Instruments 8000 TOP Series GC, accompanied by a Fisons Instruments DP 700 Data Processor (integrator). The catalysis products were eluted with a helium mobile phase on a HP-5 cross-linked 5 % phenyl methyl siloxane (30 m × 0.32 mm × 0.25 μm) capillary column. A temperature programme of 50 °C to 190 °C at 10 °Cmin⁻¹ was employed. The product peaks were identified by their retention times. Thus the expected products were run as solvent-dissolved standards to aid in this process.

GC-MS analyses were performed on an Hewlett Packard HP 6890 Series GC system accompanied by a Hewlett Packard 5973 Mass Selective Detector and controlled by a Hewlett Packard Vectra XA computer. The catalysis products were eluted with a helium carrier flow (2.0 cm³min⁻¹) on a HP5-MS cross-linked 5 % Phenylmethylsilicone capillary column (inner diameter 0.25 mm, film thickness 0.25 μm, length 30 m, phase ratio 250). The oven temperature was held at 40 °C for 5 min, before being ramped at 20 °Cmin⁻¹ up to 200 °C. The product peaks were identified by their correlation to the MS spectral library within the computer.

UV-Vis spectra were recorded on a Cintra 20 UV-Vis spectrometer and collected using GBC Spectral software. The SBA-2 Ti50 samples were analysed as a suspension in nujol, supported on filter paper within a quartz cuvette.

SBA-2-Ti Synthesis

The titanium-containing SBA-2 solids were obtained *via* a direct synthesis route. In particular all the starting materials were alkali metal-free, in order to avoid the

precipitation of titanates from solution (e.g. sodium titanate). Thus the base as tetramethylammonium hydroxide (TMAOH), was added to distilled water with stirring. Subsequently the diquatery ammonium surfactant (C16-3-1 or C18-3-1) was dissolved in this solution. Following complete homogenisation (*ca.* 30 min) the silicate, as tetraethylorthosilicate (TEOS) and titanium source, as titanium ethoxide ($\text{Ti}(\text{OEt})_4$ as a 20 %Ti solution in ethanol), were added. Thus the final mixture possessed a molar composition of 0.05 surfactant : 0.5 TMAOH : 1 TEOS : 150 H_2O : 0.02 $\text{Ti}(\text{OEt})_4$. The reaction was stirred at room temperature and maintained at pH 11-11.5 throughout. After 2 hours the colourless solid was recovered by filtration, washed repeatedly with distilled water and then dried in air at ambient temperature overnight. The surfactant molecules were removed by calcination at 550 °C, first in N_2 (1 h) and then O_2 (6 h) to form the mesoporous titanosilicate. These solids are designated SBA-2 Ti50 where the Si/Ti ratio in the initial synthesis mixture is 50/1.

Catalysis

A typical catalytic reaction is as follows. The calcined SBA-2 Ti50 solid (84 mg) was weighed into a RB flask to which the solvent (5 ml; methanol, acetonitrile or acetone) was added, followed by the alkene (5 mmol; cyclohexene or hex-1-ene). Finally a 30 wt% aqueous solution of H_2O_2 (0.567 ml, 5 mmol) was added, and the mixture set up to reflux, with stirring, for 24 hours. After reaction the suspension was centrifuged and the liquid phase analysed by gas chromatography. As a series of control experiments these reactions were also performed with pure silicate SBA-2 materials acting as the 'catalyst'.

Ti Analysis

Framework Incorporation

X-ray diffraction indicates that the as-prepared and calcined SBA-2 Ti50 solids were all well ordered. FTIR, meanwhile, showed that both the as-prepared and calcined materials possessed a stretch at 960 cm^{-1} , attributed to Si-O-Ti framework bonding in TS-1. A peak at this wavenumber, however, also appears in the titanium-free SBA-2 materials. This assignment, therefore, cannot be taken as characteristic of titanium incorporation within the SBA-2 mesoporous framework.

The UV-Vis spectra, meanwhile, indicate that titanium is present in the calcined solids. Typically an absorption maximum at *ca.* 200-212 nm can be attributed to a ligand to metal charge transfer process^{21,22} in isolated TiO_4 or HOTiO_3 units, equation 1. The observed spectra, though, develop from such an absorption maximum into a broad asymmetric feature in the 250-350 nm range, figure 4. This would be consistent with the existence of extra-framework, oligomeric Ti^{IV} species. The formation of such particles may occur because titanium ethoxide hydrolyses (and precipitates from solution) at a faster rate than TEOS. These competing rates, however, were not optimised in the synthesis of titanium-containing SBA-2.

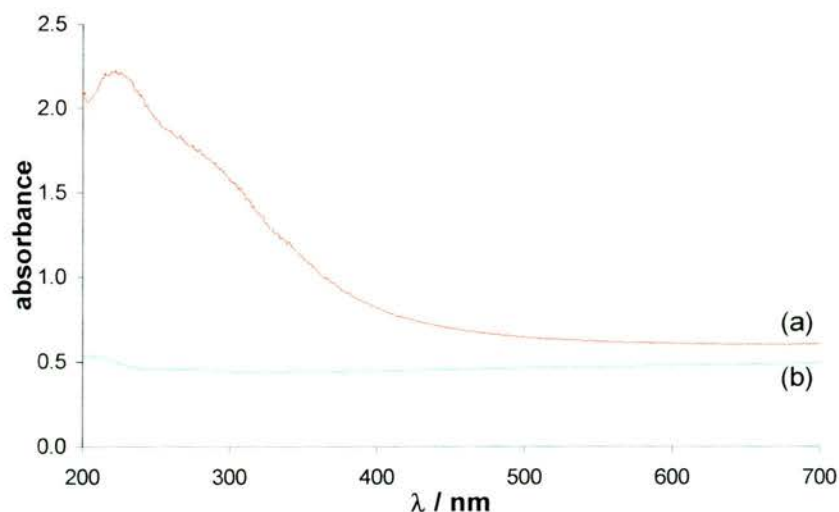


Figure 4: UV-Vis spectra of calcined SBA-2 synthesised (a) with and (b) without Ti50.

Incorporation *via* the titanocene grafting route was also attempted by Dr Martin Attfield *et al* at the Royal Institution. These scientists pioneered¹⁹ this approach, and therefore have the knowledge and expertise for successful Ti attachment. In this case, though, the reaction was unsuccessful. Presumably the relatively narrow pore diameter (c.f. MCM-41) or 2-dimensionality of the SBA-2 framework precludes diffusion of such a precursor onto the internal surfaces.

Catalysis

Having synthesised and calcined some titanium-containing SBA-2 solids, their catalytic potential was tested towards the epoxidation of cyclohexene and hex-1-ene in each of the three analysis solvents: methanol, acetonitrile or acetone. These results were compared to those of their pure silica analogues.

Perhaps reassuringly the SBA-2 control solids remained white throughout reaction. Meanwhile all the titanium-containing materials turned yellow in the presence of H₂O₂. This observation suggests that a pentacyclic titanium-peroxide species has formed within these materials. Analysis of the reaction products, however, was not straightforward.

Despite using a double reflux condenser, significant evaporation was observed over the course of the experiments. This substrate and solvent ‘disappearance’ can be explained by their low (and similar) boiling points, table 2. In particular, volume loss over 24 hours was prevalent in the cyclohexene-acetonitrile, hex-1-ene-methanol and hex-1-ene-acetonitrile reactions. As a result, the observed GC peaks are weighted in favour of the high boiling point oxygenated products, i.e. substrate conversion. In addition, often the eluted peaks did not correspond to the retention times for GC standards of the expected (literature reported) products: cyclohexeneoxide, cyclohexanediol, 2-cyclohexeneone, 2-cyclohexene-ol, etc.. Thus a GC-MS analysisⁱⁱⁱ was performed

ⁱⁱⁱ The actual injected sample was diluted 10 times in methanol in order to protect the instrument. This methanol solvent peak elutes after 1.1 min and is automatically removed from the resultant chromatogram.

upon the cyclohexene-SBA-2 Ti50-acetonitrile reaction products in an attempt to identify these ‘unknowns’, figure 5. Although the peak areas were not obtained, a qualitative analysis shows that only low cyclohexene conversion was achieved. The observed peaks at 2.4, 6.1, 6.7/6.9 and 7.6/7.7 min correlate well with the MS library spectra for cyclohexene (93 % match), cyclohexeneoxide (64 %), 2-cyclohexene-1-ol (95 %) and 2-cyclohexene-1-one (91 %), figure 6. Clearly the Ti-MCM-41 26 % and 21 % conversions, in acetonitrile and methanol respectively, reported¹⁷ by Corma *et al* have not been emulated here. Indeed the presence of oligomeric titanium species (UV-Vis) reduces the likelihood of catalytic reaction taking place. Assessment, therefore, of the influence of alkene substrate, reaction solvent or mesopore dimensions (C16-3-1 *versus* C18-3-1) was not possible given these experimental inconsistencies.

A parallel cyclohexene in MeCN experiment using *tert*-butyl hydroperoxide (80 % in di-*tert*-butylperoxide) as the oxidant was also performed. The reaction, however, was inactive, yielding a white solid. This observation tends to suggest that the mesoporous silanol surface hinders the diffusion of this organic peroxide within the material. As a result no pentacyclic titanium active species forms to catalyse the conversion of cyclohexene.

hex-1-ene	cyclohexene	methanol	acetonitrile	acetone
64	83	64.7	81-82	56

Table 2: Hydrocarbon boiling points (° C).

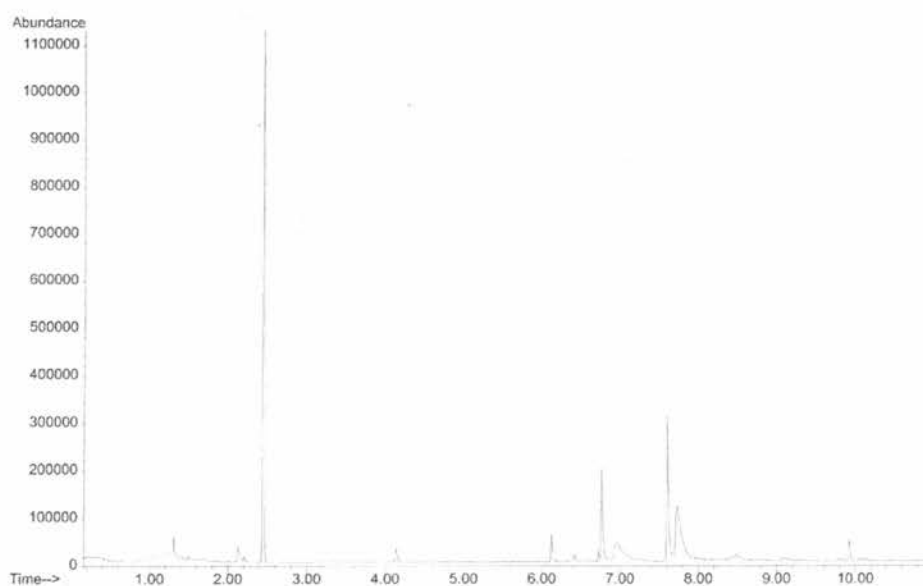


Figure 5: GCMS chromatogram of the cyclohexene-SBA-2 Ti50-acetonitrile product mixture.

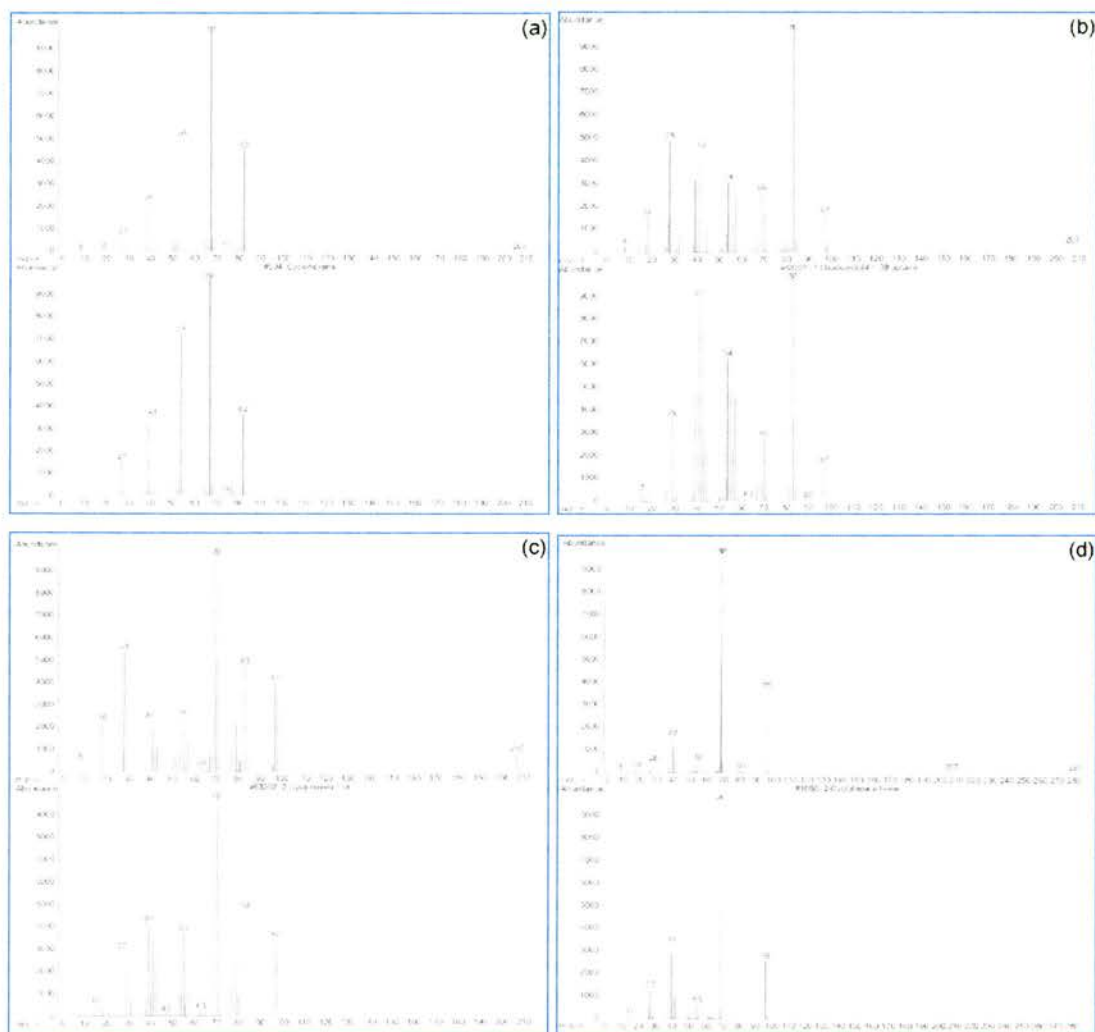


Figure 6: GCMS mass spectra (top) and corresponding MS library spectra (bottom) of (a) cyclohexene (2.4 min), (b) cyclohexeneoxide (6.1 min), (c) 2-cyclohexene-1-ol (6.7 min) and (d) 2-cyclohexene-1-one (7.6 min).

Finally, perhaps the experimental procedure could be improved for the future. Certainly an internal standard could be adopted, to enable calculation of the % loss/conversion of the substrate. In addition the problems encountered with solvent/substrate evaporation could be minimised through the use of a redesigned reaction vessel or a stirring autoclave. Meanwhile further GCMS analyses would help to confirm the nature of other unidentified GC product peaks.

Ti Summary

Direct synthesis titanium incorporation into SBA-2 is successful, producing a well ordered material. UV-Vis analysis of the calcined SBA-2 Ti50 solids , however, indicate that titanium may be present as oligomeric particles. Assessment of their potential as epoxidation catalysts, meanwhile, was hampered by substrate and solvent evaporation during the reaction. In spite of this the titanium-containing materials did turn yellow in the presence of hydrogen peroxide.

Mn Background

During this manganese study the metal centres were incorporated into zeolites by ion-exchange (Coulombic attachment), whilst the grafting approach was used for mesoporous silicates. The section, therefore, commences with the relevant theory to Electron Spin Resonance spectroscopy and mesoporous surface tethering. Following these the specific literature background to the manganese complexes incorporated within such materials is described.

Electron Spin Resonance Spectroscopy^{26,27,28}

Electron Spin Resonance Spectroscopy (ESR) is an appropriate technique for detecting unpaired electrons in organic radicals or transition metal species. The basic spectroscopic principles are similar to those of NMR. Thus the energy difference involved in an electron switching spin states (e.g. $-1/2 \rightarrow 1/2$) is detected. Transitions between these states can be induced by applying microwave radiation^{iv} to the sample, within a magnetic field. Absorption occurs at the resonance condition, with an energy given by equation 2, where \mathbf{B} is the applied magnetic field, μ_B is the Bohr magneton (equation 3) and g is a proportionality constant^v termed the g -factor.

$$\Delta E = h \nu = g \mu_B \mathbf{B} \quad 2$$

$$\mu_B = \frac{eh}{4\pi mc} = 9.724 \times 10^{-24} \text{ J T}^{-1} \quad 3$$

In particular g is responsible for the position of an absorption peak in the field range, and depends upon the particular paramagnetic ion, its oxidation state, coordination number and local distortions. An ESR spectrum, therefore, relates the absorption (usually as a first derivative) to the resonance magnetic field, figure 7a. The signal can be characterised by 4 main parameters: intensity, line width, g -factor and hyperfine

^{iv} In practice an ESR spectrometer operates at a fixed microwave frequency, and the field is varied until resonance is reached.

^v For an isolated free electron $g = 2.0023$.

splitting. These offer information on the unpaired spin concentration, recovery rate of the populations, local magnetic field and electron-nuclear spin interaction respectively.

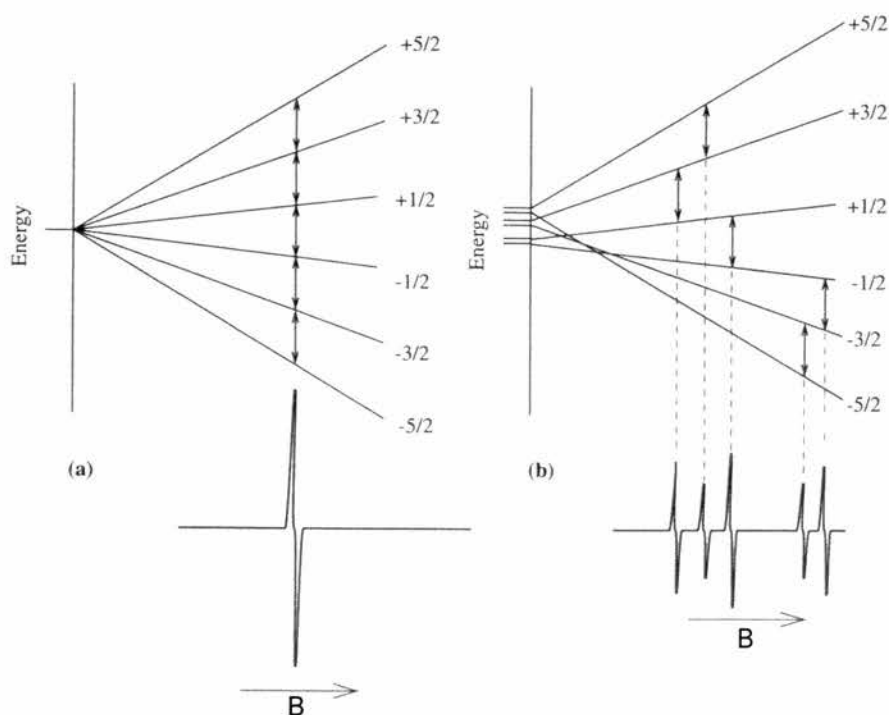


Figure 7: Fine structure in an ESR spectrum of Mn^{2+} ($S = 5/2$): (a) a symmetrical field and (b) zero field splitting.²⁸

In particular hyperfine splitting creates multiple peaks in an ESR spectrum. These arise because, in addition to the applied external magnetic field, there are 'local' magnetic fields associated with the transition metal ion itself or with the surrounding ligands (bonding structure). This can be reconciled by considering a solid containing manganese ($I = 5/2$). By definition a nuclear spin moment I will split an electronic resonance into $2I+1$ lines. For manganese in a spherically symmetric field, therefore, the first derivative should be split into $2I+1 = 6$ lines. Mn^{2+} in its high spin state, though, possesses 5 unpaired 3d electrons, i.e. electron spin moment $S = 5/2$. This can complicate matters if the electric field surrounding the paramagnetic ion is distorted, figure 7b. In the absence of a magnetic field this non-degeneracy is termed zero field splitting. Within an applied magnetic field, though, the $\Delta S = \pm 1$ electronic transitions occur at different values. Consequently any $2I+1$ nuclear spin splitting will be superimposed upon the $2S$ lines of the new signal.

Significantly, ESR is a particularly effective technique at detecting low spin concentrations. Thus the quality (sensitivity) of a spectrum can be increased by reducing the transition metal ion loading within the sample and/or lowering the analysis temperature. De Vos *et al* report²⁹ that optimum signal-to-noise ratios for manganese exchanged zeolite Y correspond to a content of $0.025 < \text{Mn}^{2+} < 0.4$ wt%. Lower temperatures, meanwhile, effectively increase the population difference between the energy levels. Finally a second derivative of the ESR signal can be used to confirm the presence of any faintly distinguishable hyperfine splitting.

Surface Modification^{30,31}

The modification of silica surfaces, to attach organic functionalities, is critical for the heterogenization of homogeneous catalysts within mesoporous materials. Several approaches have been taken to achieve this. Perhaps the most frequently used is grafting, however, the alternative techniques of surface chlorination and templated co-polymerisation are also possible. Each involves the chemical binding of an organic molecule (chemisorption^{vi}). It is the grafting method that has been used in this work.

Typically a trialkoxysilane is attached to the surface silanols in a solvent (at reflux). This has the effect of forming strong Si-O-Si (surface-tether) bonds which drive the reaction, although not all alkoxy groups necessarily bind. There are, however, only a limited number of organosilanes available for use. As a result the catalytic species is often introduced in a post modification step. The final catalyst, therefore, is tethered to the surface yet possesses a degree of mobility akin to that in a homogeneous system.

The physical structure and chemical composition of the functionalised material can be assessed by various analytical techniques, table 3. Typically a $0.3\text{-}3.0$ mmol g^{-1} catalyst loading is obtained. Such a low loading is partially determined by the concentration of surface hydroxyl species. It also, however, ensures that the active species are well

^{vi} Physisorption can also give useful supported reagents, but use is limited by their stability and recycling can be restricted by the extent of leaching.

dispersed throughout the mesoporous solid and that (because the porosity remains) the substrate is freely able to approach the catalytic centre during reaction.

Analysis	Technique	Information
Stability	TGA	assess the thermal stability and whether it is chemically bound to the surface
Loading	AAS	direct determination of the metal bound to the surface, or analysis of the filtrate after preparation
	^{29}Si MAS NMR	comparison of the Si-O-Si and Si-OH ratios before/after modification
Structure	CHN	calculation of the yield in each reaction step
	FTIR	observation of organic functionalities. For pure silica O-H, Si-O-Si and Si-OH stretches are at 3800-3200, 1090 and 900 cm^{-1} respectively
	MAS NMR	ascertain the type/quantity of organic and inorganic species present: ^{13}C , ^{29}Si , ^{31}P etc. ^{13}C MAS NMR can also indicate any presence of solvent molecules
	Adsorption Isotherms	reduction in surface area; pore size distribution and total volume often remain similar to unmodified solids

Table 3: Major analytical techniques employed for characterisation of modified silicas.³⁰

Manganese Oxidation Catalysts

Much work has been directed towards the use of manganese complexes as oxidation catalysts. More specifically this interest originates in biological systems,^{32,33} which effect highly specific transformations under mild conditions. For example, some avenues of investigation have taken their lead from the shape and form of the active species within enzymes. Thus manganese has been inserted into porphyrin and phthalocyanine ring systems (figure 8a) where these *trans* macrocyclic chelates create a planar tetradentate complex. During homogeneous oxidation, however, these organometallic catalysts often deactivate, due to the formation of μ -oxo bridged dimers. Subsequent site isolation, by encapsulation within zeolitic frameworks³⁴ or attachment to polymer surfaces has helped to prevent this, and can aid in catalysis recovery.

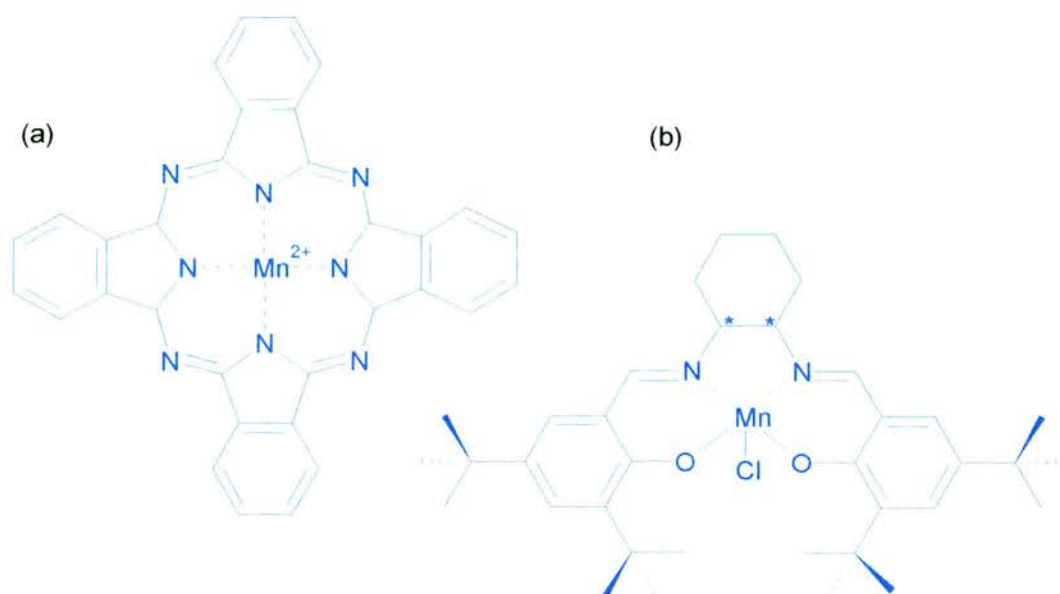


Figure 8: (a) Manganese-phthalocyanine and (b) manganese(III)-salen complexes.

Meanwhile other research has focussed upon *N,N'*-bis(salicylaldehyde)ethylenediamine (salen), a tetradentate Schiff base ligand. In particular Jacobsen and co-workers³⁵ have shown that their manganese (III) complex,^{vi} figure 8b, is an efficient alkene epoxidation catalyst. Although similar deactivation can occur, this is minimised by the introduction of steric constraints within the ligand which effectively isolate the metal centres. The salen molecule is also amenable to functionalisation by non-equivalent alkyl groups, $R^1 \neq R^2$. This, in effect, creates a chiral complex which has been investigated³⁶ towards a variety of asymmetric catalytic reactions. Again immobilisation (heterogenization) of salen ligands^{36,37,38} is an active research field.

Finally, relatively little is known³⁹ about oxygen transfer complexes with *cis* co-ordination. Exemplified by the bipyridine and 1,4,7-triazacyclononane (tacn) ligands, these non-planar complexes possess a nitrogen atom *trans* to a substitution labile co-ordination site. It is the derivatized tacn ligand that is the basis of this manganese research.

^{vi} This complex has become known as Jacobsen's catalyst.

Manganese cyclic triamine complexes

Manganese cyclic triamine complexes were first observed to activate H_2O_2 towards bleaching and epoxidation, by Unilever researchers in 1994. They reported⁴⁰ that styrene was effectively epoxidised in methanol-carbonate buffers, but required a 100-fold excess of oxidant. Subsequent work by De Vos and Bein³⁹ has attempted to understand and optimise this catalytic system. In particular they first showed that the homogeneous activity, towards alkenes, can be improved by the astute choice of reaction conditions. Indeed when the reaction temperature is lowered to 0 °C, and acetone^{viii} is used as the solvent, high turnover numbers (TONs) and epoxide selectivities can be obtained. Like manganese porphyrin systems, however, retention of the substrate configuration is not absolute. Meanwhile epoxidation yields are also dependent upon the counter ion in solution. From ESR it appears that bridging anions (SO_4^{2-} , MeCOO^-) promote the formation of μ -oxo bridged dinuclear manganese complexes (a 16-line $\text{Mn}^{\text{III}}\text{-Mn}^{\text{IV}}$ signal) which act as the active species in solution. This is possible because the *cis* chelating 1,4,7-trimethyl-1,4,7-triazacyclononane (tmtacn) ligand creates a non-polar complex, figure 9, which leaves substitution-labile coordination sites on manganese. The efficient use of H_2O_2 can be attributed, in part, to the formation of these dimers. Furthermore significant solvent oxidation (i.e. H_2O_2 oxidant loss) occurs with alcoholic (protic) solvents, whilst an absence of manganese or ligand prevents any reaction from occurring.

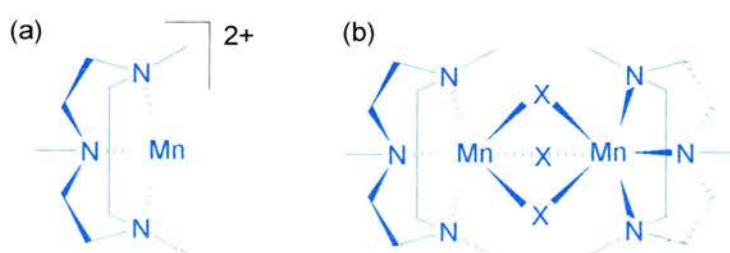


Figure 9: (a) Mn-tmtacn complex and (b) the dinuclear active species in solution, $\text{X} = \text{O}^{2-}$, OH^- or other oxygen bridges.

^{viii} Acetone, forms a peroxide complex: $\text{CH}_3\text{COCH}_3 + \text{H}_2\text{O}_2 \leftrightarrow \text{CH}_3\text{C}(\text{OOH})\text{OHCH}_3$ that essentially acts as an oxidant reservoir.

An initial aim of this thesis was to encapsulate these Mn-cyclic triamine complexes within zeolitic hosts, and subsequently test their catalytic activity. Shortly after this work was started, though, De Vos *et al* published^{41,42} exactly this. They observed that for a manganese exchanged zeolite Y, intraporous complexation by tmtacn could occur. As a result the characteristic 6-line ESR signal of zeolite co-ordinated Mn^{II} alters.^{ix} Instead a new signal over a wider field range manifests itself. This can be attributed to zero field splitting, i.e. an axial distortion of the manganese crystal field, due to ligand complexation. During catalysis, however, the 16-line signal continued to be observed, albeit slightly delayed after oxidant addition. It appears, therefore, that the dinuclear active species can form within a zeolite Y supercage, although it is sterically crowded. Meanwhile tmtacn (as opposed to its un-methylated analogue tacn) seems to provide a hydrophobic wrapping around the Mn ion, which favours olefin adsorption onto the active species and hinders further oxidant approach (i.e. H₂O₂ decomposition). An excess ligand,^x meanwhile, limits acidic side reactions, presumably by neutralising the zeolite surface. The catalytic results are in line with those of homogeneous experiments.

Finally De Vos *et al* reported⁴³ the covalent anchoring of a derivatised 1,4,7-triazacyclononane (tacn) ligand within the mesoporous material MCM-41. More specifically the hydroxy pendant arms are known⁴⁴ to assist in metal complexation and can increase the homogeneous catalytic activity (reactivity, chemo- and regioselectivity and resistance to oxidative degradation). The non-central lines in the ESR spectrum of the tethered manganese complex once again indicate that chelation has occurred. Moreover, the TONs are comparable to their zeolite heterogenized counterparts, table 4, although the specific epoxide selectivity is slightly reduced.

^{ix} See ESR background section.

^x A tmtacn: Mn ratio of 2.2:1 was used.

ref.	solid	solvent	conv. ^a	%selectivity	T(K)	rxn time
43	Mntacn(OH)-MCM-41	MeOH	(16)	86	273	1 h
41	Mntmtacn-Y	MeOH	2.1	100	273	12 h
41	Mntmtacn-Y	MeOH	0.3	100	298	12 h
41	Mntmtacn-Y	Acetone	25.3	95.4	273	12 h
42	Mntmtacn-Y	Acetone	15	92	273	-
41	Mntmtacn-Y	Acetone	6.8	97.2	298	12 h
39	Mntmtacn ^b	MeOH	(37)	91	273	-
39	Mntmtacn ^b	Acetone	(890)	89	273	-
41	Mntmtacn ^b	Acetone	55.3	84	273	12 h

(a) Turnover number in brackets, TON = (mol substrate converted) / (mol Mn), (b) homogeneous reaction.

Table 4: Manganese-cyclic triamine literature catalysis on cyclohexene.

This manganese research, therefore, aimed to assess the affect of molecular sieve structure upon the epoxidation of alkenes. The zeolites Y, hexagonal Y and L were studied for the direct complexation of tmtacn within the supercages, whilst a hydroxy derivatised tacn ligand was tethered within calcined SBA-2 and MCM-48.

Mn Experimental

Instrumentation

All X-band ESR spectra were obtained using a Bruker ER 200D spectrometer operating at 9.1 GHz with 100 kHz modulation. The solid samples were photolysed in the resonant cavity by light from a 500 W super pressure mercury arc lamp.

All XRF measurements were carried out on a Philips PW 1450/20 sequential spectrometer calibrated with a rhodium primary excitation tube. The 0.5000 g samples were first mixed with spectroflux 105 (2.666 g, Johnson Matthey) before being heated and cooled to form a glass.

Microanalyses were carried out on a Carlo Erba Elemental Analyser model 1106, suitable for weight % C, H and N determination.

The ^{13}C CP MAS NMR spectrum was obtained on a Varian UNITYplus spectrometer, operating at 300 MHz for ^1H and accompanied by a Doty Scientific MAS probe. Data from the cross-polarised (from ^1H) experiment was collected at ambient temperature with the conditions detailed in table 5. A 7mm rotor was used.

frequency (MHz)	spectral width (kHz)	spin rate (kHz)	contact time (ms)	acquisition (ms)	delay (s)	shift scale
75.430	30.0	5.0	1.0	30	1.0	TMS

Table 5: ^{13}C CP MAS NMR experimental details.

Gas Chromatography was performed, for the zeolite catalytic reactions, on a Hewlett Packard HP 6890 Series or a Philips Pye Unicam PU 4500 GC, accompanied by a Hewlett Packard (HP 3395 or HP 3394) Integrator. The catalysis products were eluted with a helium mobile phase on a Carbowax 10^x (30 m × 0.53 mm × 0.5 μm) capillary column. Various temperature programmes were employed. The tethered systems,

^x Unfortunately on this column acetone and cyclohexene elute at the same retention time.

meanwhile, employed an HP-5 boiling point column (cross-linked 5 % phenyl methyl siloxane; 30 m × 0.32 mm × 0.25 μm) within a CE Instruments 8000 TOP Series GC. These GC traces were recorded on a Fisons Instruments DP700 Data Processor (integrator) whilst the oven temperature was ramped from 50 °C to 200 °C at 10 °Cmin⁻¹

Zeolite Ion Exchange

Manganese (II) ion exchange has been carried out on zeolites Y and hexagonal Y to substitute for Na⁺ as the charge balancing cation. Typically 4.0 g of zeolite are stirred at room temperature in a 1 litre aqueous solution of Mn(COOEt)₂·4H₂O (0.1144 g) for 48 - 72 hours (pH = 6). Similarly zeolite L underwent K⁺ - Mn²⁺ ion exchange. The zeolite Y, hexagonal Y and L cation substitutions were designed to obtain on average 1 manganese per 4 supercages, equal to that of De Vos *et al.*⁴¹ The actual manganese loadings (table 6) were determined by X-ray fluorescence.

zeolite	Y	Hex Y	L
wt % (± 0.10)	0.74	0.58	0.62

Table 6: Loadings in the manganese-exchanged zeolites.

Mn-(tmtacn)-Zeolite Preparation

The heterogeneous Mn catalysts were prepared by intraporous complexation of Mn²⁺ in zeolite NaY, Hexagonal Y or L with 1,4,7 trimethyltriazacyclononane (tmtacn). Thus the manganese exchanged zeolite (with 1 Mn²⁺ per 4 supercages) was dehydrated at 250 °C for 4 hours under vacuum. Using standard schlenk line techniques the polyamine ligand^{xii} was syringed onto the dehydrated zeolite, and left to diffuse into the zeolitic cavities for 10 hours, at 150 °C, under Argon and with occasional shaking. A polyamine to Mn molar ratio of 2.2 was used as it has been reported^{41,42} to be optimal

^{xii} Care: tmtacn is a moisture sensitive colourless solid which absorbs CO₂ from the atmosphere. It is also corrosive, causing burns and is readily absorbed through the skin.

for an efficient diffusion of the ligand into the zeolite pores and also neutralises any inherent zeolitic acidity. The brown coloured zeolite-ligand mixture was stored under argon until required. ESR measurement was performed upon the zeolite encapsulated metal complex.

Tethering

The tethering process is shown in figure 10. All steps were performed using standard schlenk line techniques, under an inert atmosphere, unless stated otherwise.

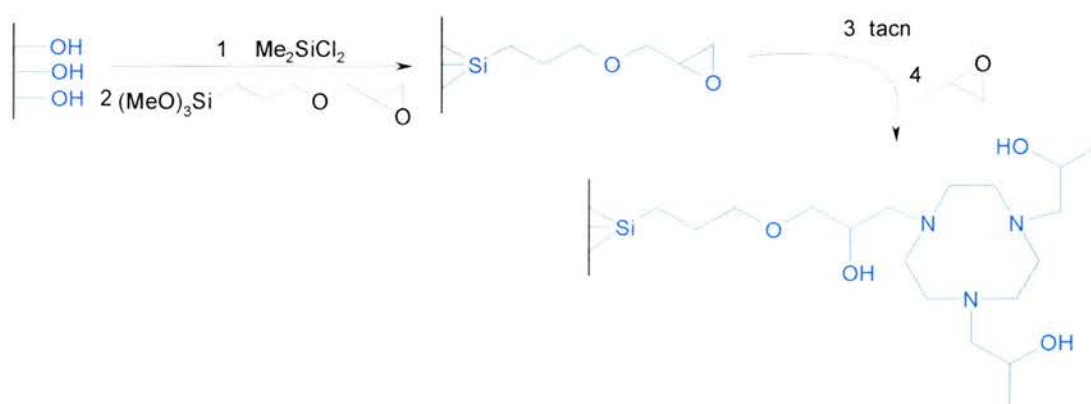


Figure 10: The tethering process in mesoporous silicates.

Siliceous SBA-2 or MCM-48 (0.5 g) was dehydrated for 1 hour under high vacuum (10^{-3} torr) at 220°C , and then allowed to cool, and filled with argon. Dry ether (12.5 ml) was added to this to form a suspension, into which dichlorodimethylsilane ($8.5 \mu\text{L}$, 0.7 mmol) was syringed. Note: dichlorodimethylsilane readily polymerises in the presence of water, thus dry solvents must be used. The external surface was subsequently deactivated by stirring this mixture at room temperature for 1 hour. Following this the schlenk flask was cooled in an isopropanol/liquid N_2 bath (*ca.* -10°C). The 3-glycidoxypropyltrimethoxysilane tether ($250 \mu\text{L}$, 1.13 mmol) was syringed into this suspension and then stirred at *ca.* -10°C for 1 hour before being slowly warmed up to RT and stirred for 16 hours. Finally the tethered solid was recovered by filtration and washed repeatedly ($3 \times 15 \text{ ml}$ dry diethylether). The tethered solids were stored under Ar.

The oxirane ring on the glycidated support was opened by reacting selectively with 1,4,7-triazacyclononane (tacn) (146 mg, 1.13 mmol) in dry ethanol (13 ml, 50 °C, 24 h). This type of ring opening is well known⁴⁴ and forms a covalently bound 3-propoxy-2-hydropropyl-tacn substituent. Subsequently the solid was filtered and washed repeatedly with dry solvent. The remaining secondary amine groups are further functionalised by reaction with 1,2-epoxypropane. Thus the 1,2-epoxypropane^{xiii} (2eq. + 20% excess, 1.56 μ L, 2.49 mmol) is added to the tethered solid, in dry ethanol (10 ml), and the suspension stirred at RT overnight (>10 h). Finally the solid is recovered and washed thoroughly with dry ethanol (3 \times 15 ml) to ensure that only covalently attached ligands remain. It is reported⁴⁴ that the additional hydroxy groups around the tacn ligand assist in complexing the metal. The final supported solid is designated by the suffix tacn(OH).

Catalysis

The general catalytic epoxidation reaction is shown schematically in figure 11.

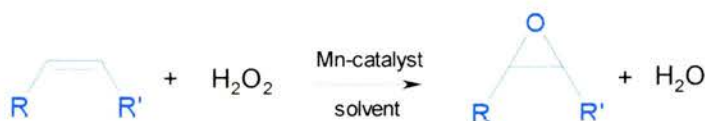


Figure 11: The catalytic epoxidation reaction.

As detailed previously, the three microporous host structures zeolite Y, hexagonal Y and L were examined. In addition the tacn-functionalised SBA-2 and MCM-48 mesoporous material were looked at. For each support a choice of one (or more) alkenes was investigated: cyclohexene, hex-1-ene or cyclohexeneone.

A typical heterogenized zeolitic experiment is as follows. The ship-in-a-bottle catalyst (0.025 g) was transferred to a 5 mm NMR tube, or 25 ml RB flask. Acetone (1.264 ml, 1 g) was added to this, followed by the alkene (1 mmol). Finally the oxidant as a 30 wt% aqueous solution of H₂O₂ (0.1134 ml, 1 mmol) was added slowly. The reaction

^{xiii} Care: 1,2-epoxypropane is a cancer agent and highly flammable.

vessel was maintained at the required temperature (RT, fridge at 8 °C or -3 °C, or ice-water bath at 0 °C) and shaken intermittently. After a 10 hour reaction the suspension was centrifuged and the liquid phase analysed by gas chromatography (Carbowax 10 column).

As a series of control experiments the homogeneous reactions were performed according to literature³⁹ procedures. Thus to a small RB flask containing $\text{Mn}(\text{COOMe})_2 \cdot 4\text{H}_2\text{O}$ (4.9 mg, 20 μmol), the acetone (1.56 ml), alkene (20 mmol) and tmtacn ligand (5.8 μL , 30 μmol) were added consecutively. This flask was then cooled in an ice-water bath and the H_2O_2 (4.53 ml, 40 mmol, 30 wt% aqueous solution diluted three times in 13.6 ml acetone) added slowly ($1/2 \rightarrow 1$ h). The reaction was maintained at 0 °C throughout. Again the products were analysed by gas chromatography. Similarly two cyclohexene control experiments were run with the un-liganded $\text{Mn}^{\text{II}}\text{-Y}$ and $\text{Mn}^{\text{II}}\text{-L}$ solids^{xiv} acting as the ‘catalyst’.

Catalytic reactions using the tethered supports were performed *as per* the MCM-41 supported experiments⁴³ of De Vos *et al.* Thus manganese sulphate (1.8 mg, 8 μmol) was added to a suspension of the functionalised solid (20 mg) in the solvent (1 g ethanol or methanol for SBA-2 or 1 g acetone for MCM-48 materials). This mixture was kept at 0 °C for 1 hour, to enable complexation, before cyclohexene (100 μL , 1mmol) was added. Finally 30 wt% aqueous H_2O_2 (177 μL , 0.156 mmol) was added gradually, and the suspension stirred first at 0 °C and then warmed to room temperature. As before, the liquid products were recovered following centrifugation, and analysed by gas chromatography (boiling point column).

The homogenous form of these tethered experiments was performed in an analogous manner. In this case, though, the 1,2-epoxypropane functionalised tacn was first synthesised in dry methanol (3.16 ml) by reacting the tacn (5.7 mg, 44 μmol) with 1,2-epoxypropane (8.3 μL , 132 μmol) at room temperature over 72 hours.

^{xiv} There was insufficient $\text{Mn}^{\text{II}}\text{-HexY}$ for a similar control experiment.

Mn Analysis

ESR Spectroscopy

All spectra were recorded at 170 K (or lower) dial temperature as this provided the most detailed output. The control experiments with zeolites Y, hexagonal Y and L gave no ESR signals, indicating that the manganese exchanged spectra are entirely due to the Mn^{II} ion. A nitroxide standard triple peak occurs at the centres of the Mn^{II} signals, thus $g_{\text{NO}} = g_{\text{Mn}} = 2.006$.

Figure 12 shows the ESR spectra obtained for Mn^{II} -NaY, with a manganese(II) loading of 0.74 wt% by XRF or 1 per 4 supercages. The distinct first derivative spectrum shows 6 hyperfine lines characteristics of symmetrical octahedral co-ordination. The lines however, are not evenly spaced,^{xv} which can be attributed to second order effects. The second derivative signals, meanwhile, indicate the possible appearance of a second octahedral site within the zeolite. This is more clearly shown after dehydration of the solid (100 °C, 24 h). Presumably the sharper line shape is due to the removal of physisorbed water from within the structure. The appearance of a second (minor) set of peaks, though, suggests that some manganese species are partially complexed by hydrating water molecules, or that there are several co-ordination sites within the zeolite structure. Either would slightly distort the pure octahedral symmetry environment. De Vos *et al* have reported²⁹ comparable hydrated-dehydrated findings in manganese exchanged zeolite A.

^{xv} The same sample was run upon a Q-band instrument (ca. 35 GHz), which offers higher resolution and minimises the second order effects. This spectrum gave a hyperfine coupling constant $A \approx 97$ G at 120 K.

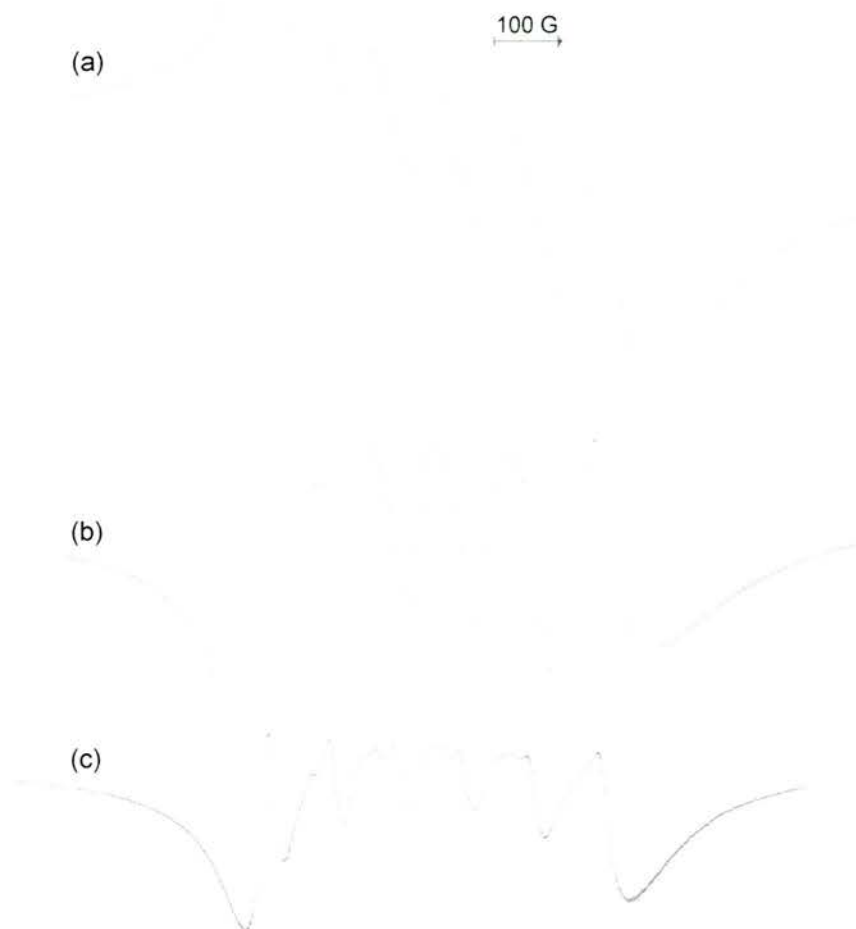


Figure 12: ESR spectra of $\text{Mn}^{\text{II}}\text{-Y}$: (a) 1st derivative, (b) 2nd derivative and (c) dehydrated sample, 2nd derivative.

A sample of 1 manganese per supercage (2.87 wt% by XRF) has also been analysed by ESR spectrophotometry. It is significant, however, that the fine structure was not observed on the first derivative. This indicates that reduction of the manganese loading results in fewer dipole-dipole interactions and thus the detection of hyperfine splitting.

The $\text{Mn}^{\text{II}}(\text{tmtacn})\text{-Y}$ spectra are shown in figure 13. Again the hyperfine structure is most clear in the second derivative. There is, however, essentially no difference (i.e. no non-central transitions) between this signal and that observed prior to tmtacn addition. This indicates that there is no zero field splitting, and suggests that chelation has not occurred. The majority of the manganese species, therefore, remain as uncomplexed ions.



Figure 13: ESR spectra of $\text{Mn}^{\text{II}}(\text{tmtacn})\text{-Y}$: (a) 1st derivative and (b) 2nd derivative.

The 1 manganese per 4 supercage spectra of hexagonal zeolite Y are shown in figure 14. The first derivative indicates that octahedrally co-ordinated manganese is present. In addition the second derivative shows that a pair of weaker transitions are superimposed upon the main 6-line signal. These indicate that manganese co-ordination may be located across several sites within the zeolite (e.g. in the hexagonal prism or in a cage) or complexation involves hydrating water molecules. There is essentially no change to this '6-line' signal following tmtacn addition, which suggests no complexation has occurred.

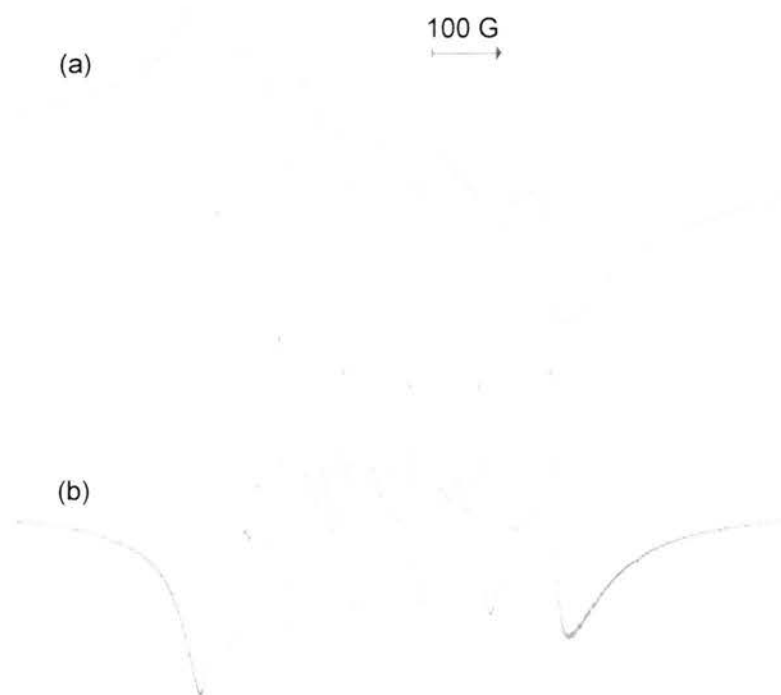


Figure 14: ESR spectra of $\text{Mn}^{\text{II}}\text{-Hex Y}$: (a) 1st derivative and (b) 2nd derivative.

The ion-exchanged zeolite L sample similarly shows a strong 6 line signal, figure 15. It is expected that manganese locates in the channel pockets of this structure. The second derivative, however, indicates that a pair of weaker electronic transitions are also generated. These, again, might be due to octahedral manganese surrounded by a hybrid zeolite-water ligand. No ESR spectrum of the Mn(tmtacn)-L material was obtained.

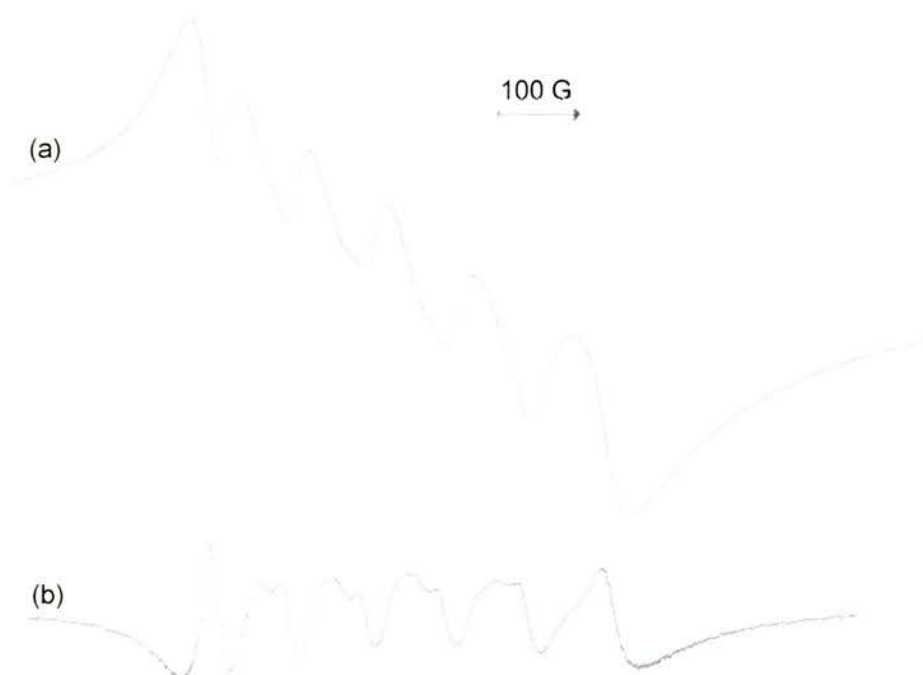


Figure 15: ESR spectra of Mn^{II}-L: (a) 1st derivative and (b) 2nd derivative.

Tethering

The tethering process within each mesoporous solid was monitored by elemental analysis. These results are summarised in table 7. In addition XRD indicates that the structural order of these solids is unaffected by their suspension in organic solvents during tethering.

	SBA-2			MCM-48		
	%C	%H	%N	%C	%H	%N
calcined				0.16	0.28	-
+ Me ₂ SiCl ₂ + 3-glycidoxypropyltrimethoxysilane	4.84	0.81	-	4.09	0.72	-
+ tacn + 1,2-epoxypropane	7.00	1.40	-	8.07	2.05	1.03

Table 7: Elemental analysis of the functionalised mesoporous materials.

It appears that the surface derivatization using first dimethyldichlorosilane (to deactivate the external surface) and then 3-glycidoxypropyltrimethoxysilane is partially successful. Based on the CHN values and assuming 100 % Me_2SiCl_2 reaction, glycido-attachment within SBA-2 was 32.7 % efficient, whilst for MCM-48 a 27.4 % yield^{xvi} was achieved. This is confirmed by the ^{13}C NMR of each filtrate, which indicate that some unreacted tether remains in solution.

The CHN analyses of the tacn(OH) materials are particularly revealing. In SBA-2 the absence of a nitrogen value suggests that no tacn is present, and that this step has not worked. Perhaps this is due to the reduced pore volume^{xvii} within this structure. Alternatively the external surface deactivation procedure may effectively block many pore openings, making the large internal surface unavailable. The increase in carbon content during tacn(OH) addition, therefore, might simply be due to physisorbed solvent. Tacn(OH) addition to MCM-48, meanwhile, appears to have been successful, giving a 50.0 % yield in this step. Thus a ^{13}C MAS NMR experiment was performed on this material in order to ascertain the nature of the carbon species present, figure 16. These resonances are in close agreement with the solution spectra of the 3-glycidoxypropyltrimethoxysilane and tacn precursors. Thus δ : 72.0 CH_2O ; 58.5 CH_2OH ; 43.7 NCH_2 ; 22.0 SiCH_2CH_2 , CH_3 ; 6.7 SiCH_2CH_2 ; -3.6 SiCH_2 (external surface). It appears, therefore, that this reaction has worked, however, the low loading contributes to the low signal-to-noise ratio. In addition it cannot be ruled out that some solvent still remains (δ : 58.5, 16.4 ethanol; 65.2, 14.1 ether), nor that the main 43.7 ppm resonance is simply physisorbed tacn.

^{xvi} Equivalent to 0.74 mmol tether (g silica)⁻¹ and 0.62 mmol tether (g silica)⁻¹ for SBA-2 and MCM-48 respectively.

^{xvii} See Synthesis chapter adsorption isotherms.

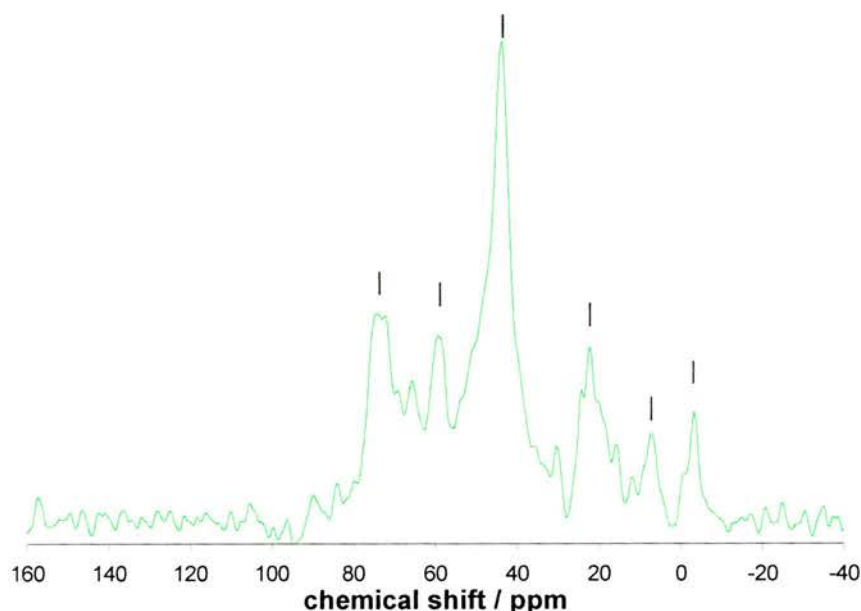


Figure 16: ^{13}C CP MAS NMR of MCM-48-tacn(OH).

Catalysis

The catalysis experiments and results are summarised in table 8. Through comparison of these results with the literature it was hoped to analyse the shape selective properties of the solid, and the electronic influences of the substrate, upon the catalysis products. As can be seen, though, the catalytic potential for these heterogenized systems is not promising.

	cyclohexene	hex-1-ene	cyclohexeneone
homogeneous tmtacn ^b	✓	14.3% (143)	8.8% (83)
Mn-Y	no rxn	-	-
Mn-L	no rxn	-	-
Mn(tmtacn)Y	✓	no rxn	no rxn
Mn(tmtacn)HexY	no rxn	no rxn	no rxn
Mn(tmtacn)L	no rxn	no rxn	no rxn
homogeneous tacn(OH) ^b	5.1% (6)	-	-
SBA-2-tacn(OH)	no rxn	-	-
MCM-48-tacn(OH) ^c	3.0% (4)	-	-

(a) percentage conversion, turnover numbers in brackets, (b) after 3 hours and (c) after 48 hours.
TON = (mol substrate converted) / (mol Mn)

Table 8: Manganese epoxidation reactions undertaken.^a

Clearly the homogeneous tmtacn reactions were successful. The resultant conversions,^{xviii} though, are lower than those reported³⁹ by De Vos *et al.* Presumably this is because the experimental technique has not been optimised, for example by a more gradual addition of H₂O₂. Meanwhile the Mn-Y and Mn-L control reactions reassuringly gave no GC product peaks. These confirm that the tmtacn ligand is required to complex the manganese ion before catalysis can occur.

Despite this an initial Mn(tmtacn)-Y experiment with cyclohexene was successful. During the reaction the zeolite complex changed colour from pale brown to dark brown, before reverting to the initial colour. It is thought that this corresponds to the formation of the catalytically active Mn^{III}-Mn^{IV} species, as reported⁴¹ by De Vos *et al.*, however ESR analysis would be required to confirm this.

In general, though, the Mn-tmtacn ship-in-a-bottle catalysts exhibit low activity, producing a conversion of <0.5 % over a 10 hour reaction. This can be reconciled by the ESR spectra, which indicate that no complexation has occurred. Moreover all these systems built up a positive pressure during the reaction. Such an observation suggests that disproportionation of the hydrogen peroxide oxidant has occurred, equation 4.



The decomposition can be attributed to a dearth of the tmtacn ligand; a lack of this highly basic amine means that the framework acidity is not effectively quenched. Thus the zeolite itself can catalyse the oxidative decomposition of H₂O₂.

Similarly the tethered experiments were less than encouraging. Although the homogeneous reaction was catalytic, the reduced conversion (c.f. tmtacn) might be attributable to the use of methanol^{ix} as a solvent. Alternatively the reaction might simply be slower because a partial deligation of this hexadentate chelate is required to form the manganese active species. The SBA-2-tacn(OH) solid, however, showed no catalytic activity, which can be attributed to the absence of any tethered tacn(OH) species. In the case of MCM-48-tacn(OH), though, only 0.31 mmol ligand (g silica)⁻¹ is available; this low concentration in itself will slow any reaction. Furthermore catalysis

^{xviii} Cyclohexene and acetone elute at the same time on this Carbowax column, thus no calculation of the % cyclohexene conversion could be made.

^{ix} It has been reported²⁰ that alcohols can themselves be oxidised by H₂O₂.

might be hindered by the difficulties in effectively solvating a hydrophobic silicate surface. Finally no real comparison of the mesoporous dimensionality can be made at these low conversions.

Mn Summary

Manganese ion-exchange within the zeolites Y, hexagonal Y and L has been successful. The corresponding ESR spectra indicate that within each solid the manganese is octahedrally coordinated. Subsequent chelation by tmtacn, however, is not achieved, and this accounts for the absence of any products after 'catalysis'. Heterogenization of tacn derivatives within SBA-2 and MCM-48 meanwhile is feasible. The low yields when tethering indicate that the experimental technique must be improved. Thus tacn functionalization was only achieved within MCM-48 and even then at a low loading: 0.31 mmol ligand (g silica)⁻¹. This solid converted 3 % cyclohexene after 48 hours.

Rh Background

This work was undertaken as a collaboration between the groups of Dr Jo-Ann Andersen (St Andrews) and Prof Carmen Claver, specifically with Dr Elena Fernández (Tarragona, Spain). The project was designed around the complementary research expertise of the two groups: rhodium hydroformylation catalysis (St Andrews) and sulphur ligand synthesis (Tarragona). Funding was provided by a British Council / Acciones Integradas research grant.

Hydroformylation

An important homogeneous catalytic reaction is the carbonylation of alkenes involving transition metal complexes. The oxo process, also known as hydroformylation, represents one of the largest industrial applications of soluble transition metal catalysts.⁴⁵ The reaction, illustrated in figure 17 involves the addition of synthesis gas (carbon monoxide and hydrogen) across a terminal double bond to produce an aldehyde. Principally these oxygenated products are used in acid, detergent or paint manufacture.



Figure 17: The generalised hydroformylation reaction.

The original process was discovered⁴⁶ by Otto Roelen at the Ruhrchemie AG company in 1938. He observed that cobalt-containing heterogeneous catalysts effected the addition of CO and H₂ to ethene to yield aldehydes and ketones. Soon afterwards, however, it was recognised that the actual catalyst is the soluble cobalt carbonyl species found in the reaction medium. The commercial process requires high temperature (150-180 °C) and pressure (>200 atm) producing a 3:1 mixture of *n:iso* addition products. Although the cobalt active species have been modified using trialkylphosphine ligands these severe reaction conditions and poor product selectivity remain. Meanwhile the replacement of cobalt by rhodium has allowed the development of processes which operate under much milder conditions: below 100 °C and at a few

atmospheres of pressure. Despite their high activity, the simple rhodium complexes initially gave a majority of branched aldehydes. This was overcome using phosphorus based ligands, such as triphenylphosphine or triphenylphosphite, which give active catalysts with selectivities for the linear aldehyde reaching 95%. More recent developments involve the use of *m*-sulphonated triphenylphosphine ligands which impart bulk and water solubility to the rhodium complex.

The mechanism⁴⁷ of hydroformylation with the modified rhodium catalysts (figure 18) has been extensively investigated by Wilkinson. It is similar to that of the cobalt complex, however an excess of ligand is important to stabilise the catalyst during product recovery, whilst the bulky shape directs product formation towards the desired linear aldehyde.

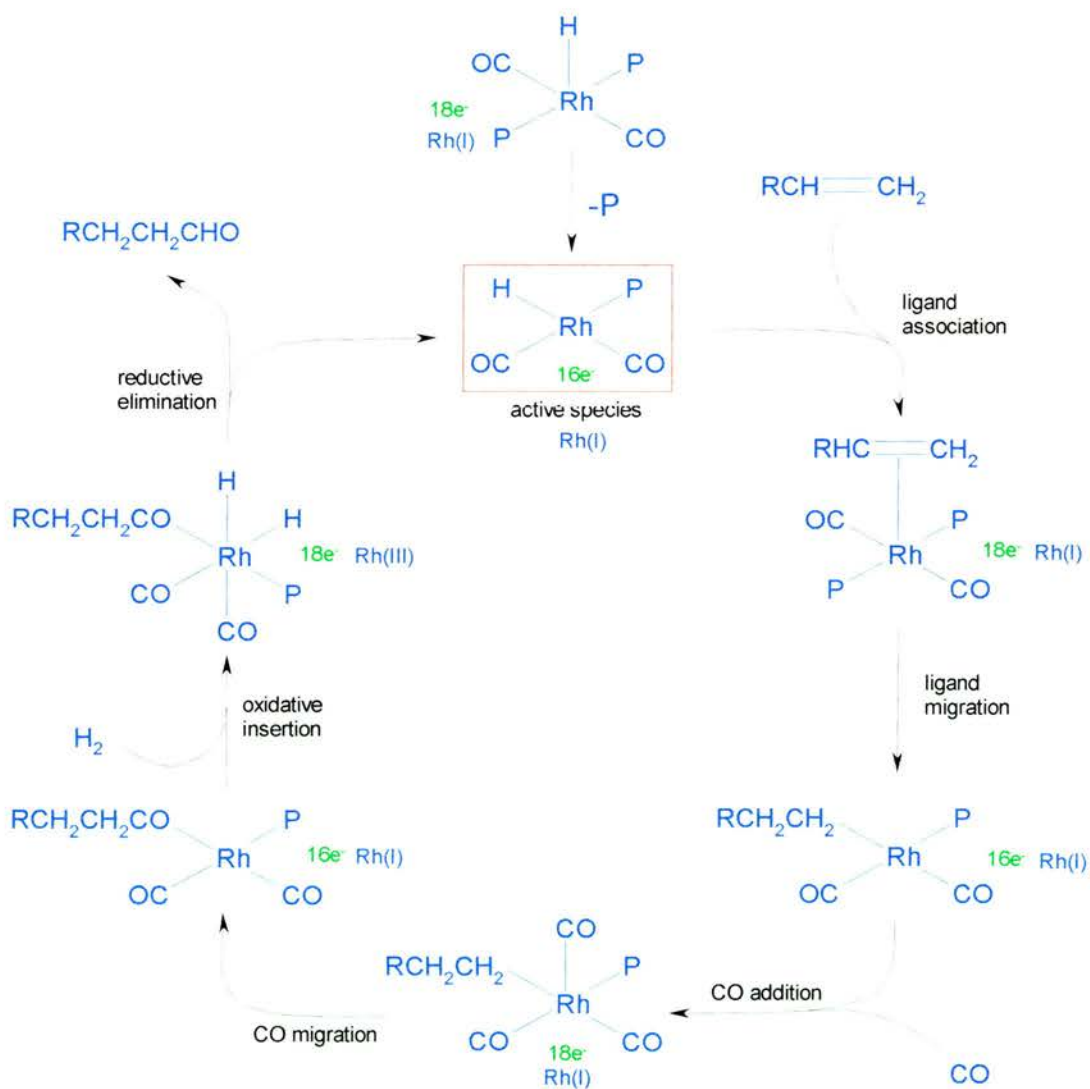


Figure 18: Rhodium catalysed hydroformylation of a terminal alkene (P = PPh₃).

Choice of Ligands

Rhodium(I) hydroformylation has traditionally employed phosphine-derived ligands to stabilise the active species. Sulphur ligands, though, were chosen for this study. Although the co-ordination of sulphur ligands has been extensively studied⁴⁸ their use in transition metal catalysed reactions is still relatively unexplored. Furthermore Carmen Claver's group has a long-standing interest in, and experience of, sulphur ligands in homogeneous catalysis. Thus (2R,3R)-2,3-*o*-isopropylidene-2,3-dihydroxy-1,4-bis(alkyl sulphanyl) butane (DIOS) derivatives were employed in this work, figure 19. It is envisioned that this asymmetrical chelate can impose its chirality upon the final hydroformylation product composition.

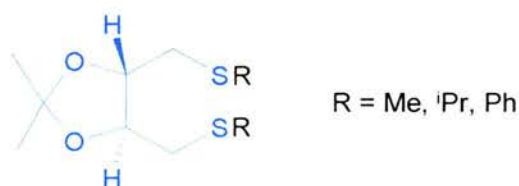


Figure 19: The DIOSR₂ ligand.

Other chiral dithioether ligands, figure 20, have previously been tested⁴⁸ for activity in the Rh(I) catalysed hydroformylation reaction. All these molecules are neutral^{xx} and, in the case of BINASR₂, no excess ligand was required to obtain efficient catalytic activity or regioselectivity. In addition the coordination of chiral thioether ligands, through sulphur to the transition metal, creates a new stereogenic centre within the complex.

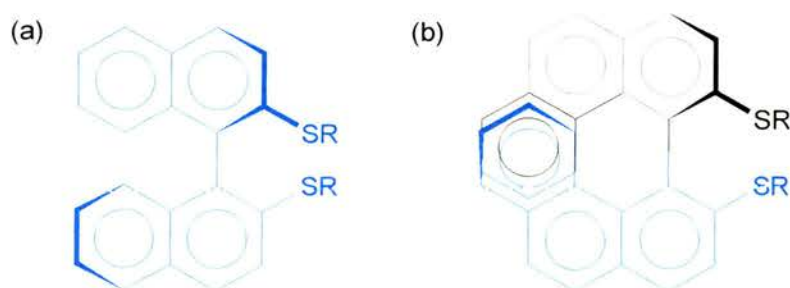


Figure 20: Two chiral sulphur containing ligands: (a) BINASR₂ = 1,1'-binaphthalene-2,2'-dithioether and (b) BIPHESR₂ = 4,4'-biphenanthrene-3,3'-dithioether. R = Me, ⁱPr.

^{xx} The catalytic ligand/Rh ratio can be optimised without affecting the final charge balance within the complex.

In the longer term, immobilisation of these asymmetric ligands would allow easy recovery of the active species. Reuse would also offset the high cost (time/effort) of asymmetric ligand synthesis. It is for these reasons that this project has focussed upon tethering DIOSR_2 ligands within the mesoporous silicate SBA-2.

Rh Experimental

Instrumentation

Microanalyses were carried out on a Carlo Erba Elemental Analyser model 1106, suitable for weight % C, H and N determination.

An HP 5890 Series II capillary column was used to separate the products, under a carrier gas pressure of 150 kPa. The following GC programme was employed. The temperature was maintained at 80 °C for 3.5 min before being increased at a rate of 10 °Cmin⁻¹ to 130 °C. The retention times of styrene, 2-phenyl propanal and 3-phenyl propanal were 5.12, 8.96 and 10.29 min respectively.

Ligand Synthesis

The DIOSR₂ ligands were synthesised according to literature procedures^{49,50} by Dr Nazira Karodia, figure 21.

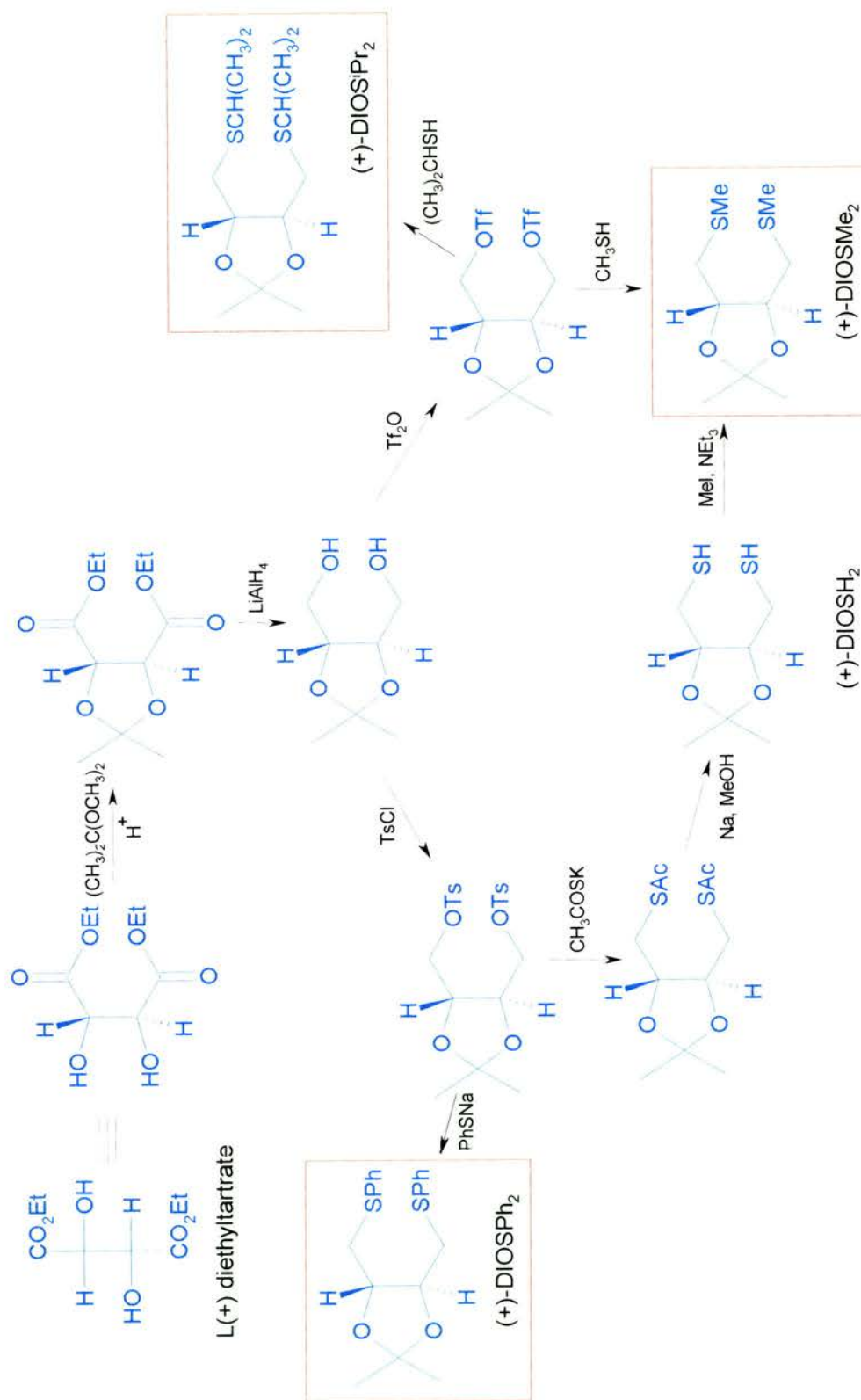


Figure 21: Synthesis scheme for the DIOSR₂ ligands used in SBA-2-supported rhodium catalysis.

Finally the ligands were deprotected, to be available for tethering onto the solid support, figure 22. Thus the protected diol (100 mmol) was added to a suspension of DOWEX 50W resin in a 1:1 acetone:H₂O solution (10 ml). The mixture was stirred at RT for 48 hours. This mixture was then filtered, the solvent evaporated, and the crude product recrystallised from ether/hexane to recover the colourless solid. The purity of the diol product was monitored by solution NMR (disappearance of ¹H 1.45 ppm, s, 6H, CMe₂; ¹³C 27.2 ppm, CMe₂ and 109.0 ppm, CMe₂).



Figure 22: Deprotection scheme for DIOSR₂ ligands.

Preparation of DIOSR₂ functionalised SBA-2

The external surfaces of SBA-2 were first deactivated with dichlorodimethylsilane, and then the internal silanol species functionalised with the glycidoxypropyltrimethoxysilane tether. The reaction conditions for this step have been described previously, in the manganese catalysis section.

Both the DIOSMe₂ and DIOSPh₂ ligands were attached to this solid; the procedure is illustrated here for DIOSMe₂. Thus a 30 % excess of the deprotected ligand (73 mg, 0.40 mmol) was weighed into a schlenk tube and flushed with argon. To this two equivalents of sodium methoxide (43 mg, 0.80 mmol) were added, followed by dry methanol (12 ml). The solution was then transferred to a flask containing the tethered SBA-2 solid (200 mg, nominally 0.3085 mmol tether). The tether-DIOSMe₂ coupling reaction was carried out under reflux, under Ar and over 24 hours. Finally the suspension was purified by soxhlet extraction using methanol, for 6 hours under Ar. Note: sodium methoxide was added to create a formal negative charge (–O[–]Na⁺) on the two DIOSMe₂ hydroxyl groups. These can then be used to ring open the tethered epoxide, figure 23.

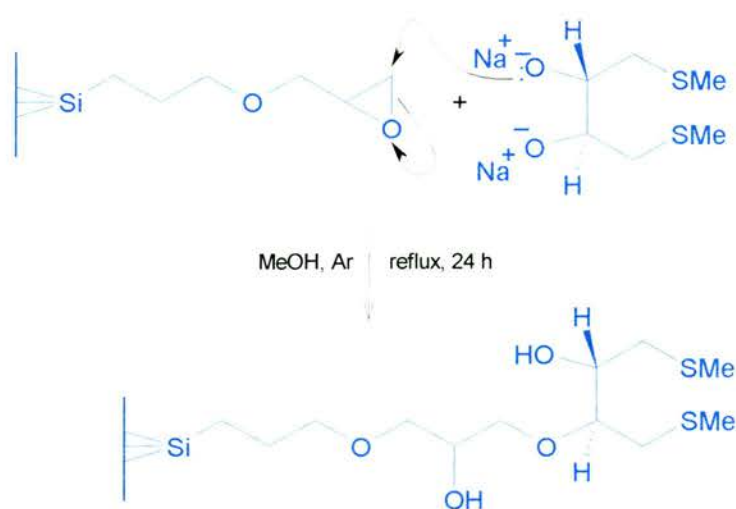


Figure 23: Tether-DIOSMe₂ coupling reaction.

Hydroformylation of Styrene

The hydroformylation of styrene, figure 24, was performed in an analogous manner to the homogeneous experiments⁵¹ of Dr Montserrat Dieguez-Fernandez. Unfortunately time constraints meant that only the SBA-2-DIOSMe₂ solid could be tested. The Rh tethered complex was formed *in situ*, figure 25.

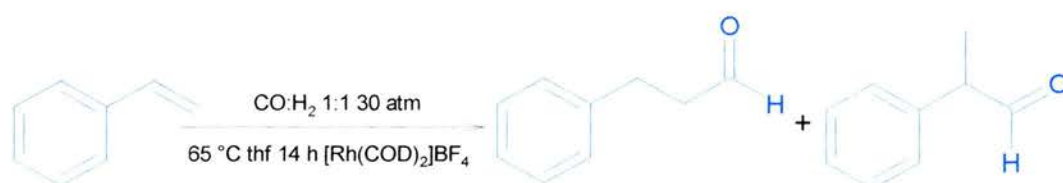


Figure 24: Hydroformylation of styrene.

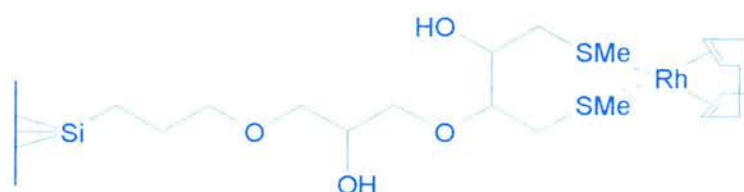


Figure 25: SBA-2 tethered rhodium complex expected to be present during styrene hydroformylation.

Thus styrene (1 ml, 8.73 mmol) was added to degassed thf (4 ml, 0.49 mmol). The rhodium source (5 mg, 0.0123 mmol), as $[\text{Rh}(\text{COD})_2]\text{BF}_4$,^{xxd} was then added to this solution. Meanwhile the autoclave, containing the SBA-2-ligand material^{xxi} (50 mg) and a magnetic stirrer bar, was pressurised with a $\text{CO}:\text{H}_2$ 1:1 mixture. A final reaction pressure of 30 atm, i.e. 15 atm CO : 15 atm H_2 , was chosen. Subsequently the rhodium containing solution was added to the autoclave. The stirred reaction ran for 14 h at 65 °C. After reaction the autoclave was depressurised and both the solid and solution recovered. The solid was reused, in a repeat experiment, under the same reaction conditions. The solvent in the solution, meanwhile, was evaporated, and the liquid product analysed by GC and solution NMR (^{13}C and ^1H).

^{xxd} COD = 1,5 cyclooctadiene

^{xxi} Assumes 10 wt% of the solid is ligand.

Rh Analysis

The tethering process was monitored by elemental analysis, table 9. As before it was partially successful. These CHN values reveal that SBA-2 functionalisation with 3-glycidoxypropyltrimethoxysilane gave a 35.4 % yield, equivalent to 0.80 mmol tether (g silica)⁻¹. Subsequent addition of the DIOSR₂ ligands, though, is particularly revealing. It appears that the DIOSMe₂ coupling reaction was 51.2 % efficient; however the analogous DIOSPh₂ addition gave only a 13.6 % yield. In the absence of any sulphur analysis it can only be assumed that these values are due to the ligand alone (i.e. not simply some remaining solvent). Furthermore they tend to suggest that the DIOSPh₂ molecule is too large to fit through an SBA-2 pore opening, and attach itself to the internal functionalised surface. The 9.1 wt% carbon loss following catalysis, meanwhile, indicates that some tether, ligand or indeed solvent may have been physisorbed within the mesoporous material during previous analyses. Finally, based upon the calculated 0.41 mmol DIOSMe₂ (g silica)⁻¹ loading, the addition of rhodium for catalysis was underestimated by 25 %.

	DIOSMe ₂			DIOSPh ₂		
	%C	%H	%N	%C	%H	%N
tether	5.23	0.66	-	5.23	0.66	-
+ ligand	8.17	1.31	-	7.32	1.52	-
after catalysis	7.43	0.93	-			

Table 9: Elemental analysis of functionalised SBA-2.

The catalytic results of the rhodium-supported hydroformylation of styrene are presented in table 10, alongside those of the analogous homogeneous reaction.

	heterogenized		homogeneous
	initial	repeat	
% conversion (TON) ^a	7.0 (50)	0.5 (4)	57.0
% <i>n</i> : <i>iso</i> ^b	35 : 65	22 : 78	31 : 69

(a) Turnover number TON = (mol substrate converted) / (mol Rh)
 (b) *n* = 3-phenyl propanal, *iso* = 2-phenyl propanal, %*n* = (*n*/(*n*+*iso*))×100

Table 10: Hydroformylation of styrene using Rh(COD)-DIOSMe₂.

It is clear that the SBA-2 supported reaction is far less active than its homogeneous counterpart. It appears, though, that some tethered rhodium complex has formed, since the repeat reaction is also, if only just, catalytically active. This reduced conversion

suggests that leaching of the rhodium complex has occurred. Indeed, following each heterogenized catalysis experiment the product solution was red coloured, characteristic of soluble Rh^{I} species. Meanwhile, the low conversions might be explained by diffusional limitations imposed upon the system due to tethering. In particular, the experimental procedure was such that the rhodium source was added to the reaction at the same time as the substrate. Each, therefore, was required to undergo diffusion before complexation (and then reaction) could occur. Meanwhile, the lack of bulky ligands, in all cases, can explain the regioselectivity tending towards the Markovnikov addition product (2-phenyl propanal). At these low conversions the % ee is not a particularly valuable guide.

No presence of any C-H stretches were observed in the FTIR spectra of the ligand-containing SBA-2 solids. Again this can be attributed to the very strong Si-O stretch at 1100 cm^{-1} overshadowing the weaker peaks.

Rh Summary

From elemental analysis it is apparent that the heterogenization of a rhodium-DIOSMe₂ complex within the mesoporous silicate SBA-2 is feasible. Subsequent use as a styrene hydroformylation catalyst, however, shows that the solid is easily recovered (by filtration) and can be recycled, although rhodium leaching occurs. It is thought that the low conversions could be improved through optimisation of the experimental technique.

General Summary

Various approaches towards incorporating transition metals within silicate frameworks have been considered, with a view to examining their catalytic potential. In general, though, the activities were disappointing. Indeed, following optimisation of the $\text{Ti}(\text{OEt})_4$ and TEOS rates of hydrolysis there is no obvious reason why titanium-containing SBA-2 should not possess epoxidation activity akin to that of other mesoporous materials. Likewise the grafting approaches to Mn and Rh incorporation within SBA-2 are comparable to literature procedures. Perhaps, therefore, the SBA-2 framework does not possess an ideal topology and/or is easily blocked during post synthetic modification. Further analysis of the tethered complexes (MAS NMR, ESR, Adsorption Isotherms) and the catalysis reaction products (GCMS) may aid in this understanding. Alternatively examination of similar 'connected-cage' mesoporous structures with larger pore diameters might be more profitable.

General References

- ¹ F Joó, Á Kathó, *J. Mol. Catal. A: Chemical*, 1997, **116**(1-2), 3.
- ² E de Wolf, G van Koten, B-J Deelman, *Chem. Soc. Rev.*, 1999, **28**(1), 37.
- ³ I Bach, DJ Cole-Hamilton, *J. Chem. Soc. Chem. Commun.*, 1998, 1463.
- ⁴ JWJ Knapen, AW van der Made, JC de Wilde, PWNM van Leeuwen, P Wijkens, DM Grove, G van Koten, *Nature*, 1994, **372**, 659.
- ⁵ N Karodia, S Guise, C Newlands, J-A Andersen, *J. Chem. Soc. Chem. Commun.*, 1998, 2341.
- ⁶ KJ Balkus, AG Gabrielov, *J. Inclus. Phenom. Molec. Recogn. Chem.*, 1995, **21**(1-4), 159.
- ⁷ RA Sheldon, J Dakka, *Catal. Today*, 1994, **19**(2), 215.
- ⁸ L Canali, E Cowan, H Deleuze, CL Gibson, DC Sherrington, *J. Chem. Soc. Chem. Commun.*, 1998, 2561.
- ⁹ N Herron, GD Stucky, CA Tolman, *Inorg. Chim. Acta*. 1985, **100**(1), 135.

Ti References

- ¹⁰ G Strukul, *Catalysis by Metal Complexes: Catalytic Oxidations with Hydrogen Peroxide as Oxidant*, 1992, Kluwer, The Netherlands.
- ¹¹ MB Smith, *Organic Synthesis*, 1994, McGraw-Hill Inc., New York, USA.
- ¹² KA Jørgensen, *Chem. Rev.*, 1989, **89**(3), 431.
- ¹³ M Taramasso, G Perego, B Notari, *Chem. Abstr.*, 1981, **95**, 206272k.
- ¹⁴ MA Cambor, M Costantini, A Corma, L Gilbert, P Esteve, A Martínez, S Valencia, *J. Chem. Soc. Chem. Commun.*, 1996, 1339.
- ¹⁵ A Corma, MT Navarro, J Pérez-Pariente, *J. Chem. Soc. Chem. Commun.*, 1994, 147.
- ¹⁶ KA Koyano, T Tatsumi, *J. Chem. Soc. Chem. Commun.*, 1996, 145.
- ¹⁷ MA Cambor, A Corma, P Esteve, A Martínez, S Valencia, *J. Chem. Soc. Chem. Commun.*, 1997, 795.
- ¹⁸ A Corma, JL Jordá, MT Navarro, F Rey, *J. Chem. Soc. Chem. Commun.*, 1998, 1899.
- ¹⁹ T Maschmeyer, F Rey, G Sankar, JM Thomas, *Nature*, 1995, **378**, 159.
- ²⁰ W Adam, A Corma, TI Reddy, M Renz, *J. Org. Chem.*, 1997, **62**(11), 3631.

- ²¹ L Marchese, E Gianotti, V Dellarocca, T Maschmeyer, F Rey, S Coluccia, JM Thomas, *Phys. Chem. Chem. Phys.*, 1999, **1**(4), 585.
- ²² GN Vayssilov, *Catal. Rev.-Sci. Eng.*, 1997, **39**(3), 209.
- ²³ D Tankanak, MA Vincent, IH Hillier, *J. Chem. Soc. Chem. Commun.*, 1998, 1031.
- ²⁴ RA Sheldon, J Dakka, *Catal. Today*, 1994, **19**(2), 215.
- ²⁵ RD Oldroyd, JM Thomas, T Maschmeyer, PA MacFaul, DW Snelgrove, KU Ingold, DDM Wayner, *Angew. Chem. Int. Ed. Engl.*, 1996, **35**(23/24), 2787.

Mn References

- ²⁶ PW Atkins, *Physical Chemistry*, 1990, 4th Ed., OUP, Oxford, UK.
- ²⁷ AR West, *Basic Solid State Chemistry*, 1988, John Wiley and Sons, Chichester, UK.
- ²⁸ A Putnis, *Introduction to Mineral Sciences*, 1992, Cambridge University Press, Cambridge, UK.
- ²⁹ DE De Vos, BM Weckhuysen, T Bein, *J. Am. Chem. Soc.*, 1996, **114**(40), 9615.
- ³⁰ PM Price, JH Clark, DJ Macquarrie, *J. Chem. Soc. Dalton Trans.*, 2000, **2**, 101.
- ³¹ JH Clark, DJ Macquarrie, *J. Chem. Soc. Chem. Commun.*, 1998, 853.
- ³² RA Sheldon, JK Kochi, *Metal-Catalysed Oxidations of Organic Compounds*, 1981, Academic Press, New York, USA.
- ³³ KA Jørgensen, *Chem. Rev.*, 1989, **89**(3), 431.
- ³⁴ KJ Balkus Jr, AG Gabrielov, *J. Inclus. Phenom. Molec. Recog. Chem.*, 1995, **21**(1-4), 159.
- ³⁵ W Zhang, JL Loebach, SR Wilson, EN Jacobsen, *J. Am. Chem. Soc.*, 1990, **112**(7), 2801.
- ³⁶ L Canali, DC Sherrington, *Chem. Soc. Rev.*, 1999, **28**(2), 85.
- ³⁷ SB Ogunwumi, T Bein, *J. Chem. Soc. Chem. Commun.*, 1997, 901.
- ³⁸ MJ Sabater, A Corma, A Domenech, V Fornés, H García, *J. Chem. Soc. Chem. Commun.*, 1997, 1285.
- ³⁹ DE De Vos, T Bein, *J. Chem. Soc. Chem. Commun.*, 1996, 917.
- ⁴⁰ R Hage, JE Iburg, J Kerschner, JH Koek, ELM Lempers, RJ Martens, US Racherla, SW Russell, T Swarthoff, MRP van Vliet, JB Warnaar, L van der Wolf, B Krijnen, *Nature*, 1994, **369**, 637.

- ⁴¹ DE De Vos, JL Meinershagen, T Bein, *Angew. Chem. Int. Ed. Engl.*, 1996, **35**(19), 2211.
- ⁴² DE De Vos, J Meinershagen, T Bein, *Stud. Sur. Sci. Catal.*, 1996, **101**(PtA+B), 1303.
- ⁴³ YVS Rao, DE De Vos, T Bein, PA Jacobs, *J. Chem. Soc. Chem. Commun.*, 1997, 355.
- ⁴⁴ DE De Vos, T Bein, *J. Organomet. Chem.*, 1996, **520**(1-2), 195.

Rh References

- ⁴⁵ FA Cotton, G Wilkinson, *Advances Inorganic Chemistry*, 1988, 5th Ed., John Wiley & Sons, New York, USA.
- ⁴⁶ WMH Sachtler, *Acc. Chem. Res.*, 1993, **26**(7), 383.
- ⁴⁷ GW Parshal, SD Ittel, *Homogeneous Catalysis*, 1992, 2nd Ed., John Wiley & Sons, New York, USA.
- ⁴⁸ JC Bayón, C Claver, AM Masdeu-Bultó, *Coord. Chem. Rev.*, 1999, **193-195**, 73.
- ⁴⁹ M Carmack, CJ Kelley, *J. Org. Chem.*, 1968, **33**(5), 2171.
- ⁵⁰ BR James, RS McMillan, *Can. J. Chem.*, 1977, **55**, 3927.
- ⁵¹ M Dieguez-Fernandez, PhD Thesis, 1997, Universitat Rovira i Virgili, Tarragona, Spain.

Conclusions & Further Work

Conclusions

The SBA-2 mesoporous silicate framework was first reported¹ by Stucky *et al* in 1995. At that time the mesoporosity of this material was particularly poorly understood. This work, therefore, aimed to rectify this. Thus the structure has been repeatedly synthesised, extensively characterised and subsequently used in catalysis. The conclusions from these findings are as follows.

Synthesis

SBA-2 forms around micelles composed of the divalent quaternary surfactant Cn-3-1. The synthesis is straightforward requiring a mixture of molar ratio 0.05 Cn-3-1 : 0.5 base : 1 TEOS : 150 H₂O and will form over 2 hours at room temperature, if well homogenised initially. Like other mesoporous silicates the framework is composed of incompletely condensed silica, contracts upon calcination and exhibits type IV adsorption isotherm behaviour. In addition the structure is thermally stable (1000 °C) and does not deteriorate over time (>6 months). The quality of the solid, however, is influenced by the reaction conditions. Of principle concern is the reaction pH. It appears that a window of pH 11-12 yields a material with the highest overall order, as demonstrated by the definition in the 3 – 5 °2θ X-ray diffraction pattern. Moreover there is a strong correlation between the synthesis pH and final framework dimensions (as the pH decreases, the unit cell size increases). This suggests that the base-derived OH⁻ ion actively participates in charge matching at the surfactant-silica interface. An increase in reaction temperature and/or time serve to enhance silicate condensation (MAS NMR), although no associated improvement in framework order is seen by XRD. Reaction temperatures above 120 °C initiate surfactant degradation (Hofmann elimination) and thereby prevent mesophase formation. In addition, the surfactant is efficiently used within the system, whilst inefficient silica use is offset by its lesser cost. Finally, tetravalent heteroatoms (Ti) may be incorporated within SBA-2, with the retention of framework order. Direct synthesis inclusion of the trivalent aluminium cation, though, reduces the structural order (XRD) and particle size (TEM). Presumably this is due to a perturbation in the subtle micelle-silicate charge balancing processes.

Mesoporous topology

Mesoporous materials are well suited to characterisation by transmission electron microscopy (TEM) as a result of the paucity of information that they yield from conventional powder techniques (XRD). In addition the calcined solids are stable in the electron beam (low water content) and can be imaged at low magnification without any loss of information (large pore dimensions). Thus the calcined SBA-2 structure, templated by spherical micelles appears as a 2D arrangement of spots (mesocages) in a high resolution TEM image. Careful inspection of these images shows that both hexagonal (ABAB...) and cubic (ABCABC...) arrangements of close packed cages are present. This is the first evidence to suggest that polytypic intergrowths, well known in zeolitic systems, can be present in mesoporous materials. Thus the hexagonal stacking sequence defines the SBA-2 framework, whilst face centred cubic ordering has been designated STAC-1 (*St Andrews – Cambridge – 1*). The TEM technique of through-focal imaging and computer image simulations have uncovered the corresponding pore connectivities. For SBA-2 straight channels form along a and are intersected in a zig-zag manner down [001]. Meanwhile STAC-1 is composed of intersecting straight channels. Each topology, therefore, comprises of a 2-dimensional channel network. Furthermore spherical and flat-sheet particles were imaged and show that within each morphology both mesoporous architectures are found. These observations, along with the presence of a 1:1 hexagonal : cubic intergrowth, within a flat-sheet particle, further suggest that micelle stacking is subtly controlled by Coulombic interactions.

Aluminium catalysis

ICP-AES has determined that direct synthesis of aluminium-containing SBA-2 is dependent upon the metal precursor. When a monomeric isopropoxide source is used, Al is more easily assimilated into the final framework, albeit at a cost to the structural order. Meanwhile an increase in the trivalent heteroatom loading further reduces this long range order. ^{27}Al MAS NMR indicates that the as-prepared materials possess tetrahedral Al species, however, calcination causes a range of 4-, 5-, and 6-fold coordination environments to develop. The Al-containing SBA-2 topology is a mild

solid acid, which is unable to catalytically crack isobutane. Nevertheless this material is effective towards butene isomerisation, and deactivates only slowly. Despite heavy-aromatic carbon build-up a type IV isotherm is retained, after an 88 hour reaction, although the total pore volume is much reduced. This suggests that the acid sites within the framework remain accessible during coking and that the mesopores are not rapidly blocked. Such a material could potentially act as a 'carbon' molecular sieve. The coked solid, though, can be regenerated (calcined) without significant loss of catalytic activity.

Transition Metal Catalysis

UV-Vis spectroscopy upon the SBA-2 solids containing titanium suggest that oligomeric Ti species are present. During catalysis these materials turned yellow – indicative of a Ti-peroxide complex. The epoxide products, however, could not be satisfactorily identified and in general catalysis was inconclusive. Meanwhile electrostatic incorporation of manganese, by ion exchange, within the zeolites Y, hexagonal Y and L was successful and quantitative. Subsequent cyclic triamine ligand incorporation did not work, nor did the tethering of an equivalent complex to the internal surfaces of SBA-2. In spite of this the tethered complex within MCM-48 exhibited some slight catalytic activity, suggesting that the experimental technique requires improvement and/or the pore volume within SBA-2 is too small to accommodate such complexes. A Rh-DIOSMe₂ complex tethered within SBA-2 was marginally catalytic towards styrene hydroformylation. This material, however, was poorly active upon reuse, suggesting that rhodium leaching or active species degradation had occurred.

Further Work

This thesis has shown that much effort has gone into understanding the synthesis requirements and final topology and catalytic potential of the mesoporous silicate SBA-2. The work, however, has also demonstrated that some areas require further investigation, or merit analogous studies.

It is clear that the Cn-s-1 surfactant forms well-ordered SBA-2 in a reproducible manner. It would be interesting, therefore, to develop similar surfactants and test their corresponding ability to micellize and template silica condensation. For example (i) alteration of the methyl-ammonium groups (to ethyl or propyl) and use of (ii) branch-tailed, or (iii) bi-tailed diquatery ammonium, (iv) diazabicyclo ammonium or (v) dendritic surfactants, figure 1, are all design possibilities. These molecules may in turn generate new mesoporous architectures or form phase pure SBA-2 or STAC-1. Indeed the development of a pure sample of STAC-1 may be achieved simply by seeding a synthesis mixture with particles in which this topology predominates. In all cases, though, TEM would be required to unambiguously distinguish the (i) morphology, (ii) phase purity and (iii) mesoporosity within the recovered material.

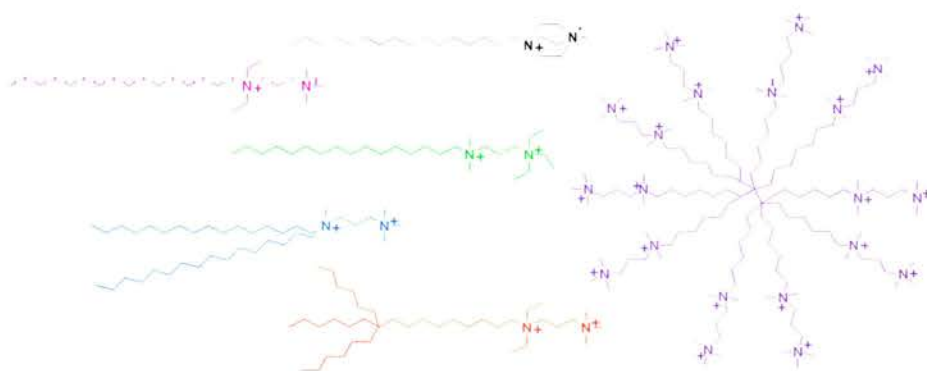


Figure 1: Designs for quaternary ammonium surfactants to act as mesoporous silica templating assemblies.

Meanwhile, on the basis of TEM investigations this work proposes specific pore connectivities for SBA-2 and STAC-1. An ensuing project, therefore, would be to take these models and generate the theoretical X-ray diffraction patterns for each. Subsequent comparison to the experimentally obtained diffractograms would confirm the proposed framework porosities.

In addition further examination of the charge matching process, during Cn-s-1 silicate aggregation, could potentially lead to the formation of a whole particle free from polytypic intergrowths. To achieve this the reaction pH requirements, influence of spectator ions (Br^- , TMA^+ etc.) or even use of tetramethylammonium fluoride as the base are worthy of more detailed assessment. Alternatively the temperature and/or time length of post synthesis drying (prior to calcination) may lead to enhanced morphological control. Indeed the synthesis of a large thin flat-sheet particle free from stacking defects, would greatly elucidate the potential uses of this mesoporous silicate.

An alternative avenue of investigation is the functionalization of the internal surface either during mesophase formation or as a post synthesis modification. For example thiol functionalised SBA-2 could be used in heavy metal absorption/complexation or, in its oxidised form, as an alternative solid acid catalyst. Base catalysis using this mesoporous topology could also be considered if, say, the internal surface was amine functionalised.

Finally further studies on the synthesis of titanium- and aluminium-containing SBA-2 would be beneficial. Particularly in reference to understanding the titanium co-ordination environment (EXAFS) and improvement in structural order as the aluminium content is increased. Temperature programmed desorption of adsorbed bases would also indicate the strength of the acid sites present. Meanwhile improvement in the tethering technique and further characterisation during this procedure (MAS NMR) is required for the materials containing encapsulated complexes. These findings may, in turn, explain the current catalysis results.

Reference

- ¹ Q Huo, R Leon, PM Petroff, GD Stucky, *Science*, 1995, **268**(5215), 1324.